A Rapid Method of Ca-alginate Microgel Particle Production and Encapsulations of Water-Soluble and Water-Insoluble Compounds via the Leeds Jet Homogenizer

Linda Christina Pravinata

Submitted in accordance with the requirements for the degree of Doctor of Philosophy

The University of Leeds
School of Food Science and Nutrition

August 2017

The candidate confirms that the work submitted is her own, except where work which has formed part of jointly-authored publications has been included. The contribution of the candidate and the other authors to this work has been explicitly indicated below. The candidate confirms that appropriate credit has been given within the thesis where reference has been made to the work of others.

This thesis has contributed to the following publication based on Chapter 3 and 5:

Pravinata, L., Akhtar, M., Bentley, P. J., Mahatnirunkul, T., & Murray, B. S. (2016). Preparation of alginate microgels in a simple one step process via the Leeds Jet Homogenizer. *Food Hydrocolloids*, *61*, 77–84.

List of Accepted Abstracts for Conferences

This work has also been presented by the author at the following events:

1. Poster presentation: “A novel technique to produce alginate submicron particles via a jet homogenizer”, IFST Jubilee Conference, 14th May 2014, London, UK.

2. Oral presentation: “A novel technique to produce alginate submicron particles via a jet homogenizer”, Food Science and Nutrition PhD conference, 24th September 2014, University of Leeds, UK.

3. Oral presentation (*Finalist*): “A rapid method to produce submicron calcium alginate gel particles using a jet homogenizer”, 3MT Competition, Leeds Postgraduate Research Conference, 4th December 2014, University of Leeds, UK.

4. Poster presentation: “A method to produce alginate gel particles”, Food Science and Nutrition Industry Networking Seminar, 19th Jan 2015, Leeds, UK.

5. Oral presentation: “Evidences of micro and/or nano-sized gel particles of calcium alginate formed via a jet homogenizer”, Food Science and Nutrition PhD conference, 16th November 2015, University of Leeds, UK.

6. Poster presentation: “Formation of micro- and nano-sized gel particles of calcium alginate via the Leeds Jet Homogenizer”, 16th Food Colloids Conference, 10th -13th April 2016, Wageningen, The Netherlands.

7. Oral presentation (ePoster session): “A simple method to produce microgel particles rapidly via Leeds Jet Homogenizer and utilization of the microgels as a mode to encapsulate flavonoids”, IFT16 Annual Meeting and Food Expo, 16th-19th July 2016, Chicago, USA.

8. Oral presentation (*1st Winner* awarded by Institute of Physics): “Simplicity is the ultimate sophistication: a simple method to produce microgel particles”, KTN Early Young Researchers, 18th October 2016, Manchester, UK.

9. Oral presentation (*Invited speaker*): “A simple method to produce alginate microgel particles and its application for encapsulation”, Food Science and Nutrition PhD conference, 16th November 2016, University of Leeds, UK.

Acknowledgements

Firstly, my utmost appreciation and sincere gratitude goes to my supervisor, Prof. Brent S. Murray for his continual efforts in providing immense knowledge, personal and academic guidance, as well as his patience. His support has been truly invaluable throughout all the time of research and thesis writing. It has been a privilege to have worked with such a humble and well-rounded supervisor.

I would like to give acknowledgement and appreciation to the following people who have brought me to the world of Food Colloids. I am indebted to Dr. Paul Cornillon from General Mills who first introduced me to colloid science through agar gel research in Purdue University, USA. Second, thanks go to Dr. Richard Ludescher from Rutgers University, USA, who placed high hopes for me to complete the PhD study. Third, thanks to Mr. Richard Metivier from Pepsico R&D, USA, who has been my guru for dairy dip emulsion formulation which is a manifestation of food colloid applications. Most importantly, these people have believed in me to fulfil my potential to complete this study.

I would like to give special tributes to the following people who have offered stimulating suggestions and help with the equipment settings: Dr. Mahmood Akthar, Dr. Anwesha Sarkar, Dr. Melvin Holmes, Dr. Nataricha Phisarnchananan, Mr. Ian Hardy, Dr. Sirwan M. Rashid, Mr. Phillip Bentley, Ms. Ophelie Torres. My appreciation also goes to the University of Leeds for funding this project through the Leeds International Research Scholarship. Furthermore, I would also like to acknowledge BSc. and MSc. students that have assisted with their projects: Mr. Phuoc Hoang, Ms. Angela Budiono, Ms. Haijuan Fu, whose good works have been highlighted in the thesis, specifically in Chapters 4 and 5.

Many thanks go to my colleagues and friends that have offered valuable support, a listening ear and encouragement during tumultuous times: Dr. Tugba Aktar, Dr. Siti Fairuz Che Ohmen, Dr. Woroud Alsanei, Mr. Sandi Daniardi, Mr. Alessandro Gullota, Ms. Papoole Valadbaigi, Mrs. Omaima Khattab, Mrs. Maggi Bransby, Mrs. Fumiko Czarnecki, Mr. Tim Carr and my mentor Dr. Daisaku Ikeda.

Dedications

I dedicate this thesis to the Bong and Pravinata families for their unconditional love and support.

I also dedicate this thesis to Ed and the Triple Cs, who have been the driving force for my motivation and success.

Abstract

Ca-alginate microgel particles have been extensively studied for use in various foods and in biomedical applications and are commonly produced using techniques, such as emulsification, prilling, microfluidic and spray-drying, which involve multiple processing steps, otherwise large particle sizes are yielded. This provides the motivation for this study: to produce the Ca-alginate microgel particles in a simple and rapid method via a Jet homogenizer developed by the University of Leeds School of Food Science and Nutrition. Furthermore, the aims are expanded to entrap water-soluble compounds (proteins and dyes) and water–insoluble compounds (polyphenols and β-carotene crystals).

The results indicated that tuneable sizes of microgel particles could be obtained from the Jet Homogenizer. Various SEM techniques revealed the microgel particles of sizes below 50 nm forming clusters in microregions of size < 1 μm, thus sonication was applied to break down the aggregates. The microgel particle sizes could be controlled by altering the concentrations and viscosities of the alginate and by changing the fluid velocity. Rheological measurements were also employed to estimate the intrinsic viscosity ([η]) and M_w of the elected alginate with low viscosity (LV) and to evaluate the apparent viscosity of the microgel suspensions over shear rates as a function of volume fraction (φ).

These microgel particles were utilized to encapsulate water-soluble cationic proteins (lactoferrin and lysozyme) and dyes (anionic erioglaucine and cationic methylene blue). Lactoferrin had shown some adsorption to the microgel particles as demonstrated from the reduction of particle size as the ζ-potential was less negative. Successful loading of erioglaucine was achieved with high loading efficiency and payloads, but rapidly released due to high porosity of the microgel particles. Lysozyme and methylene blue did not show any adsorption or entrapment but rather formed complexations with the alginate instead. The water-insoluble particles of polyphenols and β-carotene were also successfully loaded into the microgel particles as revealed by the images obtained from confocal (CLSM) and the light microscopies.

In short, the results have shown some firm evidence that Ca-alginate microgel particle formation and encapsulation of some the water-soluble and insoluble compounds within the Ca-alginate microgel particles can be achieved via this simple and effective technique.

Table of Contents

List of Accepted Abstracts for Conferences ..... **iii**
Acknowledgements ..... **iv**
Abstract ..... **vi**
Table of Contents ..... **viii**
List of Figures ..... **xi**
List of Tables ..... **xvii**
List of Abbreviations ..... **xviii**
Chapter 1 INTRODUCTION **1**
1.1 General Introduction 1
1.2 Research Aims 7
1.3 Plan of thesis 7
1.4 Backgrounds 9
1.4.1 Alginate and the gelation with cations 9
1.4.2 Flash nanoprecipitation method via Leeds Jet Homogenizer as a microreactor 12
1.4.3 Encapsulation of water-insoluble and water-soluble compounds in Ca-alginate microgel particles 16
1.4.4 Water soluble lactoferrin and lysozyme encapsulation 18
1.4.5 Water-soluble dyes erioglaucine and methylene blue dyes encapsulation 22
1.4.6 Water-insoluble polyphenolic compounds of rutin, tiliroside, curcumin, and carotenoid of β-carotene 23
1.4.7 Microgel particles characterization 25
1.5 Conclusion 35
Chapter 2 Materials and Methods **36**
2.1 Materials 36
2.1.1 Water 36
2.1.2 Alginate 36
2.1.3 Calcium chloride 36
2.1.4 Buffer solutions 36
2.1.5 Water-insoluble compounds for encapsulation 37

2.1.6 Protein solutions....38
2.1.7 Water-soluble dyes....38
2.1.8 Magnetic Nanoparticles....38
2.1.9 General Chemicals....39
2.1.10 Filters....39
2.1.11 Cuvettes....40
2.1.12 Chemicals for CLSM preparation....40
2.2 Methods....42
2.2.1 Preparation of solutions....42
2.2.2 Microgel particles production and encapsulation via the jet homogenizer....45
2.2.3 Particle separation method....51
2.2.4 Particle characterizations and physical properties measurements....52
2.2.5 Drying experiments....56
2.2.6 Miscellaneous....57
Chapter 3 Formation of Ca-alginate microgel particles via Leeds Jet Homogenizer....59
3.1 Introduction....59
3.2 Results and Discussion....60
3.2.1 Effect of Ca^{2+} and alginate concentrations in microgel particle sizes....61
3.2.2 Effect of alginate viscosity in microgel particle sizes....64
3.2.3 Effect of volume chamber to the particle size....67
3.2.4 Microgel particle separation....70
3.2.5 The microgel yield, volume fraction (φ), and rheology of the suspensions....72
3.2.6 Micrographs of microgel particles....75
3.2.7 Particle reduction via sonication....78
3.3 Conclusions....80
Chapter 4 Encapsulation of water-insoluble polyphenols and β-carotene in Ca-alginate microgel particles produced by Leeds Jet homogenizer....81
4.1 Introduction....81
4.2 Results and Discussion....82
4.2.1 Particle size distribution of the Ca-alginate microgel particles 82

4.2.2 Particle size of the polyphenol crystals and Ca-alginate microgel particles with encapsulated polyphenols.....83
4.2.3 Particle size of β-carotene encapsulated microgel particles..90
4.2.4 CLSM images of the water-insoluble materials encapsulated in Ca-alginate microgel particles 92
4.2.5 Light microscopy images of the water-insoluble materials encapsulated in Ca-alginate microgel particles.....98
4.2.6 Addition of magnetic nanoparticles (MNPs) suspension as a method of particles separation 101
4.2.7 Microgel Particle Yield.....105
4.2.8 Payload 109
4.2.9 Loading Efficiency 110
4.3 Conclusions.....116
Chapter 5 Encapsulation of water-soluble compounds in Ca-alginate microgel particles produced via Leeds Jet Homogenizer 117
5.1 Introduction.....117
5.2 Results and Discussion 118
5.2.1 Addition of lysozyme and lactoferrin during microgel formations 118
5.2.2 Amino acid composition and surface charges of lactoferrin and lysozyme 124
5.2.3 Calculation of mass ratio of lactoferrin covering the surface of a single particle of calcium alginate.....130
5.2.4 Encapsulation of water soluble dyes erioglaucine and methylene blue.....133
5.3 Conclusions.....144
Chapter 6 Conclusions and Future Works.....145
6.1 Factors that govern the microgel particle formation.....145
6.2 Rheological properties of Ca-alginate microgel suspensions 146
6.3 Microgel particle yield, payload, loading efficiencies from encapsulation. 146
6.4 Factors that affect the entrapment of encapsulated compounds onto or into the Ca-alginate microgel particles 147
6.5 Future work 147
REFERENCES 149

List of Figures

Figure 1-1. Illustration of particles stabilizing the oil droplets at the O/W interface either via (a) Pickering particles or (b) Microgel particles. 2

Figure 1-2. Methods to produce alginate microgel particles.....5

Figure 1-3. Alginate structures in G-G or M-M or G-M configurations (G: guluronate residue; M: mannuronate residue). 9

Figure 1-4. Schematic drawing of egg box junction between Ca^{2+} with the carboxylic group of guluronate chain in alginate.....10

Figure 1-5. Different approaches to produce biopolymer-based microgel particles, i.e., top down or bottom up methods. 13

Figure 1-6. Microgel particles can be filled with variety forms of compounds. 17

Figure 1-7. Lactoferrin structure in 3D ribbon diagram and the enlargement of one of the lobes with Fe^{3+} ion shown in the domain. The basic residues of arginine and lysine are highly exposed on the surface of the N-lobe (R 210, R121, and K301).....18

Figure 1-8. Lysozyme structure in (a) 3D diagram with the red spots indicate the presence of basic lysine residues on the surface (b) ribbon diagram.....20

Figure 1-9. Schematic representation of a negatively charged particles and the presence of its ions at the 'Diffuse layer' and 'Slipping plane'. 27

Figure 1-10. An illustration of different scattering patterns displayed a small (a) vs big particle (b) as illuminated by a laser beam. 28

Figure 1-11. Schematic illustration to describe the principle of confocal imaging. 30

Figure 1-12. Cone and plate geometry, where r = radius, θ = angle (in this experiment, θ = 1°), and y = gap distance. 33

Figure 2-1. Summary outline of all methods used in the experiments, from producing of the microgel, encapsulation, and characterization of the microgel particles and analysis.....41

Figure 2-2. Schematic diagram of the jet homogenizer.....45

Figure 2-3 Summary of steps to produce water-insoluble crystals and water-soluble dyes encapsulated microgel particles using the Leeds Jet homogenizer (a), separating the microgels using MNPs (b), extracting water-insoluble compounds with ethanol and dyes with Millipore water (c), and quantifying the entrapped amount from absorbance readings (d) 47

Figure 3-1. Microgel mean particle diameter (μ_z) prepared from varied Ca^{2+} concentrations at fixed 1 wt%. alginate LV (■) and from varied alginate - LV concentrations at fixed 10 mM Ca^{2+} (●). The arrows indicate the corresponding Y-axis.....61

Figure 3-2. Plot of $[(\eta/\eta 0 -1)/c]$ as a function of alginate concentration (c) to determine the intrinsic viscosity (η) of alginate LV at 25°C dissolved in Millipore water. 63

Figure 3-3. Dynamic viscosity (η) of 1 wt.% of alginate solutions over shear rates (γ) at room temperature.....66

Figure 3-4. Microgel particle mean diameters (μ_z) produced via Leeds Jet Homogenizer (LJH) in 80:20 ratio S block from 10 mM Ca^{2+} and 1 wt.% alginate low viscosity (LV), medium viscosity (MV), and high viscosity (HV).....66

Figure 3-5. Jet homogenizer diagram to illustrate the changes of volume of S and D blocks are affecting the volume of A and C chambers.....67

Figure 3-6. The microgel particle mean diameters (μ_z) from alginate LV and HV produced via Leeds Jet Homogenizer (LJH) using volume chamber of S and D blocks.....69

Figure 3-7. The fluid velocities (v) of alginate LV and HV in S and D blocks in the Leeds Jet Homogenizer (LJH).....69

Figure 3-8. (a) Pictures of microgel suspension concentrate solutions after drying at 47 % moisture loss (φ= 0.065) and centrifuged for 48,000 g for 20 minutes (b) Micrographs of the microgel particles from top and bottom of the centrifuge tubes viewed by light microscope at 20x magnification. 71

Figure 3-9. The density (ρ) of microgel suspension as a function of moisture loss due to air-drying at room temperature. The inset graph is a plot of calculated φ as a function of moisture loss. 72

Figure 3-10. Viscosity of microgel suspension at different volume fraction (φ) as a function of shear rates (γ). 73

Figure 3-11. Viscosity of microgel suspension at φ = 0.035 (before drying) and viscosity of sediment (microgel particles) and supernatant (aquaeous phase) after centrifugation for 20 minutes at 48,000g. The inset graph is a rescaled plot of the viscosity of microgel suspension at φ = 0.035 and supernatant.....74

Figure 3-12. Micrographs obtained via SEM method of (a) 1 wt.% alginate LV solution (b) microgel particles prepared from 1 wt.% alginate and 10 mM Ca^{2+} and (c) enlarged microgel particles images of (b) with higher magnification and approximated microgel particle sizes 76

Figure 3-13. Micrographs of microgel particles prepared from 1 wt.% alginate and 10 mM Ca^{2+} obtained via (a) FE-SEM, (b) TEM, (c) E-SEM, (d) enlarged from (c) to show the presence of aggregates ..77

Figure 3-14. Particle size distribution by volume percentage (V) of Ca-alginate microgel particles prepared from 1 wt.% alginate and 10 mM $CaCl_2$ in the 80:20 S block of the jet homogenizer before (———) and after (----------) sonication. 78

Figure 3-15. Ratio of Ca-alginate microgel particles mean diameter after (μ_z^s) and before (μ_z^o) sonication versus sonication time (t).....79

Figure 4-1. Particle size of Ca-alginate microgel particles produced from 20 mM Ca^{2+} and 2 wt.% of alginate in 0.02 M of imidazole buffer pH 5 and 8. 83

Figure 4-2. Particle size distribution of water-insoluble polyphenols (1 mM of rutin, tiliroside, and curcumin dispersed in Millipore water) as measured by Mastersizer (a) and filtered through Whatman 1 µm as measured by Zetasizer (b) 84

Figure 4-3. Particle size (μ_z) of 1mM rutin, tiliroside and curcumin dispersed in Millipore water filtered through Whatman 1 µm as measured by Zetasizer 84

Figure 4-4. Particle Sauter mean diameter (d_{32}) of Ca-alginate microgel particles with or without the insoluble polyphenols at pH 5 and 885

Figure 4-5. The particle size (r) of 100 µM tiliroside + 0.05 M NaCl versus ζ-potential. 87

Figure 4-7. Average net charge of curcumin as a function of pH, The dotted lines indicates the pHs used in the current study. 89

Figure 4-8.The ζ-potential of Ca-alginate microgel particles with and without polyphenols at pH 5 and 8 in 0.02 M imidazole buffer 89

Figure 4-9. Particle size of β-carotene crystals stabilized with TW20 dispersed in water (a) mixed at 24,000 rpm with Ultraturrax (b), added with 2 wt.% alginate and mixed at 24,000 rpm with Ultraturrax (c), homogenized and encapsulated in microgel particles (d) 91

Figure 4-10. CLSM image and its enlargement area of (a) dispersion of 1 mM tiliroside and (b) suspension of Ca-alginate microgel particles entrapped with 0.5 mM tiliroside made via the Leeds Jet Homogenizer (LJH), both were in 0.02 M imidazole buffer pH 5 and contained 2 wt.% gelatin to immobilize the particles. 93

Figure 4-11. The z-scan cross section of CLSM image of tiliroside encapsulated in ca-alginate gel particle at 458 nm (a) and 488 nm (b) excitation 94

Figure 4-12. CLSM images of encapsulated of (a) 0.5 mM tiliroside at pH 8, (b) 0.5 mM curcumin at pH 5, (c) 0.5 mM curcumin at pH 8 of 0.02 M imidazole bufffer. 95

Figure 4-13. CLSM images of β-carotene+TW20 encapsulated in Ca-alginate microgel particles.....97

Figure 4-14. Light microscope images of Ca-alginate microgel particles at pH 5 (a) and pH 8 (b) and curcumin encapsulated in Ca-alginate microgel particles at pH 5 (c) and 8 (d).....98

Figure 4-15. Micrographs of microgel particles with no β-carotene (a) and β-carotene encapsulated microgel particles with TW20 (b) ...99

Figure 4-16. Micrographs of (a) 1 wt.% curcumin and (b, c) 1 wt.% tiliroside encapsulated in κ-carrageenan microgel particles, made from 4 wt.% κ-carrageenan and 50 mM Ca^{2+} 100

Figure 4-17. Micrographs of (a) 1 wt.% rutin, (b and c) 1 wt.% crocetin, and (d) 1 wt.% naringin encapsulated in pectin microgel particles, made from 3 wt.% LM pectin and 25 mM Ca^{2+}.....100

Figure 4-18. Density values of water-insoluble compounds used for encapsulation.....101

Figure 4-19. Particle size (d_{32}) of Ca-alginate microgel particles (Ca-ALG) with and without magnetic nanoparticles (MNPs) at different refractive indices (n).....102

Figure 4-20. Particle size distribution of β-carotene encapsulated in Ca-alginate microgel particles with and without magnetic nanoparticles (MNPs) 103

Figure 4-21. Schematic illustration of surface area ratio of Ca-alginate microgel particles and magnetic nanoparticles (MNPs).....104

Figure 4-22. Microgel yield of Ca-alginate microgel particles with MNPs (0.02 %wt. concentration) and with or without the encapsulated materials 106

Figure 4-23. Correlation between the microgel yield of polyphenols (a) with physical properties of the crystals, i.e., density (b), Mw (c), crystal size (d).....108

Figure 4-24. Payloads of encapsulated microgel particles and their correlation with the polyphenol crystal sizes (displayed as an inset figure).....109

Figure 4-25. Loading efficiencies of encapsulated microgel particles and its correlation with the charge densities of the crystals (displayed as an inset figure) 111

Figure 4-26. Chemical structures of water-insoluble particles with its protonated and deprotonated state with N = number of charges113

Figure 5-1. Comparison of zeta potential (ζ) and Z-average (μ_z) of calcium alginate gel particles prepared from 1% alginate in the 80 block at various lysozyme concentrations (C) and 10mM $CaCl_2$ in 20 block: ζ and μ_z at pH 8 (■ , □); ζ and μ_z at pH 10 (●, ○). Lysozyme was added (a) in the alginate phase, ((b) calcium phase, (c) after the microgel had been formed.....120

Figure 5-2. Visual aspects of the cloudiness formed during mixing lysozyme in bicarbonate buffer at pH 8 with (a) 1 wt.% alginate solution (b) 10 mM $CaCl_2$ at pH 8 in bicarbonate buffer 121

Figure 5-3. Comparison of zeta potential (ζ) and Z-average (μ_Z) of Ca-alginate microgel particles prepared from 1 wt.% alginate in the 80 block and 10mM $CaCl_2$ in 20 block at various [lactoferrin]; ζ and μ_z at pH 6 (▲ , ∆); ζ and μ_z at pH 8 (■, □).....123

Figure 5-4. Number of charges (N) of lactoferrin, lysozyme, and guluronate or mannuronate as a function of pH.....126

Figure 5-5. Plot of mole charge ratio of the alginate monomers ($alginate_m$) to lactoferrin and lysozyme as a function of pH at 1 wt.% alginate and 0.1 wt.% proteins. 127

Figure 5-6. (a) Lactoferrin structure in 3D and ribbon diagram with the blue domain indicates the patches of positively charged amino acids mainly concentrated in N-terminus
(b) Schematic diagram of lactoferrin attachment to the surface of the microgel created a barrier for the lactoferrin to be incorporated inside the microgel due to unevenness distribution of charged surface patches. 129

Figure 5-7. Schematic drawings of the location of lysine residues (N=6) on the lysozyme surfaces with three orientations in the x, y and z directions.....129

Figure 5-8 Particle size distribution of lactoferrin at concentration of 0.32 wt.% in bicarbonate buffer at pH 6 (solid line) and 8 (dashed line) 130

Figure 5-9. A schematic figure to illustrate the calculation of lactoferrin surface coverage 131

Figure 5-10. Theoretical mass ratio of lactoferrin to alginate (m/M) required to cover 10% of the surface of Ca-alginate microgel particles at different diameters (d). 133

Figure 5-11. Chemical structures of water soluble dyes of erioglaucine and methylene blue 134

Figure 5-12. Total charges of erioglaucine and methylene blue as a function of pH. The dashed lines represent the elected pH in this study, i.e., 6.8 (blue). 134

Figure 5-13. Micrographs of erioglaucine encapsulated in Ca-alginate microgels produced via the jet homogenizer prepared from (a) 2 wt.% alginate+10ppm dye and 10 mM Ca^{2+} and (b) with 1 wt.% alginate+10 ppm dye and 20 mM Ca^{2+}, using 20x magnification lens.....136

Figure 5-14. Concentrations of erioglaucine (ER) and methylene Blue (MB) in the microgel vs. in the aqueous phase.....137

Figure 5-15. Microgel yield, loading efficiencies, and payloads of erioglaucine (ER) and methylene blue (MB) encapsulated in the ca-alginate microgels 138

Figure 5-16. Possible interactions of Erioglaucine with alginate 140

Figure 5-17. Percentage release of Erioglaucine/ER (a) and Methylene Blue/MB (b) released from the Ca-alginate microgel particles prepared from 1 wt.% alginate and 10 mM Ca^{2+} for (S) and 2 wt.% alginate and 20 mM Ca^{2+} for (L) as a function of time during dye extraction.....140

Figure 5-18. Four possible resonances of MB dimers, with a, b, ('sandwich') and c, d ('head to tail'). 142

Figure 5-19. Dimerization equilibrium of $2MB_{monomer} \leftrightarrow MB_{dimer}$ 142

List of Tables

Table 2.1. Types of alginate with different levels of apparent viscosity (η) 36

Table 2.2. Chemicals used to prepare the buffer solutions.....37

Table 2.3. Raw material suppliers and physical properties which include molecular weight (Mw), refractive index (n), and density (ρ) of water-insoluble compounds for encapsulation 37

Table 2.4. Raw materials suppliers, molecular weight (), and the solvent used to dissolved water-soluble compounds for encapsulation ..38

Table 2.5. List of chemicals used to produce magnetic nanoparticles .39

Table 2.6. List of chemicals used to prepare samples for CLSM analysis 40

Table 2.7. List of the absorbance peak, concentration range, and trendline equations of the encapsulated materials used to generate the standard curves.....50

Table 2.8. List of microscopes used in the experiments.....54

Table 3.1. The calculated fluid velocity (v), shear rates ($\dot{\gamma}$), and Reynold number (Re) of microgel suspension produced via the LJH using alginate LV, HV, and MV using S block.....67

Table 3.2. Maximum volume of the chambers containing alginate (A) and Ca^{2+} (C) for different S and D blocks for the same volume ratio of 80:20 67

Table 3.3. Particle sizes and densities of the microgel particles at different centrifuged locations 71

Table 4.1. Particle volume mean diameter (d_{43}) of Ca-alginate microgel particles with or without insoluble polyphenols at pH 5 and 8.....85

Table 4.2. Charge density of the polyphenol crystals 112

Table 5.1 Values of pK_a of amino acid residue side chains used to calculate charge of lysozyme and lactoferrin, taken from Damodaran (1996).....124

Table 5.2. Amino acid compositions of lysozyme (Manwell, 1967) and lactoferrin (Steijns & van Hooijdonk, 2007) 125

Table 5.3. Zeta potentials of the microgel particles with and without the water soluble dyes encapsulated.....138

List of Abbreviations

Abbreviations

ALG	alginate
Ca-ALG+BC	Calcium alginate microgel particles containing β-carotene
Ca-ALG+CU	Calcium alginate microgel particles containing curcumin
Ca-ALG+ER	Calcium alginate microgel particles containing erioglaucine
Ca-ALG+MB	Calcium alginate microgel particles containing methylene blue
Ca-ALG+R	Calcium alginate microgel particles containing rutin
Ca-ALG+T	Calcium alginate microgel particles containing tiliroside
CLSM	Confocal Laser Scanning Microscopy
CIJ	Confined Impingement Jet
Da	Damkohler number
D block	Double volume chamber in the jet homogenizer
DF	Dilution Factor
d.nm	Diameter in nanometres
ER	Erioglaucine
E-SEM	Environmental scanning electron microscopy
FE-SEM	Field emission scanning electron microscopy
G	guluronate
G_f	Guluronate fraction
GDL	Glucono delta lactone
GI	Gastro-intestinal
HLB	Hydrophilic lipophilic balance
HV	High viscosity
K_D	Dimerization constant
k_r	Reaction rate constant
(L)	Large
LJH	Leeds jet homogenizer
LV	Low viscosity
M	Mannuronate
M/G	Mannuronate to guluronate
MB	Methylene blue
MNP	Magnetic nanoparticle

MV	Medium viscosity
P	Probability value
PAA	4-phenylazoanililine
PGE_2	Prostaglandin E_2
pI	Isoelectric point
PSD	Particle size distribution
Re	Reynolds number
(S)	Small
S block	Single volume chamber in the jet homogenizer
S.G.	Specific gravity, $g.cm^{-3}$
SEM	Scanning electron microscopy
TEM	Transmission electron microscopy
TW20	Tween 20
t_m	Mixing time, ms
t_r	Reaction time, ms
wt.%	Percentage by weight

Symbols

n	Refractive index
v	Fluid velocity, $m.s^{-1}$
γ	Shear rates, s^{-1}
τ_r	Shear strain, Pa
ρ	Density, kg L^{-1} or $g.ml^{-1}$
ρ_m	Density of the microgel particles
ρ_s	Density of the microgel suspension
μ_z	Z-average mean diameter, nm
μ_z^s	Z-average after sonication
μ_z^o	Z-average before sonication
λ	Wavelength, nm
$\Delta\rho$	Density difference, kg L^{-1} or $g.ml^{-1}$
η	Viscosity, Pa.s
η_s	Viscosity of the solvent or base fluid, Pa.s
$[\eta]$	Intrinsic viscosity ($g.ml^{-1}$)
η_r	Relative viscosity

η_0	Viscosity in the absence of solute, Pa.s
K	Empirical constant in Mark-Houwink equation, characterized by solute-solvent interaction
α	Empirical constant in Mark-Houwink equation, characterized by solute-solvent interaction
ε	Molar extinction coefficient, $mol^{-1}.dm^3.cm^{-1}$
φ_m	Volume fraction at maximum packing
φ_{RCP}	Volume fraction random close packing
φ_o	Effective volume fraction
N	Number of
ζ	Zeta potential, mV
B^o	nucleation rate
R	Universal gas constant, 8.314×10^{-3} kJ.mole^{-1}k
T	Temperature (in Kelvin)
S	Degree of supersaturation
γ	Interfacial tension, $N.m^{-1}$
V_M	Molar volume, $m^3.mole^{-1}$
N_A	Avogadro constant, 6.022×10^{23} $mole^{-1}$
π	Mathematical constant, 3.14
C_r	Concentration of reactant, M
D	Diffusion coefficient
d_H	Hydrodynamic radius of a particle
d	diameter
k_b	Boltzmann's constant, 1.38×10^{-23} m^2 kg s^{-2} K^{-1}
U_E	Electrophoretic mobility
V_p	Particle velocity, $m.s^{-1}$
E_f	Electric field strength, $V.cm^{-1}$
$f(k_a)$	Henry's function
ε	Dielectric constant, $F.m^{-1}$
d_{32}	Particle mean diameter (surface area as weighting factor) or Sauter mean diameter
d_{43}	Particle mean diameter (volume as weighting factor) or Debroukere mean diameter

Ω	Angular velocity, rad.s^{-1}
M	Torque, N.m
m_m	Weight or mass of the microgel particles, g
m_s	Weight or mass of microgel suspension, g
m_i	Initial weight of microgel suspension, g
m_c	Weight of concentrated microgel suspension, g
X_T	the total weight of the encapsulated compounds in the system, g
X_m	the total weight of the encapsulated compounds inside the microgel particles, g

Chapter 1 INTRODUCTION

1.1 General Introduction

Microgel particles are defined as colloidal particles (with a size range of 100 nm to 1000 μm) comprising a high degree of cross-linked three dimensional polymer networks that are able to swell or deswell by absorbing or expelling solvent (typically water) in response to external stimuli, such as pH, temperature, and salinity. (Dickinson, 2015; Pelton & Hoare, 2011; Seiffert, 2013). Because of their responsiveness to the external environments, these 'intelligent' small particles have a wide range of uses in foods, biomedical and pharmaceutical applications (Augst, Kong, & Mooney, 2006; Malsten, 2011; McClements, 2017), oil recovery (Ben et al., 2011), ink-based 3D printing (Nakamura et al., 2008), and as microlenses and photonic crystals in sensing applications (Lyon, Hendrickson, Meng, & Iyer, 2011).

The materials used to construct the microgel particles are diverse, utilizing synthetic or biopolymers with high molecular weight (M_w). For food, pharmaceutical, and oral care industries, the biopolymer microgels are preferable due to their compatibility, natural and sustainable sources, and their affordability compared to high-cost petrochemical-based synthetic polymers (Pashkovski, 2011). These edible microgels have been developed using a range of materials, mostly proteins and polysaccharides that have long been used in food products for influencing the product quality and stability (McClements, 2015). Some comprehensive review articles about food biopolymer microgels that have highlighted the methods to fabricate the microgel particles, methods of characteristics, and their applications as foods are available and will be further expanded in this chapter (Dickinson, 2015; McClements, 2015, 2017; Rayner, 2015).

Microgel particles can undergo deformation and rearrangement at interfaces, thus they are known to be 'surface active', and can be utilized as food emulsion stabilizers (Dickinson, 2015). Food-grade protein microgel particles are just one type of novel food particle that might be exploited via the Pickering mechanism (de Folter et al., 2012; Destribats et al., 2014; Rayner,

2015). Although the microgel particles are classified as soft particles unlike Pickering stabilizers which are mostly hard particles, they can still form a viscoelastic monolayer at the O/W interface and act as good stabilizers as long as they maintain a size and contact angle sufficient to secure their interfacial attachment. 'Mickering' emulsions, as coined by Schmidt et al. (2011), is an elegant expression to describe an emulsion stabilized by protein microgel particles, see Figure 1-1. Sağlam, Venema, van der Linden, & de Vries (2014) and Dickinson (2015) have recently reviewed a number of advances in the production of nanoscale protein microgel particles of well-defined sizes or shapes and their applications in food industry. Many of these methods rely on heating globular proteins in relatively dilute solution and at extremes of pH, particularly whey protein (Schmitt et al., 2010; Schmitt & Ravaine, 2013).

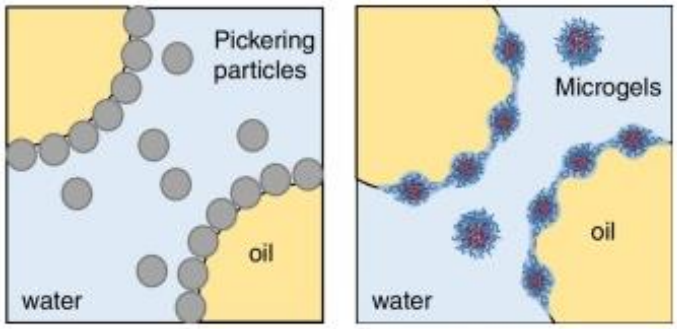

(a) **(b)**

Figure 1-1. Illustration of particles stabilizing the oil droplets at the O/W interface either via (a) Pickering particles or (b) Microgel particles. (Figure from Rayner, 2015)

Microgel particles can also be synthesized from polysaccharide-derived sources: plants (e.g., starch, cellulose, pectin, gum arabic), animals (e.g., chitosan, gelatin), bacteria (e.g., xanthan gum, gellan gum) and algae (e.g., carrageenan, alginate). In their recent reviews, Dickinson (2015) and Rayner (2015) discussed some microgel particles derived from starch with different particle sizes and application in foods as emulsion stabilizers via Pickering stabilization in their native granular state or for lipid encapsulation in partially gelatinized state. Microgel particles formed using hydrocolloids have also been reviewed by Burey et al. (2017) which encompassed their usage in food

applications not only limited as gelling agents and stabilizers or texture modifiers, but also as controlled release agents.

The present study focuses on the microgel particles constructed from alginate and a cross-linker of Ca^{2+}. Ca-alginate microgel particle production has been a much studied research area because they are biodegradable, biocompatible, non-toxic, and can be produced in less harsh processing conditions (George & Abraham, 2006; Gombotz & Wee, 1998; Kailasapathy, 2006; Paques, 2015; Shilpa, Agrawal, & Ray, 2003). Once they have been formed, the microgel particles can be extremely resilient, e.g., to boiling and shear, and they also have the added advantage of being sensitive to acid and Na^{+} which can be useful in digestion phase. Paques (2015) categorized the alginate microgel applications either as capsule (nutrients, proteins, drugs), or carrier (cells, enzyme, etc.), as a building block of new structure. For example, alginate microgel particles have been favoured as encapsulating agents for oral delivery of protein or peptide drugs (George & Abraham, 2006), ibuprofen drug (Caballero et al., 2014), probiotic (Anal & Singh, 2007; Kailasapathy, 2006), and scaffolds in tissue engineering (Augst et al., 2006; Eiselt et al.,, 2000; Kuo & Ma, 2001).

The alginate microgel particles can also be formed in conjunction with other biopolymers, for example:

(i) Chitosan - to deliver the antibiotic of nisin, proteins of ovalbumin, BSA, and insulin, lipophilic turmeric oil and curcumin (Anal et al., 2003; Cegnar & Ker, 2010; Chandrasekar, Coupland, & Anantheswaran, 2017; Das, Kasoju, & Bora, 2010; Goycoolea, Lollo, & Remun, 2009; Lertsutthiwong, Rojsitthisak, & Nimmannit, 2009). Additionally, chitosan is claimed to improve the stability of the microgel particles and reduce the pore size (Paques et al., 2014). Moreover, the cationic property of chitosan forms an ionic interaction with the negatively charged mucin, hence its mucoadhesion property is enhanced (Acosta, 2009; Semenova & Dickinson, 2010).

(ii) Carrageenan - to deliver betamethasone (Mohamadnia et al., 2007). The addition of sulphate groups from the carrageenan chain provides greater resistance in swelling as affected by saline solutions.

(iii) Gellan – to fabricate 3D structure of scaffolds (Akkineni et al., 2016). Addition of gellan indicated an increase of gel stiffness and thus gave a positive impact in shape conformity and also exhibited a lower degree of swelling compared to pure alginate in the composite scaffolds.

Ca-alginate microgel particles are extremely simple to prepare. The calcium cross-bridging is very strong, thus by simply dripping or spraying alginate solution into a calcium ion solution will give 'instantaneous' solidification of the alginate droplet in the calcium solution (Brun-Graeppi et al., 2011; Quong et al., 1998). Such methods have been reviewed by Shilpa, Agrawal, & Ray (2003) and more recently by Paques et al. (2014). Anal et al. (2003) delivered bovine serum albumin protein loaded into chitosan alginate beads with sizes from 0.46 mm to 0.66 mm using a 27 gauge blunt ended needle. Ouwerx et al. (1998) also produced the beads via the same method with a syringe needle, and the particle size was in the millimetre scale, ranging from 2.4 mm to 3 mm. Won et al. (2005) was successful in immobilizing bacterial lipase using the alginate gel particles with the sizes around 1 mm to 3 mm produced by a drop-wise method. However, such simple preparation methods generally give rise to particles that are too large (typically no smaller than 25 microns) in terms of settling out of the particles, blending them into other ingredients and disadvantageous in terms of their effects of organoleptic properties where they are used in foods (Paques, 2015).

Paques et al. (2014) reviewed a variety of techniques to produce smaller alginate microgel particles possessing a narrower size distribution (Figure 1-2). These variants generally involve modification of the spraying nozzles and shear fields in the receiving calcium bath, or modification of the forces between them via electric fields and/or mechanical vibration. It is not easy to control the spraying of alginate solution, which is rheologically complex; thus it is difficult to control and reduce the droplet size consistently before it contacts the calcium-rich phase. The minimum gel particle size formed by these methods still tends to be of the order of tens of microns.

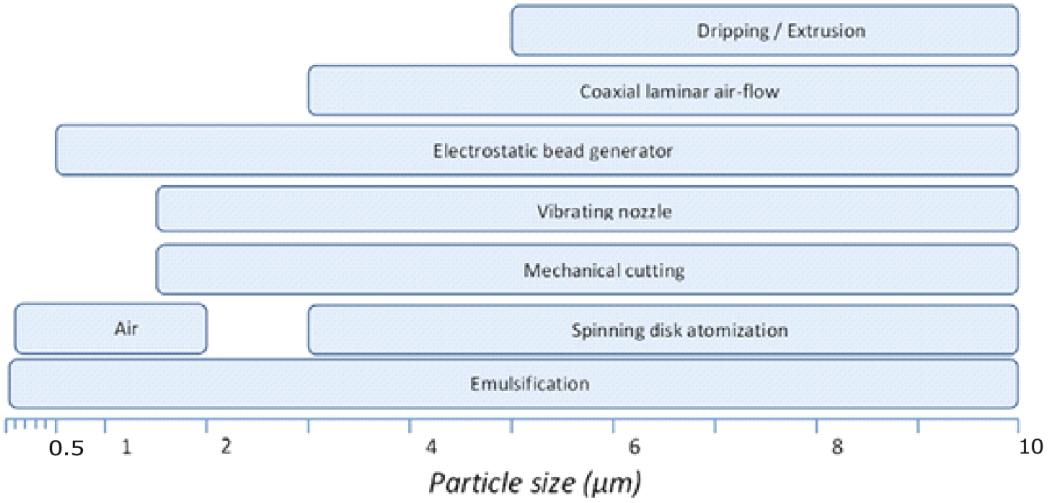

Figure 1-2. Methods to produce alginate microgel particles (Figure from Paques et al., 2014).

The advantage of smaller microgel sizes is that the release is more rapid based on diffusion mechanism or surface erosion due to greater specific surface area exhibited from smaller particles. There are other advantages of small size in terms of the ease of mixing and blending of smaller particles, their lower tendency to settle or aggregate, plus their access to narrower capillaries and junction zones, or the relative ease with which they may be able to cross other biopolymer barriers, such as the mucin layers coating the gut and other epithelial surfaces (Acosta, 2009).

Various methods have been developed to try to produce increasingly smaller particles. The microfluidic method is another common technique to produce monodispersed micrometre- to nanometre-sized Ca-alginate microgel particles as reviewed by McClements (2017) and Seiffert (2013), however the challenge is on how to scale up the production with such limited channels. The highest throughput of microfluidic device with 15 channels has been developed by Romanowsky et al. (2012) with the yield of 1.5 kg in 5.2 kg of microgel suspension per day (flow rate: 215 ml.h^{-1}). Another route is via emulsification or microemulsion phases (Machado et al., 2012) by first solubilizing the alginate and calcium into separate water-in-oil (W/O) emulsion and then mixing the two. Microemulsions require considerable amounts of surfactant to form the droplets

and the W/O emulsion route requires some method of initiating the slow release and diffusion of calcium ions from the other phase to gel the aqueous droplets containing the alginate (Amici et al., 2008; Poncelet et al., 1992). Recently Paques et al. (2013) described a method where calcium nanoparticles dispersed in the oil phase act as the source of cross-linking ions under relatively mild pH, resulting in particles of around 1 μm and even as low as 200 nm. Their method has the merit of being one of the least elaborate methods that may provide a route to making large quantities of truly micron or sub-micron particles. Here, we present an even simpler method via Leeds Jet Homogenizer (LJH), requiring no oil phase whatsoever, and therefore no need for subsequent oil removal. This instrument exists in a batch-to-batch system for a small scale production and in a continuous-cycle system for the possibility of a large-scale production.

Most Ca-alginate microgel particle formation techniques involve complicated processing steps in producing small particles or otherwise use simple techniques yielding large particle sizes. Thus, this study contributes to the production of submicron Ca-alginate microgel particles via a simple one-step approach using an in-house built Leeds Jet homogenizer. This study also explores the encapsulation of protein biopolymers (lactoferrin and lysozyme), solid particles of polyphenol and carotenoid crystals, and small molecules of food dyes into the Ca-alginate microgel particles.

1.2 Research Aims

The objectives of this study are as follows:

1. To produce submicron Ca-alginate microgel particles using a jet homogenizer.
2. To investigate the ingredients and processing parameters in controlling the microgel particle sizes.
3. To examine the rheological properties of Ca-alginate microgel suspensions.
4. To utilize these microgel particles for encapsulation of water-soluble (dyes and proteins) and water-insoluble compounds (rutin, tiliroside, curcumin, β-carotene).
5. To determine the microgel yield, payload, and loading efficiencies from the encapsulation.

1.3 Plan of thesis

This thesis comprises a continuum of research studies from the synthesis of microgel particles to the characterization and utilization of the microgel particles for encapsulation purposes. The following synopsis of each chapter outlines the scope of this study:

Chapter 1 – This provide literature review about alginate physical properties and its applications as microgel particles in food systems and in the pharmaceutical industry. It also expands the objectives of this study.

Chapter 2 – This chapter discusses the materials and methods used to formulate the Ca-alginate microgel particles. The detailed processing parameters in the production of the microgel particles via the LJH will also be outlined in chapter.

Chapter 3 – This results and discussion chapter outlines factors that affect the Ca-alginate microgel particle sizes, the microgel particle separation, and characterization via light scattering and microscopy techniques.

Chapter 4 – This chapter explores the potential encapsulation ability of the microgel particles in entrapping the water-insoluble crystals of polyphenols and β-carotene as a delivery system for water-insoluble health-benefit compounds.

Chapter 5 – This chapter looks into the possibilities of the entrapment of dyes and surface adsorption of lactoferrin and lysozyme onto or into the microgel particles.

Chapter 6 – This chapter provides concluding remarks including recommendations for future work.

1.4 Backgrounds

1.4.1 Alginate and the gelation with cations

Alginate originates from brown algae (*Phaeophyceae*), specifically the species of *Laminaria hyperborea, Macrocystis pyrifera, and Ascophyllum nodosum* (Gombotz & Wee, 1998b). It can also be synthesized by bacteria, mostly isolated from *Pseudomonas aeruginosa* and *Azotobacter vinelandii* because these bacteria are able to exude a polysaccharide biofilm (Draget, 2009; Pawar & Edgar, 2012). The current commercial available alginates are mostly sourced from algae rather than bacteria (Pawar & Edgar, 2012).

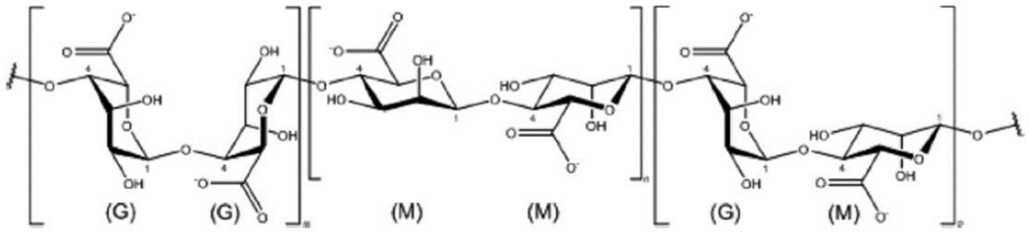

Figure 1-3. Alginate structures in G-G or M-M or G-M configurations (G: guluronate residue; M: mannuronate residue).

(Figure from Agulhon et al., 2012)

Alginate is a linear unbranched polysaccharide constructed with random block polymers of β-D-mannuronate (M) and α-L-guluronate (G). The molecular arrangements can be in homopolymeric (G-G or M-M) and heteropolymeric forms (G-M) (Agulhon et al., 2012; Pawar & Edgar, 2012), see . The molecular weight of alginate varies from 32,000 to 400,000 kDa depending on the composition of the guluronic and mannuronic, which are dependent on the algae species (Augst et al., 2006; Lee & Mooney, 2012). Lower mass of alginates can also be achieved via acid hydrolysis or degradation with hydrogen peroxide (H_2O_2) as methods outlined by Ramnani et al., 2012. Li et al. (2010) prepared low M_w of alginate via H_2O_2 degradation and the M_w of alginate was reduced from 254.5 kDa (native state) to 12.2 kDa (oxidized state). The M/G ratio plays an important role in the alginate gelation. The higher the guluronic acid concentration (smaller M/G) ratio provides a more rigid gel

structure and the high M/G ratio alginate gives rise to a more elastic gel structure (Augst et al., 2006; Draget, 2009; Zhao et al., 2011).

Alginate can form a gel via ionic and acid gelation. In ionic gelation, it occurs due to electrostatic interaction of the negatively-charged COO^- in the guluronate chains with cations. The pK_a of guluronic and mannuronic acids are at pH 3.65 and 3.38, respectively (Draget, Skjåk Bræk, & Smidsrød, 1994), thus alginate is considered as an anionic polysaccharide at neutral pH. The guluronate residue was mainly responsible for ionic gelation. While in acid gelation at a pH below the pK_a, alginate can turn into an acid gel (Draget, Skja, & Smidsrød, 1997).

The gelation of alginate Ca^{2+} is known to form an 'egg box' junction, which is a term coined by Grant et al. (1973) to illustrate the arrangement formed when calcium ions interact with blocks of guluronic acid residue in alginates. Braccini & Pérez, 2001 confirmed the 'egg box' model was favourable energetically and structurally for guluronic acids in alginate because of the formation of compact dimers that produced well adapted cavities to fit in Ca^{2+} ions (Braccini & Pérez, 2001) with a binding ratio of 4:1 of guluronate to calcium ions, see Figure 1-4. A minimal block of eight contiguous guluronate residues in the alginate chain is required to form a stable junction zone, which is also referred as a cooperative model for this formation (Stokke et al., 1991).

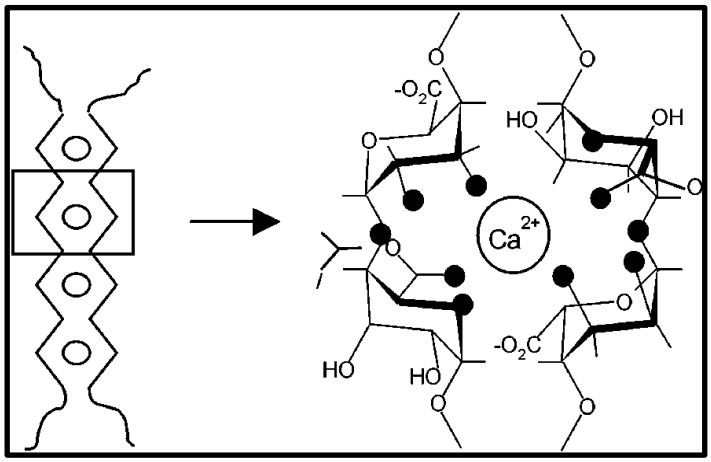

Figure 1-4. Schematic drawing of egg box junction between Ca^{2+} with the carboxylic group of guluronate chain in alginate. (Figure from Braccini and Perez, 2001)

Calcium is not the only ion responsible for the gelation of alginate; it can be extended to other cationic ions. Ouwerx et al. (1998) studied the affinity of alginate with other cations and showed the following binding affinity: Cd^{2+} > Ba^{2+} > Cu^{2+} > Ca^{2+} > Ni^{2+} > Co^{2+} > Mn^{2+} (stronger gel was formed as binding affinity with cations was increased). Alginate will not form gel with Na^{+} and Mg^{2+} ions (George & Abraham, 2006), thus they can be used as a non-gelling ions to rupture the Ca-alginate microgel via ion replacement (Brun-Graeppi et al., 2011). Although binding with Ca^{2+} is not the strongest affinity with alginate, it has been predominantly used for food applications because it is food grade, non-toxic, readily available, and low cost (Paques, 2015). The uniformity of alginate microgel particle shape is also dependent on the type of cations used to cross-link. Ouwerx et al. (1998) observed that alginate microgel particles formed from calcium ions were more uniform in shape than those formed using copper ions. According to their observations, the higher the affinity of cations with alginate, the more rough surfaces the beads formed and the less uniform.

In designing the microgel particles as outlined by McClements (2017), the particle gelation step is one of the primary steps to form the microgel particles. The gelation mechanism of carboxylate groups in alginate with Ca^{2+} (ionic gelation) can be further classified as external and internal gelation. In external gelation, Ca^{2+} ions diffuse into the alginate phase from outside into the inside of alginate structure, thus creating a concentration gradient of Ca^{2+} higher on the surface than the core of the microgel particles (Paques, 2015). Most of the microgel particles formed via dropwise methods or syringe methods are formed via external gelation, which is considered to be a fast gelling method. In internal gelation, Ca^{2+} is introduced slowly either via insoluble form of calcium source, such as $CaCO_3$, aided with GDL to gradually lower the pH and release the Ca^{2+} to trigger *in-situ* gelation (Paques, 2015). Emulsification methods or some microfluidic methods mostly rely on this internal gelation to form the microgel particles, which is claimed to be a more homogenous gelation due to even distribution of Ca^{2+} in the alginate phase but prone to syneresis (Paques et al., 2014).

1.4.2 Flash nanoprecipitation method via Leeds Jet Homogenizer as a microreactor

In principle, there are two main approaches to produce biopolymer-based microgel particles which are either classified as ‘top down’ or ‘bottom up’ methods, see Figure 1-5. The top down approaches start with bulk solid or liquid materials that are broken down into smaller particles; examples of such methods are shredding, milling or grinding, homogenization to produce emulsion, and extrusion (Joye & McClements, 2014). While in the bottom up approaches, small building blocks of particles are involved in creating larger particles via a self-assembly mechanism influenced by external conditions such as pH, ionic strength and temperature (Joye & McClements, 2014). Examples of such methods are precipitation, coacervation, inclusion complexation and fluid gel formation (Joye & McClements, 2014). Despite numerous methods for producing these biopolymer-based microgel particles, the key selections in choosing the most compatible method will depend on the biopolymer charges, solubility, usage of surfactant and physical state of the microgel. For industrial interests, methods that are cost efficient, generate high-production output, ease of handling and cleaning, and low energy-consumption are preferable for commercialization.

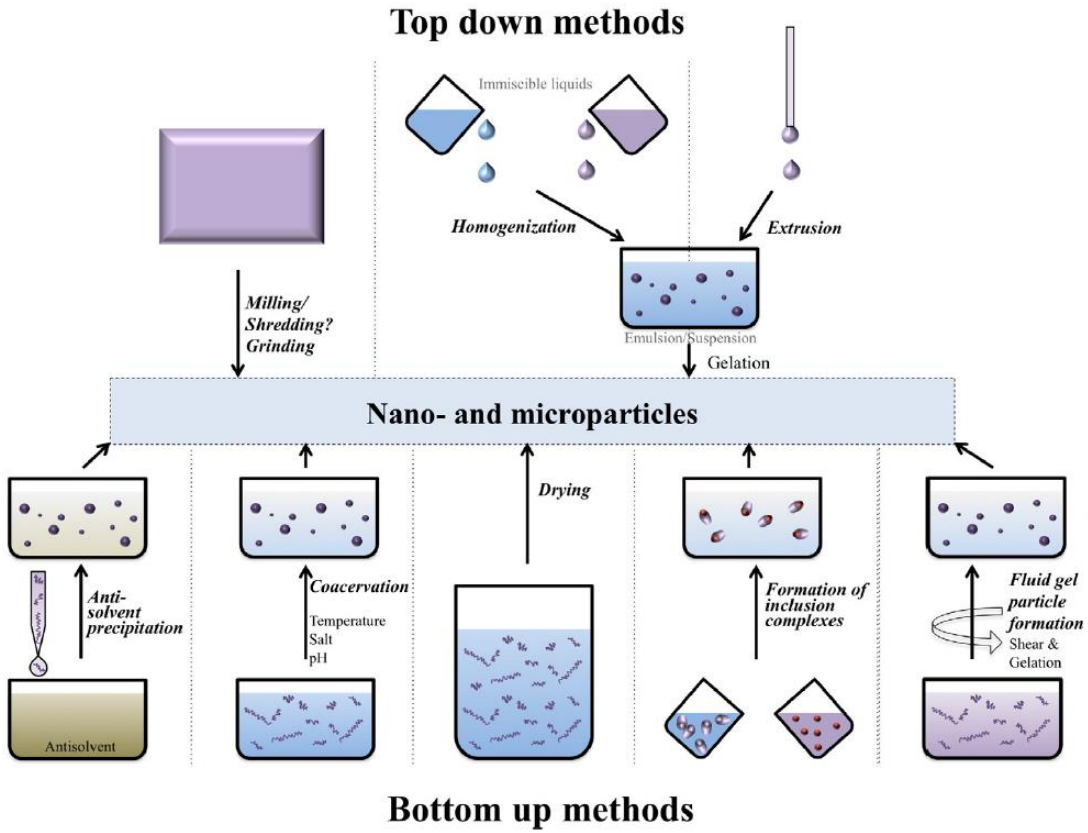

Figure 1-5. Different approaches to produce biopolymer-based microgel particles, i.e., top down or bottom up methods. (Figure from Joye & McClements, 2014)

The LJH is essentially a confined impingement jet T-mixer that serves as a microreactor to form microgel particles via the 'Flash Nanoprecipitation' method (Johnson & Prud'homme, 2003), see Chapter 2 – Methods section. The basic steps that are involved in the flash nanoprecipitation consist of nucleation, molecular growth, and aggregation or agglomeration, which are driven by the degree of supersaturation of the solute (Marchisio, Rivautella, & Barresi, 2006). The nucleation rate (B^o) is related to the degree of supersaturation (S) via the following Eq.1-1 (Matteucci et al., 2006):

$$B^o \infty \exp\left(-\frac{16\pi\gamma^3 {V_M}^2 N_A}{3\,(RT)^3(\ln(1+S))^2}\right) \qquad \textbf{1-1}$$

where γ is the interfacial tension, V_M is the molar volume, N_A is the Avogadro's number, R is the ideal gas law constant, and T is the temperature. The higher the degree of supersaturation, the higher the nucleation rate.

The nucleation rate is the key in controlling the particle size (Dirksen & Ring, 1991). Primarily, nucleation is classified as either (i) homogenous – occurs without the presence of a solid interface, or (ii) heterogeneous – occurs in the presence of a solid interface of foreign seed (Dirksen & Ring, 1991). In homogenous nucleation, the supersaturated solute molecules at a critical number are combined to form the 'embryo' (Dirksen & Ring, 1991). In heterogeneous nucleation, the presence of foreign seeds help to lower the surface tension of the 'embryo' being formed, thus new particle can be formed at lower supersaturation point (Dirksen & Ring, 1991). The stable embryo is known as nuclei. Nuclei can continue to grow to become larger particles referred to as a 'molecular growth process'. Marchisio et al. (2006) explained the process of nucleation, molecular growth, and aggregation of barium sulphate nanoparticles formation in a confined impingement jet (CIJ) reactor.

Nucleation and molecular growth are competing processes because both consume solute molecules, thus the result of this competition determines the particle size. The higher the nucleation rate, that is, when more solute molecules are used up for nucleation process rather than for molecular growth, the smaller the particles that are generated. In the aggregation or agglomeration processes, it occurs after the particles are formed, and no

uptakes of solute molecules are required; thus the particles size is affected by the Brownian motion and the balance between the intermolecular forces such as Van der Waal, electrostatic, or hydrophobic. Therefore, the chemical constituents and the mixing device to produce the particles are important in determining the particle size. The higher the mixing rate the higher the nucleation rate will be obtained, thus the smaller the particles that are created (Marchisio et al., 2006).

The processes of nucleation, molecular growth, and aggregation in agar and alginate microgel particle formation have been observed by Fernández Farrés & Norton (2014) and Norton, Jarvis, & Foster (1999) based on rheological measurements of controlled gelation mechanisms for both biopolymers. Fang et al. (2007) also proposed that 3-step processes were involved in the binding process of Ca^{2+} to alginate: (i) nucleation of a single guluronate unit with Ca^{2+} to form monocomplex, (ii) molecular growth of dimerization of 'egg box' junction zone from these pairing monocomplex (iii) aggregation due to the association of multimers to form clusters. Understanding of the mechanism of Ca-alginate gelation provides an insight on how the microgel particles are being formed and what factors determine the particle size during mixing in the jet homogenizer.

In flash nanoprecipitation, a rapid mixing occurs in the jet homogenizer. The key factor in generating this rapid mixing is the presence of a region of high energy dissipation. A high turbulent flow rate is generated from jet homogenizer with a high Reynold number estimated at around $1x10^5$ (Burgaud, Dickinson, & Nelson, 1990; Casanova & Higuita, 2011). At such a high turbulent flow, the molecules come into contact rapidly, thus the mixing time is very small, i.e. within a millisecond timescale for solid phase formation (Casanova & Higuita, 2011).

The Damkohler number (Da), which is defined as the ratio of mixing time (t_m) to the reaction time (t_r) for a chemical reaction to occur, is used as a reference parameter to characterize the particle formation. When Da <1, that is, the mixing time is faster than the reaction time, nanoparticles can be generated (Casanova & Higuita, 2011; Johnson & Prud'homme, 2003). A few examples of

these nanoparticles formation at Da <1, such as 80 nm of barium sulphate nanoparticles (Marchisio et al., 2006), 55 nm of β-carotene nanoparticles (Han et al., 2012), and < 300 nm of itraconazole drug nanoparticles (Matteucci et al., 2006). Casanova & Higuita (2011) adopted the same principle by using the jet homogenizer to produce 100 nm $CaCO_3$ nanoparticles formed by the rapid precipitation of sodium carbonate and calcium chloride. Sodium caseinate was added to stabilize the nanoparticles electrostatically to prevent them from aggregating after homogenization. The precipitation method as mentioned above is essentially an extension of the bottom-up approach in constructing the nanoparticles. However, the jet homogenizer can also be applied for a top-down approach, e.g. Matsumiya & Murray (2016) recently produced soy protein isolate microgel particles ($d_{4,3}$ from 31 to 84 µm) by breaking down its macrogel structure via this method.

This jet homogenizer method can be potentially more advantageous compared to other methods in terms of operation, cleaning, and cost because it is a low-energy consumption technique with no complicated operating system, high reproducibility, and fast processing time (Han et al., 2012; Marchisio et al., 2006). A possibility of scaling up is also prominent for industrial applications. The usage of computational fluid modelling has been studied by Gavi, Marchisio, & Barresi (2007) to simulate mixing and reaction time scales of barium sulphate nanoparticles in a confined impinged jet reactor for scaling-up purposes.

1.4.3 Encapsulation of water-insoluble and water-soluble compounds in Ca-alginate microgel particles

Encapsulation technology is undergoing continuous research, due to its ability to enhance the availability of bioactive or functional ingredients. It helps to protect the encapsulated compounds to reach the desired sites for a controlled release either via fragmentation, erosion, diffusion or swelling (McClements, 2017). Microgel particles can offer a perfect vehicle to deliver such functions, encapsulating a variety of compounds ranging from small molecules, solid particles or liquid droplets, structured micelles or vesicles, and so on, as illustrated in Figure 1-6 (McClements, 2017). Emulsion filled microgel particles are one of the examples of these filled microgels that have recently

been reviewed by Torres, Murray, & Sarkar (2016) as a platform to deliver lipophilic molecules.

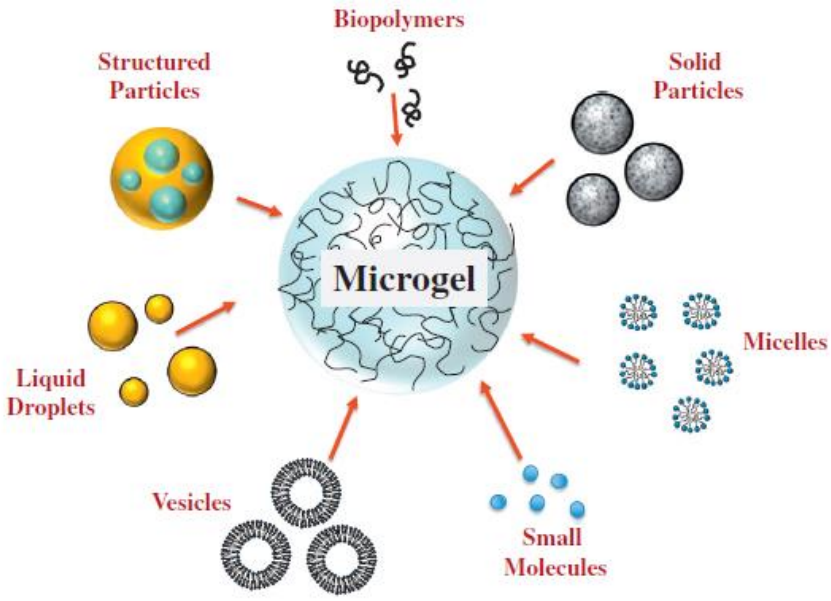

Figure 1-6. Microgel particles can be filled with variety forms of compounds.

(Figure from McClements, 2017)

For pharmaceutical applications, encapsulation is able to deliver the drug in a protected manner against any degradation from enzymes or acid attacks before its delivery to the desired specific sites. According to Gombotz & Wee (1998), alginate is commonly used as drug delivery system because it exhibits some mucosadhesive property to adhere with mucosal tissues, such as the digestive tract and nasopharynx. Although mucin has a net negative charge, it also has some positive charge regions comprised of histidine, lysine and arginine which may serve as potential sites for electrostatic mucin-alginate interaction (Nordgård & Draget 2011). Nevertheless, mucin-polysaccharide interaction is a complex phenomenon, not only governed by the electrostatic interactions of charged-contrast groups, but also determined by many other factors such as M_w, charge density, and chain flexibility, as revealed by Menchicchi et al. (2015). For food applications, the success criteria in encapsulation technology is to ensure the encapsulated compounds can be incorporated into the food matrix without degrading the quality attributes

(McClements, 2012). Thus, it is important to understand the compounds to be encapsulated at molecular level, to elucidate the benefits of encapsulation of these compounds for food applications, and to review existing encapsulation techniques presently available that elect alginate biopolymer to protect these compounds.

1.4.4 Water soluble lactoferrin and lysozyme encapsulation

Lactoferrin is commonly found in cow's and human milk with the reported concentrations of 0.1–0.4 $mg.ml^{-1}$ and 1–3 $mg.ml^{-1}$, respectively (Wakabayashi, Yamauchi, & Takase, 2006). The usage of cow's milk derived lactoferrin, i.e. bovine lactoferrin, is permitted as a nutritional supplement because it is recognized as GRAS (Generally Recognized as Safe) ingredient by the US Food and Drug Administration (Wakabayashi et al., 2006). Lactoferrin is a globular protein with M_w of 80 kDa and known as iron-binding glycoprotein with two molecules of Fe^{3+} present in the two lobes as shown in Figure 1-7 for its chemical structure (Baker & Baker, 2005; Lonnerdal & Iyer, 1995). The two lobes are prone to be thermally denatured at 61 ^{o}C and 93 ^{o}C (Bengoechea, Peinado, & McClements, 2011). The pI of lactoferrin is reported at pH of 8.5 which makes it positively charged at neutral pH (Peinado et a., 2010).

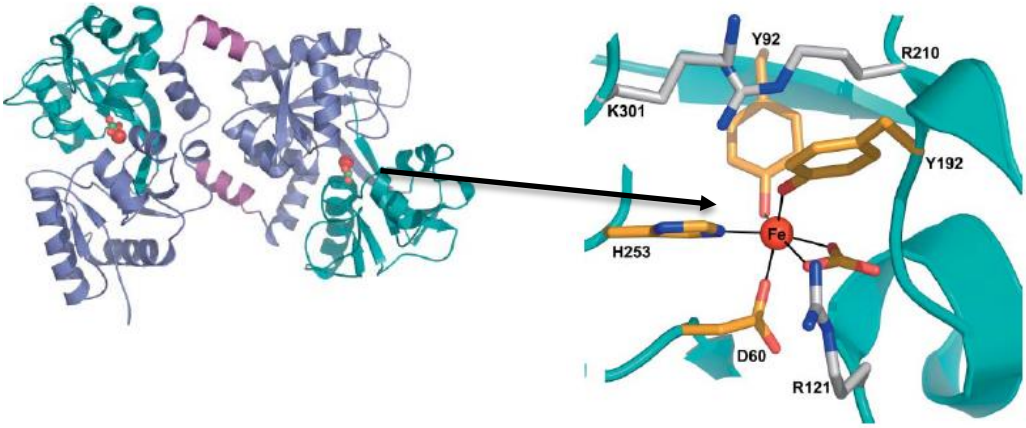

Figure 1-7. Lactoferrin structure in 3D ribbon diagram and the enlargement of one of the lobes with Fe^{3+} ion shown in the domain. The basic residues of arginine and lysine are highly exposed on the surface of the N-lobe (R 210, R121, and K301).

(Figure from Baker & Baker, 2005)

The ability of lactoferrin to withhold some iron has enhanced its antibacterial property by sequestering iron from iron-requiring bacteria, for example *E.coli* 0-111 (Lonnerdal & Iyer, 1995). In addition, lactoferrin health benefits are extended to be used as immunomodulatory activity, anticancer, anti-inflammatory, etc., as reviewed by (Lonnerdal & Iyer, 1995; Wakabayashi et al., 2006). The method to purify lactoferrin, commonly from whey protein, is considered expensive due to low recovery using the mainstream technique of ion-exchange column chromatography (Noel, Prokop, & Tanner, 2002; Wakabayashi et al., 2006), but yet its versatility is on the rise. In addition, generally high oral dose of lactoferrin is required for disease treatments; for example, high oral dose from 1.8 $g.day^{-1}$ up to 7.2 $g.day^{-1}$ in a human clinical study for hepatitis C patients (Okada et al., 2002). Thus, the needs to encapsulate this high-cost lactoferrin in a concentrated form is demanded by food and pharmaceutical applications to ensure its efficacy is delivered.

There are many research studies about lactoferrin inclusion either via complexation with alginate alone or alginate/chitosan by exploiting the charge contrast from anionic alginate and cationic lactoferrin. Inclusion of 20–30 wt.% lactoferrin in chitosan/alginate/calcium complex microgel beads with the size of 1–3 mm was successfully loaded by Onishi et al. (2010). The initial release burst up to 60 % lactoferrin in the gastrointestinal tract was attributed to the lactoferrin present on the surface of the microgel, thus coating with chitosan helped to prolong the release (Onishi et al., 2010). Bokkhim et al. (2016) produced Ca-alginate microgel beads without chitosan coating with a size range of 2.5–3.1 mm containing different forms of bovine lactoferrin, i.e., apo-, native-, and holo- lactoferrin via the extrusion-gelation method. Alginate alone (without added Ca^{2+}) can also form submicron particles via electrostatic complexation with lactoferrin as exploited by Peinado et al. (2010), but they are unstable to high salt concentration, and prone to aggregation. The stability was improved as lactoferrin was used to coat oil droplets and then later alginate was deposited onto the surface of these lactoferrin coated oil droplets (Tokle, Lesmes, & McClements, 2010). Lactoferrin on its own can be used as a cage or a nanocapsule to trap other materials. There are some developments of lactoferrin vesicles or nanoparticles to encapsulate β-casein (McCarthy et al.,

2014), β-carotene (Chen et al., 2014), and anthocyanin (Zhang et al., 2014). Some of these methods mentioned above produced large microgel particles in the order of millimetre scale, while other methods to produce smaller particles in submicron scale required multiple steps of emulsification or complexation.

Lysozyme is a globular protein with M_w of 14.3 consisting of 129 amino acid residues with pI around 11 with its highest source from hen's eggs, i.e., about 3.5 % of total egg white proteins (Dismer & Hubbuch, 2007; You et al., 2010). Its chemical structure is shown in Figure 1-8, with high basic residues of lysine and histidine, but also contains some tryptophan residues and the lobes are glued with disulfide linkages (Wu et al., 2008).

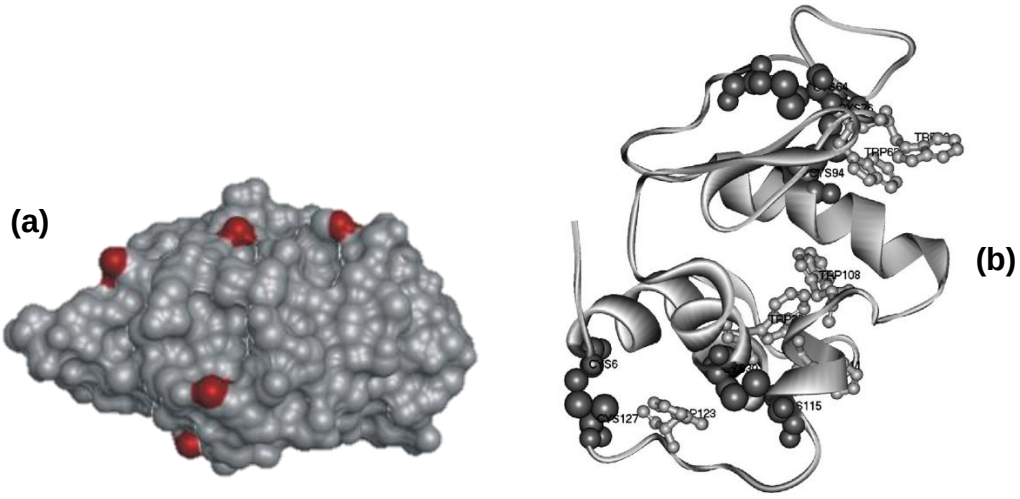

Figure 1-8. Lysozyme structure in (a) 3D diagram with the red spots indicate the presence of basic lysine residues on the surface (b) ribbon diagram.

Figures from (a) Dismer & Hubbuch (2007); (b) Wu et al. (2008)

Lysozyme has a long history being used as a natural preservative in foods, its bacteriolytic property works by disrupting the peptidoglycan of bacterial cell wall (Liburdi, Benucci, & Esti, 2014). Examples of lysozyme preservative functions as an effective inhibitor for pathogens and putrefactive bacteria, such as *Listeria monocytogenes* in meat products (Hughey, Johnson, & Wilger, 1989), *Clostridium perfringens* in chicken intestine (Liu et al., 2010) *Clostridium tyrobutyricum* causing late blowing during cheese ripening (Schneider, Becker, & Pischetsrieder, 2010), lactic acid bacteria in wine and

beer production (Liburdi et al., 2014). It also has a wide range of applications in pharmaceutical for human-milk resemblance in infant-formula, tooth decay prevention, anti-oxidant and anti-cancer properties as reviewed by Proctor, Cunningham, & Fung, 1988; You et al. (2010). Thus, encapsulation of lysozyme for anti-bacterial coating, enzyme immobilization, and drug delivery purposes has been extensively studied.

Utilizing the charge contrast that exists between cationic lysozyme and anionic alginate, many methods of protein inclusion in the alginate matrix rely on this complexation. Wells & Sheardown (2007) produced lysozyme encapsulated within alginate microgel particles via drop-wise method in a Ca^{2+} bath solution. A partial dissolution of microgel particles was initiated by using 0.1 N NaCl, then lysozyme was loaded by soaking the microgel particles into the protein solution. Fuenzalida et al. (2016) investigated the effect of alginate M/G ratio, M_w and molar charge ratio alginate to protein in the formation of lysozyme-alginate nanoparticles. Their study provided an insight about the capability of alginate in cross-linking with lysozyme increasing as the chain length of alginate was increased, i.e., more lysozyme were retained at higher M_w of alginate. Lysozyme appeared to be folded into the alginate network rather than tightly cross-linked at lower M_w. Addition of calcium ions to increase the rigidity of the polymer chain aided its ability to cross-link with more lysozyme.

The lysozyme-alginate complexation is not just limited as nanoparticle or microgel particles conformation, but can also be extended as thin film which was recently studied by Amara et al. (2016) to produce an antimicrobial film against some gram positive bacteria. Owing to its excellent foaming properties, lysozyme microbubbles are another interesting type of microgel application for foods and biomedical applications. Lysozyme on its own has also been used as the ‘shell’ structure to encapsulate negatively charged ascorbic acid (pK_a of 4 and 11.3) by utilizing its cationic property with ζ–potential of 40 ± 3 mV at pH 7 as measured by Cavalieri et al. (2013). The lysozyme microbubble can also be stabilized using alginate via the microfluidic method as explored by Park, Tumarkin, & Kumacheva (2010).

Such a wide range of studies of lysozyme and lactoferrin inclusion in alginate biopolymer has provided many success stories of protein encapsulation. To our knowledge, the methods of protein incorporation in the alginate microgel particles have not been investigated using the jet homogenizer method presented in Chapter 2.

1.4.5 Water-soluble dyes erioglaucine and methylene blue dyes encapsulation

Erioglaucine, an organic acid aminotriphenylmethane dye, is also known as Acid Blue 9 which is commonly found in food, cosmetic, and pharmaceutical products (Jank et al., 1998). It is an anionic dye at neutral pH due to the presence of sulfonate groups. Erioglaucine has a high extinction coefficient, ε = 2.14 X 10^5 $mol^{-1}.dm^3.cm^{-1}$ at 630 nm (Barakat et al., 2001; Jank et al., 1998) which is useful as a dye for tracing the water pathways in clayed soil (Flury & Markus, 2003). There are a growing public concern about the environmental pollution caused by low-biodegradable dyes because they can have a detrimental ecological impact (Liu et al., 2008). In the pharmaceutical industry, it is a common practice to use erioglaucine as a standard solution (at concentration of 2 $g.l^{-1}$) to be treated with sodium hypochlorite (NaOCl) until it is decolourized before discarding it into the sewerage system (Jank et al., 1998). However, this treatment introduces side products of chlorine derivatives, thus some extensive studies have investigated the entrapment of the dyes into gels or beads of synthetic polymers as a possible way to remove them from wastewater streams (Liu et al., 2008).

Methylene blue is a versatile dye used as a biological stain for bacteria (Misra et al., 1994), as a marker for diagnosis of oral cancer (Riaz et al., 2013), a drug treatment for malaria (Meissner et al., 2006), and a textile dye (Davies, 1963). Due to its heavy usage, the removal process of the dye from wastewater is an on-going effort to minimize contamination into natural sources as in erioglaucine dye. Methylene blue belongs to phenothiazinium group which is a cationic dye at neutral pH (Hossain, Kabir, & Suresh Kumar, 2012). According to Duman et al. (2016), the negative heath impact of cationic dyes in wastewater is more prominent because it can potentially bind with the negatively charged cell membrane surfaces (Duman et al., 2016). Despite that,

methylene blue nanoencapsulation can be useful for cancer therapy, called 'Photodynamic therapy' which employs photosensitizer compounds, such as porphyrins, chlorins, and phthalocyanines, including methylene blue, to produce reactive species of singlet oxygens that selectively and permanently damage tumour cells (Tang et al., 2004). Thus methylene blue encapsulation in Ca-alginate microgel particles will be presented in this study as a contribution to the expanding list of methylene blue applications.

1.4.6 Water-insoluble polyphenolic compounds of rutin, tiliroside, curcumin, and carotenoid of β-carotene

There is significant evidence that dietary intake of fruits, vegetables, coffee, tea, nuts and soy prevent chronic diseases owing to the presence of health promoting phytochemicals (Del Rio et al., 2013). The particular compounds of interest in this study are the flavonoids rutin and tiliroside, curcumin, and β-carotene.

Rutin, also known as vitamin P, has a rich source in tartary buckwheat with a total content of 36.5 $mg.g^{-1}$ in seeds and other edible parts of the plant as reported by Zhang et al. (2012). Its health benefits as an antioxidant, anticancer, anti-hypertension, and anti-inflammatory have been comprehensively reviewed by Giménez-Bastida et al. (2016) and Zhang et al. (2012). Tiliroside can be found in linden, strawberry and rosehip (Goto et al., 2012). It possesses similar health functions to rutin and more recent findings have also shown the hepatoprotective effect against induced liver injury in mice (Matsuda et al., 2002) and anti-obese effects in normal mice and obese-induced mice (Goto et al., 2012; Ninomiya et al., 2007). Both compounds are classified as glycosidic flavonoids attributed to the presence of sugar moieties in the flavonol backbone, i.e., rutinoside and glucoside+coumaroyl moieties in rutin and tiliroside, respectively (Luo et al., 2011). Both flavonoids have low solubility in water: 0.2 mM (Macedo et al., 2014) and 2.1 μm (Luo et al., 2012) for rutin and tiliroside in water, respectively. They also have low $\log_{10}P$, 0.27 and 2.71 for rutin and tiliroside, respectively, thus their insolubilities in water make them as viable candidates as Pickering stabilizers, which have been demonstrated by Luo et al. (2012) for O/W emulsions.

Curcumin is commonly isolated from turmeric and has long been known to cure and prevent many types of illnesses. Prasad et al. (2014) summarized over 6000 published articles about the health benefits of curcumin supported with clinical evidence, in which they called curcumin the 'golden spice' due to a wide range of protections exhibited. Curcumin is a planar polyketide chemical with aromatic end groups that which can undergo keto-enol tautomerism in alkaline conditions; at pH > 8 the enol form is more dominant than the keto form (Sharma, Gescher, & Steward, 2005). It has a $\log_{10}P$ value of 3 (Jannin et al., 2015) and solubility in water only 0.25 mM at pH 8 (Tønnesen, 2006) . Despite such vast advantages of curcumin, its oral bioavailability is very low, thus many strategies have been employed to improve it (Prasad et al., 2014; Sharma et al., 2005). Curcumin-loaded nanoparticles have been used widely as functional ingredients in foods or drugs. The most recent development is by loading curcumin into solid lipid nanoparticles of stearic acid, with tripalmitin as the lipid core stabilized with Span 80 and Tween 20 emulsifiers (Behbahani et al., 2017). Another recent study by Zheng et al. (2017) compares curcumin delivery systems at pHs of 3 and 7 via aqueous DMSO solution, O/W emulsion, alginate beads, and chitosan beads. Their findings suggest that the suitable delivery system is determined by the final application of the curcumin particles, for examples, chitosan beads have better protection in neutral products or beverages and O/W emulsion droplets work best in acidic environments.

β-carotene is the most commonly studied carotenoid because of its multi-functionalities as a natural colorant and as an antioxidant, and anticancer drug for neuroblastoma and lung cancers, as reviewed by (Gul et al., 2015). β-carotene is a precursor of vitamin A, has demonstrated its protection against blindness initiated by age-related macular degeneration and cataract (Gul et al., 2015). β-carotene is highly lipophilic with $\log_{10}P$ value of 17 (León et al., 2003), it contains eight isoprenoid units and can exist as cis- and trans-isomers (Mattea, Martín, & Cocero, 2009). It can also easily undergo oxidation via oxygen, temperature, light (Cao-Hoang, Fougère, & Waché, 2011). Thus, nano- or microencapsulation of β-carotene has been viewed as a way to protect it from these degradations (Gul et al., 2015). Astete et al. (2009) have successfully retarded the degradation of β-carotene caused by oxidation and

pH via encapsulation into 120 to 180 nm particles of Ca-alginate microgel particles with the addition of lecithin as a stabilizer to improve this natural pigment in water. Zhang, Zhang, & McClements (2016) have also synthesized filled β-carotene in lipid droplet form in alginate hydrogel beads using a commercial encapsulator unit with particle sizes of 285 μm and 661 μm prepared from 0.5 % and 1 % alginate, respectively, soaked in a 10 % $CaCl_2$ solution. The result from their studies indicated that a reduction of the lipid digestion rate within the simulated small intestine phase in the encapsulated form versus the un-encapsulated β-carotene lipid droplets which implies the protection mechanism of the microgel particles in delivering it to the large intestine sites. The particle sizes also matter in digestion; the smaller the droplet size the higher the bioavailability which is attributed to a greater amount of lipase required per unit area of small versus big particle sizes (Salvia-Trujillo et al., 2013).

In addition to the aforementioned protection benefits of nano- or microencapsulation, encapsulation can also aid in masking unpleasant tastes (Fang & Bhandari, 2010; Zhao et al., 2010). Phenolic compounds are known to be intrinsically bitter, thus encapsulating them in microgel particles can be beneficial for food applications. Moreover, efforts for ease of dissolution in hydrophilic beverage systems can also be achieved via formation of small microgel particle sizes; particle sizes of < 20 nm can easily be dispersed to create transparent beverages (Acosta, 2009). A high priority on developing foods or supplements that are enriched with the health-promoting phytochemicals is in a continual progression line. The most recent developments of nano- and microencapsulation as delivery systems are comprehensively reviewed by Souza et al. (2017).

1.4.7 Microgel particles characterization

Measurements or particle characteristics (i.e., size, shape, charge, rheology) are very important in determining the physicochemical and functional properties of the microgel particles or suspension (McClements, 2015). Many of these analytical tools for microgel characterisation have been employed as

analytical instruments for emulsion stability, which may be beneficial from an industry stand point to utilize them for multiple functions.

1.4.7.1 Dynamic Light Scattering techniques (DLS)

In their swollen state, the microgel particles are nearly transparent to the naked eye because their refractive index is close to that of water (Pelton & Hoare, 2011). Thus, it is a challenge to detect the particle size based on the refractive index (n) contrast between the microgel particles and the dispersed medium (commonly water), unless they are filled with encapsulated materials with higher or lower n. However, these particles can still undergo Brownian motion, which can be useful for particle size detection based on mobility. The smaller the particle, the more rapid the Brownian motion, and vice versa. Temperature can also have an effect; the higher the temperature, the more rapid the Brownian motion. The light scattering technique is a common method to measure particle size based on this principle. When the particles are illuminated with a laser beam, the intensity of the scattered light fluctuates at a rate dependent on the size of the particles (Nobbmann et al., 2007). The smaller the particle, the more rapid the movement which leads to a faster rate of signal fluctuation. The velocity of the Brownian motion is defined by the translational diffusion coefficient (D) which can be converted into particle diameter (d_H) using Stokes-Einstein equation below (Nobbmann et al., 2007):

$$d_H = \frac{k_b T}{3\pi \eta D} \qquad \textbf{1-2}$$

where k_b is the Boltzmann constant, T is the temperature, and η is the viscosity of the dispersed medium. The overall particle diameter is referred as Z-average, which is defined as the intensity-weighted mean diameter derived from the fitted particle size distribution.

1.4.7.2 Zeta-potential measurement

Generally, almost all microgel particles have some surface charges either positive or negative. The ζ-potential is a key measurement to determine the charges of the microgel particles as a response to the stimuli such as pH, ionic strength, and presence of charged neighbouring particles or cross-linker ions. Figure 1-9 provides an illustration of a single negatively charged particle

that is ionically bound with counter ions at the 'Stern layer'. The next layer is referred to as the 'Diffuse layer' which is populated by additional counter ions that are attracted to the negatively charged particle but repelled by the ions on the Stern layer. The Stern layer and Diffuse layer are usually known as the 'Double layer' with the outer boundary of 'Slipping plane'. The electrostatic potential at the Slipping plane is where the ζ-potential is measured.

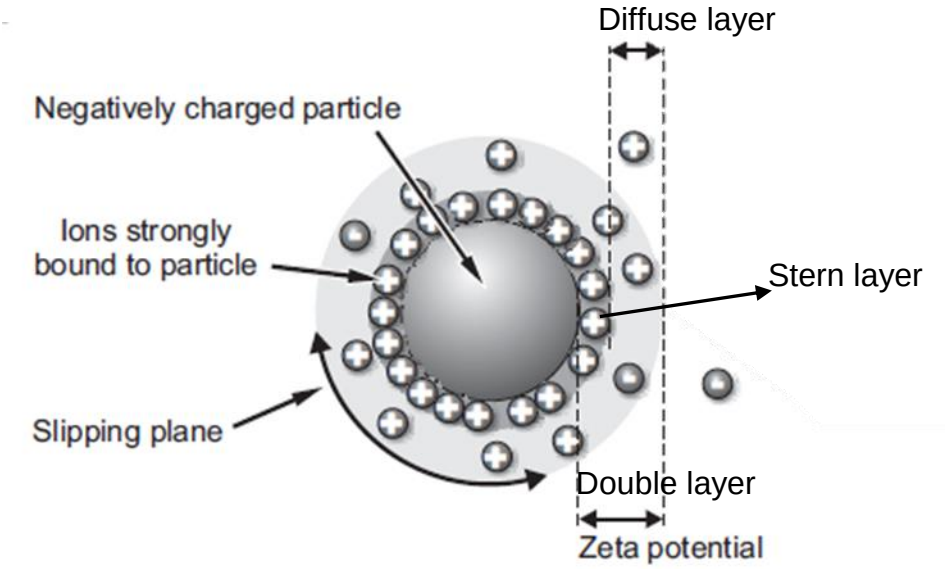

Figure 1-9. Schematic representation of a negatively charged particles and the presence of its ions at the 'Diffuse layer' and 'Slipping plane'.

(Figure from Malvern, 2011)

The electrophoretic mobility (U_E) of a particle describes the velocity (V_p) of a particle generated by a given electric field strength (E_f), and is expressed by the following Eq.1-3.

$$U_E = \frac{V_p}{E_f} \qquad \textbf{1-3}$$

The electric field strength can be calculated with known parameters of the applied voltage and distance between the electrodes, see Eq.1-4.

$$Ef = \frac{applied\ voltage}{distance\ between\ electrodes} \qquad \textbf{1-4}$$

The capillary cell Malvern DTS1061 had a distance of 6 cm, and applied voltage was 150 Volts, thus the electric field strength was about 25 V.cm^{-1}.

The electrophoretic mobility is related to ζ-potential via Henry equation (Eq.1-5) in which the ζ-potential is directly proportional to the electrophoretic mobility.

$$U_E = \frac{2\varepsilon\,\zeta\,f(k_a)}{3\eta} \qquad \textbf{1-5}$$

where ε is the dielectric constant, ζ is the ζ-potential, η is the viscosity of the dispersed media (i.e., water, η = 8.9 x 10^{-4} Pa.s at room temperature), and $f(k_a)$ is the Henry's function; $f(k_a)$ = 1.5 for dispersion in polar media based on the Smoluchowski approximation. The Smoluchowski approximation is based on the assumption that the double layer thickness is not larger than the particle diameter.

1.4.7.3 Laser diffraction method

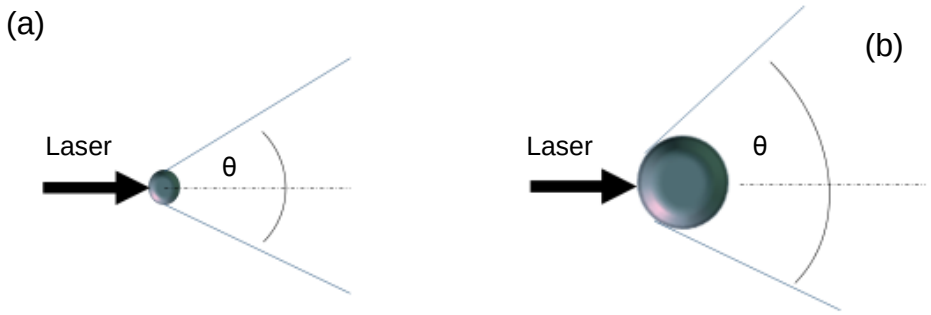

Figure 1-10. An illustration of different scattering patterns displayed a small (a) vs big particle (b) as illuminated by a laser beam.

A laser diffraction method, also known as static light scattering, works differently than the Brownian motion principle in dynamic light scattering. It is a particle sizing method based on the light scattering pattern, i.e., intensity vs. scattering angle (McClements, 2015). As the light beam propagates through the microgel suspension, the scattering pattern behaves differently depending on the particle size, see Figure 1-10. The obtained scattering pattern data is converted into a particle size distribution (PSD) using a mathematical model

known as ‘Mie Theory’ with an assumption that the particles are homogenous spheres and the refractive indices of the particles and the dispersing medium are known. The concentration of the microgel particles in the suspension has to be diluted, i.e., < 0.1 wt.%, to avoid a multiple scattering effect (McClements, 2015).

The mean diameter of the measured particle size is usually expressed as d_{32} (also known as Sauter mean) and d_{43} (also called as the Debroukere mean) (Horiba Instrument Catalog, 2014). Depending on which weighting factor is used whether surface area (d_{32}) or volume of the particles (d_{43}), the equations to calculate these mean values are shown in the equations below (Berg, 2010).

$$\bar{d}_{32} = \frac{\sum n_i A_i d_i}{\sum n_i A_i} \qquad \textbf{1-6}$$

$$\bar{d}_{43} = \frac{\sum n_i V_i d_i}{\sum n_i V_i} \qquad \textbf{1-7}$$

where n_i is the number of particles in class i, A_i is the particle surface area or V_i particle volume in class i, d_i is diameter of the i^{th} particle.

1.4.7.4 Light Microscopy

Light microscopy is the most basic method to examine the surface of the microgel particles by reflected light. The instrument typically consists of a light source, a series of lenses, and an eyepiece or digital camera (McClements, 2015). The resolution of the light microscopy depends on the wavelength of the light source (λ) and the objectives, i.e., 0.5λ for dry versus 0.33λ immersion objectives, respectively (Berg, 2010). Based on the λ, the resolution of light microscopy can be as low as 200 nm, but in practice objects that are < 1000 nm are not easily detectable with this tool (McClements, 2015). Thus, many advancements of this method have been developed to provide more localized images based different chemical components within the samples, for example X-ray, Fourier transform infrared (FTIR) imaging and surface-enhanced resonance spectroscopy (SERS) imaging microscopy (McClements, 2015).

1.4.7.5 Confocal Light Scanning Microscopy (CLSM)

The basic principle in CLSM is illustrated in Figure 1-11 where the entire specimen is illuminated by scanning one or more focused laser beams and the emitted light from the focal plane in the specimen is detected by a photomultiplier tube (PMT) through a detection pinhole (Struder-Kypke, 2013). The detection pinhole eliminates signals from out-of-focus light because the areas of non-focal planes are blocked by the pinhole. The signals are then transformed into electrical signals which are converted to images by the specific software and displayed on the computer screen. CLSM has a capability to generate three-dimensional (3D) images of structures without the need of complicated preparation and able to distinguish between two or more components using fluorescent dyes. For a colloidal delivery system, this specific feature of CLSM can be utilized to examine the spatial location of different components within the samples (McClements, 2015). It can also be used to examine the mass transport of a specific component within the microgel particles that can be tagged with an appropriate fluorescent dye (McClements, 2015).

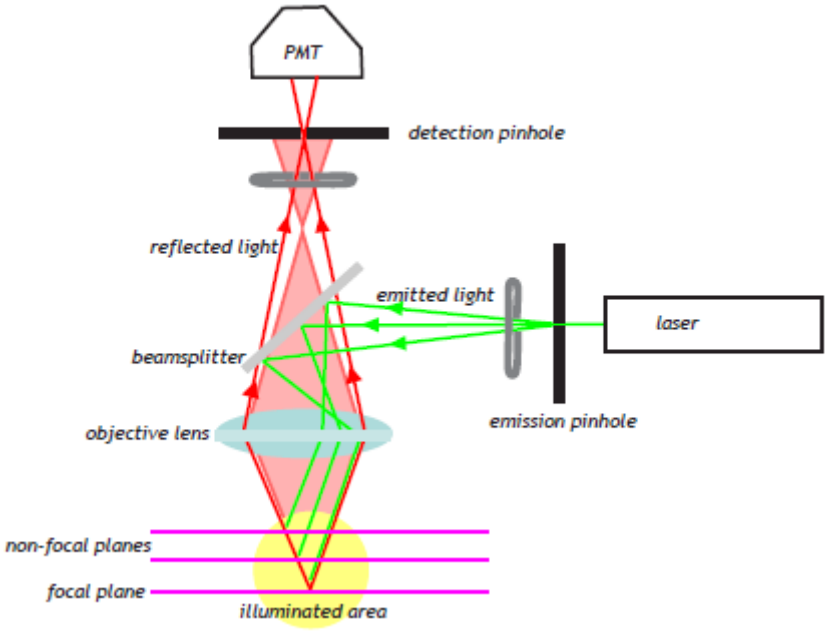

Figure 1-11. Schematic illustration to describe the principle of confocal imaging. (Figure from Struder-Kypke, 2013)

1.4.7.6 Electron microscopy

Electron microscopy can be used to assess the morphological, size, structural, and chemical properties of different materials. Different types of microscopy techniques employed in this study to provide images of the microgel particles, these include SEM, environmental SEM (E-SEM), field emission (FE-SEM), and transmission (TEM).

SEM is one of the most common electron microscope and typically uses a 5-30 keV electron beam. The beam is focused to a fine probe and then scanned over the surface of the sample. The signals emitted from the scan are then collected by a detector and relayed to a computer to generate the images. SEM provides topological surface information about the sample over a relatively large area. In conventional SEM, samples are placed in a vacuum, thus the aqueous phase needs to be removed by drying or evaporation. For non-conductive samples like microgel particles, this can be a challenge but it can be overcome by coating the dried samples with conductive metals such as Pt or Au via sputter deposition. The metal coating prevents some charge build-up which otherwise can cause thermal damage to the sample and image distortion. The Cryo-SEM required a cryogenic treatment to the sample to replace the water with the amorphous ice crystals which can minimize the artefacts or loss of structure during the imaging process (Davis, 2005). SEM that uses field emission guns (FE-SEM) has a spatial resolution in the order of 2 nm and can be used to view images of individual particles within aggregate structure (Davis, 2005). In TEM, a thin specimen thickness is required (<1 μm) to allow the transmission of an electron beam. With the resolution in the order of 0.2 – 0.3 nm, TEM is a powerful technique to provide information not only about particle size, shape, and aggregation, but also the analysis of internal structure, chemical composition, and crystallographic information (Davis, 2005).

All the methods mentioned above require either drying or lyophilisation treatments to the non-conductive microgel samples. E-SEM with a resolution of 5 nm (Davis, 2005), allows the non-conductive wet samples to be imaged without the need of metal coating by using water vapour as a gas ionization detector in a moderate vacuum chamber (Berg, 2010). E-SEM may offer the

best solution if the hydrated state is a mandatory in characterising the microgel structure.

1.4.7.7 Rheology measurements

The rheology of microgel suspension has become a much discussed topic due to its diverse applications that can exploited in the area of food microstructure and soft matter systems. The unique property of the Ca-alginate microgel suspension, i.e., behaving solid-like at high concentration but remaining deformable, may enhance the sensory experience in mouth in replacing fat droplets and yet still maintain the microstructure of the original product (Fernandez Farres, Douaire, & Norton, 2013). The lubrication property of Ca-alginate microgel suspension (up to 4 %wt. microgel particles) was related to its tribology by measuring the friction coefficient as determined by (Farres et al., 2013). They concluded from the viscosity of the microgel suspension and the particle elasticity, Ca-alginate microgel particles (< 10 µm in size) exhibited a high lubrication property which has a positive implication of replacing of oil droplet in O/W emulsion with the microgel particles to produce low fat products.

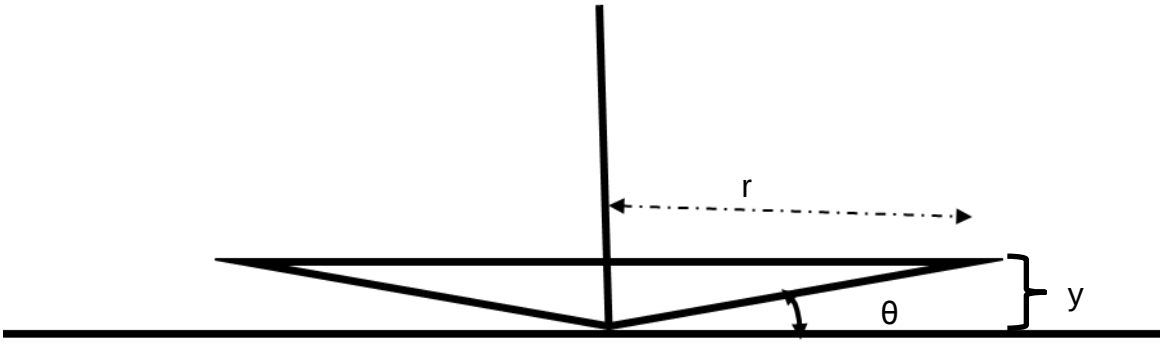

Figure 1-12. Cone and plate geometry, where r = radius, θ = angle (in this experiment, θ = 1º), and y = gap distance.

The rheological properties of alginate solution and microgel suspension were determined via a rheometer. The rheometer works on shearing principle between particular geometries. In the present study, the viscosity values of Ca-alginate microgel suspension or alginate solutions were obtained via cone and plate geometry, see . This geometry offers some benefits in term of the minimal

amount of sample can be used and the shear rate can be kept constant across the whole gap because of the angle on the top plate (Braun & Rosen, 2000). This geometry is also suitable for measurement of shear thinning fluid such as alginate.

From the known radius (r), angle (θ), and the gap distance (y), the shear rate (γ) for small angle can be calculated via Eq.1-8 where Ω equals to the angular velocity.

$$\gamma = \frac{\Omega}{\theta} \qquad \textbf{1-8}$$

The torque (M), which is a function of the shear stress (τ_r) at radius (r), is defined by Eq.1-9 and rearrangement of the Eq.1-9 to Eq.1-10 will solve the shear stress (τ_r) at radius (r).

$$M = \tau_r \frac{2\pi r^3}{3} \qquad \textbf{1-9}$$

$$\tau_r = \frac{3M}{2\pi r^3} \qquad \textbf{1-10}$$

the apparent viscosity (η), which is the ratio of shear stress (τ_r) to the shear rate (γ), is defined as the following Eq.1-11:

$$\eta = \frac{3M\theta}{2\pi r^3 \Omega} \qquad \textbf{1-11}$$

Alginate solution is highly soluble in water and it exhibits a shear thinning behaviour in solution like other biopolymers. The viscosity of alginate is mainly dependent on the M/G ratio, as previously stated that the guluronic chain has higher degree of stiffness compared to the mannuronic chains. In addition, its natural origin whether bacterial or seaweed, also dictates some differences in the alginate rheological properties, especially in the flow behaviour and consistency which will determine the apparent viscosity (Clementi, Mancini, & Moresi, 1998; Mancini, Moresi, & Sappino, 1996). When alginate solution cross-linked with Ca^{2+} to form microgel particles, the microgel particles become insoluble (Jha et al., 2016) and they can be suspended either in the solutions consisting of free alginate or in a solvent such as water at

certain volume fraction (φ). According to Poon, Weeks, & Royall (2012) the quickest way to obtain φ is via centrifugation. The obtained sediment corresponds to the volume of the microgel particles and supernatant to the volume of the free water between the particle (Cassin et al., 2000). This method has been used by Cassin et al. (2000) and Fernandez Farres, Douaire, & Norton (2013) to determine φ of agar and alginate microgel particles.

The rheological behaviour of microgel suspensions is a complex matter, depending on the particle φ, particle softness, particle size and shape, the viscosity of the base solution and presence of potential interaction forces from their surrounding environment (Ganguly & Chakraborty, 2009; Shewan & Stokes, 2012; Shewan & Stokes, 2015). At low φ ($\varphi < 0.05$), the viscosity of the microgel suspension follows the continuous phase (Ching, Bansal, & Bhandari, 2016). The viscosity of microgel suspension (η) at low φ follows the seminal Einstein equation (Eq.1-12).

$$\eta = \eta_s \, (1 + 2.5\varphi_o) \qquad \textbf{1-12}$$

where η_s is the viscosity of the solvent or the base fluid, φ_o is the effective volume fraction.

At higher φ, the rheology of the suspension is determined by the particle softness (Ching et al., 2016). In hard sphere theory, the particle volume and size are fixed, thus particle mobility is depending upon the space confined by its nearest neighbours (van der Vaart et al., 2013). At high φ, the available space for particle motion becoming small, thus the viscosity at high φ (φ_m) is equal to the viscosity at maximum packing fraction (φ_{RCP}, RCP = random close packing), i.e., $\varphi_m = \varphi_{RCP} = 0.64$. The viscosity of hard sphere suspension can be predicted via the following equations (Shewan & Stokes, 2015):

$$\frac{\eta}{\eta_s} = \eta_r = \left(1 - \frac{\varphi_o}{\varphi_m}\right)^{-2} \qquad \textbf{1-13}$$

$$\left(\frac{1}{\sqrt{\eta_r}}\right) = 1 - \frac{\varphi_o}{\varphi_m} \qquad \textbf{1-14}$$

where η equals to the viscosity at Newtonian region, η_s is the viscosity of the solvent or the base fluid, η_r is the relative viscosity, and φ_o is the effective volume fraction.

Taking into account that microgel particles are commonly exist as soft colloidal particles which they can swell and de-swell, thus the φ_o may vary. Therefore, the hard sphere theory is not always applicable to predict the rheology microgel suspension. The deviation of hard sphere theory can be seen as the calculated φ_m = 0.58 – 0.74 (Ching et al., 2016; Poon et al., 2012; Shewan & Stokes, 2012). The soft sphere suspension requires many cautionary steps in predicting the viscosity which involves some intricate computations depending not only the φ but also the elastic modulus as a function of φ, the stress-strain response, etc. The rheology phenomenon of hard sphere versus soft sphere suspension has been reviewed by Shewan & Stokes (2015) and van der Vaart et al.(2013), which remains as an evolving research study at present.

1.5 Conclusion

As a summary, the current status and developments of microgel particles (particularly in the form of Ca-alginate system) and the backgrounds of the chemical components used in this study have been reviewed in this present chapter. The variety of methods to improve the health benefits functionality of the proteins, polyphenol, and carotene compounds or to retain the dyes via encapsulation are still being studied. However, rapid methods in producing microgel particles can only be observed in few studies as mentioned above. Thus, in this study we will probe the possibility of utilizing jet homogenizer to produce submicron microgel particles rapidly. In order to prove the efficacy of the methods, there is a need to answer the following research questions (i) what factors or processing parameters in controlling the particle sizes of the Ca-alginate microgels produced via the jet homogenizer (ii) whether the method can be utilized to encapsulate some water-soluble and water-insoluble compounds, and (iii) the amount of entrapped particles or yield if they are entrapped. These questions will be answered in the following chapters.

Chapter 2 Materials and Methods

This chapter provides the details about the materials and methods used in this study.

2.1 Materials

2.1.1 Water

Purified water was used to dissolve the chemicals or to suspend the microgel particles. The water purification was performed using Millipore apparatus (Millipore, UK) with resistivity exceeding 18.2 $m\Omega.cm^{-1}$.

2.1.2 Alginate

There were two types of alginate used in the experiments (see Table 2.1) with different level of viscosities as measured by a Kinexus rheometer (Malvern, UK) at a constant shear rate of 10 s^{-1}. The M/G ratio of the alginate used was unknown because the suppliers withhold this information for confidentiality. The alginates were used as received, no further purification was performed.

Table 2.1. Types of alginate with different levels of apparent viscosity (η)

Types	Supplier	η of 1 wt.% alginate in water at 10 s^{-1} (Pa.s) at 25°C.
Alginic acid sodium salt, low viscosity (LV)	AlfaAesar (Heysham, UK)	0.008 ± 0.00006
Alginic acid sodium salt, high viscosity (HV)	Alfa Aesar (Heysham, UK)	0.708 ± 0.018

2.1.3 Calcium chloride

Calcium chloride dihydrate (M_w = 147 $g.mole^{-1}$) was purchased from Sigma Chemicals (St. Louis, Missouri, USA) with a purity of 99.5 %. The compound was used as purchased without further purification.

2.1.4 Buffer solutions

The following chemicals were used to prepare the buffer solutions and for pH adjustment.

Table 2.2. Chemicals used to prepare the buffer solutions

Name of chemicals	Suppliers
Sodium bicarbonate ($NaHCO_3$)	Fischer Scientific (Loughborough, UK)
Imidazole ($C_3H_4N_2$)	Sigma Chemicals (St. Louis, MO, USA)
Hydrochloric acid (0.5 M)	Convol by BDH Chemicals (Poole, Dorset, UK)
Sodium hydroxide (1 M)	(Fischer Scientific, Loughborough, UK)

2.1.5 Water-insoluble compounds for encapsulation

The following chemicals were water-insoluble compounds used for encapsulation purposes.

Table 2.3. Raw material suppliers and physical properties which include molecular weight (M_w), refractive index (n), and density (ρ) of water-insoluble compounds for encapsulation

Name of chemical	Suppliers	M_w (g.mole^{-1})	n	ρ (g.cm^{-3})
Rutin trihydrate, 97%	Alfa Aesar (Heysham, UK)	664.58	1.77	1.82
Curcumin, 95% (from Turmeric rhizome)	Alfa Aesar (Heysham, UK)	368.39	1.42	1.28
Ronacare® Tiliroside,	Merck KGaA (Darmstadt, Germany)	594.53	1.76	1.69
β-Carotene, >97%,	Sigma-Aldrich Co. (St. Louis, MO)	536.87	1.56	0.94

All these water-insoluble compounds above were solubilised with 99.99% ethanol (ρ = 0.79 kg.l^{-1}) manufactured by VWR Internationals (Fontenay-sous-

Bois, France). For preparation of β-carotene encapsulation, polyoxyethylene sorbitan monolaurate (Tween 20) (purchased from Sigma Aldrich, St. Louis, MO, USA) were used as a surfactant during the encapsulation.

2.1.6 Water soluble compounds used for encapsulation

The following chemicals were water-soluble compounds used for encapsulation purposes, which consist of proteins and dyes.

Table 2.4. Raw materials suppliers, molecular weight (), and the solvent used to dissolved water-soluble compounds for encapsulation

Name of chemical	Suppliers	M_w	Solvent used
Lysozyme from chicken egg white	Sigma Chemicals (St. Louis, MO, USA)	80 kDa	Sodium bicarbonate (20 mM) pH 8 and 10
Lactoferrin Bioferrin 2000	Glanbia Nutriotional (Middlesbrough, UK)	14.3 kDa	Sodium bicarbonate (20 mM) pH 6 and 8
Erioglaucine disodium salt	Sigma-Aldrich (St. Louis, MO, USA)	792.85 $g.mole^{-1}$	Millipore water (pH 6.8 ± 0.2)
Methylene blue, 98.13%	Alfa Aesar (Heysham, Lancashire, UK)	319.86 $g.mole^{-1}$	Millipore water (pH 6.8 ± 0.2)

The proteins and dyes were used as purchased without further purification or concentration.

2.1.7 Magnetic Nanoparticles

The following chemicals were used to produce the magnetic nanoparticles (MNPs), see Table 2.5. A high performance Neodymium magnet (First Magnets®) with 28 mm dia. x 11 mm thick coated with PTFE Teflon (manufactured by from Magnet Experts Ltd, Newark, UK) was used to collect the magnetic nanoparticles.

Table 2.5. List of chemicals used to produce magnetic nanoparticles

Chemical names	Supplier	[C]
Iron III chloride hexahydrate ($FeCl_3.6H_2O$), M_w = 270.3	Sigma-Aldrich Co. (St. Louis, MO, USA)	1 M
Iron II chloride tetrahydrate ($FeCl_2.4H_2O$), M_w = 198.81	Acros Organics (New Jersey, USA)	2 M
Ammonia solution (NH_4OH), 35%, S.G.= 0.88	Fischer Scientific (Loughborough, UK)	1 M

2.1.8 General Chemicals

2.1.8.1 Sodium azide (NaN3)

Sodium azide from Sigma-Aldrich (St. Louis, MO, USA) was added at a very low concentration (0.01 wt. %) to the alginate stock solution as a preservative.

2.1.8.2 Sucrose

Sucrose from BDH AnalaR Poole by VWR International Ltd. (Dorset, UK) was added to the microgel suspension to increase the density of the aqueous phase.

2.1.9 Filters

There were several types of filters used during the experiments, see below for the details.

2.1.9.1 Syringe Filter

Prior to particle size measurement using Zetasizer, 1 µm filter Whatman Puradisc 25 TF (GE Healthcare Life Science, Buckinghamshire, UK) was attached to a 5 ml syringe filled with 2 ml of microgel suspension.

2.1.9.2 Filter paper

Filter paper of *Fisher*brand by Fisher Scientific (Loughborough, UK) grade 111 (12–15 µm pore size) with diameter size 110 mm was used to filter the extracted microgel particle materials from alcohol extraction.

2.1.10 Cuvettes

There are several types of cuvettes used depending on the experiments, see below for the details.

2.1.10.1 PMMA UV Vis cuvette

Disposable cuvettes 1.5 ml PMMA (Brand Gmbh + Co, Wertheim, Germany) with a dimension of 12.5 x 12.5 x 45 mm were used for particle size distribution analysis and spectrophotometry measurements.

2.1.10.2 Folded electrophoresis capillary cells

Folded capillary cells DTS 1061 purchased from Malvern (Worcestershire, UK) were used for measuring the surface charge.

2.1.11 Chemicals for CLSM preparation

The following table listed the chemicals to prepare the samples for CLSM .

Table 2.6. List of chemicals used to prepare samples for CLSM analysis

Chemical Names	Suppliers	Purpose
Gelatine from bovine skin	Sigma-Aldrich Co. (St. Louis, MO)	To immobilize the Brownian motion of microgel particles in suspension
Fluorescein isothiocyanate-dextran (FITC-dextran), M_w avg ≈ 2,000,000	Sigma-Aldrich Co. (St. Louis, MO)	To provide fluorescence background to the microgel suspension.
Immersion liquid Type F, n = 1.518	Leica Microsystem CMS Gmbh (Wetzlar, Germany)	To enhance the resolution of the images

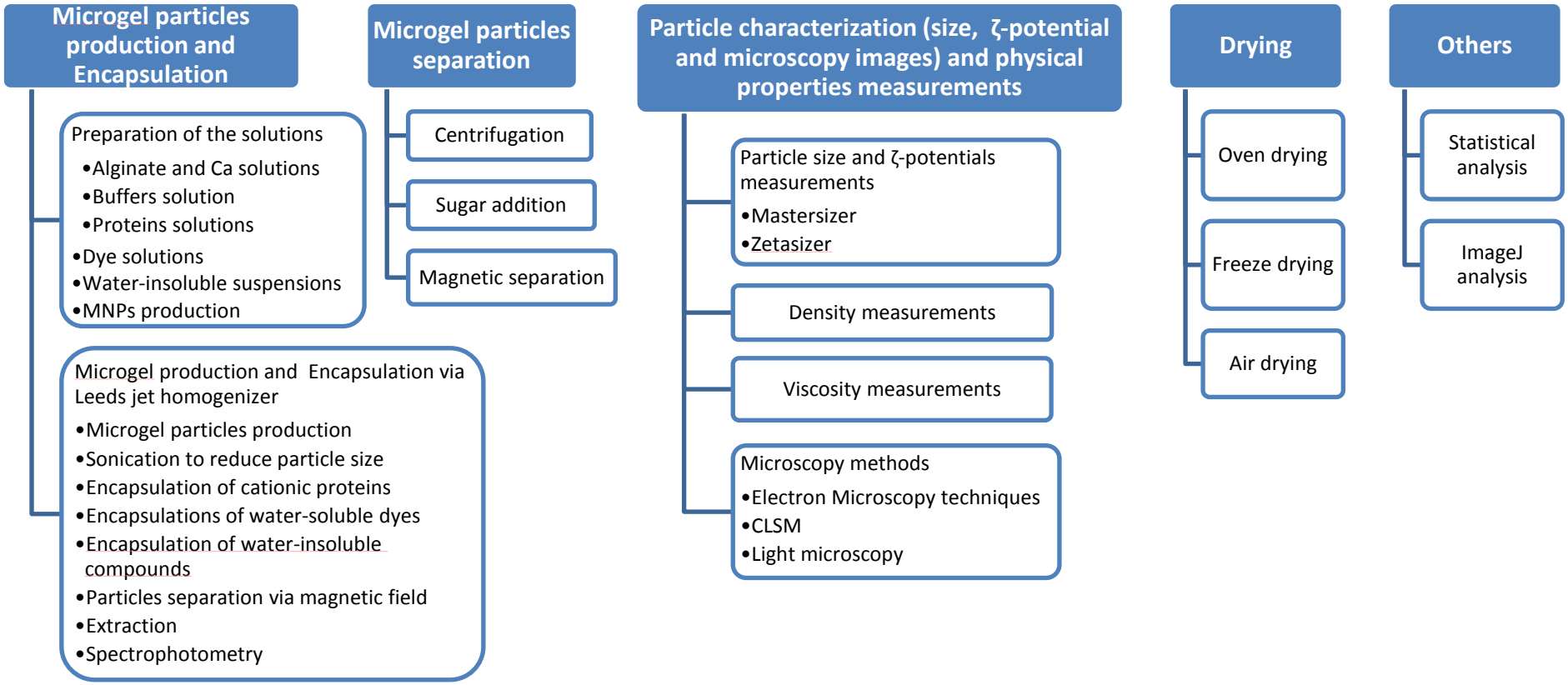

Figure 2-1. Summary outline of all methods used in the experiments, from producing of the microgel, encapsulation, and characterization of the microgel particles and analysis.

2.2 Methods

There are many methods involved in the process of producing and analysing the microgel particles and encapsulations. Figure 2-1 provides the summary of all the methods used in the experiments.

2.2.1 Preparation of solutions

2.2.1.1 Alginate and Ca^{2+} solutions

Stock solutions of alginate were prepared at 2 wt.% and 4 wt.% concentrations by weighing a certain amount of alginate powder and Millipore water according to the concentration levels required. The solution was heated to 60 ^{o}C and stirred for 2 hours to ensure a homogenous solution was produced and the alginate was completely dissolved. Afterwards, the solution was cooled down to room temperature and 0.01 wt.% sodium azide was mixed into the solution. The stock alginate solutions were refrigerated for further usage. To make 1 or 2 wt.% alginate solutions, the stock solutions 2 and 4 wt.% were diluted to 1:1 wt. ratio with Millipore water or buffer solutions.

Varied concentrations of $CaCl_2$ solution at 10 mM, 20 mM, and 50 mM were prepared. The $CaCl_2$ (was dissolved in Millipore water and because of its highly hygroscopic nature, it was readily dissolved with a magnetic stirrer without any heat treatment.

2.2.1.2 Buffer solutions

To make the buffer solutions, the buffer salts were prepared in Millipore water in a volumetric flask to reach 20 mM of concentration for both buffers. The buffers were adjusted with 0.5 M hydrochloric acid (Convol by BDH Chemicals Poole, Dorset, UK) and 1 M of sodium hydroxide (Fischer Scientific, Loughborough, UK) to reach desired pH levels, i.e., pH 6, 8, and 10 for bicarbonate and pH 6 and 8 for imidazole.

2.2.1.3 Protein solutions

The proteins were dissolved in a 20 mM sodium bicarbonate buffer. Lysozyme powder was dissolved in pH 8 and 10 buffer solutions, while lactoferrin powder was dissolved in pH 6 and 8 sodium bicarbonate buffers.

After mixing with buffer, the lysozyme solution remained clear, i.e., no turbidity was observed. The lactoferrin solutions turned orange because of the iron that is inherently bound to it.

Choosing the right buffer to fix the pH in protein solutions creates some challenges because of possible interactions between the ions in the buffers with the microgel constituents and proteins. A phosphate buffer was used initially in the microgel production containing lysozyme. However, it was discontinued due to possible interaction between Ca^{2+} with the phosphate ions in the buffer solution (Gombotz & Wee, 1998). Imidazole can bind with the haem iron of the proteins (Verras & Ortiz de Montellano, 2006) thus it created cloudy solutions after mixing at concentrations as low as 0.1 wt.% lactoferrin in 20 mM imidazole. A sodium bicarbonate buffer was chosen as a buffer in protein containing microgel particle suspensions, although the sodium bicarbonate buffer might not be the best option due to CO_2 loss over time which leads to a subtle increase of pH (Perrin and Dempsey, 1974). To overcome this, the buffer was freshly prepared and the particle size distribution and surface charge measurements were performed immediately upon microgel production within less than 2 hours.

2.2.1.4 Dye solutions

A stock solution of 100 ppm of each dye, i.e., erioglaucine or methylene blue, was prepared by dissolving the dye powder in Millipore water. This dye stock solution was diluted with alginate solutions (either 1 or 2 wt.%) to make up 10 ppm as the final concentration in the alginate phase.

2.2.1.5 Water-insoluble suspensions

For water-insoluble polyphenols encapsulation, 0.02 M imidazole buffer solution was used to suspend the insoluble polyphenol crystals with initial concentration of 1 mM before mixing 1:1 wt.ratio with 4 wt.% alginate. No sign of turbidity or precipitation was observed in dissolving polyphenols with imidazole which indicated no interaction between the buffer and the polyphenols. For β-carotene suspension, the crystals were simply suspended in Millipore water at 2 wt.% (37 mM) concentration with addition of 6 wt.% Tween 20 (TW20) before mixing 1:1 wt. ratio with 4 wt.% alginate solution.

2.2.1.6 Preparation of magnetic nanoparticles (MNPs) suspension

The MNPs were produced via the method outlined by Garcia-Alonsoa, Fakhrullin, & Paunov (2010) by mixing $FeCl_2$ and $FeCl_3$ with ammonia solution as a reducing agent. The chemical reactions for this MNP production are outlined as follows:

a. In aqueous solution, the ammonia becomes protonated.

$$NH_3 + H_2O \Leftrightarrow NH_4^+ + OH^-$$

b. Mixing of $FeCl_2$ and $FeCl_3$ in the presence of protonated ammonia, yields the iron oxide precipitate (Fe_3O_4)

$$2FeCl_3 + FeCl_2 + 8NH_4OH \rightarrow Fe_3O_4 + 8NH_4Cl + H_2O$$

Based on the chemical reactions above, the steps to produce the magnetic particles are outlined below:

1 M $FeCl_3$ was mixed with 2 M $FeCl_2$ at a 4:1 volume ratio (20 ml of $FeCl_3$ to 5 ml of $FeCl_2$) with a glass rod stirrer (preferred over metal rod or magnetic stirrer). The 1 M NH_4OH solution was added slowly into the mixture while stirring. Immediately upon mixing with NH_4OH, a dark blob of MNPs started to appear. The mixture was incubated at room temperature for 1 hour. Afterwards, the precipitate was separated by placing a high performance Neodymium magnet (First Magnets®) on the side of the beaker and the remaining NH_4OH solution was decanted. Then, the precipitate was washed several times with Millipore water until the pH of the water used for washing reached pH 7.5. After the final wash, the precipitate was suspended in Millipore water at a concentration of 1 g per 20 ml of water. The MNPs suspension was sonicated using a Sonics Vibra Cells ultrasonic processor (Sonics and Materials Inc., CT, USA) for 30 minutes at 130 watt and 60 amps. The temperature was measured after 30 minutes of sonication, it rose from room temperature to 40 to 41 ^oC.

2.2.2 Microgel particles production and encapsulation via the jet homogenizer

2.2.2.1 Microgel particles production

Production of microgel was performed using a jet homogenizer designed by University of Leeds, School of Food Science and Nutrition (see Figure 2-2). It consisted of two feeding blocks (A and C) which allowed two liquid streams to come in contact through an orifice (E) with a diameter of around 0.5 mm. The volume ratio of these A and C blocks could be altered with other ratios (for example, 70:30, 90:10, 45:55). The volume ratio used for all the subsequent experiments was 80 to 20. After testing other ratios, the 80:20 ratio was found to be optimal in producing the smallest particles with diameter less than 1 µm (Bentley, 2013). The alginate was placed in the 80 block (A) and calcium was placed in the 20 block (C). The pressure could be adjusted from 100 to 400 bar, however the optimal pressure was found to be at 300 bar and above, at which the microgel particle size was found to be within nanoregion scale (Mahatnirunkul, 2013).

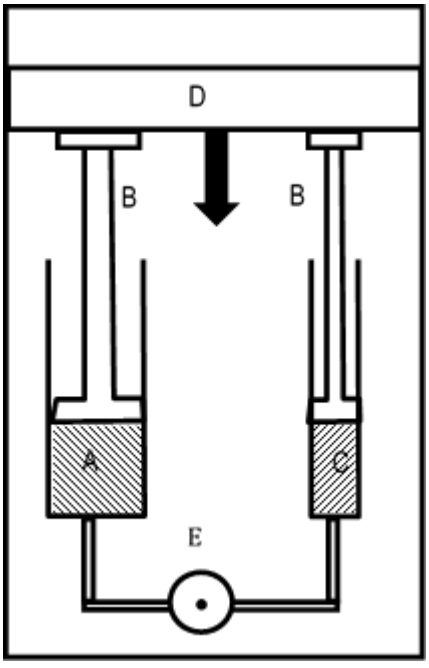

A = Alginate phase in 80 volume ratio
B = pistons
C = $CaCl_2$ phase in 20 volume ratio
D = pneumatic ram
E = sample outlet

Figure 2-2. Schematic diagram of the jet homogenizer

In the jet homogenizer, a pneumatic ram (D) is used to push the pistons (B) into feeding blocks (A and C). A high energy dissipation was generated from the kinetic energy when the liquid streams were converted into a turbulent

motion through collision and redirection of the liquids from A and C to fit into the orifice (E). This occurrence created a further rapid mixing, and thus small particles were generated. The microgel suspension was then collected into a beaker placed underneath the outlet (E).

2.2.2.2 Particle size reduction via sonication

The microgel suspension was subjected to ultrasound for further particle reduction. In this experiment, a minimum of 2 ml aliquot of homogenized and diluted microgel suspension was subjected to a Sonics Vibra Cells ultrasonic processor (Sonics and Materials Inc., CT, USA) with 130 watt at varied times from 2 to 30 minutes and pulsed for every 2 seconds at 40 amps. The tip of ultrasonic probe was immersed into the middle of the sample tubes during sonication. To maintain the temperature during sonication, the samples were placed into an ice cooling bath with a thermocouple inserted into the sample. The temperature was kept below 35^{o}C throughout the sonication process.

2.2.2.3 Encapsulation of cationic proteins in the microgel particles

For the inclusion of lysozyme into the microgel particles, several mixing routes were attempted during the experiments. In the first mixing route, lysozyme solution was mixed with 2 wt.% alginate at 1:1 wt. ratio and placed into the 80 block (Figure 2-2.A). Second, the lysozyme solution was mixed with 20 mM $CaCl_2$ solution at 1:1 wt. ratio in 20 block (Figure 2-2.C.). Lastly, an extra step was taken by mixing the lysozyme after the particles were formed in the jet homogenizer, i.e., lysozyme in the 20 block (Figure 2-2.C.) and microgel suspension (made with 1 wt. alginate and 10 mM Ca^{2+}) was placed in 80 block (Figure 2-2.A). The concentrations of lysozyme were adjusted depending on which mixing route was pursued. The final concentrations of lysozyme in the microgel suspension remained the same range whichever method was used, ranging from 0.01 to 0.25 wt.%. While, lactoferrin was incorporated by mixing into the Ca^{2+} phase at concentrations from 0.02 to 8 wt.%. The rationale for increasing the concentration of lactoferrin up to 8 wt.% was to achieve 1:1 mass ratio of alginate to lactoferrin.

2.2.2.4 Encapsulation of water-insoluble compounds in the microgel

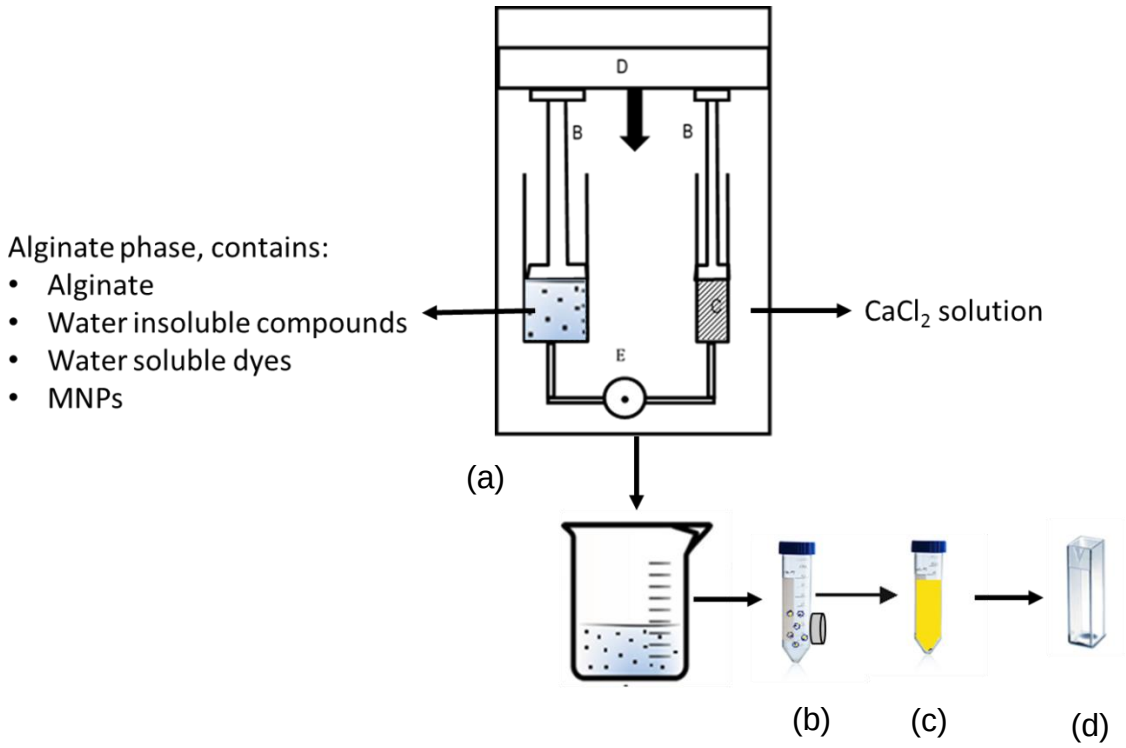

Figure 2-3 Summary of steps to produce water-insoluble crystals and water-soluble dyes encapsulated microgel particles using the Leeds Jet homogenizer (a), separating the microgels using MNPs (b), extracting water-insoluble compounds with ethanol and dyes with Millipore water (c), and quantifying the entrapped amount from absorbance readings (d)

Figure 2-3 outlines the steps involved for the production of encapsulated microgel particles via the jet homogenizer, particle separation via a magnetic field, extraction, and finally the quantification of the encapsulated materials via UV-Vis spectrophotometry. 1 mM initial concentrations of the insoluble polyphenols and 37 mM for the β-carotene (with or without TW20) were mixed into 25 ml of Millipore water using an IKA Labortechnik Ultraturrax T25 S7 (Janke & Kunkel GmbH & Co, Funkentstort, Germany) at 24,000 rpm for 2 minutes. Then the water-insoluble suspension was mixed with 4 wt.% alginate stock solution at 1:1 wt. ratio. At this stage, 0.02 wt.% (wet weight basis) of MNPs suspension was spiked into the alginate phase. The MNPs and water-insoluble compounds were suspended into alginate solution via application of

the Ultraturrax for 2 minutes at 24,000 rpm. A mild sonication was applied to the suspension of alginate with encapsulated materials and nanomagnets suspension using a PUL 55 sonicator (Kerry Ultrasonic Ltd., UK) for 5 minutes to remove any air bubbles. The final mixture contained 2 wt.% alginate and the concentrations of encapsulated materials were 0.5 mM for the insoluble polyphenols and 18.5 mM for the β-carotene with or without 3 wt.% Tween 20.The mixture was then placed in the jet homogenizer in the 80 block immediately after mixing. The microgel particles with encapsulated materials were produced with the jet homogenizer at 300 bar by placing the mixture of encapsulated materials and alginate in the 80 block and 20 mM $CaCl_2$ in the 20 block.

2.2.2.5 Encapsulation of dyes in the microgel particles

For encapsulation of the dyes, the microgel particles were produced using 1 wt.% and 2 wt.% alginate solutions mixed with 10 mM and 20 mM $CaCl_2$ solutions, respectively. In this experiment, the same volume ratio was applied, where the $CaCl_2$ solution was placed in 20 block whilst the 80 block contained a homogeneous mixture consisting of sodium alginate solution, dye solution and MNPs suspension (Figure 2-3). The concentrations of added dye solution and MNPs suspension in the mixture was 10ppm and 0.01%, respectively. The procedure of producing 1 wt.% and 2 wt.% dye encapsulated microgels was repeated in triplicate. In addition, 1 wt.% and 2 wt.% blank microgel samples were also prepared as described above with the absence of dye solutions.

2.2.2.6 Separation of microgel particles from aqueous phase via magnetic field

As the microgel suspension exited from the jet homogenizer it was collected in a glass beaker, and the sample was transferred into a 50 ml centrifuge tube. The centrifuge tubes containing encapsulated materials were wrapped in thick aluminium foil to avoid direct exposure to sunlight (UV) to prevent any potential photodegradation. A strong magnet was placed on the side of the centrifuge tube for water-insoluble containing microgel samples for 30 minutes. For dyes containing microgel samples, a magnetic stirring bar was

placed inside of the tube to monitor the harvested microgel particles adhered to the magnet which otherwise would not easily be detected in this intensely coloured blue solution. Consequently, the microgel particles with and without encapsulated water-insoluble compounds and dyes were expected to be attracted towards the magnet because of the presence of MNPs that were potentially encapsulated within the microgel particles. Within 30 minutes, a layer of microgel particles was apparent either adhering to the tube wall or to the magnetic stirring bar as an indicator of the attraction between the encapsulated MNPs with the magnets. The supernatant aqueous phase was then decanted into separate tubes.

2.2.2.7 Extraction of encapsulated compounds in microgel particles.

The collected microgel particles were diluted either with Millipore water or alcohol to extract the encapsulated materials. About 50 µl of the harvested microgel particles was pipetted into 5 ml of ethanol for alcohol extraction for 30 minutes. While for dyes containing samples, about 1 g of the microgel particles was dissolved in 10 g of Millipore water for 30 minutes. The supernatant fluid was also extracted with Milllipore water or alcohol at the same ratio. The amount of water or alcohol used for dilution was recorded to calculate the dilution factor. The extracted solvent was filtered using *Fisher*brand filter paper (Fisher Scientific, Loughborough, UK) grade 111 to remove any extracted microgel particle materials before placing into the cuvette for absorbance readings.

2.2.2.8 Spectrophotometer Measurement

Based on the Beer's Law method (see Eq.2-1) under the same condition, i.e., same ε and L, one can predict the concentration based on the proportionality of the known concentration versus absorbance (A).

$$A = \varepsilon\ L\ c \qquad \textbf{2-1}$$

where ε equals to the molar exctinction coefficient (M.cm^{-1}), and L is the cell path length (cm), and c is the concentration (M).

2.2.2.9 Standard curve preparation

Standard curves were generated for each compound of interest with known concentration plotted against the absorbance at a certain absorption wavelength. Absorbance reading and wavelength maxima were determined using a UV-Vis Spectrophotometer (Jenway 6715 from Bibby Scientific Ltd, Staffordshire, UK). A serial dilution was performed from stock solutions of erioglaucine, methylene blue, rutin, tiliroside, curcumin, and β-carotene. Stock solution of 0.5 mM (for the insoluble crystals) and 100 ppm (for water-soluble dyes) were prepared. Then they were further diluted to a certain concentration range until it reached the absorbance of less than 1.5 at λ maxima as reported in Table 2.7. Linear correlation lines were obtained from fitting the absorbance versus the known concentrations of those compounds; with the intercept set at zero and $R^2 \geq 0.98$ for all curves which indicated a strong correlation between the absorbance and concentration. The trendline equations of these standard curves in Table 2.7 were used to calculate the unknown concentration of the encapsulated materials entrapped in microgel particles after extraction.

Table 2.7. List of the absorbance peak, concentration range, and trendline equations of the encapsulated materials used to generate the standard curves

Chemical compounds and its solvent	λ maxima (nm)	Concentration levels	Trendline equations*
Erioglaucine in water	630	0.01 to 10 ppm	y = 0.1333x
Methylene blue in water	665	0.1 to 2 ppm	y = 0.2348x
Rutin in alcohol	360	0.005 to 0.05mM	y = 12.771x
Tiliroside in alcohol	325	0.001 to 0.05 mM	y = 28.908x
Curcumin in alcohol	420	0.0001 to 0.01 mM	y = 53.635x
β-carotene in alcohol	450	0.01 to 0.115 mM	y = 13.504x

*y = absorbance, x= concentration

2.2.2.10 Quantification of the amount of encapsulated materials via spectrophotometry method

To quantify the encapsulated compounds entrapped into the microgel particles, about 1 ml of the filtered solution obtained from the extraction was placed in a PMMA cuvette and an absorbance reading was recorded. The absorbance was converted to its molar concentration using the trendline equations stated in Table 2.7. The conversion of molar concentration to mass (mg) of the encapsulated materials was calculated using Eq.2-2. The microgel particles containing no encapsulated materials (blank) were also measured for the absorbance value, and gave results close to zero in concentration within the standard experimental error in water-insoluble containing experiments. For water-soluble dyes, the blank samples exhibited some absorbance, thus its concentration was taken into account to calculate the concentrations of the entrapped dyes.

$$M = C\ x\ V\ x\ DF\ x\ MW\ x\ 10^{-3} \qquad \textbf{2-2}$$

where M is the mass of the encapsulated compounds (mg), C is the Molar concentration of the encapsulated compounds in mM, V is the volume of alcohol or Millipore water used for the extraction of the encapsulated compounds, DF is the dilution factor which is the reciprocal of the alcohol or water used for dilution, and M_w is the molecular weight of the encapsulated compounds (g.mole^{-1}).

2.2.3 Particle separation method

2.2.3.1 Centrifugation

Separation of the particles was performed not only via magnetic field by addition of MNPs, but also via centrifugation. The centrifugation method was applied for microgel particles without any encapsulated materials. The microgel suspension was centrifuged at 20,000 rpm (48,343 g) for 20 minutes at 25^{o}C using high speed Beckman Coulter (Avanti J-301) to collect the sediments of microgel particles.

2.2.3.2 Sucrose addition

Sucrose addition was used to increase the density of the aqueous phase, thus the microgel particles could be separated because of the density gap between the aqueous phase and the microgel particles was possibly more accentuated. The procedure of sucrose addition was simply adding 24 wt.% of sucrose to the microgel suspension and stirred for 10 minutes with a magnetic stirrer. The sucrose was readily dissolved in the suspension within 10 minutes. Afterwards, the mixture was centrifuged at 20,000 rpm (48,343 g) and paused for every 5 minutes (20 minutes total) using high speed Beckman Coulter (Avanti J-301) to further analyze its density and particle size based on the location of the test tube after the centrifugation.

2.2.4 Particle characterizations and physical properties measurements

2.2.4.1 Particle size and ζ-potential measurements

The particle size distribution measurement was performed using a Zetasizer Nano-ZS (Malvern instruments, Worcestershire UK) for small particles (< 1 µm). Prior to particle size measurements using the Zetasizer, the Ca-alginate microgel suspension as exited from the jet homogenizer was further diluted with Millipore water at 1:10 weight ratio to prevent aggregation. In addition to dilution, samples were filtered with a 1 µm Whatman filter to remove any large aggregate particles or dust. Presence of large particles can affect the size distribution, because they restrict the free diffusion pattern of the target particle of interest, otherwise a biased value could have been reported (Malvern Instruments, 2011). The samples were placed into disposable PMMA cuvettes and the particle sizes were measured at 25^{o}C. The wavelength of the laser source was at 633 nm and the light scattering was detected at 173^{o}. Experiments were done in triplicate.

The size distribution of large particles (> 1 µm) in microgel suspension with or without encapsulated materials generated from mixing 2 wt.% alginate and 20 mM $CaCl_2$ in the jet homogenizer was measured using a Mastersizer (Malvern Instruments, Worcestershire UK). The refractive index (n) of the

continuous phase water was 1.33 and the n for the water-insoluble compounds encapsulated microgel particles varied from 1.4 to 2.4. The particle size distribution was not very sensitive to the changes of the refractive index range mentioned above. The obscuration range was set at 1–4 %, and absorption index was from 0.01 to 0.1.

The ζ-potentials of the microgel particles were measured using Zetasizer Nano-ZS (Malvern Instruments, Worcestershire UK). The samples were placed in folded capillary electrophoresis cells DTS1061 (Malvern, Worchestershire, UK) which had positive and negative charged electrodes at either ends of the tube, spaced 6 cm apart. The viscosity of the dispersed media (i.e., water, η = 8.9 x 10^{-4} Pa.s at room temperature) and the Henry's function ($f(k_a)$ = 1.5 for dispersion in polar media based on the Smoluchowski approximation). Triplicate samples were measured.

It is imperative to determine the pH of the dispersed media when the ζ-potential is being measured, since the ζ-potential is an index of the magnitude of the electrostatic repulsion between particles, thus altering [H^+] may affect this interaction. Therefore, when making the microgel particles containing proteins and water-insoluble compounds, buffer solutions were used to dissolve the proteins, or dilute the gel particles to fix the pH of the system. For water-soluble dyes containing microgel, the pH of water was determined prior to ζ-potential measurements and was found to be stable around 6.8 ± 0.2.

2.2.4.2 Density Measurement

The density of the suspensions was measured with a density meter (Anton Paar DMA 4500M, Austria). The microgel suspension was injected through a syringe into the inlet of the density meter gently to eliminate possibility of incorporating air into the syringe. The density meter had a camera to view the internal loop of the sample as it was being injected and thus the presence of air bubbles could be detected. The density reading was recorded at room temperature between 24.78–25.02 ^{o}C. Triplicate samples were measured and the average values were reported.

2.2.4.3 Viscosity measurement

The viscosity of microgel suspension was measured with a Kinexus Rheometer (Malvern Instruments, Worcestershire UK) which was equipped with *rSpace* software to control the probe and to provide measurement and analysis of the results. The temperature was set at 25 °C with a 5 minute time window to achieve a steady state condition. The cone and plate cartridge (CP2/60:PL65) was used in every sample. About 1 to 2 ml of microgel suspension was placed on top of the plate. The applied shear rates was ranged from 0.1 to 10 s^{-1} for each sample.

2.2.4.4 Microscopy Measurements

There were several microscopy techniques used throughout the experiments, i.e., multiple versions of electron microscopies, light microscopy, and confocal methods. All of them possessed different strength in magnification and applied to different type of microgel samples, see Table 2.8. They are also involved in different sample preparation procedures which are outlined below.

Table 2.8. List of microscopes used in the experiments

Types of microscope	Brand/Manufacturer	Magnification and applied voltage	Types of samples analyzed
Light Microscope	Celestron Digital LCD (California, USA)	10x, 20x, 40x, and 60x	microgel suspension
SEM	JEOL JSM 6390A (Japan)	7,000x at 10 to 20 kV	freeze-dried microgel particles
Field Emission SEM (FE-SEM)	Inspect F50 by FEI (Czech)	100,000x at 20 kV	freeze-dried microgel particles
Environmental SEM (E-SEM)	Quanta 200P by FEI (Czech)	7,000x at 10 kV	microgel suspension
TEM	Tecnai G2 Spirit by FEI (Czech)	200,000x	microgel suspension
CLSM	Leica TCS SP2 (by Leica Microsystems, Manheim, Germany)	40x oil immersion	Encapsulated microgel particles with a mixture with gelatin and FITC-dextran

For SEM preparation, a small piece of the freeze-dried microgel suspension was pulled apart and its cross section was glued onto a chrome-coated steel-plate sample holder. The sample was sputter coated with Au/Pd using JEOL JFC-1600 Auto Fine Coater (JEOL Japan) for 200 seconds at 30 mA. The SEM was also attached with EDS Spectrometer JED 2300 (JEOL, Japan) which measured the composition of microgel particles at varied spots. For the environmental SEM (E-SEM) and TEM sample preparation, a small drop of the microgel suspension was placed onto a TEM grid and air dried for at least 30 minutes.

For samples intended for CLSM experiments, 4 wt.% gelatin was heated up to 35^{o}C and stirred for more than 30 minutes. The microgel suspension was mixed with 4 wt.% gelatin at 1:1 weight ratio. FITC-dextran was added into the mixture of microgel and gelatin mixture at a concentration of 0.2 wt.%. The samples was placed onto a welled slide with a dimension of 30 mm in diameter and 3 mm in depth and refrigerated overnight to solidify. The Leica TCS SP2 confocal microscope was used (Leica Microsystems, Manheim, Germany) to view the samples, using a laser source used of Ar/ArKr (488, 514 nm) with 40x oil-immersion lens. A drop of immersion liquid type F (Leica Microsystem CMS Gmbh, Wetzlar, Germany) placed on the cover slip to enhance the resolution. Both PMT detectors were activated to detect signals from two different fluorophores, i.e., the polyphenols or β-carotene and FITC-dextran at different excitation bands, so that both the encapsulated crystals and microgel particles could be visualized in situ. The fluorescence excitation wavelengths were set at 458 nm for the polyphenols and 514 nm for β-carotene. The signals from emission were collected from 460 – 480 nm for polyphenols and from 530 – 580 nm for β-carotene. The FITC-dextran was excited at 488 nm for polyphenols and β-carotene samples. The fluorescence emission of FITC-dextran was collected from 500 – 550 nm in polyphenols containing samples and from 490 - 510 nm in β-carotene containing microgel particles. Both emission and excitation were performed at different wavelengths to avoid any interference of the signals.

For light microscopy samples, the microgel particles formed via jet homogenizer were immediately analyzed under the microscope (Celestron Digital LCD, California, USA) with 60x magnifying lens. A few drops of the gel particles in suspension were placed on a slide and sealed with cover slip. The scale was created using a disc micrometer reticle with 10 mm length and 100 division (Leica Microsystems Inc., Buffalo, NY, USA).

2.2.5 Drying experiments

There were several types of drying experiments conducted to determine either solid content or the yield of particles in dry basis, to prepare samples for electron microscopy analysis, or to increase the concentration of the particles.

2.2.5.1 Oven Drying

For mass balance quantification, the microgel particles obtained from the sediment of centrifuged microgel suspension were collected to determine the dry yield. The microgel suspension was centrifuged at a speed of 20,000 rpm (48,384 g) for 20 minutes using high performance centrifuge Beckman Coulter (Avanti J-301) with a fixed angle rotor (Avanti J.30-50 Ti). The sediment, which presumably was the microgel particles, was then dried using Anderman oven UL 48 (Memmert GmbH + Co., Schwabach, Germany) at temperature of 105^{o}C for 24 hours. The weight of the microgel particles before and after drying were recorded, thus the % solid yield could be computed using Eq.2-3. Oven drying at 105^{o}C temperature for 24 hours was also applied to magnetic nanoparticles to determine the solid content. The solid content of the magnetic nanoparticles was 0.19 ± 0.01 % solid. The measurements were done in triplicates for all these drying experiments.

$$\%\ \text{solid or yield} = \frac{wt.\ before\ drying - wt.\ after\ drying}{wt.\ before\ drying} \text{x}100\% \qquad \textbf{2-3}$$

2.2.5.2 Freeze Drying

To prepare samples for SEM and FE-SEM analysis, the microgel suspension was freeze-dried using a benchtop lab scale freeze dryer Christ Alpha 1-4 LDP Plus (Martin Christ GmbH, Germany). About 80 g of the microgel suspension was placed into a wide opening glass plate with a

diameter of 22.5 cm to provide a large surface area for drying. Triplicate samples were produced for this measurement. These plates containing microgel suspension were frozen using a blast freezer BF051ET (Valero, Banbury, UK) at -30 ^{o}C for 3 hours. Afterward, these frozen samples were freeze-dried for 25 hours at -50 ^{o}C and 0.04 mbar. Using the mass balance equation (Eq.2-3), the freeze-dried microgel suspension yielded 0.77 wt.% solid. With that number, the solid recovery was almost 100 % because the amount of solid originally added was 0.8 wt.% alginate (1 wt.% alginate in 80 block or 80% volume ratio), which was close to 0.77 wt.% recovered solid. This indicated that freeze drying process for 25 hours was efficient to remove the free water.

2.2.5.3 Air Drying

To increase the number of the microgel particles, about 80 g of the microgel suspension was placed in a large glass plate (diameter of 22.5 cm) and then air dried in a fume cupboard for 7 hours at room temperature. The fume cupboard had a positive airflow system with a fan pulling the ambient air to evaporate the moisture. The moisture loss was obtained by subtracting 100 % to the % solid or yield (Eq.2-3). About 60 ± 12 % of moisture was removed after 7 hours drying. By drawing the moisture out of the microgel suspension, the particles became more concentrated, and thus it would be visible to monitor the particles via centrifugation due to density gradient.

2.2.6 Miscellaneous

2.2.6.1 Statistical Analysis

All the experiments were performed in triplicate with the mean value and standard deviation expressed as the error bars unless stated otherwise. The difference in mean values were analysed using SPSS (IBM Statistics 22 SPSS). The significant difference was reported in the $p < 0.05$ using student's t-test and ANOVA. The correlation factor was determined using Pearson's test.

2.2.6.2 Image J analysis

A few of the SEM images were analyzed using ImageJ software to predict the particle size. The scale provided from the SEM image was

converted into pixel unit in ImageJ. The threshold value was set using the automatic setting. The background noise was removed, thus contrast of brightness and darkness was more enhanced. The pixels concentrated with dark spots with the holes enclosed were considered as the microgel particles. ImageJ calculated the area of each particle. Assumed the particles were spherical in shape, thus the diameter of the particles could be determined. A histogram was plotted from these calculated diameters to examine the size distribution of the microgel particles.

Chapter 3 Formation of Ca-alginate microgel particles via Leeds Jet Homogenizer

3.1 Introduction

The Leeds Jet Homogenizer (LJH) is effectively a high pressure T-mixer that was developed by the School of Food Science and Nutrition, University of Leeds. The advantage of this particular homogenizer is the presence of two separate chambers which allows two immiscible solutions to remain separate until they come into contact in the T-mixer. It has been used to make fine emulsion of oil droplets by filling one chamber with an aqueous phase and the other with oil phase and mixing them under extremely high shear (Burgaud et al., 1990). Another advantage of the homogenizer is its ability to produce reproducible small droplet sizes with only relatively small quantities of samples, which is beneficial when dealing with expensive and limited supply of ingredients (Burgaud et al., 1990). In this study, we deviate from the traditional function of the jet homogenizer as an emulsion producer to fabricate microgel particles by allowing calcium and alginate to be rapidly precipitated at high shear rate. Johnson & Prud (2003) elucidated the techniques of creating nanoparticles through 'Flash Nanoprecipitation' method by using a confined impinging jet (CIJ) to allow a rapid mixing of two fluids. The impinging jet is a good choice due to its ability to deliver mixing times less than reaction times and thus rapid precipitation can lead to nanoparticles formation (Johnson & Prud, 2003).

This aim of this chapter is to provide a greater understanding about what factors or parameters govern the size of the microgel particles when formed via the LJH. The specific objectives of this chapter are: (i) to evaluate the role of the formulation and processing parameters that affect the microgel particle size (ii) to investigate the ways to separate the microgel from the aqueous phase and estimate its yield, and lastly (iii) to visualize the morphology of these microgel particles via several microscopy techniques. The following discussion will review whether or not these factors are meaningful relative to the particle size of the microgel particles.

3.2 Results and Discussion

The Ca-alginate microgel particles were prepared using the LJH, in which the mixing of the two components of alginate and Ca^{2+} is characterized by the Damkohler number (Da), i.e., the ratio between mixing time (t_m) and reaction time (t_r), as expressed in Eq.3-1.

$$Da = \frac{t_m}{t_r} \quad \textbf{3-1}$$

The mixing time (t_m) is defined as (Eq.3-2)

$$t_m = \left(\frac{v}{\varepsilon}\right)^{1/2} \quad \textbf{3-2}$$

where v is to the fluid velocity ($m.s^{-1}$) and ε is the high energy dissipation ($W.kg^{-1}$) generated by the mixing process in the high pressure jet homogenizer, i.e., 4.1×10^6 $W.kg^{-1}$ at 300 bar (Casanova & Higuita, 2011).

The v could be estimated from the time to evacuate the total volume (V) of the of the Ca-alginate microgel suspension as it exits through a circular orifice with diameter (d) = 5×10^{-4} m; the v is expressed as Eq.3-3.

$$v = \frac{V/A}{t} = \frac{4V}{\pi d^2 t} \quad \textbf{3-3}$$

With the measured V of 12 ± 0.4 ml of the microgel suspension evacuated from 80:20 volume ratio using a small volume chamber (S block) and with t = 0.75 ± 0.09 s, thus the estimated $v_{average}$ was around 88 ± 11 $m.s^{-1}$, which was close to that estimated by Casanova & Higuita (2011): 92 $m.s^{-1}$. Thus, the estimated t_m of mixing Ca^{2+} and alginate (from Eq.3-2) is around 5 ms.

To obtain the Da, it is necessary to determine the t_r for the gelation between alginate and Ca^{2+}, which is expressed in Eq. 3-4

$$t_r = \frac{1}{k_r C_r} \quad \textbf{3-4}$$

where k_r is the reaction rate constant ($M^{-1}.s^{-1}$) for Ca-alginate gel formation via inter-particle interaction and C_r is the concentration of the reactant in molar (M). Fernández Farrés & Norton (2014) have measured the $k_r C_r$ for the formation of alginate fluid gels at specific concentrations of 10 mM Ca^{2+} and 1 wt.% alginate

LV (low viscosity) as 0.0003 s^{-1}, thus the calculated t_r equals to 3333 seconds. From Eq.3-1, the Da is calculated to be 1.6 x 10^{-6} which is in the fast mixing mode when Da <<<1, thus submicron particles are generated.

3.2.1 Effect of Ca^{2+} and alginate concentrations in microgel particle sizes

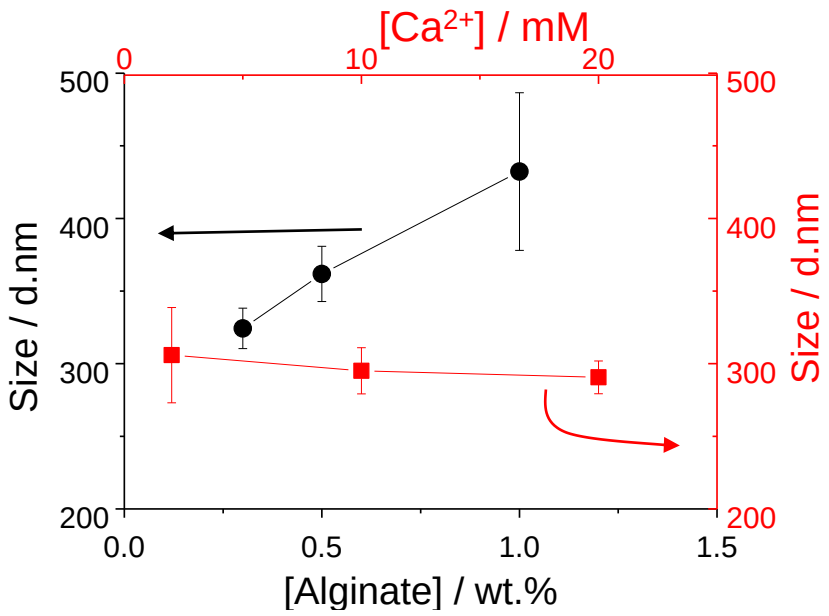

Figure 3-1. Microgel mean particle diameter (μ_z) prepared from varied Ca^{2+} concentrations at fixed 1 wt%. alginate LV (■) and from varied alginate - LV concentrations at fixed 10 mM Ca^{2+} (●). The arrows indicate the corresponding Y-axis.

Figure 3-1 shows the microgel particle sizes prepared from different alginate concentrations and a fixed 10 mM Ca^{2+} are proportionally increased with an increase in alginate concentration. The microgel particle sizes as measured via the Zetasizer (see Chapter 2.2.4.1 for method) are in ascending order: 324 ± 14 < 362 ± 19 < 432.3 ± 54 nm, as the alginate concentrations are increased from 0.3, 0.5, to 1 wt.%. Although the microgel particle size from 1 wt.% alginate might have a large standard deviation, the mean difference of microgel sizes between 1 wt.% and 0.5 wt.% alginate was significant, $p < 0.05$. Increasing alginate concentrations would decrease of the reaction time (t_r), thus Da would be increased and larger particles are therefore expected.

Altering $[Ca^{2+}]$ concentrations from 2 mM to 20 mM at fixed 1 %wt. alginate concentration did not seem to have any impact on microgel particle

sizes; the particle size remained constant at 297.2 ± 22.2 nm, which also confirmed by the $p > 0.05$ from the ANOVA test. This lack of further reduction in microgel particle sizes may be due to the depletion of available COO^- groups to be cross-linked with saturated amount of Ca^{2+}. Although some studies have shown a decrease of particle size of Ca-alginate-chitosan microparticles prepared from 0.05 wt.% alginate (M/G = 2.0) with increases in $[Ca^{2+}]$ up to 0.75 mM due to tighter coiling of the alginate nucleus, no further increase was observed in highly saturated Ca^{2+} environment Chandrasekar, Coupland, & Anantheswaran (2017). Similarly, the findings by Velings & Mestdagh (1995) also showed no further volume reduction impact from increasing $[Ca^{2+}]$ from 0.05 M to 0.33 M, due to sufficient enough Ca^{2+} to cross link all the guluronate (G) residues in the alginate (M/G = 2.3).

Stokke et al. (1991) reported that a minimum of 8 contiguous guluronic acid residues were required to form a stable junction zone. In addition, Braccini & Pérez (2001) also determined 4 oxygen atoms from the guluronate residues were bound to a single Ca^{2+} ion to form 'egg box' structure. With 4 to 1 ratio of guluronate and Ca^{2+}, we can predict the minimum Ca^{2+} concentration to occupy the G sites of alginate in the current study. Some major techniques to measure the M_w and M/G ratio of alginate are ^{1}H nuclear magnetic resonance (NMR), circular dichroism (CD) spectroscopy, or size exclusion chromatography with multi-angle light scattering analysis (SEC-MALS). In this study, the intrinsic viscosity ($[\eta]$) was calculated from Eq.3-5 based on the measured dynamic viscosity (η) of alginate LV solutions at different concentrations: 0.1, 5, and 10 g.ml^{-1}, when they reach constant η at the shear rate (γ)= 10 s^{-1}. The viscosity in the absence of solute (η_o) equals to the viscosity of water at 25^{o}C, i.e., 8.9 x 10^{-4} Pa.s.

$$[\eta] = \lim_{c \to 0} \left[\frac{\frac{\eta}{\eta_0} - 1}{c} \right] \qquad \textbf{3-5}$$

$[\eta]$ was determined by extrapolating the admittedly crude plot of $\left[\frac{\frac{\eta}{\eta_0}-1}{c}\right]$ vs. c at c = 0 g.ml^{-1} (see Figure 3-2). The $[\eta]$ for alginate LV used in this study was thus estimated ≈13.2 ml.g^{-1}. However, the extrapolation was extended to the

non-diluted alginate concentration (> 0.1 g.ml-1) which might explain the non-perfect fitting of the correlation factor (R^2 = 0.75).

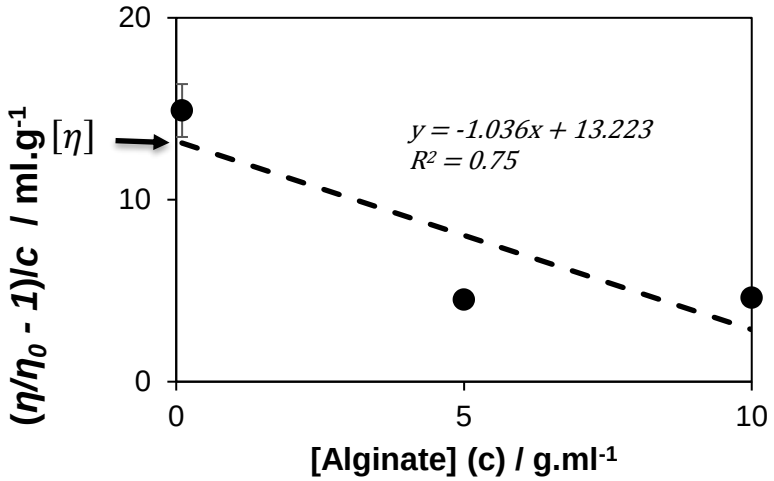

Figure 3-2. Plot of $[(\eta/\eta_0 - 1)/c]$ as a function of alginate concentration (c) to determine the intrinsic viscosity ($[\eta]$) of alginate LV at 25°C dissolved in Millipore water.

The intrinsic viscosity $[\eta]$ can be related to M_w of a polymer via the Mark-Houwink equation (Eq.3-6) :

$$[\eta] = K.{M_w}^{\alpha} \qquad \textbf{3-6}$$

where K and α are the empirical constants characterized by solute-solvent interaction. The Mark Houwink approximation is strictly valid only for Newtonian fluids, however low viscosity polymers with shear thinning behaviour such as alginate LV in a diluted concentration can be treated as close to Newtonian fluid, especially if high shear rates are involved (Morris, 1990). High viscosity alginate is excluded from this approximation due to a higher degree of entanglement exerted from a longer chain lengths which gives rise to strong non-Newtonian behaviour (Pamies et al., 2010). Using literature values of K and α for alginate (in the presence of 0.1 M NaCl) as determined by Mancini, Moresi, & Sappino (1996), i.e., 1.228 x 10^{-4} and 0.963, respectively, the M_w of alginate LV in this study is estimated around 168 kDa. This estimated value might be overestimated because Millipore water (pH 6.8 ± 0.2) was used as the

solvent instead of 0.1 M NaCl, thus the repulsive forces would impact polymer-solvent interaction.

Other similar M_w value of alginate LV, i.e., 143 kDa, has been reported by Pamies et al. (2010) for alginate isolated from *Macrocystic pyrfera.* The fractional composition of G and M ratio for alginate from *Macrocystic pyrfera* is comprised of 0.39 G and 0.61 M residues (Pamies et al., 2010). Assuming the distribution of G units in the alginate chain is in blocks of 8 contiguous units, in a 100 ml of microgel suspension containing 1 wt.% alginate (assuming density ~1), the moles of the G units can be determined using Eq.3-7, where m is the mass of alginate (g), G_f is the fraction of guluronate = 0.39, and the estimated M_w of alginate ≈ 168 kDa.

$$mole\ of\ G\ units = \frac{m}{M_w}\ x\ G_f \qquad \textbf{3-7}$$

Based on the calculation above, 0.002 mmoles of G units per g of alginate are potentially participated in cross-linking Ca^{2+} ions. With a mole ratio of 4:1 guluronate to Ca^{2+} to form compact dimers, the minimum Ca^{2+} to occupy the G units per g of alginate is 0.0005 mmoles, which translates to 0.008 mM Ca^{2+} concentration in 100 ml of microgel suspension. Hence, at 10 mM of $CaCl_2$, the microgel suspension is highly saturated with Ca^{2+} ions, i.e., there are enough Ca^{2+} ions to fully occupy all the G units. This possibly explains why the microgel particle sizes remain constant with the increase of Ca^{2+} concentrations (Figure 3-1).

3.2.2 Effect of alginate viscosity in microgel particle sizes

displays the dynamic viscosity of 1 wt.% alginate solutions: low viscosity (LV), high viscosity (HV), and a mixture of LV and HV at 1:1 wt. ratio (medium viscosity-MV) over a range of shear rates from 0.1 to 10 s^{-1}. These alginate solutions behave like most high M_w polymer solutions, i.e., shear thinning (Mancini et al., 1996), which is more pronounced in HV alginate. The LV and MV are slightly shear thinning at low shear rate (γ < 1 s^{-1}), at higher shear rate they behave like Newtonian fluids. At 0.1 s^{-1} shear rate, viscosities of these alginate solutions at 1 wt.% are 0.005, 0.17, and 1.64 Pa.s for LV, MV, and HV, respectively. On mixing 1:1 wt. ratio of alginate LV and HV, the MV viscosity was well below the average for the two, confirming that other factors determine

its viscosity, such as M_w, M/G ratio or distribution of G units in the chain (polyguluronate is known to be a stiffer chain than polymanuronnate chain - Mackie, Noy, & Sellen,1980). Thus, Figure 3-3 shows the LV was more dominant in affecting the overall viscosity of alginate solutions, possibly due to the higher proportion of the M fraction (0.69).

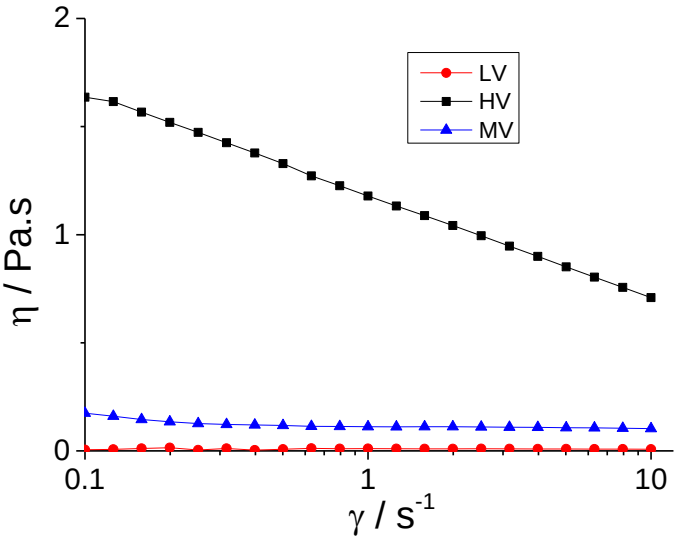

Figure 3-3. Dynamic viscosity (η) of 1 wt.% of alginate solutions over shear rates (γ) at room temperature

The microgel particles sizes prepared from these alginate solutions at 1 wt.% with 10 mM Ca^{2+} via LJH are outlined in Figure 3-4. The microgel particle sizes were correlated with viscosity at 0.1 s^{-1} (correlation factor = 0.92), i.e., 339 ± 45 nm, 401 ± 33 nm, and 460 ± 24 nm from LV, MV, and HV, respectively, with $p < 0.05$. This is attributed to the higher degree of Ca^{2+} cross-linking in higher M_w alginate. Although the M_w via [η] was estimated for LV but not for HV, HV will have a higher M_w due to longer chain length and more G units being present (Padol, Draget, & Stokke, 2016).

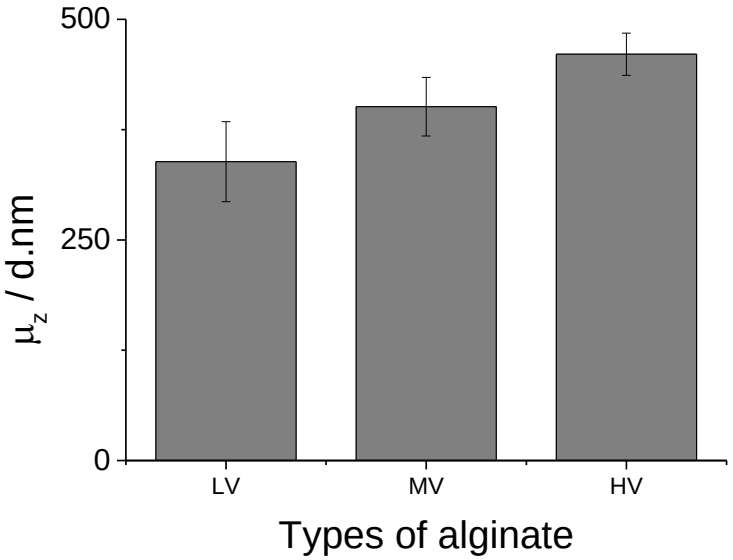

Figure 3-4. Microgel particle mean diameters (μ_z) produced via Leeds Jet Homogenizer (LJH) in 80:20 ratio S block from 10 mM Ca^{2+} and 1 wt.% alginate low viscosity (LV), medium viscosity (MV), and high viscosity (HV).

Whether the viscosity of alginate solutions measured at these shear rates has any effect in the mixing behaviour in the LJH is open to question. The maximum shear rates (γ) can be determined using Eq.3-8:

$$\gamma = \frac{8v}{d} \qquad \textbf{3-8}$$

where v is the fluid velocity and d is the diameter of the orifice. Based on the v for each different viscosity of alginate solution as tabulated in Table 3.1 and d = 5 x 10^{-4} m, the calculated shear rates could be as high as 10^6 s^{-1}. Given the shear thinning nature of the alginate solutions, it seems unlikely that viscosity at these high shear rates has a significant influence on microgel particle size and formation. The viscosity drop in shear thinning polymers is due to the depletion of chain entanglements at high shear rate (Morris, 1990).

The Reynolds number (Re) can also be estimated from Eq.3-9, based on the stated v in Table 3.1 for alginate LV, MV, and HV.

$$Re = \frac{\rho\, v\, d}{\eta} \qquad \textbf{3-9}$$

If the η of the alginate solutions at these high shear rates (see above) is assumed to be similar to η of water, i.e., 10^{-3} Pa.s at room temperature, the calculated Re values are outlined in Table 3.1. (Density (ρ) of alginate solutions assumed ~1 g.ml^{-1}). The result indicates that the impact of viscosity is negligible in the turbulence mixing flow, i.e., $Re > 10^4$ for all alginate solutions.

Table 3.1. The calculated fluid velocity (v), shear rates (γ), and Reynold number (Re) of microgel suspension produced via the LJH using alginate LV, HV, and MV using S block

Types of alginate	Fluid velocity/ v (m.s^{-1})	Shear rates/γ (s^{-1})	Re
LV	78.7 ± 5.0	1.3 x 10^6	4.4 x 10^4
MV	93.1 ± 15.6	1.5 x 10^6	5.2 x 10^4
HV	91.8 ± 12.6	1.5 x 10^6	5.2 x 10^4

Thus it can be concluded that the variation in the microgel particle size due to different alginate solutions (LV, HV, MV) is mainly influenced by the higher degree of Ca^{2+} cross-linking as more G units are present in higher M_w alginates, rather than the fluid velocity, shear rate, or the Re values.

3.2.3 Effect of volume chamber on the particle size

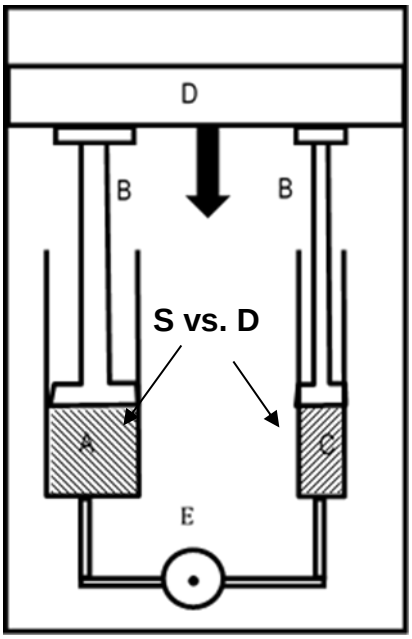

Table 3.2. Maximum volume of the chambers containing alginate (A) and Ca^{2+} (C) for different S and D blocks for the same volume ratio of 80:20

Block types	Alginate chamber (A) / ml	Ca^{2+} chamber (C) / ml
S	16.6	4.1
D	33.3	8.3

Figure 3-5. Jet homogenizer diagram to illustrate the changes of volume of S and D blocks are affecting the volume of A and C chambers

For the same volume ratio of 80:20, the jet homogenizer blocks used in the jet homogenizer have different volume capacities in containing the alginate (chamber A) and Ca^{2+} (chamber C), i.e., S (single) and D (double), see Figure 3-5. The inner diameters of the S blocks are about 0.5 cm smaller than that of the D blocks with the same piston height. Consequently, it affects the volumes of chambers containing alginate and Ca^{2+} in the S blocks which are about a half of those in the D block, see Table 3.2. The sums of alginate and Ca^{2+} volumes from S and D blocks are the maximum volume of microgel suspensions that can be produced, i.e., 21 and 42 ml, respectively. However, the actual total volumes of the microgel suspension evacuated from the S and D blocks were only 12 ± 0.4 and 23 ± 1.4 ml. There were about 42 – 45 % unaccounted loss of the alginate and Ca^{2+} solutions which might be trapped inside the chambers or pipes.

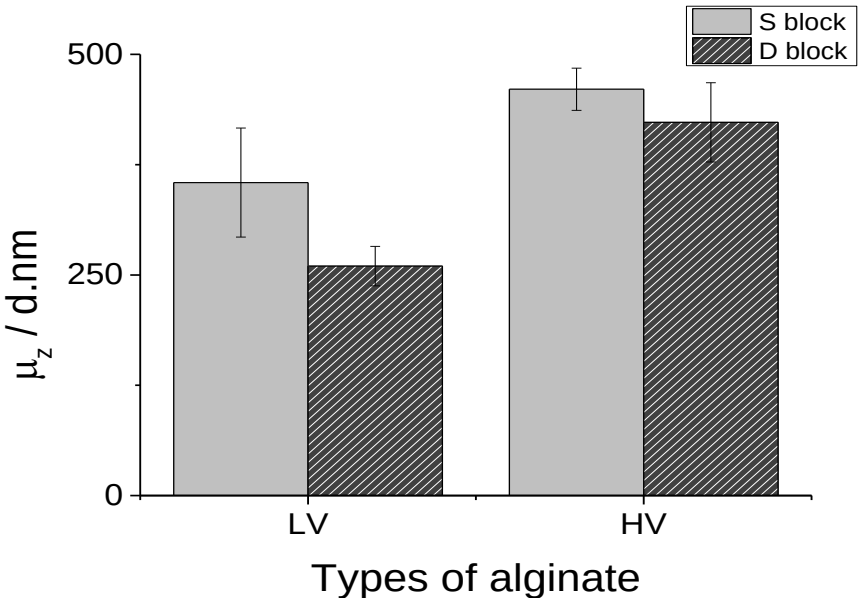

Figure 3-6. The microgel particle mean diameters (μ_z) from alginate LV and HV produced via Leeds Jet Homogenizer (LJH) using volume chamber of S and D blocks

With these two volume chambers, the microgel particle sizes produced are depicted in Figure 3-6. The microgel particle size became smaller as the volume of the chambers was larger. The Z-average (μ_z) of the microgel particles from 1 wt.% alginate LV and 10 mM Ca^{2+} are 355 ± 60 nm and 260 ± 22 nm prepared using the S and D blocks, respectively. Similarly, the microgel

particles produced with alginate HV gave larger particles in the S than D block. The differences in the particle sizes between these two volume chambers were significant with $p < 0.05$ for both alginate LV and HV.

The effect of volume of the chambers on the microgel particle size is primarily influenced by the fluid velocity (v). With the total volume in S less than in D block, based on Eq.3-3 the v values produced in the S block vs. D block were calculated to be 78.7 ± 5.0 m.s^{-1} vs. 220 ± 40.7 m.s^{-1} in alginate LV and 91.8 ± 12.6 m.s^{-1} vs. 564.5 ± 442.1 m.s^{-1} in alginate HV (see Figure 3-7). The higher standard deviation in alginate HV is due to a large error in measuring the evacuation time of the microgel suspension, because it was difficult to handle high viscosity liquids via the pistons in the D blocks. In general, the larger the volume of the mixing chamber, the higher the fluid velocity which consequently affects the t_m. The t_m of S vs. D blocks were calculated using Eq. 3-2; at higher speed the t_m was increased from 4.4 to 7.3 ms in alginate LV and from 4.7 to 11.7 ms in alginate HV, respectively. Higher t_m creates a smaller Da, thus particle sizes of the microgel particles become smaller.

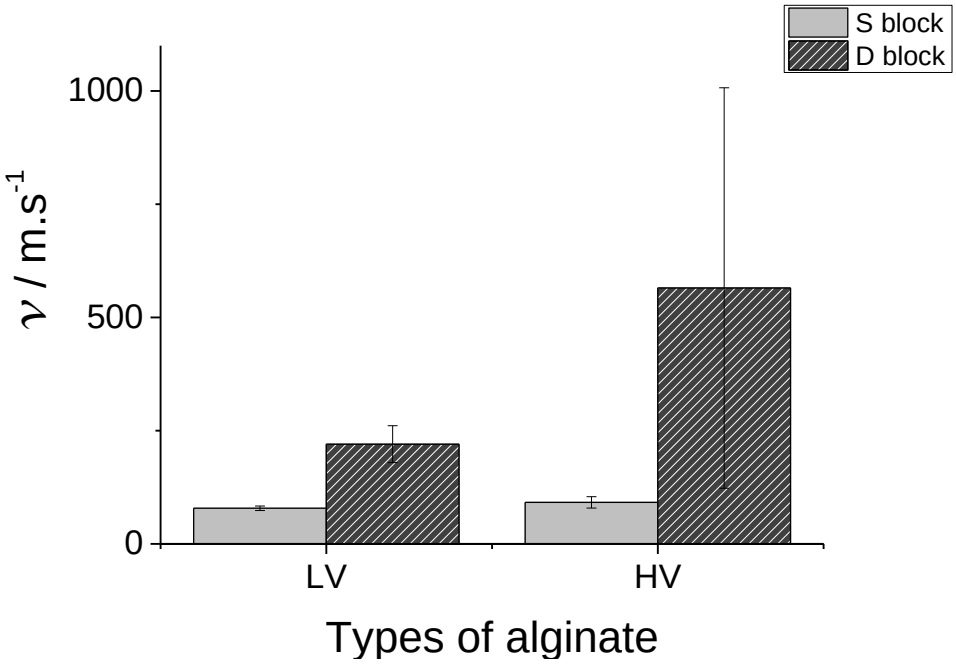

Figure 3-7. The fluid velocities (v) of alginate LV and HV in S and D blocks in the Leeds Jet Homogenizer (LJH)

3.2.4 Microgel particle separation

To separate the intact microgel particles from the excess aqueous phase, several methods were employed, such as (i) adding sucrose up to 24 wt.% to the suspension to increase the density of aqueous phase to 1.1 $g.ml^{-1}$ (ii) air-drying the microgel suspension to produce microgel particles concentrate and (iii) both methods (i and ii) were subjected to ultra high speed centrifugation to collect the microgel particles.

By adding sucrose it was expected to improve the microgel particle separation due to a larger density difference ($\Delta\rho \approx 0.1$ $g.ml^{-1}$) between the microgel particles and the aqueous phase. However, no apparent separation was observed after centrifugation for 48,000 g up to 20 minutes (pausing for every 5 minutes to monitor the particle separation). This is possibly because of the competition of free water and also a potential interaction between sucrose and alginate via hydrogen bonds (Russ, Zielbauer, & Vilgis, 2014). This interaction was reflected in a significant change of the measured ζ-potentials, i.e., less negative for microgel particles in the presence of sucrose from -59.4 ± 9 mV (no sucrose) to -24.2 ± 4.3 mV (with sucrose). Another reason is because the presence of sucrose in the suspension will draw more water out of the microgel particles via osmosis, causing them to shrink and become more dense, thus it defeats the initial objective of a greater $\Delta\rho$.

Another way to separate the microgel particles was by increasing the number of microgel particles (increasing the φ) via the air-drying method at room temperature (22 ± 3°C). After evaporation, the concentrated microgel suspension was centrifuged at 48,000g for 20 minute. Evaporating the free water by air-drying seems to be effective, i.e., the microgel particles were visibly separated and settled on the bottom of the centrifuge tubes (see Figure 3-8a). The microgel particle size and density were measured via Zetasizer and Density meter, respectively (see Chapter 2.2.4.1 and 2.2.4.2 for methods). The results for the supernatant (top) and the sediment (bottom) are shown in Table 3-3. As predicted, the more dense and bigger microgel particles will settle as the sediment, thus they are more apparent when visualized via the light microscope (Figure 3-8b).

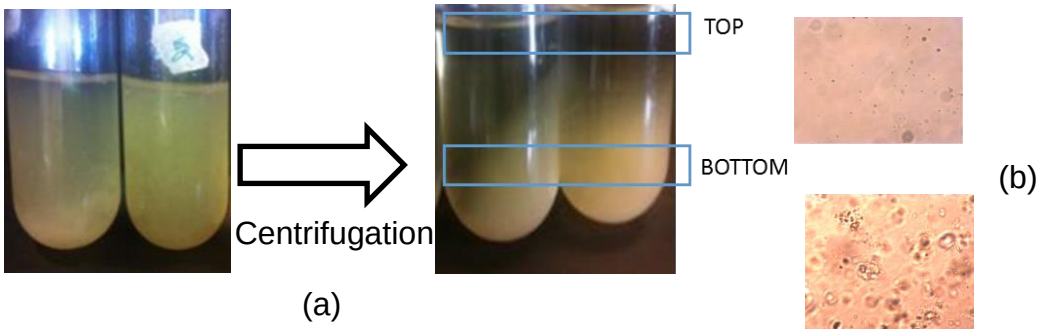

Figure 3-8. (a) Pictures of microgel suspension concentrate solutions after drying at 47 % moisture loss (φ= 0.065) and centrifuged for 48,000 g for 20 minutes (b) Micrographs of the microgel particles from top and bottom of the centrifuge tubes viewed by light microscope at 20x magnification.

Table 3.3. Particle sizes and densities of the microgel particles at different centrifuged locations

Tube location	Particle size (μ_z) / d.nm	Density (ρ)/g.ml^{-1}
TOP	113.3 ± 24.1	1.0066 ± 1.5 x 10^{-4}
BOTTOM	294.0 ± 76.8	1.0071 ± 1.2 x 10^{-4}

The microgel suspension was concentrated via air drying at room temperature (22 ± 3^{o}C) and the density increased as more moisture was removed with a linear correlation factor of R^2 ~1. The moisture loss is calculated using Eq.3-10 below:

$$\%\, Moisture\ loss = \frac{m_i - m_c}{m_i}\ x\ 100\ \% \qquad \textbf{3-10}$$

where m_i is the initial mass of microgel suspension and m_c is the mass of concentrated microgel suspension. The plot of $\%\, moisture\ loss$ against the density of microgel suspension (ρ_s) has a linear correlation ($R^2 \approx 1$) with a trendline equation displayed in Figure 3-9. Assuming at 100 % moisture loss the microgel particles would be tightly packed with minimal interstitial space between them, thus the ρ_s equals the density of the microgel particles (ρ_m); the calculated ρ_m is ~1.01 g.ml^{-1} based on the trendline equation in Figure 3-9. This assumption might be over- or underestimated because of shrinkage of the

microgel particle, or incomplete particle packing and compression. For example: after drying at 47 % moisture loss the particle size was reduced from 298 ± 11.4 nm to 277.4 ± 17 nm, $p < 0.05$. However, the measured ρ_s of the microgel suspension concentrated to 95 % moisture loss was close to the calculated value, i.e., 1.016 vs. 1.009 g.ml^{-1} (*ca*. < 1 % error).

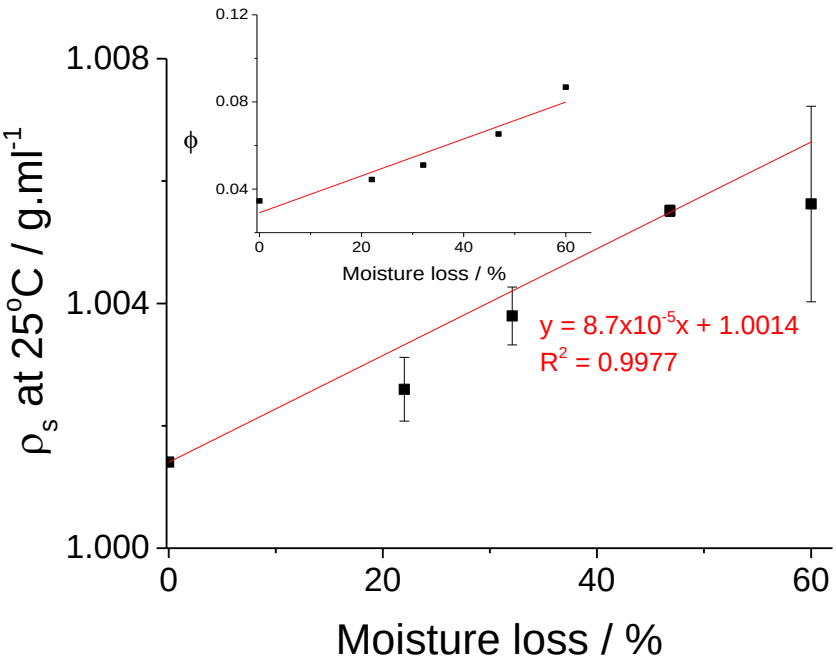

Figure 3-9. The density (ρ) of microgel suspension as a function of moisture loss due to air-drying at room temperature. The inset graph is a plot of calculated φ as a function of moisture loss.

3.2.5 The microgel yield, volume fraction (φ), and rheology of the suspensions

The microgel yield, as measured via centrifugation, can be calculated via Eq.3-11 below, where m_m is the mass of the microgel particles $m_m$obtained in the sediment collected during centrifugation and m_s is the total mass of the microgel suspension.

$$Microgel\ Yield\ (\%) = \frac{m_m}{m_s}\ x\ 100\% \qquad \textbf{3-11}$$

The yield of the microgel particles prepared from 1 wt.% alginate and 10 mM Ca^{2+} using S block and D block before drying were 3.5 ± 1.0 % and 4.2 ± 1.0 %, respectively, with no significant difference between S and D block.

The microgel yield can be converted to microgel volume fraction (φ) which is defined as the fraction of microgel particle volume as a proportion of the total microgel suspension volume, assuming the density of the microgel particles (ρ_m) as ≈ 1.01. The φ of microgel particles in the suspension can then be calculated via Eq.3-12.

$$\varphi = \frac{\frac{m_m}{\rho_m}}{\frac{m_s}{\rho_s}} \qquad \textbf{3-12}$$

The m_s and ρ_s are the mass and density of microgel suspension before and after drying (measured experimentally), respectively. The calculated volume fractions are displayed as an inset graph in Figure 3-9, showing the increase of φ in parallel with the increase of moisture loss, as expected.

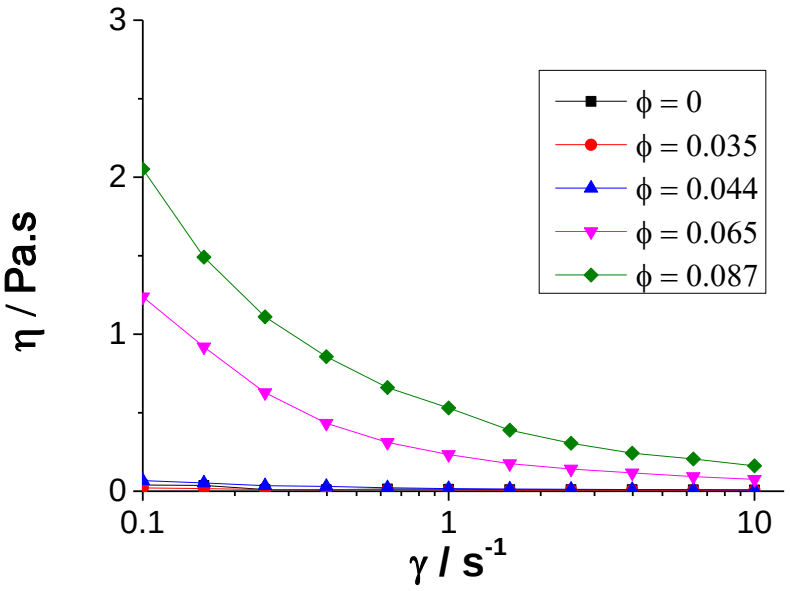

Figure 3-10. Viscosity of microgel suspension at different volume fraction (φ) as a function of shear rates (γ).

The increase in φ obviously also has an impact on the viscosity of the microgel suspension Figure 3-10 shows the viscosity of microgel suspensions

with different φ as a function of shear rates. At low φ ($\varphi \leq 0.044$), the viscosities are weakly shear thinning at low shear rates ($\gamma < 1\ s^{-1}$) and eventually reach constant and behave like Newtonian fluid at higher shear rates. However, at $\varphi \geq 0.065$, the viscosity is much higher at low shear rate and the rheology of the suspension exhibits a more pronounced shear thinning behaviour. Volume fraction is a measure of the free volume available for the particles. The increase in φ causes the microgel particles to have less free volume due to closer packing, hence its viscosity behaves more solid-like at high φ (Ching et al., 2016). While at low φ, the viscosity of the microgel suspension behaves like the viscosity of 1 wt.% alginate solution ($\varphi = 0$), shear thinning with the increase of shear rates at $\gamma < 1\ s^{-1}$, and then it reaches a plateau Newtonian apparent viscosity at $\gamma > 1\ s^{-1}$.

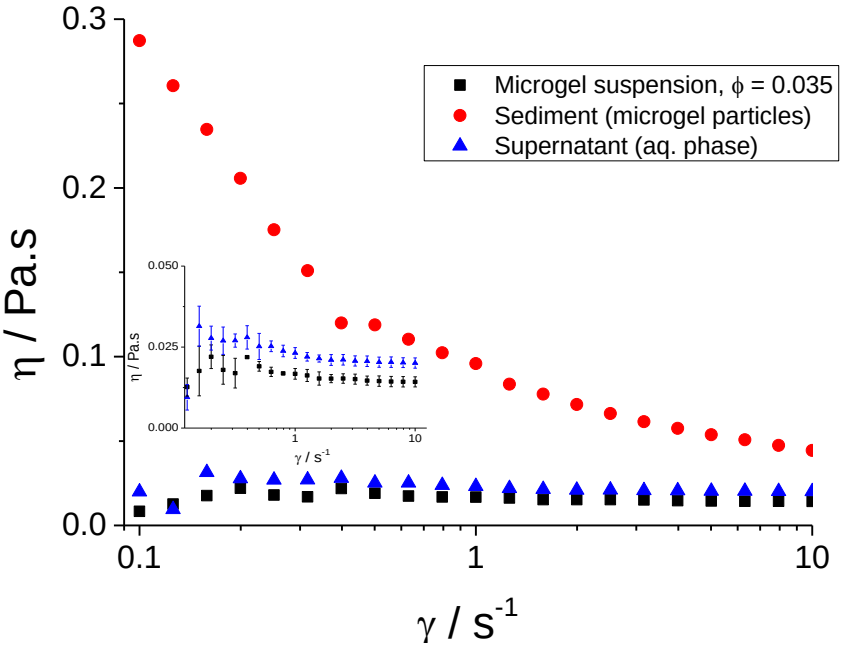

Figure 3-11. Viscosity of microgel suspension at φ = 0.035 (before drying) and viscosity of sediment (microgel particles) and supernatant (aquaeous phase) after centrifugation for 20 minutes at 48,000g. The inset graph is a rescaled plot of the viscosity of microgel suspension at φ = 0.035 and supernatant.

Figure 3-11 displays the viscosity of the microgel suspension compared to that of the supernatant and sediment after centrifugation. The viscosity of the

microgel suspension behaves similarly to that of the supernatant (the aqueous phase), i.e., practically Newtonian behaviour. It can be noticed from the inset graph in Figure 3-11 that the supernatant viscosity is slightly higher compared to the microgel suspension viscosity over the shear rates range measured (0.1-10 s^{-1}). This could be possibly due to the Ca^{2+} cross-linking excess alginate molecules in the bulk that have not been incorporated into microgel particles. The viscosity of sediment behaves similarly as the microgel suspension at high φ ($\varphi \geq 0.065$) confirming the solid-like rheology of the microgel concentrate due to tighter packing or crowding of the microgel particles.

3.2.6 Micrographs of microgel particles

Electron micrographs of the microgel particles obtained via SEM are shown in Figure 3-12b/c, prepared from 1 wt.% alginate and 10 mM Ca^{2+} (see Chapter 2 for the methods of preparation). Figure 3-12a shows a micrograph of 1 wt.% alginate solution as a blank – no particles were observed. Due to difficulties of beam damage, it was a challenge to obtain clear images of samples at higher magnification. The particle sizes of the microgel particles obtained at higher magnification vary between ~127 and 264 nm. For a more quantitative approach, Figure 3-12b was analysed using ImageJ software to determine the mean size of the counted objects. The area of these objects in pixels was converted to diameter of circular objects of equivalent area, in nm. This gave a mean diameter of 140 ± 50 nm, reasonably close to the sizes indicated from the images with higher magnification (Figure 3-12c) but slightly smaller than the DLS measured μ_z less than 300 nm (if produced via D block) possibly due to aggregates measured as large microgel particles, but also possible shrinkage in the SEM due to the vacuum conditions.

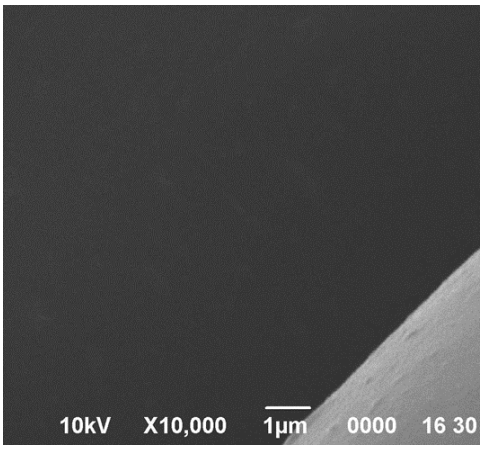

(a)

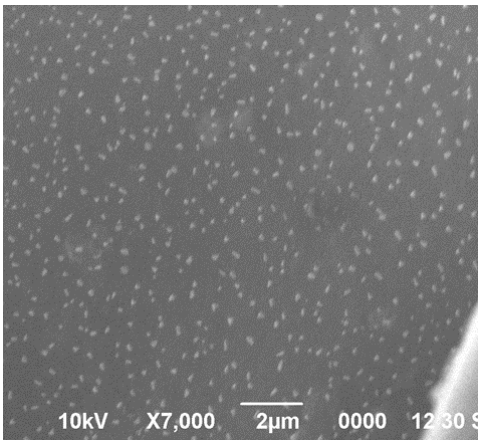

(b)

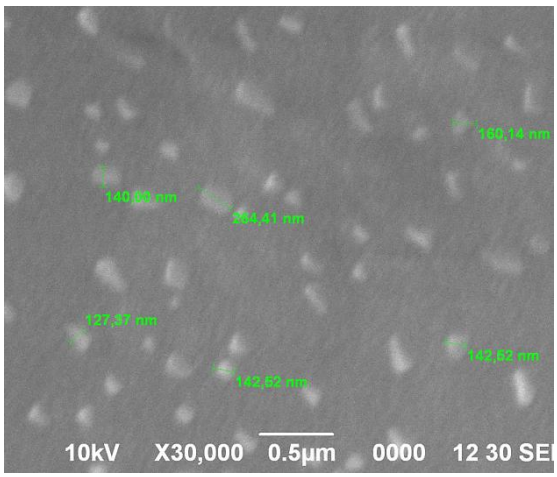

(c)

Figure 3-12. Micrographs obtained via SEM method of (a) 1 wt.% alginate LV solution (b) microgel particles prepared from 1 wt.% alginate and 10 mM Ca^{2+} and (c) enlarged microgel particles images of (b) with higher magnification and approximated microgel particle sizes

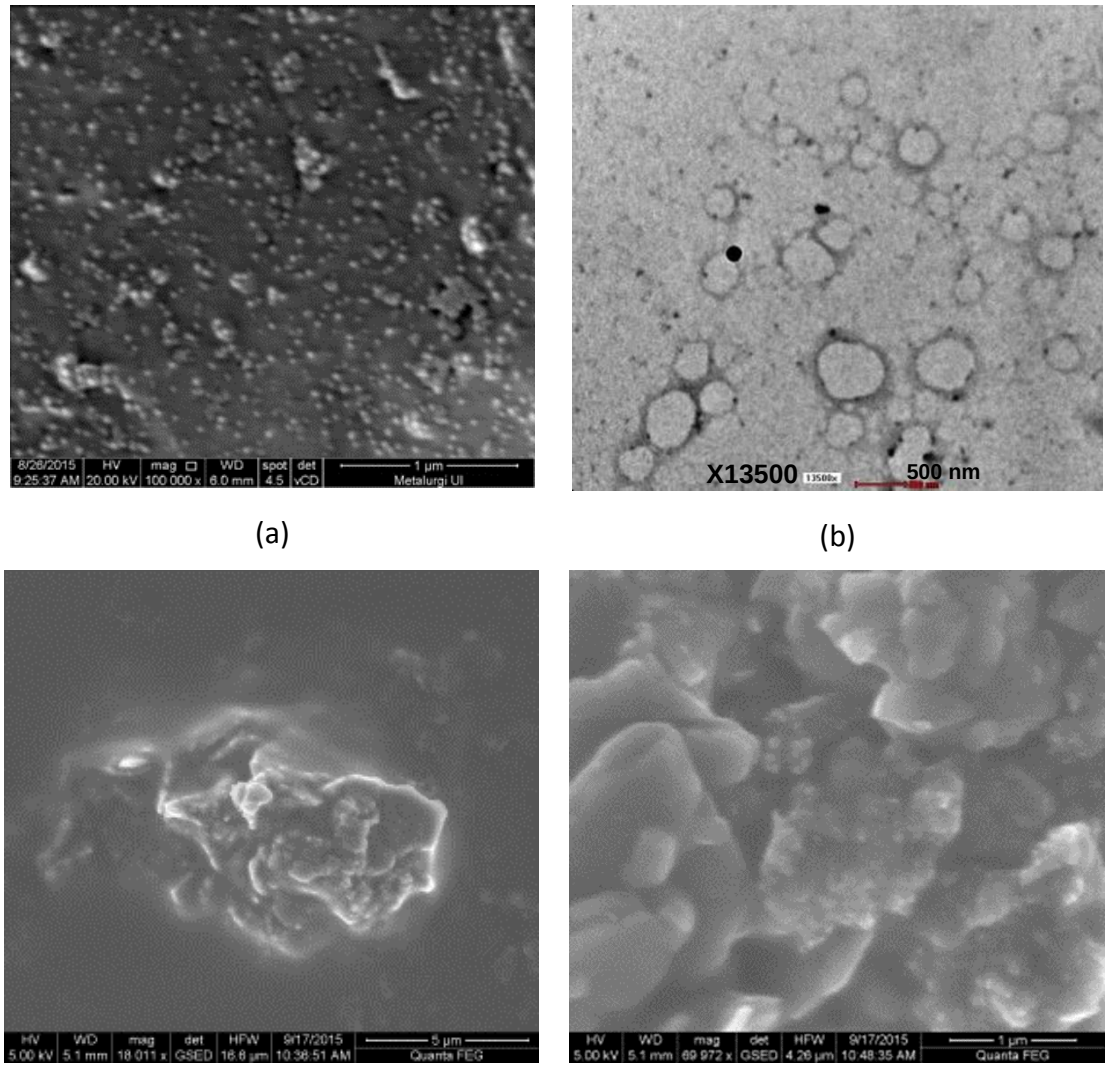

(a) (b)

(c) (d)

Figure 3-13. Micrographs of microgel particles prepared from 1 wt.% alginate and 10 mM Ca^{2+} obtained via (a) FE-SEM, (b) TEM, (c) E-SEM, (d) enlarged from (c) to show the presence of aggregates

Figure 3-13 shows the microstructure of the microgel particles obtained via other types of SEM, i.e., Field emission (FE-SEM), Transmission (TEM), and Environmental (E-SEM). With higher magnification in Figure 3-13a via FE-SEM, there is the suggestion that the microgel particles consist of nano-sized particles (< 50 nm) and some of these are forming clusters or aggregates. Similarly for images obtained from E-SEM and TEM (Figure 3-13b and Figure 3-13c/d), the microgel particles appear to be forming aggregates or clusters.

3.2.7 Particle reduction via sonication

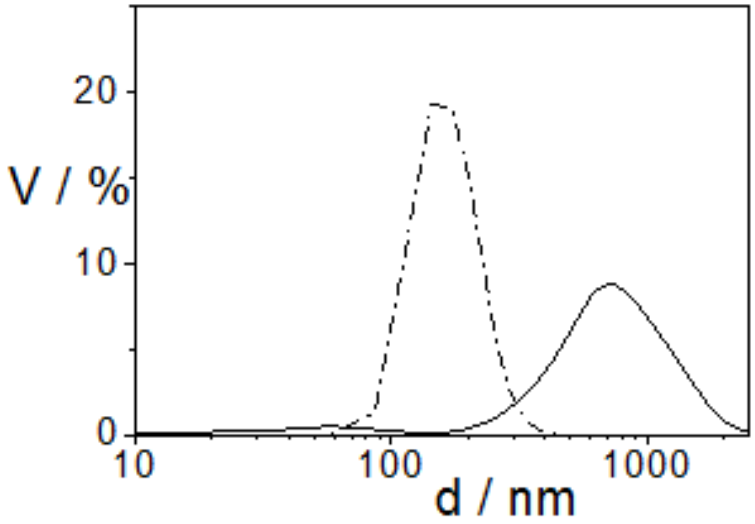

Figure 3-14. Particle size distribution by volume percentage (V) of Ca-alginate microgel particles prepared from 1 wt.% alginate and 10 mM $CaCl_2$ in the 80:20 S block of the jet homogenizer before (———) and after (----------) sonication.

Figure 3-14 shows the detailed particle size distribution (*PSD*) determined via Zetasizer. The vol.% PSD suggested that there were two populations of particles – a lower volume one below 100 nm in size and a larger one with a peak size at just under 1 µm. A broad distribution might be expected due to some tendency for the primary particles to aggregate (Santos et al., 2013). Sonication was therefore applied to disintegrate the aggregates. Figure 3-14 shows that sonication caused the PSD to become narrower and monomodal, with the 2 peaks at ~100 nm and 1 µm shifting to give a single peak centred on ~150 nm. This suggested that the larger particles may indeed have been aggregates of the smaller microgel particles. Similar effects of sonication on alginate gel particles have been observed elsewhere (Lertsutthiwong et al., 2008; Santos et al., 2013).

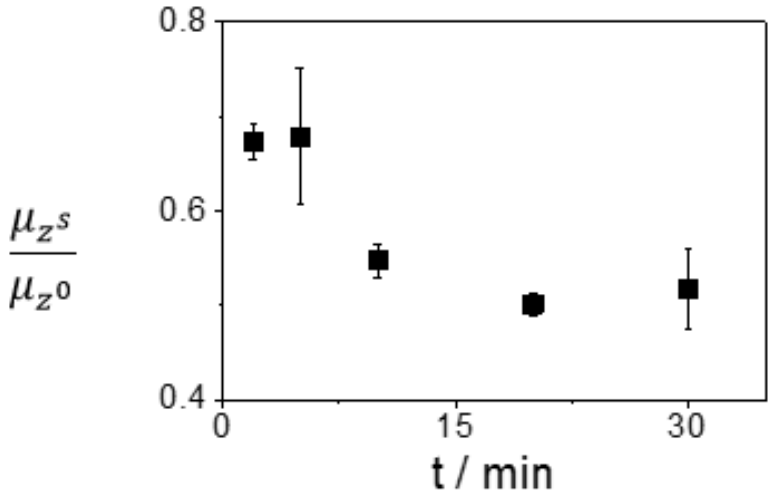

Figure 3-15. Ratio of Ca-alginate microgel particles mean diameter after (μ_z^s) and before (μ_z^o) sonication versus sonication time (t).

Figure 3-15 shows the ratio of the Z-average diameter after sonication (μ_z^s) to that before sonication (μ_z^o) *versus* sonication time. Up to *ca.* 15 min sonication there was a decrease in particle size with longer sonication time. For example, 10 min sonication produced an almost 50% reduction in μ_z^s. Sonication for longer than 15 minutes did not produce any further decrease in size, suggesting the primary particle size had been achieved. On the contrary, prolonged sonication or higher power sonication tended to produce an increase in particle size. This was perhaps because microscopic local heating caused by the cavitation processes during sonication (Kardos et al., 2001) caused surface melting of gel particles and enhanced their fusion and aggregation, even though the bulk temperature of the sample was maintained below 35 ºC. Therefore, sonication should be used with caution when trying to dis-aggregate such particles.

3.3 Conclusions

The microgel particle sizes produced via the LJH are controllable depending on the physical properties and concentrations of the starting materials of alginate and Ca^{2+} as well as the fluid velocities. Increasing the alginate concentration has resulted in larger microgel particles due to the increase of Da. Whilst, the increase of Ca^{2+} concentration does not have any impact in the microgel particle sizes because all the guluronate residues are saturated with Ca^{2+} at 10 mM concentration. The fluid velocity which is affected by the volume of the chambers (S vs. D blocks) has also an influence in microgel particle size reduction at higher volume leads to higher t_m, thus Da becomes smaller. From the rheology data, the intrinsic viscosity $[\eta]$ and the M_w of the alginate LV used in this study were estimated around 13.2 ml^{-1}.g and 168 kDa, respectively. The microgel particle were separated via centrifugation method and the calculated yields were 3.5 and 4.2 % for S and D block, respectively. The micrographs of the microgel particles obtained from electron microscopy techniques showed their presence in aggregates or clusters, thus sonication was employed to breakdown into primary microgel particles.

From this study, it has proven the capability of the LJH to produce microgel particles with tuneable sizes which can provide a fundamental knowledge to produce microgel particles from other types of Ca^{2+} sensitive polysaccharides and for potential encapsulation functionalities.

Chapter 4 Encapsulation of water-insoluble polyphenols and β-carotene in Ca-alginate microgel particles produced by Leeds Jet homogenizer

4.1 Introduction

The aim of this chapter is to explore the possibilities of entrapping water-insoluble compounds such as flavonoids (rutin and tiliroside), curcumin and β-carotene into Ca-alginate microgel particles produced via the Leeds Jet Homogenizer (LJH). These compounds have been widely studied for their potential health benefits as antioxidants, anti-cancer agents, immunomodulatory effects, etc. (Galati & O'Brien, 2004; Gul et al., 2015; Soobrattee, Bahorun, & Aruoma, 2006). Therefore, entrapping them in water-dispersible microgel particles could be beneficial as a means to increase their incorporation into foodstuffs and control their uptake.

The inclusion of water-insoluble crystals was achieved via the LJH with the parameters detailed in Materials and Method section. It is critical to note that the water-insoluble solid compounds remained as their innate crystalline states prior to mixing into the LJH. The solubility limits of tiliroside, rutin, and curcumin in water are 2.1 μM at pH 8 (Luo et al., 2012), ~0.1 mM (Mauludin, Müller, & Keck, 2009), and 0.25 mM at pH 8 (Tønnesen, 2006), respectively. Rutin has a sugar moiety attached to the flavonol structure, which contributes to higher solubility compared to tiliroside, despite their chemical structures falling into the same family of flavone ring (Luo et al., 2012). At the concentration used in this study, i.e., 0.5 mM or 500 μM, these polyphenols should be mostly insoluble and remain in their crystalline form. The oil soluble compound of β-carotene has a high melting point, i.e., 178 ^{o}C (Coronel-Aguilera & San Martín-González, 2015). Thus, its presence should also be in the crystalline form under the experimental conditions of the current study, which was conducted at room temperature (20 ± 4 ^{o}C). Incorporating them in the crystalline forms deliberately would simplify the mixing step in the LJH by dispersing them in alginate phase.

4.2 Results and Discussion

4.2.1 Particle size distribution of the Ca-alginate microgel particles

In the previous chapter (Chapter 3), the microgel particles were produced by the LJH using alginate and Ca^{2+} at concentrations of 1 wt.% and 10 mM, respectively, and the particle size fell into < 1 µm size regime. In this study, larger particle sizes were produced for encapsulation purposes. This was achieved by increasing the concentration of alginate and Ca^{2+} up to 2 wt.% and 20 mM, respectively. As a direct consequence of increasing the concentration of alginate, the reaction time (t_r) decreases as higher concentrations, so larger particles are formed. Higher alginate concentration would also increase the viscosity, translating to lower Re, which might indirectly impact the decrease in t_m (Matteucci et al., 2006). However, this latter case will have less impact because the shear rates in the LJH will be very high, so the apparent viscosity will be lowered due to the shear-thinning nature of the alginate solutions. The particle size generated with these concentrations was thus larger, e.g. ranging from 1 < µ < 300 µm.

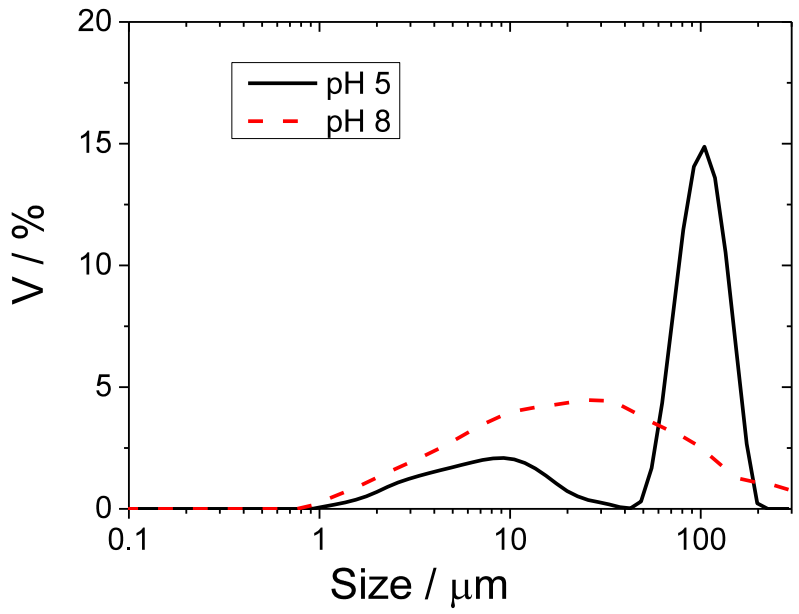

Figure 4-1. Particle size of Ca-alginate microgel particles produced from 20 mM Ca^{2+} and 2 wt.% of alginate in 0.02 M of imidazole buffer pH 5 and 8.

The microgel particles were produced here at pH 5 and 8 in 0.02 M imidazole buffer (see). At pH 8, the particle size distribution displayed a broad monomodal curvature ranging from 1 to 250 µm with a peak at around 30 µm. At pH 5, the size distribution had a bimodal distribution with peaks at around 10 µm and 100 µm. In general, most microgel particles were below 300 µm at both pHs. Such a broad size distribution aids entrapment of the range of sizes of the water-insoluble crystals (typically less than 200 µm in size).

4.2.2 Particle size of the polyphenol crystals and Ca-alginate microgel particles with encapsulated polyphenols

4.2.2 The measured particle sizes of the insoluble polyphenol compounds via Mastersizer were between 0.1 to 100 µm, as shown in Figure 4-2a. Tiliroside possessed the smallest particle size with peaks at around 0.3 µm and 1 µm while curcumin had the broadest particle size distribution (peaks at around 10 µm and 100 µm) and rutin's particle size was ~20 µm. These particle sizes were obtained by dispersing them into Millipore water (at pH 6.8 ± 0.2) via Ultraturrax at 24,000 rpm without passing through the LJH. It would be unsurprising to find them in aggregated forms, whereas passage through the LJH might break up such aggregates. There were some nanocrystals of polyphenols present, since upon filtration via 1 µm Whatman filter and measurement via Zetasizer submicron particulates were detected – see Figure 4-2b and Figure 4-3. The Z-average (μ_z) from the smallest to the largest were as follows; tiliroside (182.4 nm) ≥ rutin (210.8 nm) ≥ curcumin (217.3 nm). With such small particle sizes, the inclusion of these polyphenol nanocrystals into the micron-sized of the microgel particles was expected to easily take place.

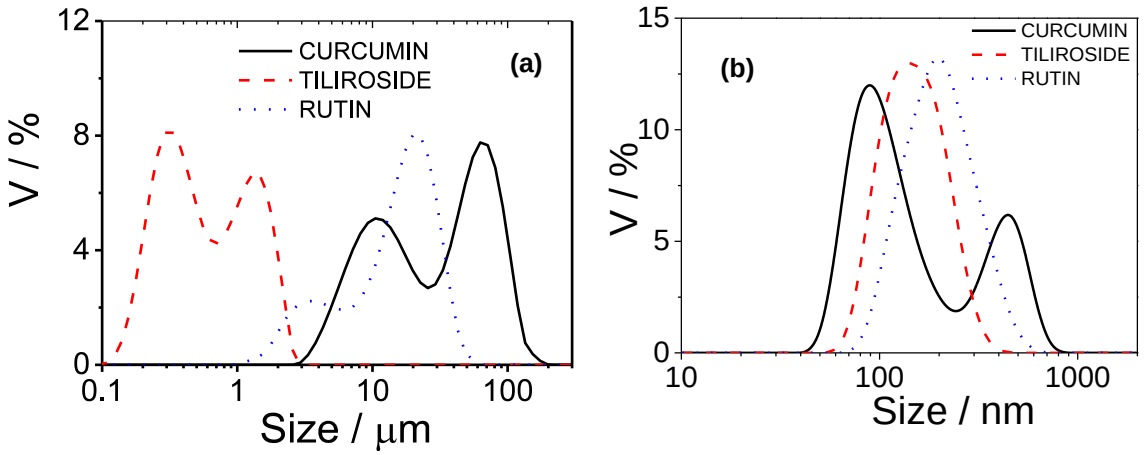

Figure 4-2. Particle size distribution of water-insoluble polyphenols (1 mM of rutin, tiliroside, and curcumin dispersed in Millipore water) as measured by Mastersizer (a) and filtered through Whatman 1 μm as measured by Zetasizer (b)

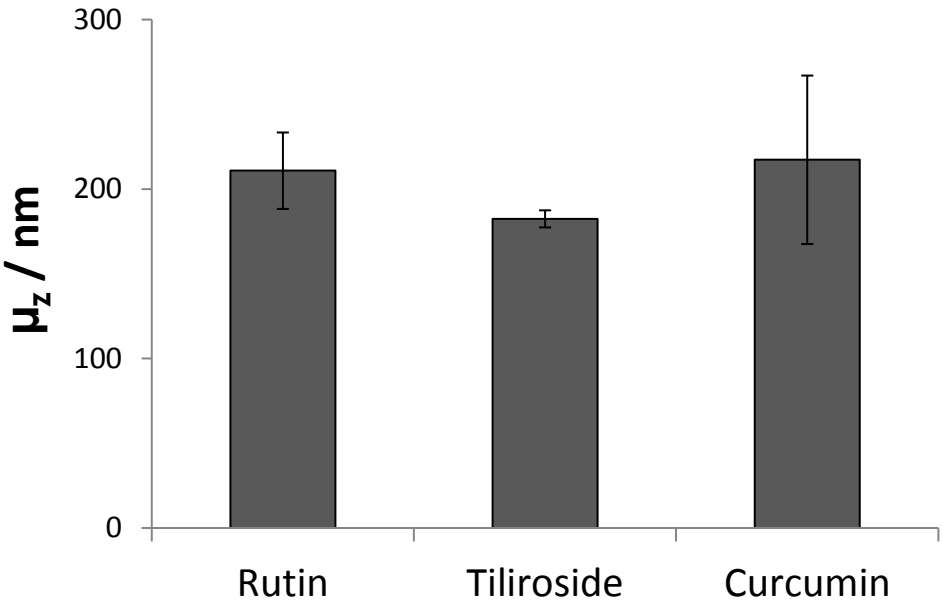

Figure 4-3. Particle size (μ_z) of 1mM rutin, tiliroside and curcumin dispersed in Millipore water filtered through Whatman 1 μm as measured by Zetasizer

The Sauter mean diameter (d_{32}) of the microgel particles with and without the entrapped polyphenols at pH 5 and 8 is displayed in Figure 4-4. The d_{32} of these microgel particles with encapsulated polyphenols followed the

same size order as the μ_z of the nanocrystals of polyphenols (Figure 4-3). Tiliroside, with the smallest nanocrystals (182.4 nm), gave the smallest d_{32} in the encapsulated form (Ca-ALG+T) with values of around 3.4 µm and 0.1 µm at pH 5 and 8, respectively. The nanocrystals of rutin and curcumin were roughly around the same size (210.8 nm and 217.3 nm, respectively), the d_{32} for both in encapsulated forms also reflected this size difference. The d_{32} of Ca-ALG+CU and Ca-ALG+R were around 8 µm at pH 5 and 11 µm at pH 8 with higher mean diameter at higher pH. Thus, the size of polyphenol nanocrystals possibly dictates the final size of the entrapped microgel particles, via them acting like 'nuclei' during the formation of the microgel particles.

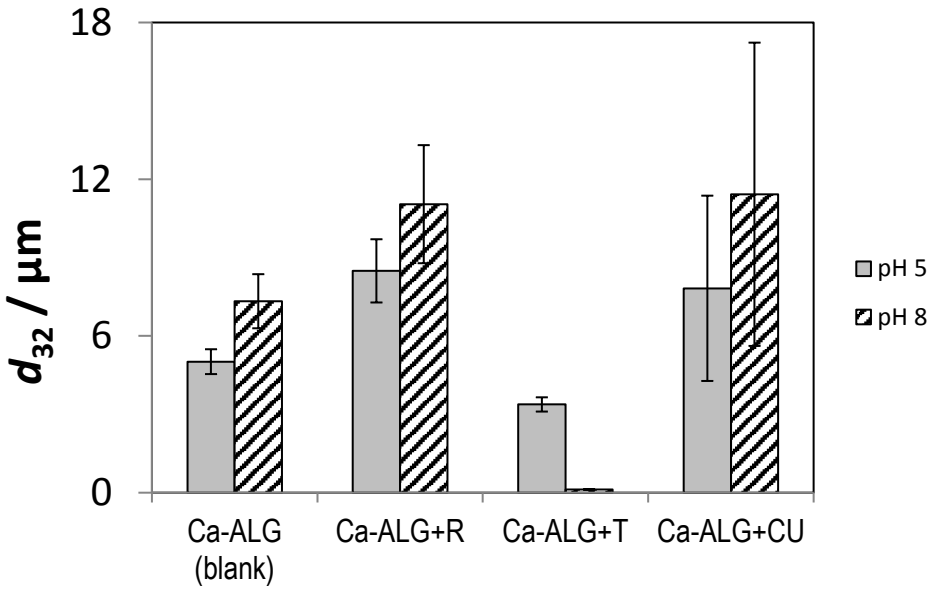

Figure 4-4. Particle Sauter mean diameter (d_{32}) of Ca-alginate microgel particles with or without the insoluble polyphenols at pH 5 and 8

Table 4.1. Particle volume mean diameter (d_{43}) of Ca-alginate microgel particles with or without insoluble polyphenols at pH 5 and 8

	Ca-ALG Blank (µm)	Ca-ALG+R (µm)	Ca-ALG+T (µm)	Ca-ALG+CU (µm)
pH 5	12.0 ± 1.0	40.4 ± 9.2	7.3 ± 1.5	264.6 ± 105.9
pH 8	16.7± 2.5	43.9 ± 7.4	6.4 ± 1.3	268.0 ± 99.7

As observed, there was an effect of the pH in the microgel particle mean diameter: d_{32} for the microgel particles without polyphenols (Ca-ALG Blank) was smaller at pH 5 than pH 8, see Figure 4-4. The d_{32} for the Ca-ALG Blank were 5.0 ± 0.5 µm and 7.3 ± 1.0 µm at respective pH 5 and 8. The volume mean diameter (d_{43}) tabulated in Table 4.1 also showed a similar trend: the d_{43} for Ca-ALG Blank were 12 µm at pH 5 versus 16.7 µm at pH 8. The mean difference at pH 5 and 8 for both d_{32} and d_{43} were significantly different with $p < 0.05$. The shrinkage of Ca-ALG Blank at low pH was probably due to the loss of electrostatic repulsion between COO^- groups in alginate chains in the presence of abundantly available H^+ ions (Li et al., 2011). With the pK_a of the COO^- groups approximately 3.5 (Lee & Mooney, 2012), the microgel particles are inclined to be swollen at higher pH due to mutual repulsion between the negatively charged chains and greater uptake of water (Zhang et al., 2015).

Similar pH trends were observed with rutin encapsulated in the microgel particles (Ca-ALG+R). The mean diameters (both d_{32} or d_{43} values) at pH 5 were smaller than pH 8 (Figure 4-4 and Table 4.1). Comparing pH 5 vs. 8, the d_{32} of Ca-ALG+R were 8.5 ± 1.2 µm vs. 11 ± 2.3 µm ($p < 0.05$) and the d_{43} were not significantly different between 40.4 µm vs. 43.9 µm. Rutin's pK_a is ~7.1 (the OH group in the C_7 location of the flavone ring) and was therefore prone to changes in dissociation between pH 4 and 8 (Herrero-Martínez et al., 2005). Thus at pH 8, there would be an increase in electrostatic repulsion from negatively charged rutin and deprotonated of COO^- groups in alginate chain, which might be expected to lead to larger particle size. Conversely, at pH 5, the Ca-ALG+R particle became smaller due to attractive forces in more positively charged environment between rutin and alginate.

Tiliroside encapsulated in the microgel particles (Ca-ALG+T) behaved differently. Ca-ALG+T exhibited smaller size at pH 8 compared to pH 5; d_{32} were 3.4 ± 0.3 µm and 0.1 ± 0.01 µm at pH 5 and 8, respectively (Figure 4-4). The d_{43} values in Table 4.1 also confirm that the particle size was larger at lower pH for Ca-ALG+T. Luo et al. (2012) measured the particle size and ζ-potential of tiliroside crystals in imidazole buffer from pH from 2 to 8 in the presence of 0.05 M NaCl (see Figure 4-5) (there was no added NaCl in this current study, but the presence of salt is not expected to impact the ζ-potential

values significantly). Their results showed an increase in tiliroside particle size when the ζ-potential changed from negative to positive at lower pH. The increase of particle radius of tiliroside was more pronounced as its ζ-potential was close to zero. Although the particle size of tiliroside crystals at pH 5 and 8 was not measured in this study, however, the size distribution of the 1 mM tiliroside crystals at pH neutral (6.8 ± 0.2, closer to pH 8) as shown on Figure 4-2b displayed the some portion of these nanocrystals at < 100 nm.

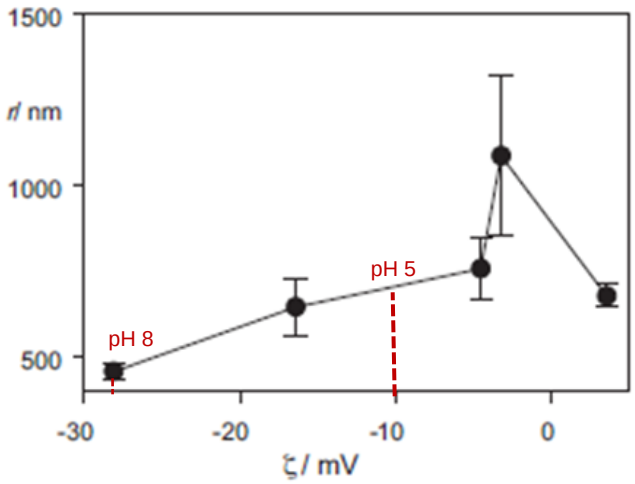

Figure 4-5. The particle size (r) of 100 µM tiliroside + 0.05 M NaCl versus ζ-potential. (Figure after Luo et. al., 2012)

Luo et al. (2012) postulated that at low pH the tiliroside has a tendency to form intermolecular aggregates that cause the particle size to be larger. This could be key to understanding why Ca-ALG+T particle size was larger at pH 5 vs. pH 8. Perhaps the entrapment occurred when the tiliroside crystals were still in aggregated form at pH 5. Although at pH 5 the ζ -potential of tiliroside was not zero, but around –10 mV (from Figure 4-5), we postulated the particle size of tiliroside at pH 5 was at least 50 % larger than at pH 8. The LJH is known to provide a very rapid mixing, but apparently it still cannot prevent this tiliroside aggregation, i.e., aggregate formation must occur at a faster timescale compared to the reaction time of Ca-alginate bridging, thus aggregates of tiliroside crystals are entrapped.

The d_{32} of curcumin encapsulated in Ca-alginate microgel particle (Ca-ALG+CU) was smaller at pH 5 , i.e., 7.8 ± 3.5 µm, compared to pH 8, i.e., 11.4 ± 5.8 µm, respectively, although the difference was not significant (with $p > 0.05$ due to large standard deviation for both pHs, see Figure 4-4). The d_{43} results also reflected the high variability, thus almost no difference in d_{43} between pH 5 and 8 (Table 4.1). The average net charge of curcumin as a function of pH was reported by Wang et al. (2010) in their Supporting document (see Figure 4-6), by taking into account of each of the functional groups in curcumin structure. The pK_a of the keto-enol group was 8.4, and that of both phenol groups were 9.9 and 10.5. At the pH values used here, the net charge of curcumin would be zero at pH 5 and slightly less than zero (~-0.25 net charge) at pH 8. The lack of difference in particle size both d_{32} and d_{43} of Ca-ALG+CU is thus supported by the lack of difference in average net charge of curcumin at both pH 5 and 8.

Figure 4-7 shows the ζ-potential of the microgel particles with or without flavonoids at pH 5 and 8. All these microgel particles exhibited less negative values at pH 5 compared to pH 8, which suggests the effect of pH on the dissociation of the alginate carboxylates dominates. At both pHs, the ζ-potentials of Ca-ALG+R and Ca-ALG+T tended to be more negative compared to Ca-ALG Blank. This suggests that significant amounts of rutin and tiliroside could be adsorbed to or trapped in the surface of the microgel particles. The ubiquitous presence of OH functional groups in polyphenols could be mainly responsible for the adsorption to the microgel particles either via Ca^{2+} cross-linking or hydrogen bonding interactions.

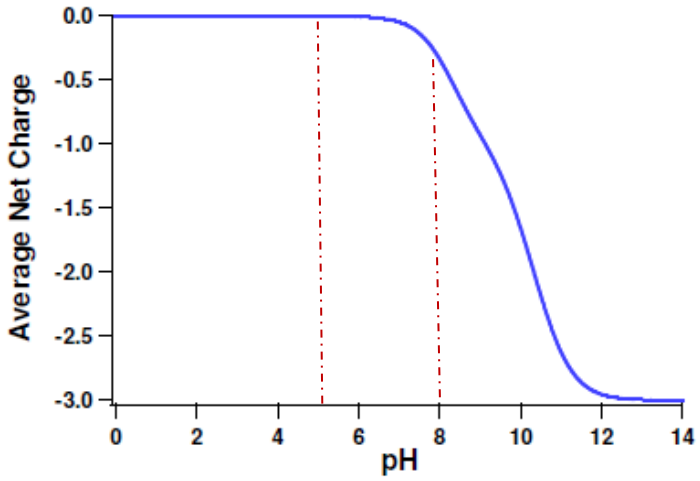

Figure 4-6. Average net charge of curcumin as a function of pH, The dotted lines indicates the pHs used in the current study.

(Figure after Wang et al., 2010)

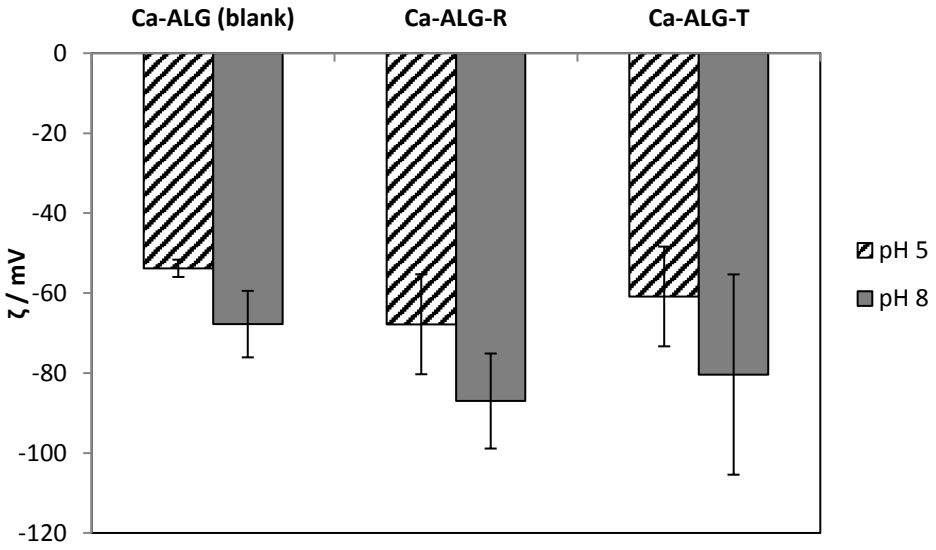

Figure 4-7.The ζ-potential of Ca-alginate microgel particles with and without polyphenols at pH 5 and 8 in 0.02 M imidazole buffer

4.2.3 Particle size of β-carotene encapsulated microgel particles

Figure 4-8 shows the particle size of β-carotene crystals at each mixing stage and its encapsulated form in the microgel particles (Ca-ALG+BC+TW20). For β-carotene encapsulation, a dispersion of insoluble crystals of β-carotene and Millipore water plus Tween 20 (TW20) was formed using the Ultraturrax at its highest speed, 24000 rpm, followed by a sonication step. This coarse dispersion of β-carotene in water produced a broad spectrum of particle sizes centred on 5.4 ± 2.6 μm. As it was dispersed into the alginate phase (2 wt.% alginate concentration) before passing into the LJH, the particle size of the β-carotene crystals became larger, with a peak size distribution centred at 15.4 μm. Depletion flocculation potentially occurred when mixing the polymer with the β-carotene. A similar phenomenon was observed when β-carotene oil droplets were mixed with mucin during in-vitro digestion steps by Salvia-Trujillo, Qian, Martín-Belloso, & McClements (2013). They found an enlargement of the droplet size of β-carotene in the mouth and stomach during the early onset of digestion due to high level of mucin, which they attributed to depletion flocculation. Although there was some enlargement of β-carotene crystals as they were dispersed into 2 wt.% alginate, after passing through the LJH the size of Ca-ALG+BC+TW20 was reverted back to close to original crystals size of ~5.5 μm. (This proves the efficacy of LJH as a technique for breakdown of these organic crystals into smaller size).

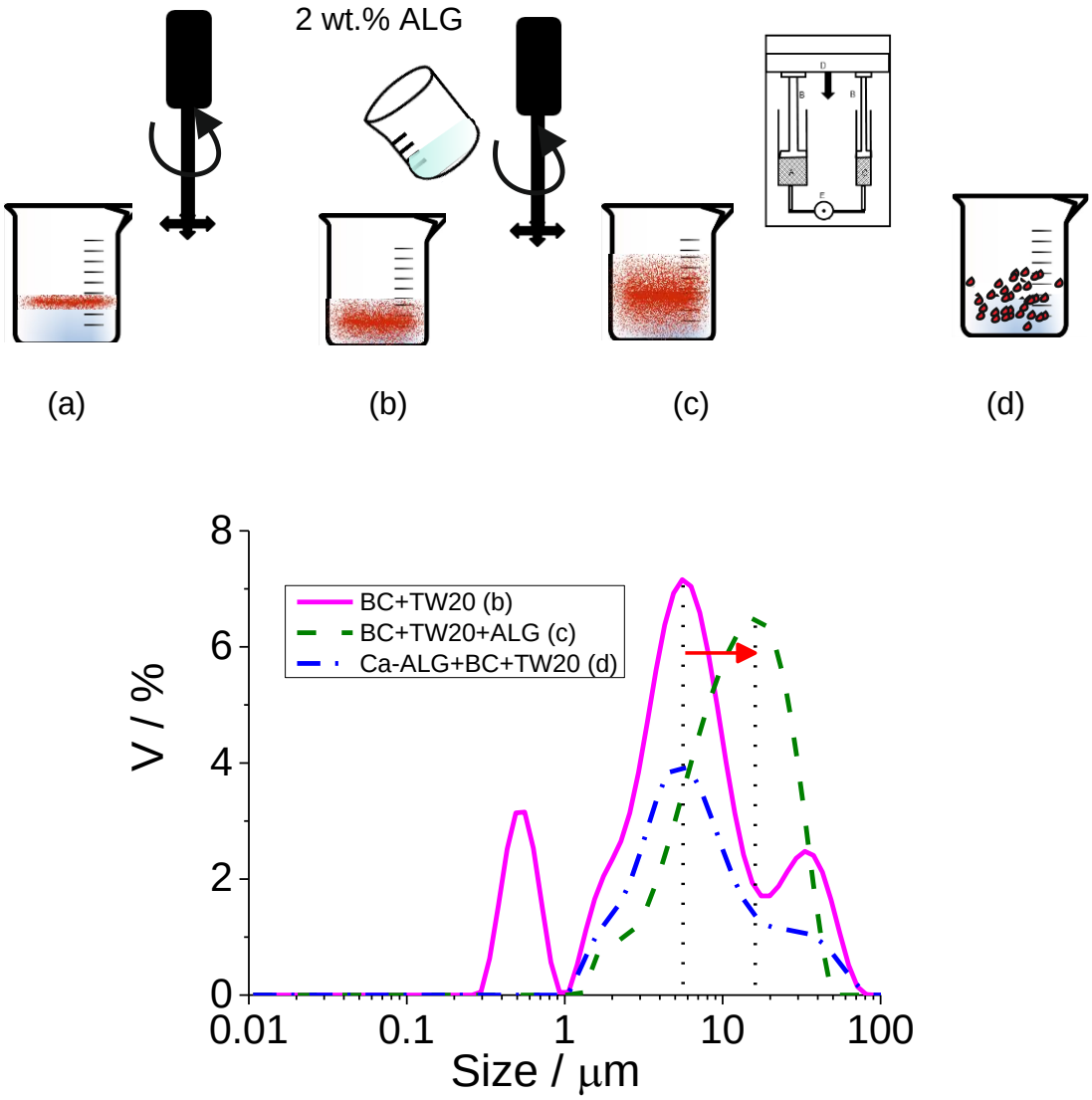

Figure 4-8. Particle size of β-carotene crystals stabilized with TW20 dispersed in water (a) mixed at 24,000 rpm with Ultraturrax (b), added with 2 wt.% alginate and mixed at 24,000 rpm with Ultraturrax (c), homogenized and encapsulated in microgel particles (d)

4.2.4 CLSM images of the water-insoluble materials encapsulated in Ca-alginate microgel particles

The CLSM method benefited from the autofluorescence properties of rutin, tiliroside, curcumin and β-carotene to prove their positioning within the microgel particles. This enabled us to visualize the success, or not, of the encapsulation. The microgel particles do not fluorescence, but by adding FITC-dextran, a large M_w dextran, it dyed the aqueous phase to highlight the presence of the microgel particles, which appeared as dark objects against the aqueous fluorescent background.

Figure 4-9 shows CLSM images that differentiate between a dispersion of the insoluble tiliroside crystals in the aqueous phase versus a suspension of the the microgel particles with entrapped tiliroside. With no microgel particles present in the dispersion (Figure 4-9a), there was no appearance of the dark objects at 488 nm excitation and the insoluble tiliroside particles at 458 nm excitation were distributed evenly. In the microgel suspension (Figure 4-9b), the tiliroside crystals appeared to be in more aggregated clusters at 458 nm excitation. At 488 nm excitation it was clearly seen that these bright clusters were coterminous with the dark objects that were the microgel particles. This was good direct evidence that clusters of insoluble tiliroside particles were entrapped within the nascent microgel particles.

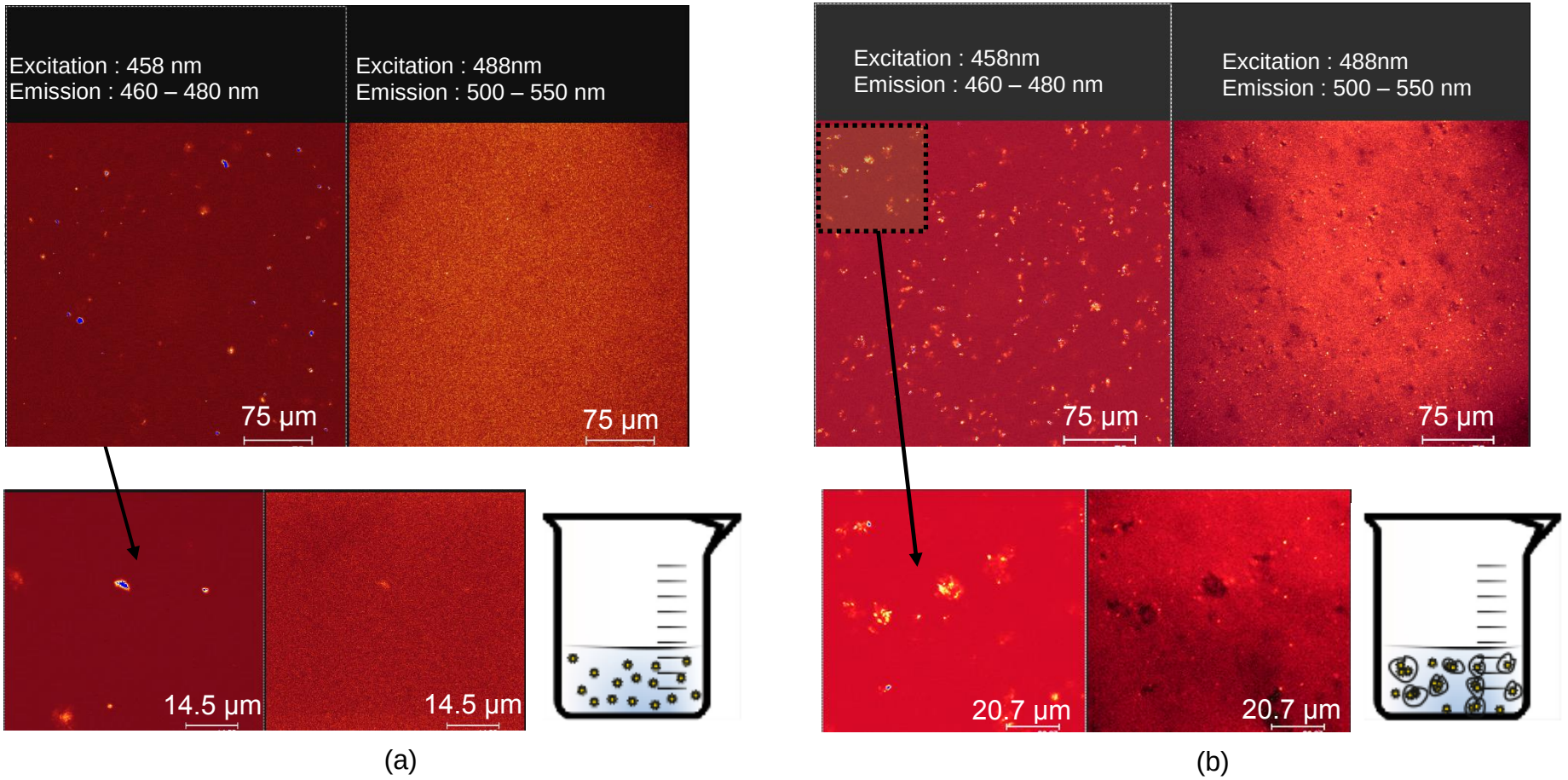

Figure 4-9. CLSM image and its enlargement area of (a) dispersion of 1 mM tiliroside and (b) suspension of Ca-alginate microgel particles entrapped with 0.5 mM tiliroside made via the Leeds Jet Homogenizer (LJH), both were in 0.02 M imidazole buffer pH 5 and contained 2 wt.% gelatin to immobilize the particles.

However, as with all 2D images, it is difficult to precisely know whether these tiliroside particles are trapped inside or attached to the surface of the microgel particles. There seemed to be no measurable difference in the diameters of the tiliroside particles at 458 nm excitation and the microgel particles at 488 nm excitation from Figure 4-9 above. A z-scan of the 3D image was also experimented with twenty slices of cross section generated, see Figure 4-10. At 458 nm excitation, the fluorescence signal was detected throughout the twenty slices of the cross section. This indicated that tiliroside crystals were conceivably entrapped inside of the microgel particles.

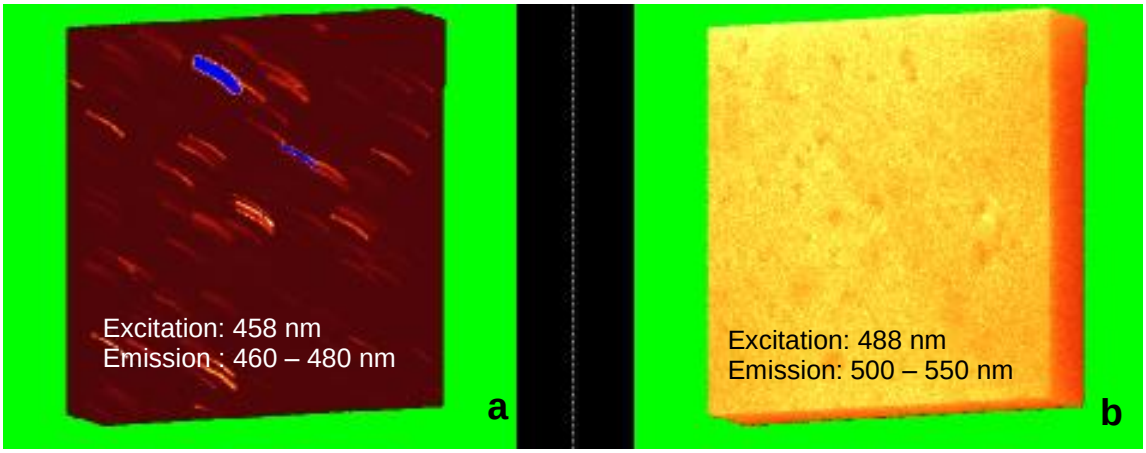

Figure 4-10. The z-scan cross section of CLSM image of tiliroside encapsulated in ca-alginate gel particle at 458 nm (a) and 488 nm (b) excitation

Representative CLSM images of other encapsulated polyphenols in the microgel particles are shown in Figure 4-11. Unfortunately, the magnification was not uniformly scaled for each image due to in situ enlargement when zooming in on the particles. Although the line scale could be used as a benchmark for sizing, we ought to keep in mind that CLSM is not a recommended analytical tool to determine the particle size, unless thousands of objects are counted. However, the CLSM images clearly showed clusters of the polyphenols retained in the microgel particles. From the Figure 4-11, it could be concluded that despite difference in pH, i.e., 5 and 8, the encapsulation of these insoluble particles was still achieved.

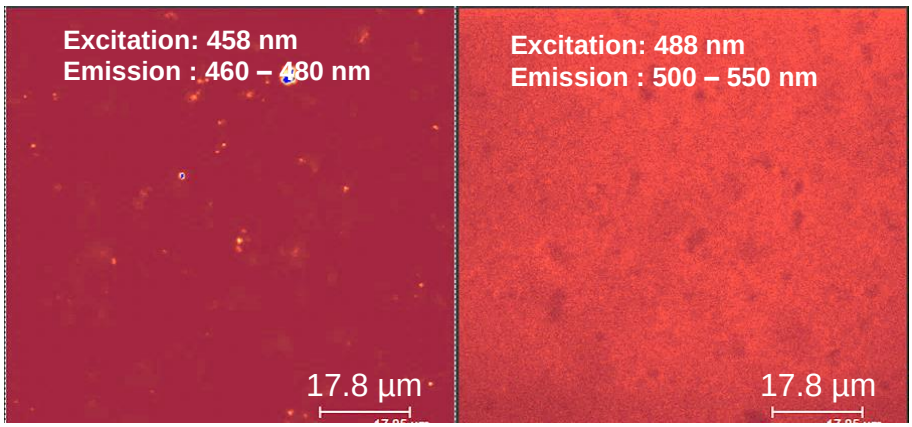

(a)

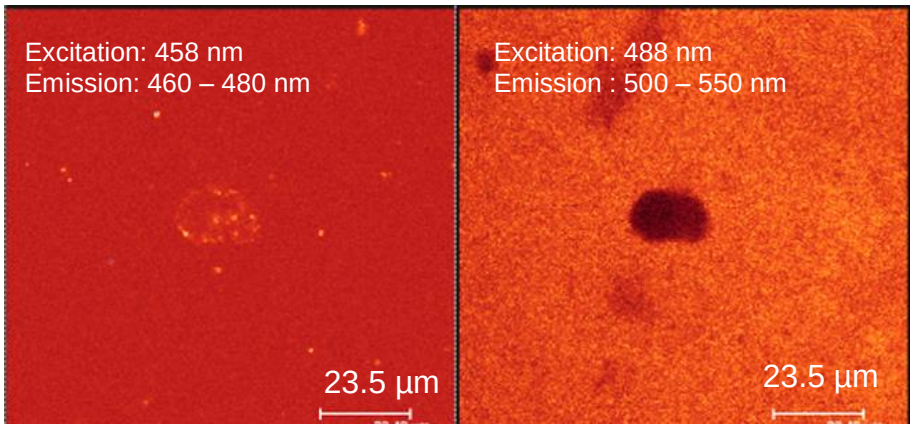

(b)

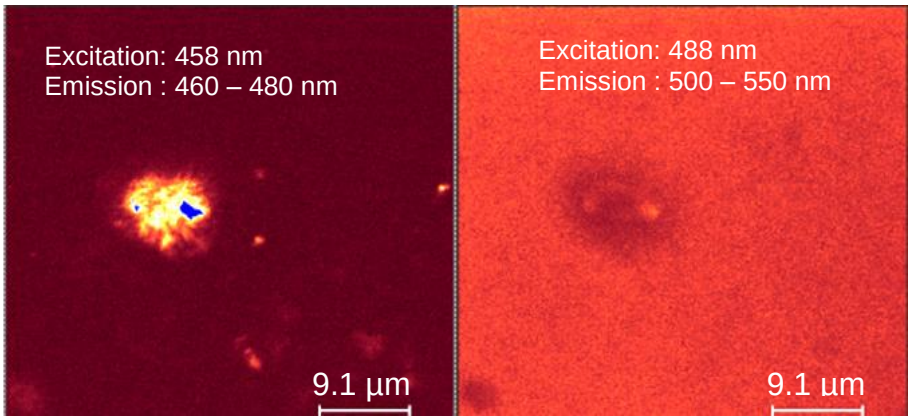

(c)

Figure 4-11. CLSM images of encapsulated of (a) 0.5 mM tiliroside at pH 8, (b) 0.5 mM curcumin at pH 5, (c) 0.5 mM curcumin at pH 8 of 0.02 M imidazole bufffer.

Again, similar findings were observed for β-carotene encapsulation (Figure 4-12). The excitation wavelength of β-carotene was at 514 nm, while FITC dextran was excited at 488 nm. Even though β-carotene was oil soluble, Nile red was not used as the dye of choice to locate the compound because it interfered with the fluorescence spectra of β-carotene. Nile red excitation maximum is at 514 nm and emission at 633 nm, thus it interfered with the fluorescence signal from β-carotene which was excited at the same wavelength. Therefore, FITC was advantageous in this system because it did not interfere with β-carotene excitation. From the Figure 4-12, it is seen that the clusters of β-carotene crystals at 514 nm excitation appeared coterminous with the microgel particles visualized using 488 nm excitation. This signified that the entrapment of β-carotene crystals in the microgel particles was achievable via the LJH.

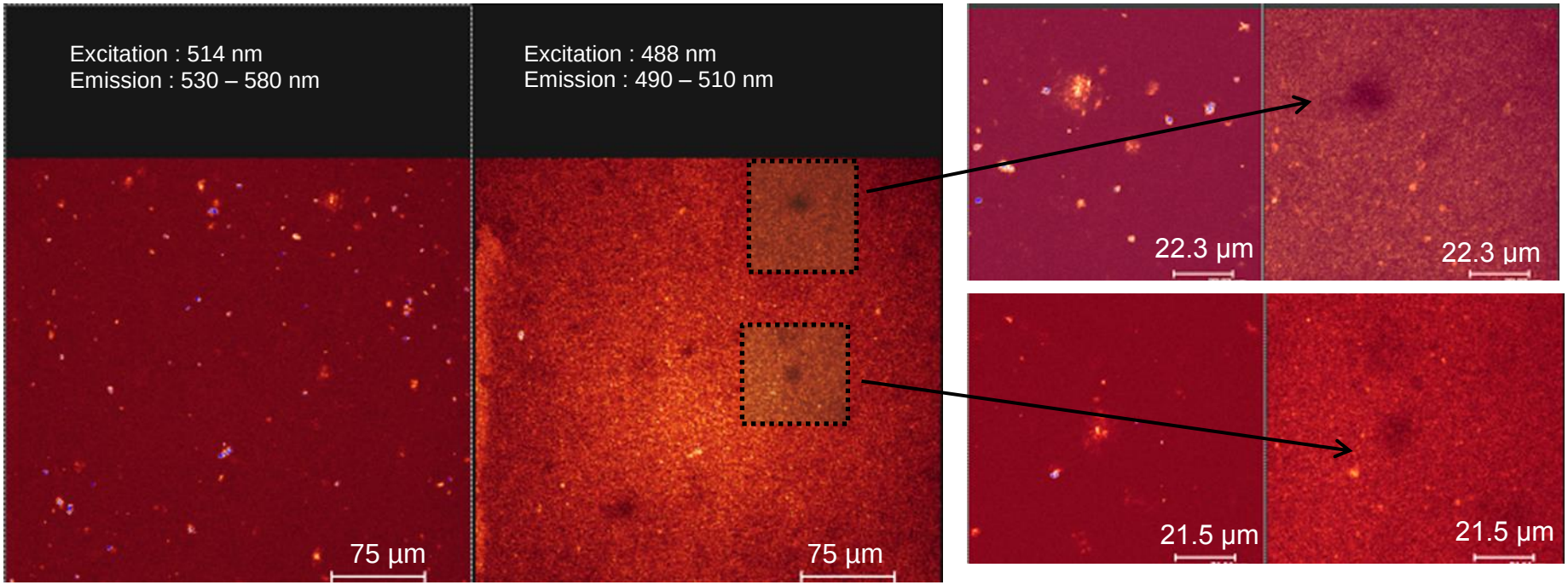

Figure 4-12. CLSM images of β-carotene+TW20 encapsulated in Ca-alginate microgel particles

4.2.5 Light microscopy images of the water-insoluble materials encapsulated in Ca-alginate microgel particles

Some light microscopy images for encapsulated curcumin in Ca-alginate microgel are shown in Figure 4-13. The samples were filled into a welled slide (~3 mm depth). Viewed in 2D, these microgel particles could be seen as in either circular or elongated elliptical rings which represented the boundary layer of the microgel particles. In the microgel particles without curcumin (blank) sample, there were large amounts of these 'opened ring' particles (Figure 4-13 a and b) while the encapsulated curcumin particles had more of the 'filled rings' (Figure 4-13 c and d). These filled rings revealed the entrapped curcumin in the microgel particles.

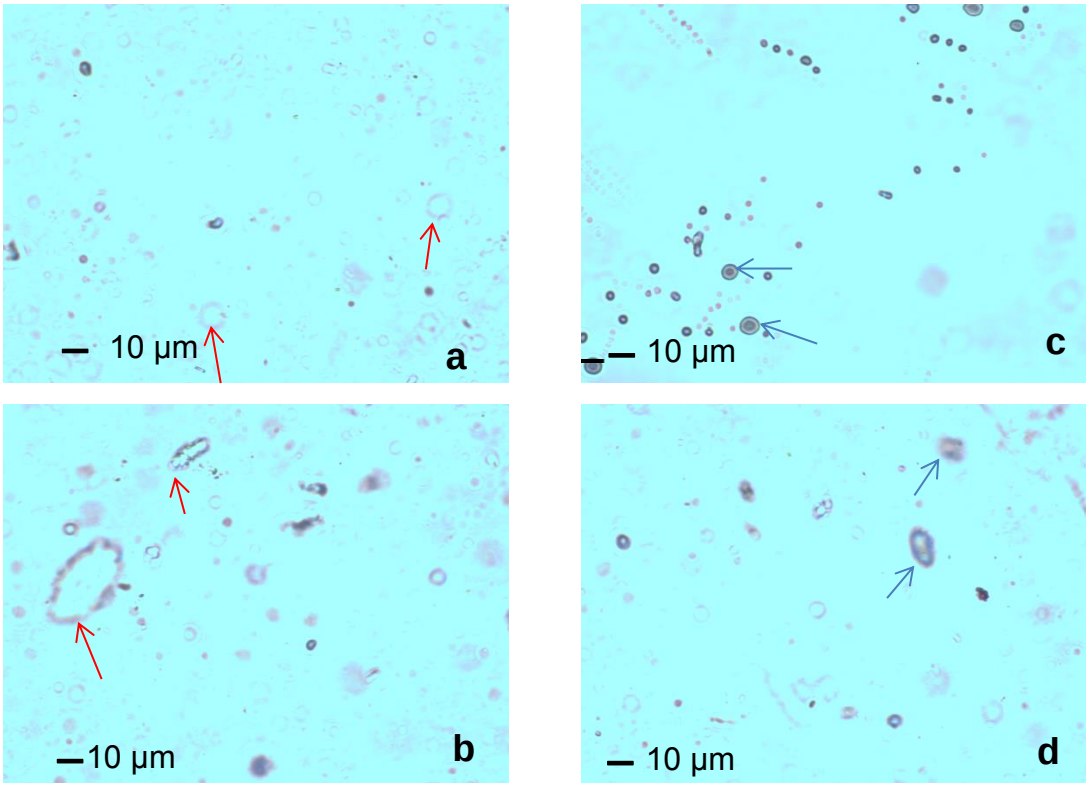

Figure 4-13. Light microscope images of Ca-alginate microgel particles at pH 5 (a) and pH 8 (b) and curcumin encapsulated in Ca-alginate microgel particles at pH 5 (c) and 8 (d)

Light microscopy images of encapsulated β-carotene are displayed in Figure 4-14. The particle shape was not as rounded as the curcumin samples. The sample preparation was slightly different than with the curcumin samples. The sample was smeared and pressed onto the slides to remove any excess liquid and to immobilize the particles, thus the particles might have been squashed due to excessive pressure against the cover slip. However, these micrographs still provided a tangible picture of encapsulated β-carotene in the microgel particles with TW20 which is represented by these bright red particles.

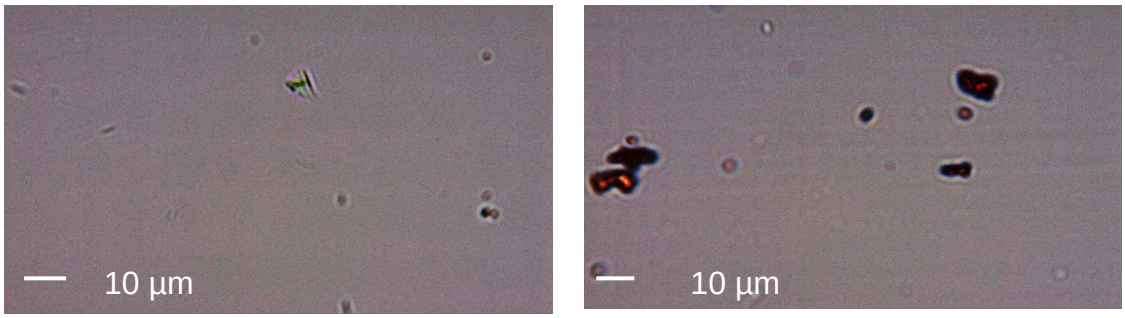

(a) (b)

Figure 4-14. Micrographs of microgel particles with no β-carotene (a) and β-carotene encapsulated microgel particles with TW20 (b)

The results with alginate encouraged us to attempt the same encapsulation technique with other calcium sensitive biopolymers: κ-carrageenan and pectin. Figure 4-15 and Figure 4-16 summarise some of the results. There are some apparent 'boundary walls' (which represent the nascent of microgel particles) with some of the flavonoid crystals entrapped inside and also some free crystals on the outside of the microgel particles. Thus, the methodology seems quite general and broadens the potential for producing a wide range of different types of polysaccharide-based microgel particles.

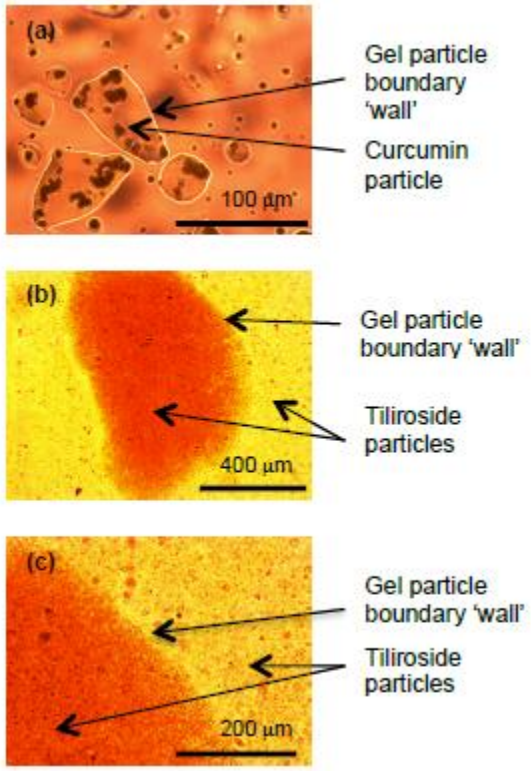

Figure 4-15. Micrographs of (a) 1 wt.% curcumin and (b, c) 1 wt.% tiliroside encapsulated in κ-carrageenan microgel particles, made from 4 wt.% κ-carrageenan and 50 mM Ca^{2+}

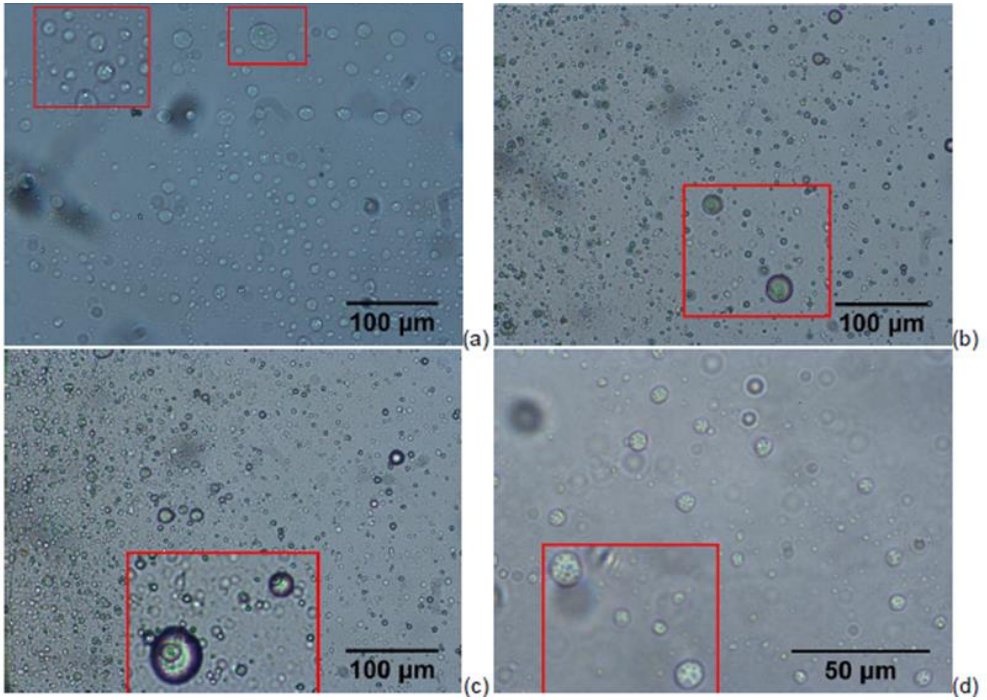

Figure 4-16. Micrographs of (a) 1 wt.% rutin, (b and c) 1 wt.% crocetin, and (d) 1 wt.% naringin encapsulated in pectin microgel particles, made from 3 wt.% LM pectin and 25 mM Ca^{2+}

4.2.6 Addition of magnetic nanoparticles (MNPs) suspension as a method of particles separation

In Chapter 3, the Ca-alginate gel particles were separated via centrifugation. The centrifugation was performed at high speed, i.e., 20,000 rpm (48,343 g), due to the low density difference between the microgels and the aqueous phase (although density of the microgel particles was unknown, it was expected to be ~1 based on the large proportion of water they contain). However, when polyphenols or β-carotene were encapsulated, this should have led to a much wider density gap. Figure 4-17 outlines the density of these polyphenols and β-carotene crystals benchmarked against the predicted Ca-alginate microgels density. In this case, when centrifugation was performed, all these insoluble particles (whether they were entrapped or not) would either sink to bottom of the tube (for density > 1, i.e., polyphenols) or rise to the top (for density <1, i.e., β-carotene). Thus, the quantification of microgel particle yield or loading efficiency could not rely on centrifugation separation alone because of these un-entrapped portions of the polyphenol and β-carotene crystals.

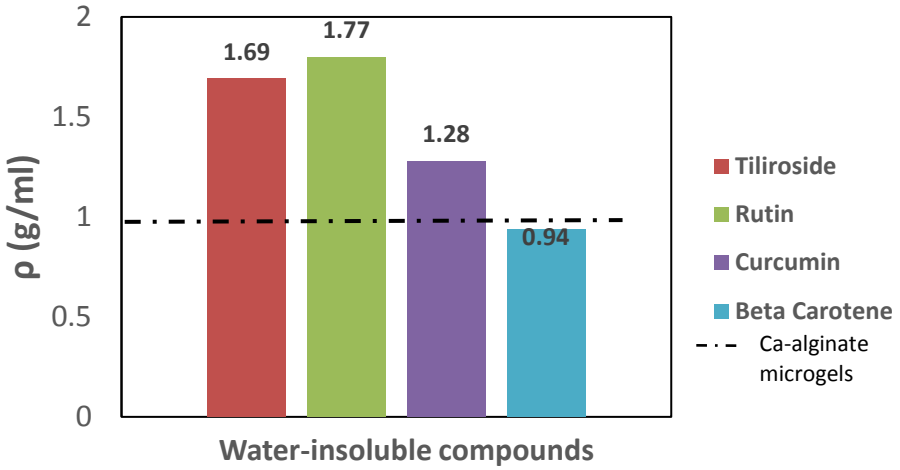

Figure 4-17. Density values of water-insoluble compounds used for encapsulation

To enable better separation of encapsulated and non-encapsulated materials, MNPs were loaded into the microgel particles by mixing them into the alginate phase during homogenization. By entrapping these MNPs along with the insoluble particles, it enabled harvesting the encapsulated microgel

particles via application of a magnetic field. The impact of adding the MNPs on the size of the microgel particles can be observed in Figure 4-18. The d_{32} of the microgel particles with or without MNPs were not significantly different across various refractive indices, which encompassed the refractive indices of the polyphenols: 1.45 (rutin), 1.75 (tiliroside), or 2.42 (iron oxide).

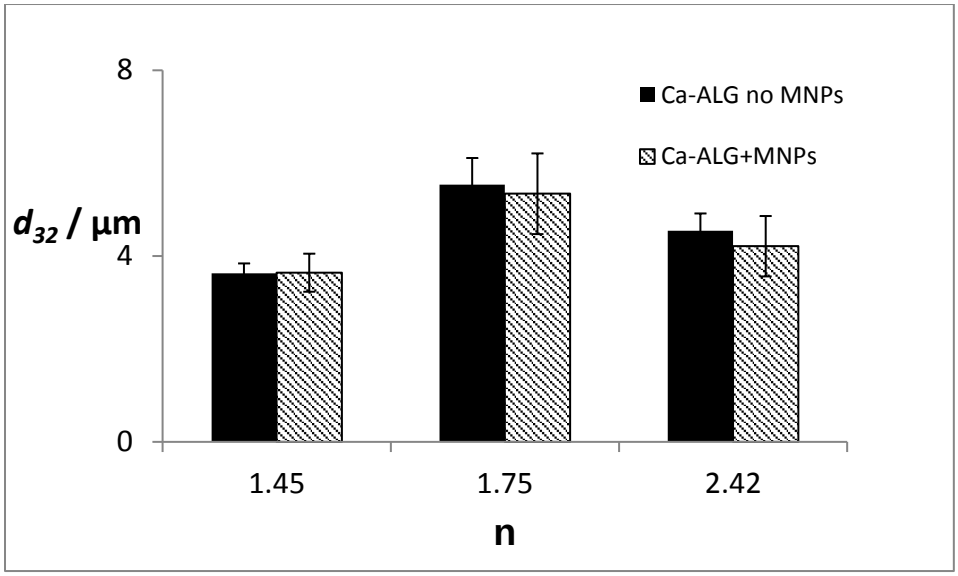

Figure 4-18. Particle size (d_{32}) of Ca-alginate microgel particles (Ca-ALG) with and without magnetic nanoparticles (MNPs) at different refractive indices (n)

Addition of the MNPs also did not influence any changes of the $d_{3,2}$ of the microgel particles with or without β-carotene. For β-carotene encapsulation, the average of d_{32} of the β-carotene + TW20 encapsulated in microgel particles with or without the MNPs were similar, i.e., 4.91 ± 0.12 µm and 5.44 ±0.49 µm, respectively. Figure 4-19 shows no significant shift of the size distribution peaks as the MNPs were added into the Ca-ALG+BC+TW20. Thus, the addition MNPs did not appear to have any impact on the particle size which implied a minimal interaction of MNPs with the microgel particles or β-carotene.

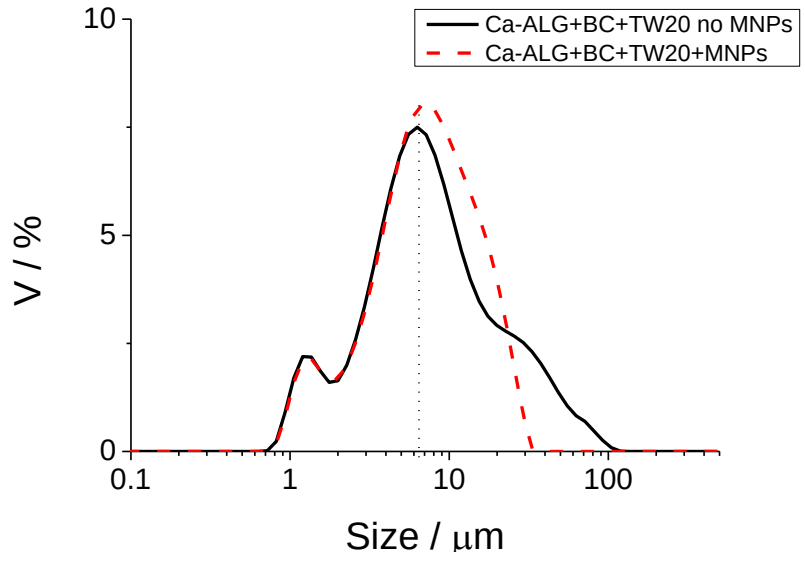

Figure 4-19. Particle size distribution of β-carotene encapsulated in Ca-alginate microgel particles with and without magnetic nanoparticles (MNPs)

Polyphenols are known to chelate with metal ions due to the presence of negatively charged hydroxyl groups which can bind the positively charged metal ions strongly via electrostatic interaction. We measured the ζ-potential of the MNPs and the value was close to neutral, i.e., 1.26 ± 0.02 mV. The MNPs were in the form of iron II and III oxides and their minimal charge would be expected to minimize their interaction with alginate or the insoluble polyphenols. Moreover, the concentration of magnetic suspension spiked into the alginate phase was low, i.e., 0.02 wt.% (wet weight). Considering the dry weight of the magnetic suspension was only 0.19 ± 0.01 wt.%, only ~0.004 wt.% of the iron particles was the content. At such low concentrations, it is therefore not surprising that the MNPs did not significantly change the microgel particle formation with or without polyphenols and β-carotene.

However, another concern to address was whether the concentration of MNPs was high enough to cover the whole surface area of the microgel particles and possibly inhibit the entrapment of water-insoluble compounds. If we assume the microgel particle is a spherical (see Figure 4-20), the total

surface area covered by the MNPs can be calculated using Eq.4-1. The area of MNPs to cover the surface is defined by Eq.4-2. By knowing the ratio of : A_{MNP} we can determine the number concentration of MNPs required to fully cover the whole surface of a microgel particle, assuming $r_{microgel}$ = 5 µm and r_{MNP} = 67 nm.

$$A = 4\pi (r_{microgel} + r_{MNP})^2 \quad \textbf{4-1}$$

$$A_{MNP} = \pi (r_{MNP})^2 \quad \textbf{4-2}$$

With maximum surface packing density of 0.9069, the ratio of $A_{microgel}$:A_{MNP} equals to 1:20,474.

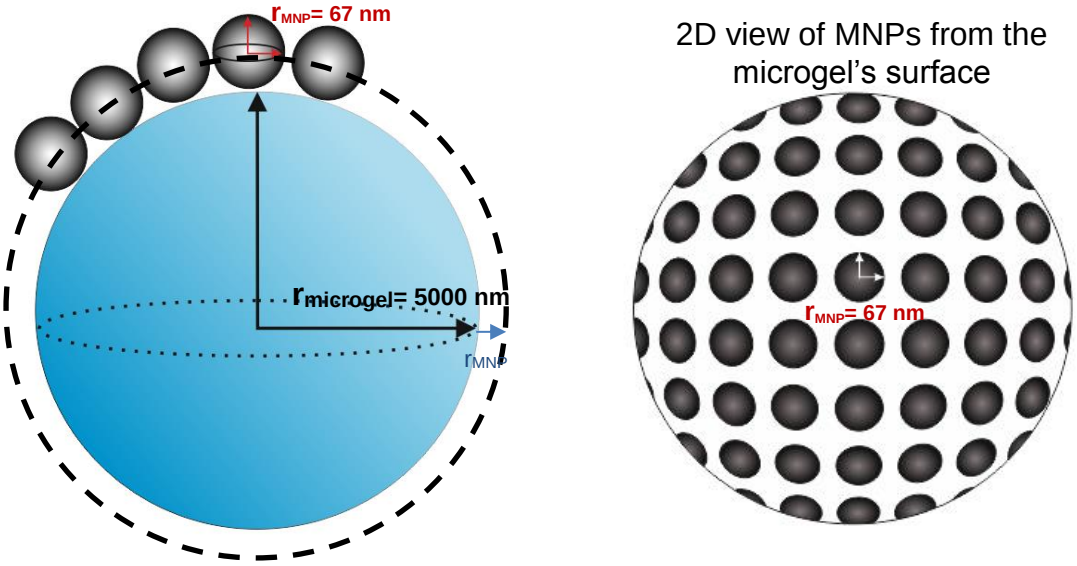

Figure 4-20. Schematic illustration of surface area ratio of Ca-alginate microgel particles and magnetic nanoparticles (MNPs)

If we have a known amount of microgel suspension, i.e., 1 g, which contains ~5 wt.% of microgel particles and 0.004 wt.% (solid content) of MNPs, we can determine their volumes using Eq.4-3. Assuming the densities of microgel and MNPs are ~1 g.ml^{-1} and 5.2 g.ml^{-1}, respectively, (Ianoş et al., 2012), respectively.

$$V = \rho \times M \quad \textbf{4-3}$$

where V = Volume (ml), M = mass (g), ρ = density (g.ml^{-1}).

The total surface area for microgels and MNPs in 1 g suspension can be calculated using Eq.4-4.

$$A = \frac{V}{r} \qquad \textbf{4-4}$$

where A = Area, V = volume, r = radius.

From the above calculations, the total surface areas of microgel and MNPs in 1 g of microgel suspension equal to 1 x 10^{16} nm^2 and 1.1 x 10^{14} nm^2, respectively. Thus, the ratio of total surface area of the microgel versus MNPs will be 100:1, i.e., the total surface area of the microgel particles far exceeds the capacity of the magnetic nanoparticles to completely cover their surface, even discounting the fact that some of these magnetic nanoparticles will be entrapped inside the microgel particles. Therefore, the MNPs are unlikely to affect interaction of encapsulated material with the surface of the microgel particles.

4.2.7 Microgel Particle Yield

The microgel particle yield was defined by the following Eq.4-5 (similar as Eq.3-11)

$$Microgel\ Yield = \frac{m_{\,m}}{m_s}\ x\ 100\ \% \qquad \textbf{4-5}$$

where $m_{\,m}$ is the mass of the microgel particles separated magnetically from the suspension (g) and m_s equals to the total mass of the suspension (g)

The microgel yields are reported in Figure 4-21. When water-insoluble crystals were encapsulated, the microgel yield improved by at least 2-fold, ranging from 10.7 % to 29.4 %. The highest microgel yields were Ca-ALG+BC with or without TW 20, i.e., 21.7 % and 29.4% respectively. Although there was a trend of lower microgel yield in Ca-ALG+BC+TW 20, the result was not significantly different, $p > 0.05$. The microgel particle yields of Ca-ALG+R vs. Ca-ALG+CU were 20.8 % vs. 15.1 %, respectively, with no significant difference ($p > 0.05$). The microgel yield of Ca-ALG+T, i.e., 10.7 %, was the lowest, with $p < 0.05$ compared to Ca-ALG+R. A plausible explanation for such an improvement in microgel yield is that these insoluble particles serve as

"nuclei" to promote formation of new microgel particles, akin to heterogeneous nucleation phenomenon as described in Chapter 1. The water-insoluble crystals may have triggered the *in situ* bridging between calcium and alginate aiding the formation of microgel particles. Therefore, a trend of increasing microgel yield was observed as water-insoluble crystals were integrated into the microgel particles.

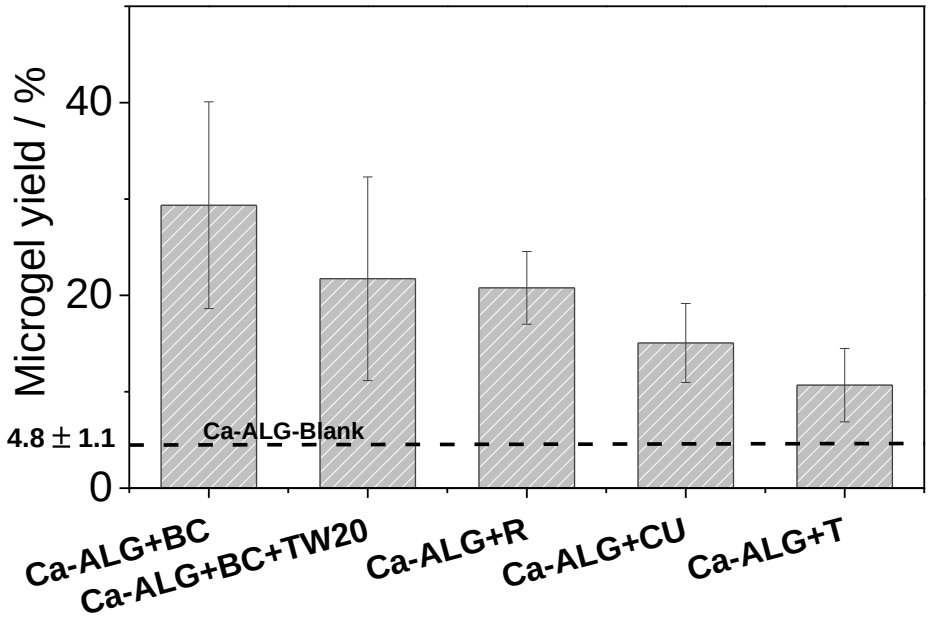

Figure 4-21. Microgel yield of Ca-alginate microgel particles with MNPs (0.02 %wt. concentration) and with or without the encapsulated materials

The physical properties of the polyphenols, such as density, M_w, and particle size, were considered to see if there was any correlation with the microgel yield (Figure 4-22). The microgel yield did not correlate with the density order of these water-insoluble particles (correlation coefficient was < 0.3), see Figure 4-22b. The density of tiliroside and rutin were in similar range, 1.69 vs. 1.77 g.ml^{-1}, respectively, while curcumin was 1.29 g.ml^{-1}. However, the microgel yield of tiliroside was the smallest, and others were in the same range of values. The lack of correlation with density suggests there was no significant gravitational separation occurring during the separation via the magnetic field. The order of molecular weight of these insoluble materials also did not affect

the microgel yield (Figure 4-22c). Tiliroside and rutin had similar M_w, i.e., 594.53 g.mole^{-1} vs. 664.58 g.mole^{-1}, respectively, while curcumin has the lowest M_w, 368.39 g.mole^{-1}. However, the M_w and bulk density of these compounds do not necessarily show any relationship to the size of their insoluble crystals.

Tiliroside did not have the lowest M_w and density, but it had the smallest crystal size (Figure 4-22d). Interestingly, it appeared that the microgel yield was mildly correlated to particle size of the polyphenols crystals (correlation coefficient was 0.72): the smaller the particle size, the lower the microgel yield. The particle size of the tiliroside crystals was 182.4 nm and resulted in lower yields than with rutin and curcumin. The crystal sizes were approximately in the same range for rutin and curcumin (~210 nm), and the microgel yields were approximately the same for those two compounds. This again points to some effect of the insoluble crystals acting as ‘nuclei’ for microgel particle formation.

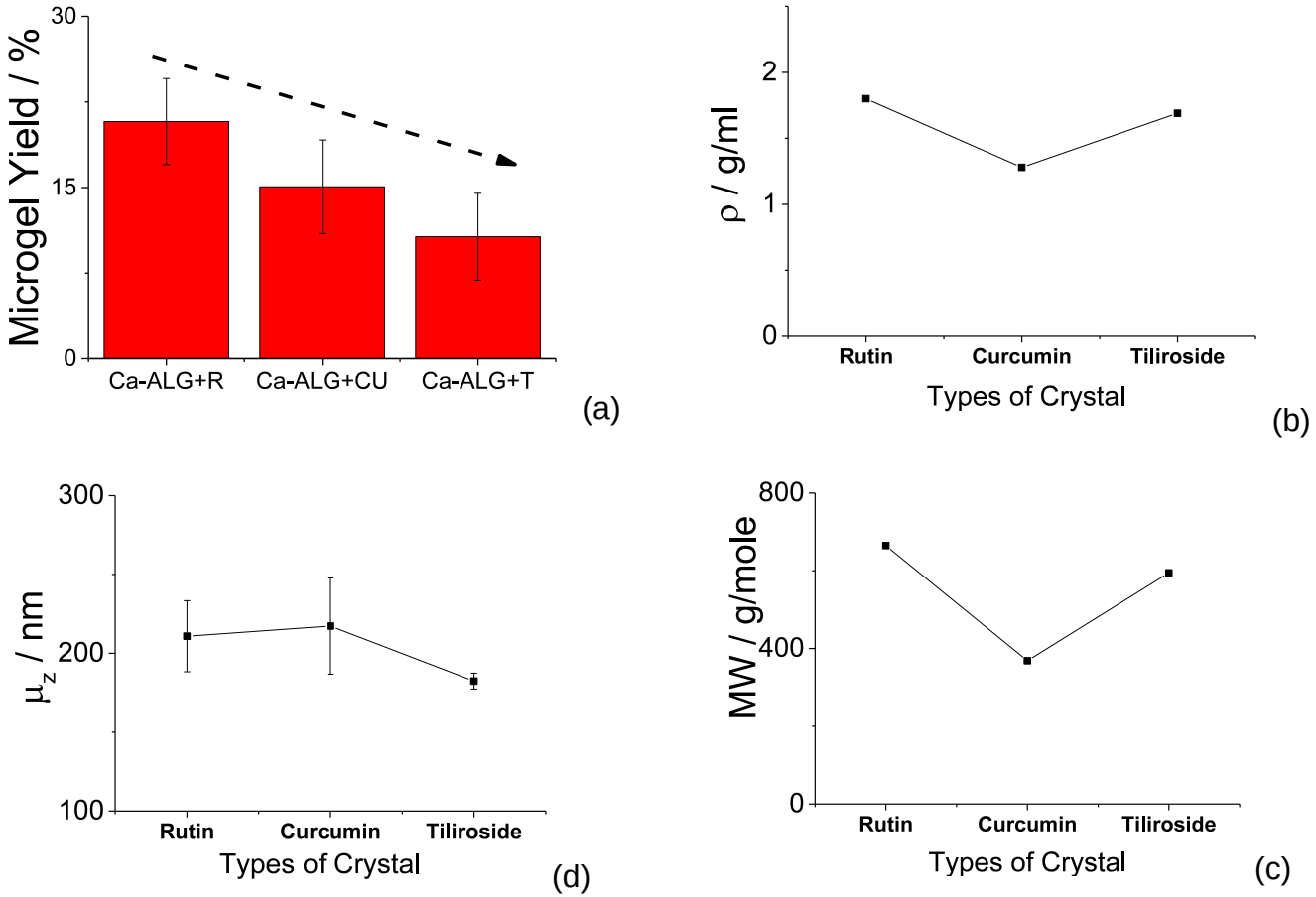

Figure 4-22. Correlation between the microgel yield of polyphenols (a) with physical properties of the crystals, i.e., density (b), M_w (c), crystal size (d)

4.2.8 Payload

The payload was defined by Eq.4-6:

$$Payload = \frac{X_m}{m_m}\ x\ 100\% \qquad \textbf{4-6}$$

where X_m is the mass of the encapsulated compounds in the microgel particles (g) and m_m is the mass of the microgel particles magnetically separated from the suspension (g).

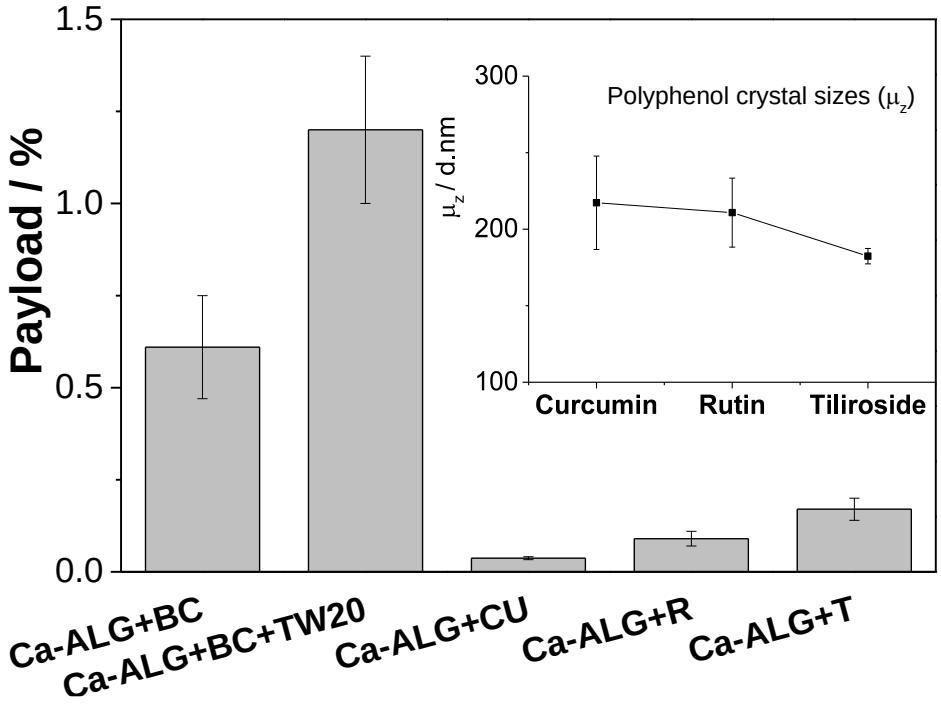

Figure 4-23. Payloads of encapsulated microgel particles and their correlation with the polyphenol crystal sizes (displayed as an inset figure)

In general, the microgel particles encapsulated with water-insoluble compounds had payloads between 0.037 % to 1.2 %, with curcumin the lowest and β-carotene the highest, i.e., 0.61 % for Ca-ALG+BC and 1.2 % for Ca-ALG+BC+TW20 (Figure 4-23). This was due to the higher initial concentration of β-carotene than polyphenols in the original alginate solution used for encapsulation. However, comparing the payload of BC with or without TW20, there was a significant increase of payload as TW20 was introduced into the system, with $p < 0.05$. TW20 is an anionic surfactant, with an HLB value of 16.7. With such a high HLB value, it commonly serves as a surfactant for O/W

systems, which is pertinent to this system, i.e., β-carotene crystals contained within Ca-alginate microgels (mostly containing water). Possibly TW20 resulted in β-carotene crystals having a greater affinity for the hydrophilic microgel particles.

The same concentration (0.5 mM of rutin, tiliroside, curcumin was loaded into the alginate phase before microgel particle formation, thus the payloads can be more easily compared against each other. The order of the payload from the highest to the lowest was: Ca-ALG+T > Ca-ALG+R ≥ Ca-ALG+CU. Payload of Ca-ALG+T was significantly higher with $p < 0.05$ compared with Ca-ALG+R and Ca-ALG+CU. Thus, smaller crystals resulted in a higher payload (the correlation coefficient was -0.97), presumably because the smaller crystals were more easily trapped inside the microgel particles as they were formed.

In summary, particle size of the insoluble crystals played an important role in determining the final payload and microgel yield.

The payloads maybe considered low if compared with the same compounds encapsulated using different methods. For example, (Nguyen et al., 2015) encapsulated curcumin in chitosan nanoparticle complex produced via spray drying and obtained payloads > 80 %. However, the curcumin concentration used in their study was 27 times higher than our current study. Moreover, the microgel particles in our study were in liquid suspension, not in the form of a powder as produced by spray drying. Drying certainly will draw the moisture out, and thus increase the payload tremendously. Freeze-dried curcumin loaded microcapsules (yeast cells) also had a high payload (around 10 % and 21% in curcumin in water and in 50% v/v alcohol suspension, respectively), but again starting with a much higher (5 times) concentration of curcumin initially (Paramera, Konteles, & Karathanos, 2011).

4.2.9 Loading Efficiency

Loading efficiency was also quantified to gauge the relative ease with which the different water-insoluble compounds were trapped inside the microgel particles. Loading efficiency, sometimes referred to as encapsulation efficiency, is defined as the following:

$$\boldsymbol{Loading\ Efficiency} = \frac{\boldsymbol{X_m}}{\boldsymbol{X_T}}\ \boldsymbol{x}\ \boldsymbol{100\%} \qquad \textbf{4-7}$$

where X_m is the mass of the encapsulated compounds found inside the microgel particles (g) and X_T is defined as the total mass of the encapsulated compounds in the system (g).

As depicted from Figure 4-24, the loading efficiencies of Ca-ALG+T and Ca-ALG+R were the highest, i.e., 57% and 58 % respectively, followed by Ca-ALG+CU, i.e., 37 %. The lowest loading efficiency was for β-carotene: Ca-ALG+BC and Ca-ALG+BC+TW20 were 21.5 % and 30.9 % respectively, significantly lower compared to flavonoids mentioned above, with $p < 0.05$.

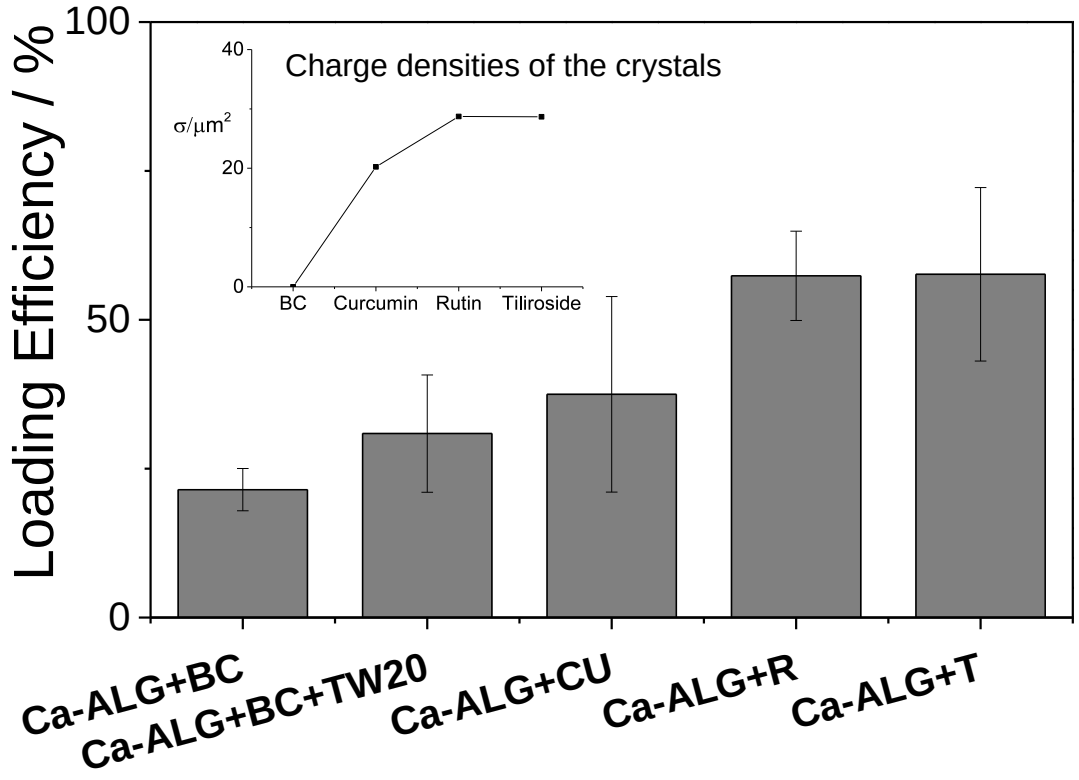

Figure 4-24. Loading efficiencies of encapsulated microgel particles and its correlation with the charge densities of the crystals (displayed as an inset figure)

To try and explain why the encapsulation efficiency of the flavonoid crystals was much higher than the oil soluble β-carotene, the charge density per unit surface area (μm^2) of these insoluble compounds was estimated. One

hypothesis was a higher charge density would produce a higher loading efficiency because there will be more binding sites available to interact with the alginate. The maximum possible number of charges highlighted in the chemical structures of water-insoluble compounds is visually depicted in Figure 4-25. The maximum number of electronic charges comes mainly from the hydroxyl groups at the surface of the crystals which could bind with alginate via Ca^{2+} ion cross-linking or via hydrogen bonding depending on the pH of the system.

Table 4.2. Charge density of the polyphenol crystals

Chemical	No. of charge/molecule	μ_z (in nm)	Surface area (μm^2)	Charge density (charges per μm^2)
Curcumin	3	217.3	0.15	20.2
Rutin	4	210.8	0.14	28.7
Tiliroside	3	182.4	0.10	28.7

Table 4.2. shows the calculated charge densities based on the assumptions that all the crystals were spherical and that all the charges were exposed on the surface. On this basis, rutin and tiliroside possessed the highest charge density, i.e., 28.7 charges per μm^2 for both compounds. They also had the highest loading efficiency, i.e., 58 % for Ca-ALG+R and 57 % for Ca-ALG+T. The loading efficiency of tiliroside was approximately the same as rutin's, despite tiliroside having the smallest crystal size. The extra OH group in the flavone ring of rutin raises its charge density to be on a par with tiliroside. Thus, this could explain why both yielded similar loading efficiencies. However, there seems to be a significant lack of knowledge of the actual surface charge distribution on flavonoids crystals.

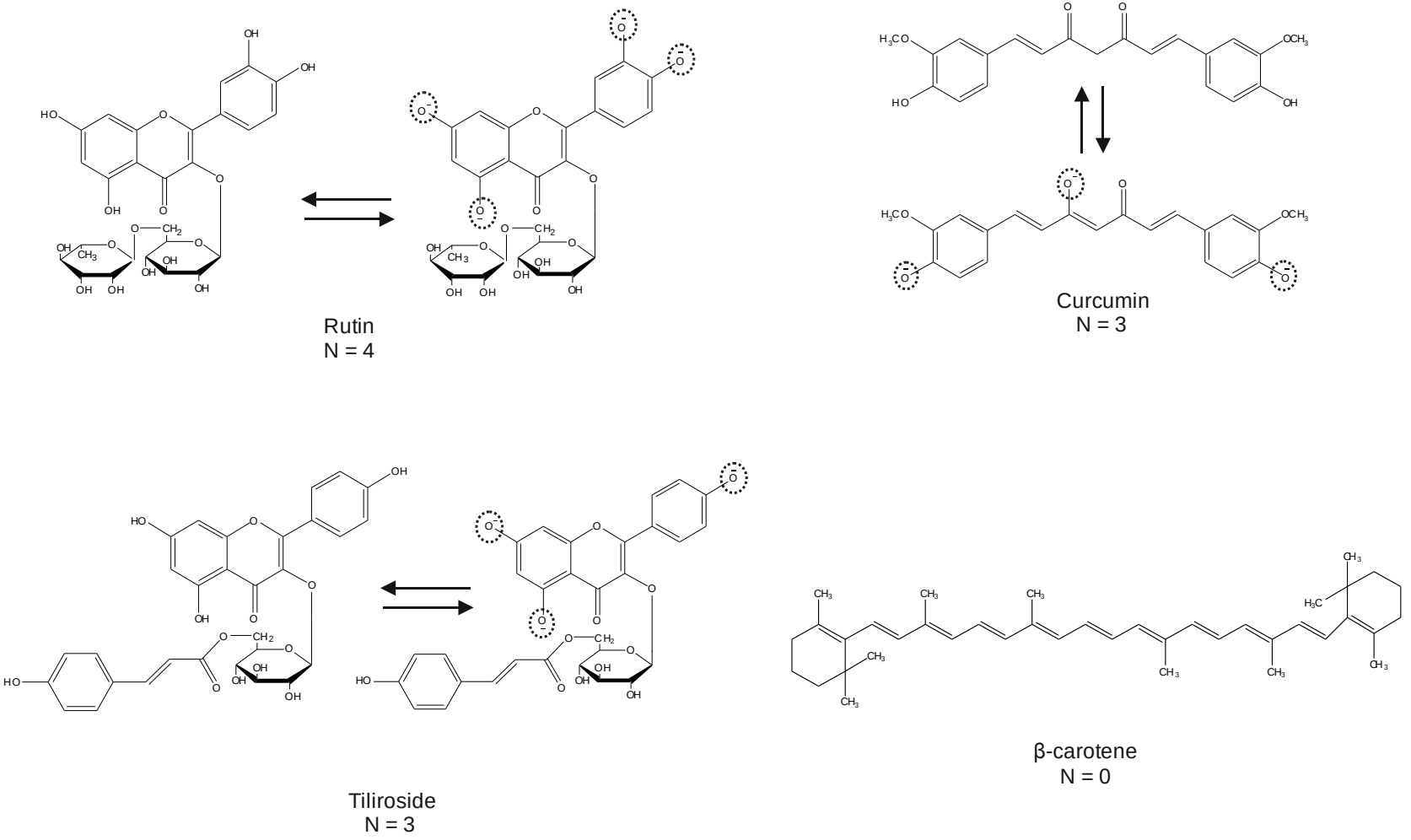

Figure 4-25. Chemical structures of water-insoluble particles with its protonated and deprotonated state with N = number of charges

The microgel particles were produced at close to neutral pH, i.e., 6.8 ± 0.2. This condition would promote full ionization of the carboxylic acid groups in the alginate, while the charges of rutin and tiliroside (pK_as were around 7 as reported by Herrero-Martínez et al., 2005) would be closer to neutral. Although rutin and tiliroside may be neutrally charged at that pH, attractive forces still can exist to modulate the interaction with alginate at the molecular level. Indeed, with such oxygen-rich molecules as rutin and tiliroside, alginate-flavonoid binding could be mediated mainly by hydrogen bonding interactions. The oxygens present in the form carbonyl group or carboxyl groups in the flavone rings and the vicinal sugar moiety chain could also contribute to hydrogen bonding, which provides another possible explanation of why rutin and tiliroside had the highest loading efficiency. A review article, written by Bordenave, Hamaker, & Ferruzzi (2014), posits that hydrogen bonding and ionic interactions promote the association of non-starch polysaccharides with flavonoids. However, all of the above does not take into account the fact that the water-insoluble materials may crystallize into a number of different forms, each with differing surface charge characteristics.

There are 3 possible forms of charged curcumin molecular species: Cur^{0} (neutral), Cur^{-1} (monoanionic), Cur^{-2} (dianionic), Cur^{-3} (trianionic) when it undergoes deprotonation. Wang et al. (2010) reported the apparent pK_a of curcumin was at around 8.3 in water, and the pK_a values of the individual functional groups were: 8.4 and ~10 for keto-enol and phenol, respectively. The keto-enol tautomer and the hydroxyl groups in phenols could be foreseen as the binding sites to the alginate. At pH 6.8, the protonated OH groups in curcumin mostly occupied at the binding sites would favour to dipole-dipole interaction between those functional groups and deprotonated COO^{-} group of alginate. Although charge-dipole or charge-charge forces was considered to be a strong interaction, there were only a few of these bonds available (no. of charges was only 3), thus less chance of interactions available between curcumin and alginate. This low number of charges in curcumin per surface area (i.e., 20.2 charges per μm^2) could explain why curcumin had lower loading efficiency (37 %) as compared to rutin and tiliroside (58 % and 57 %, respectively).

β-carotene is a non-polar compound, derived from eight isoprene units. The chemical structure of β-carotene (Figure 4-25), with no hydroxyl groups or any other polar functional groups suggests that neither electrostatic nor hydrogen bonding are available to facilitate interaction of β-carotene with alginate. This possibly explains why β-carotene gave the lowest loading efficiency (< 31 % with or without TW20). In general, the loading efficiencies seemed to correlate with the charge densities of the water-insoluble crystals, with correlation coefficient of 0.94.

'High' or 'low' loading efficiencies and payloads should take into account the recommended daily intake of such materials. For example, if we consumed half of a teaspoon (2.5 ml) of Ca-ALG+BC suspension, assuming the density almost equals to 1, 2.5 ml equals to 2.5 g of Ca-ALG+BC, containing 0.735 g of microgel particles (particle yield 29.4 %). With the payload of 0.6 %, these particles would have ~4.4 mg of β-carotene. The Food Standards Agency of UK government recommended the dietary intake of Vitamin A of 700 μg for adults > 19 years old (Food Standards Agency, 2007), which translates to 4.2 mg β-carotene to meet desired requirement. Thus, by taking a half of teaspoon of Ca-ALG+BC, one would fulfil the daily recommended intake of β-carotene per day. Whilst the microgel particles may therefore seem a promising delivery vehicle of Vitamin A precursor, it is critical to note that different physical states of β-carotene will also have an influence on its digestion fate in the GI tract (Xia, McClements, & Xiao, 2015). These authors speculated higher bioaccessibility of β-carotene when it was solubilized in an emulsion rather than co-ingestion of the crystalline state, due to more efficient lipid digestion. Thus, future work might involve pre-emulsifying the β-carotene in an oil based solvent prior to embedding it into the microgel particles via the LJH.

To our knowledge, there is no definitive recommended daily intake for rutin. Some studies have suggested that intake of 180 mg per day gives a therapeutic effect against certain chronic disease (Kreft, Knapp, & Kreft, 1999). On the contrary, another study revealed that a high concentration was not always needed: level as low as 1 μM of rutin had a significant impact on reducing the level of prostaglandin PEG_2 which was a biological factor known to regulate immunosuppressive activity in the body (Giménez-Bastida et al.,

2016). The recommended daily intake for rutin remains as uncharted territory. However, regardless of the lack of knowledge of an appropriate level, encapsulation of rutin in microgel particle would probably be a useful carrier for formulation application in food and pharmaceutical products.

4.3 Conclusions

The new technique of encapsulation of water-insoluble compounds in microgel particles produced via LJH and the entrapment efficiency were outlined in this chapter. It has been shown that the jet homogenizer can serve as a multi-faceted equipment, from creating emulsions to encapsulating materials in microgel particles. Many mainstream approaches to fabricate gel particles such as spray drying, prilling, or using proprietary encapsulators, produce high yields of particles but the sizes are considerably larger (>1 um) than can be produced in the jet homogenizer. For LJH, the particle yields may be considered low, but smaller particles can be produced. It was shown that particle yield, payload and encapsulation efficiency seemed to be mainly dependent on the size and surface charge density of the particle being encapsulated, probably via the types of interaction that enable them to bind with alginate. Loading of insoluble particles actually tended to improve the microgel yield. High numbers of hydrogen bonding moieties in rutin and tiliroside gave the highest loading efficiency (> 50 %). Payloads were low but only because we started with low concentrations of the health benefit compounds (0.5 mM for polyphenols and 18.5 mM for β-carotene) in the starting solution. Regardless of the low payloads, encapsulation of water-insoluble compounds via jet homogenizer showed high loading efficiencies which makes it worthwhile to pursue further as a means of generating microgel particles for health and well-being functions.

Chapter 5 Encapsulation of water-soluble compounds in Ca-alginate microgel particles produced via the Leeds Jet Homogenizer

5.1 Introduction

This chapter delves into attempts to control protein adsorption into and onto the microgel particles via addition of cationic proteins, i.e., lysozyme and lactoferrin, and also water-soluble dyes. Alginate is known for its strong negative charge, e.g. the measured ζ-potential = -80 mV at neutral pH as reported by Bokkhim et al. (2015). On cross-linking with Ca^{2+} during microgel formation, the ζ-potential was reduced but still remained negative (i.e., around -60 mV in neutral pH, see Chapter 3.2.4). Thus, addition of compact cationic proteins could potentially serves as 'surfactants' to stabilize the microgels and limit their growth and aggregations during and after their formation. The hypothesis is that positively charged proteins of appropriate size would tend to form an adsorbed layer on the surface of the microgel particles and hence limit their growth and/or fusion in size rather than be encapsulated within the particles. The balance of adsorption versus encapsulation is expected to depend on the relative charge and size of the biopolymers and the pore size of the particles. At the same time, microgel particles where the proteins are strongly trapped at the surface or within the particles could both act as carriers for such proteins.

Another aim is to investigate the possibilities of entrapping water soluble dyes, e.g., erioglaucine (an anionic dye) and methylene blue (a cationic dye). These dyes have high molar extinction coefficients (ε): 7.6×10^4 $mol^{-1}.dm^3.cm^{-1}$ at 664 nm for methylene blue (Hossain et al., 2012) and 2.14×10^5 $mol^{-1}.dm^3.cm^{-1}$ at 630 nm for erioglaucine (Barakat et al., 2001). With such high extinction coefficients, the entrapped dyes can be quantified via UV-Vis spectrophotometry. Methylene blue is a versatile dye used to stain biological materials and also a useful medication for malaria, oral cancer marker, etc., thus it offers a merit to entrap the dye in microgel as a candidate for drug delivery vehicle. Erioglaucine is a food colour and a common contaminant in

wastewater, hence the encapsulation mechanism of erioglaucine into microgel particles has a number of potential uses, whilst also potentially acting as a model system for the encapsulation of other water soluble anionic substances.

5.2 Results and Discussion

Lysozyme and lactoferrin were elected to test how they might influence the particle size and the net surface charge of the microgels, knowing they are strongly positively charged at the chosen pH during microgel formation. Lysozyme is rich in patches of lysine (N = 6 residues, pK_a = 10.2) on its periphery which potentially govern the surface charge (Dismer & Hubbuch, 2007). The pI of lysozyme is around pH 11 (Ethève & Déjardin, 2002), thus below this pH lysozyme would be positively charged. Lactoferrin contains 2 molecules of Fe^{3+} (Baker & Baker, 2005) with a reported pI of around pH 8.5 (Peinado et al., 2010) and so at pH < 8.5 lactoferrin is positively charged. Alginate consists of sugar units of guluronic and mannuronic acids with pK_a values of 3.65 and 3.38, respectively (Draget et al., 1994) and it is negatively charged at pH > 6. Hypothetically, if these proteins bound to the surface of the microgels electrostatically, they would induce the ζ potentials to be less negative and the particle size might be reduced with an increase in the concentration of positively charged protein.

5.2.1 Addition of lysozyme and lactoferrin during microgel formations

Many different mixing modes were attempted to incorporate lysozyme onto the surface of the microgel particles. Either lysozyme was added in the (1) alginate phase, (2) calcium phase, and (3) *after* the microgel had been formed. The particle size (Z-average) and net surface charge (ζ-potential) results for each mixing mode are displayed in Figure 5-1. From Figure 5-1a where lysozyme was added into the alginate solution, the Z-average remained constant across all concentrations at around 214 ± 14 nm at pH 8 and 194 ± 9.6 nm at pH 10. Figure 5-1b shows where lysozyme was added into the Ca^{2+} phase the Z-average also remained constant, i.e., 193.7 ± 6.3 and 192.5 ± 17.9 nm at pH 8 and 10, respectively. A separate set of microgel particles was prepared where the lysozyme was added *after* microgel particle formation. By

adding the lysozyme after the microgels were formed it was thought that this might enhance lysozyme adsorption to the microgel surface. However, the results in Figure 5-1 showed no difference whether lysozyme was added before or after the microgels were formed: Z-average were 197.8 ± 8 and 190.8 ± 7.4 nm at pH 8 and 10. It was clearly seen that at both pH 8 and 10 there were no clear decreases or increases in Z-average values as the [lysozyme] was increased, regardless of the mode of lysozyme addition.

The ζ-potential values in Figure 5-1 a, b, and c, all show similar trends, with no distinct indication of the ζ-potential was being less negative as [lysozyme] was increased at either pH 8 or 10. The ζ-potentials across all lysozyme concentrations were around -40 ± 1 and –28.7 ± 0.9 mV at pH 8 and 10, respectively. These results again suggest that lysozyme has little ability to accumulate to any significant extent at the surface of the microgel particles, whether it is added during or after particle formation.

The ζ-potential of the microgel particles with lysozyme was more positive in magnitude at pH 10 than pH 8 at all lysozyme concentrations. At first sight, this might suggest that the microgel particles were coated with lysozyme to a similar extent at all lysozyme concentrations resulting in the smaller positive ζ-potential at pH 10. However, the ζ-potentials of lysozyme containing microgels had similar values as when [lysozyme] = 0. For some reason, the ζ-potentials when [lysozyme] = 0 were also less negative at pH 10 than at 8, although the charge on the carboxyl groups of the alginate is not expected to vary in this pH range. Possibly this was partly due to the sodium bicarbonate buffer used in the experiment. The initial pH of 20 mM sodium bicarbonate buffer was around 8.2 ± 0.1 and 1 M NaOH was used to raise to pH 10. The contribution from the Na^+ ions might have increased its ionic strength and thus lowered the initial ζ-potential at higher pH to become less negative (Carneiro-Da-Cunha et al., 2011). However, despite the ζ-potential difference between pH 8 and 10, overall the addition of lysozyme did not have any significant impact on both the Z-average and ζ-potential values across all lysozyme concentrations within the standard deviation, i.e., there was no sign of adsorption of lysozyme onto the surface of the microgel particles despite the cationic state of lysozyme at pH 8 and 10.

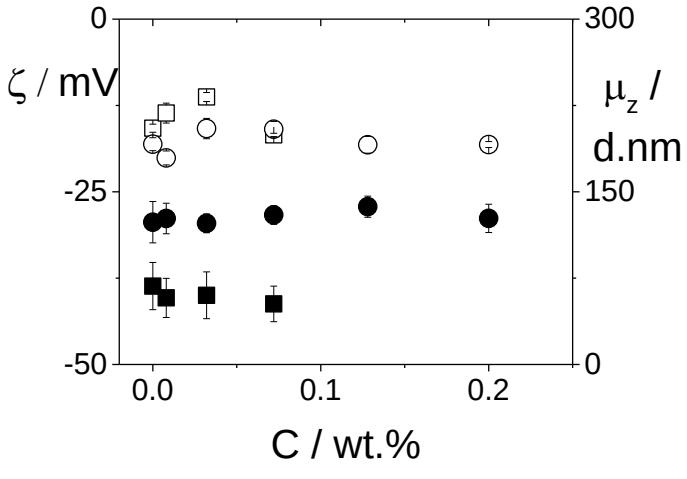

(a)

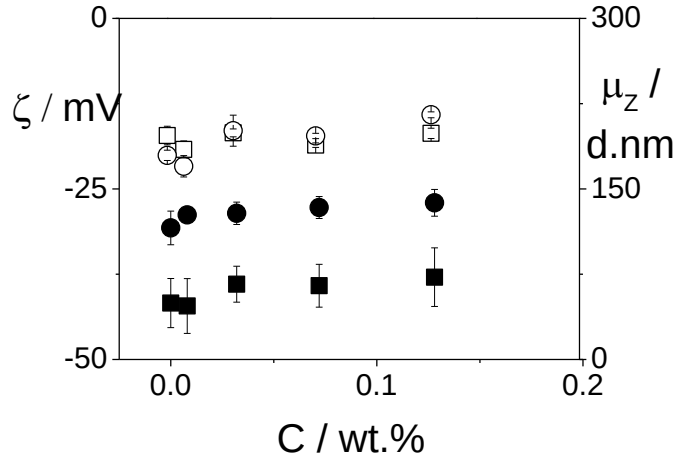

(b)

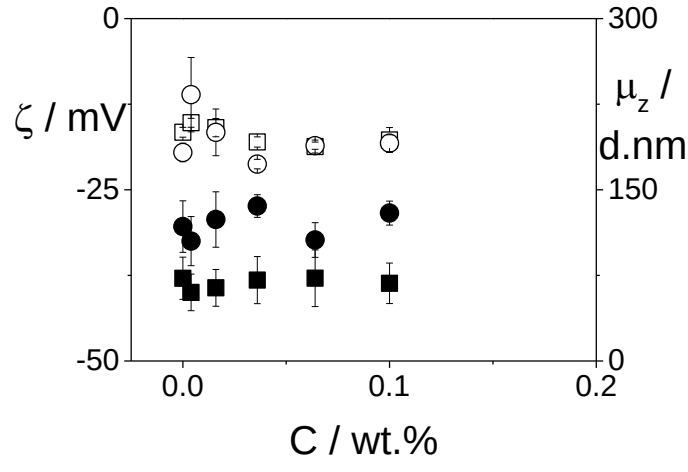

(c)

Figure 5-1. Comparison of zeta potential (ζ) and Z-average (μ_z) of calcium alginate gel particles prepared from 1% alginate in the 80 block at various lysozyme concentrations (C) and 10mM $CaCl_2$ in 20 block: ζ and μ_z at pH 8 (■ , □); ζ and μ_z at pH 10 (●, ○). Lysozyme was added (a) in the alginate phase, ((b) calcium phase, (c) after the microgel had been formed.

There was also the possibility of exchanging of the Ca^{2+} ions in the microgels with Na^{+} ions in the sodium bicarbonate buffer. This ion exchange occurs at the threshold of 0.6 mole fraction of Na/Na+Ca as determined by Ouwerx et al. (1998). The mole fraction of Na/Na+Ca in the microgel suspension was 0.8 (and even higher at pH 10), which would make the Ca-alginate microgel particles susceptible to degradation. If there was any lysozyme entrapped in the microgel particles, it would be released because of microgels dissolution. Thus, the lysozyme might more readily to form complexes with either alginate or calcium in the bulk solution rather than exerting any significant effect on the microgel particle size. Evidence for such complex formation was visually obvious by the presence of cloudiness (precipitates) during the microgel production process, as described below.

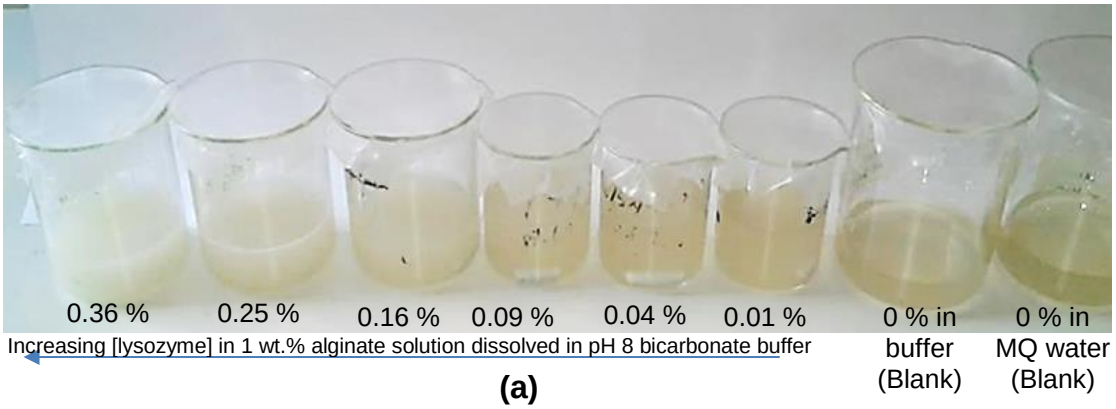

(a)

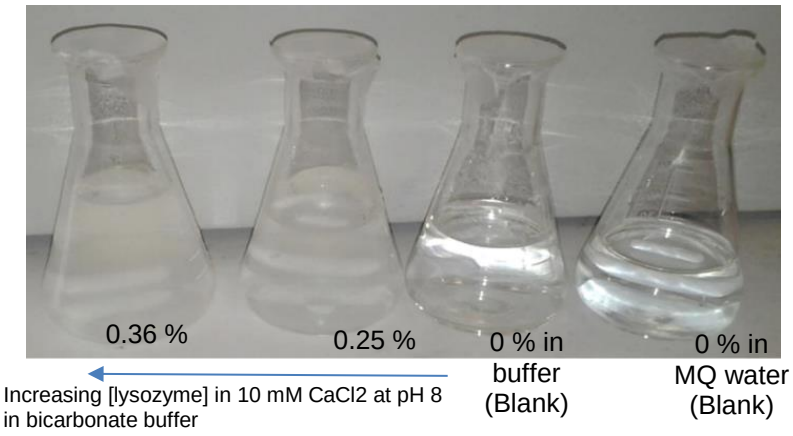

(b)

Figure 5-2. Visual aspects of the cloudiness formed during mixing lysozyme in bicarbonate buffer at pH 8 with (a) 1 wt.% alginate solution (b) 10 mM $CaCl_2$ at pH 8 in bicarbonate buffer

Visually, precipitation could be observed immediately after mixing lysozyme with the alginate or calcium chloride solutions (Figure 5-2). Higher turbidity was obvious in the 1 wt.% alginate solution with the increase of [lysozyme], which suggested that lysozyme was preferentially associated with the alginate in a dose-dependent manner. Some precipitation was also noticed on mixing of lysozyme with $CaCl_2$, though this was not as noticeable as with alginate. Interaction between Ca^{2+} and CO_3^- ions in the buffer could prime the formation of aragonite or calcite crystals in the presence of lysozyme (Yang et al., 2006). As observed in Figure 5-2b, on mixing bicarbonate buffer into the $CaCl_2$ solution no cloudiness was observed until the lysozyme was introduced into the mixture, indicating lysozyme somehow facilitated the precipitation process. Lysozyme-mediated calcification is believed to be the origin of the biomineralization required for the development of the exoskeleton structure of avian eggshells (Polowczyk, Bastrzyk, & Fiedot, 2016). Lysozyme is thought to serve as a 'buffer storage' of CO_3^- ions (Wang et al., 2009) at the pH of egg shell formation (pH 6 – 8). According to Wang et al. (2009), the reaction is dose-dependent; higher [lysozyme] led to more precipitates. Similar observations are seen in Figure 5-2b; the higher [lysozyme] samples appear to be more cloudy. Thus, the interaction between lysozyme and Ca^{2+} in the presence of the sodium bicarbonate buffer could prevent the lysozyme from being entrapped in the microgel, possibly because there was little lysozyme available.

Learning from the lysozyme experiments, the inclusion of lactoferrin in the microgel particles was pursued through mixing lactoferrin into the Ca^{2+} phase rather than into the alginate phase. No turbidity was apparent during mixing the lactoferrin into Ca^{2+} or alginate solutions before homogenization up to 0.8 wt.% of [lactoferrin]. The results of addition of lactoferrin on the particle size and ζ-potential of the microgels formed are displayed in Figure 5-3. There was a significant ($p < 0.05$) decrease in Z-average (from 200 to 100 ± 8 nm) observed with increasing concentration of [lactoferrin]. The ζ-potential also became significantly ($p < 0.05$) less negative, changing from –32 ± 3 to – 21.8 ± 1.4 mV as [lactoferrin] was increased from 0 to 0.8 wt.%. Both the size and ζ-potential results suggested that at least some lactoferrin adsorbed to the

surface of the microgel particles and this possibly helped to limit their size during particle formation. The decreasing trend of the particle size and increasing (positive) trend of the ζ-potential were observed at both pH 6 and 8, with less differences between these two pH values compared to with lysozyme.

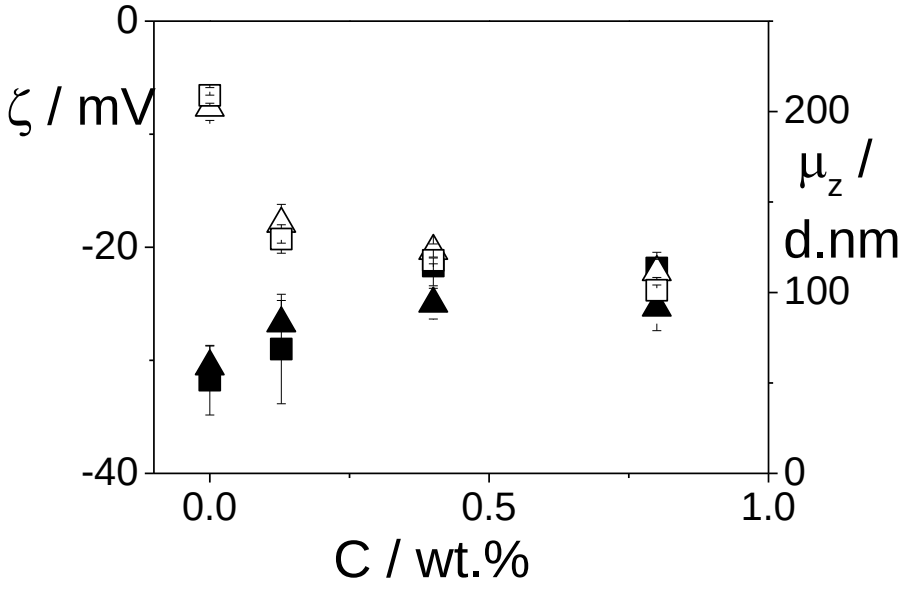

Figure 5-3. Comparison of zeta potential (ζ) and Z-average (μ_Z) of Ca-alginate microgel particles prepared from 1 wt.% alginate in the 80 block and 10mM $CaCl_2$ in 20 block at various [lactoferrin]; ζ and μ_z at pH 6 (▲, Δ); ζ and μ_z at pH 8 (■, □).

The particle size and ζ-potential results with lactoferrin were therefore very much different than with lysozyme. Adsorption seemed feasible with lactoferrin but not lysozyme. Bysell & Malmsten, 2006 studied the effect of peptide length/size on the distribution the entrapped peptides in negatively charged polyacrylic acid and poly-(APTAC) microgels, and found that large peptides were more inclined to form a shell layer surrounding the de-swollen microgel particles, and their bulkiness created a barrier to further penetration inside the gel core. Small peptides tended to be distributed evenly throughout the microgel, both in the core and shell. Compared to lysozyme (ca. 4 nm diameter, Damodaran, 1996) with a M_w = 14.3 kDa, lactoferrin is a considerably larger protein (ca. 10 nm diameter, Chen et al., 2014) with a M_w of

80 kDa. Thus, another reason why lactoferrin tended to end up more on the outside of the particles was due to its larger size.

5.2.2 Amino acid composition and surface charges of lactoferrin and lysozyme

Besides the protein size, it seems obvious that electrostatic interactions probably played a major role in determining the interaction of protein and the alginate. Since lysozyme and lactoferrin are widely studied proteins; their amino acid compositions are well known, see Table 5.2. Therefore, we calculated the expected total charges of these proteins as a function of pH using the mean pK_a values of the ionisable amino acid side chains as shown in Table 5.1 using the Henderson-Hasselbach equation (Eq.5-1). The total charges are expressed in the form of α, where α is the degree of dissociation of the ionisable group.

$$\alpha = \left[10^{(pK_a - pH)} + 1 \right]^{-1} \quad \textbf{5-1}$$

Table 5.1 Values of pK_a of amino acid residue side chains used to calculate charge of lysozyme and lactoferrin, taken from Damodaran (1996)

Amino acid residue	pK_a
Asp	4.6
Glu	4.6
His	7.0
Lys	10.2
Arg	12.0
Cys	8.8
Tyr	9.6

Table 5.2. Amino acid compositions of lysozyme (Manwell, 1967) and lactoferrin (Steijns & van Hooijdonk, 2007)

Types of amino acids	Amino acid residue	N* in chicken egg-white lysozyme	N* in Bovine lactoferrin
Acidic side chains	Asp	8	36
	Glu	2	40
Basic side chains	His	1	9
	Lys	6	54
	Arg	11	39
Polar neutral side chains	Asn	13	29
	Gln	3	29
	Ser	10	45
	Thr	7	36
	Val	6	47
	Cys	8	34
Hydrophobic aromatic side chains	Phe	3	27
	Trp	6	13
	Met	2	4
	Tyr	3	22
Hydrophobic aliphatic side chains	Ala	12	67
	Ile	6	15
	Leu	8	65
Unique amino acids	Gly	12	48
	Pro	2	30
Total amino acid residues		**129**	**689**

***N = number of amino acid residues**

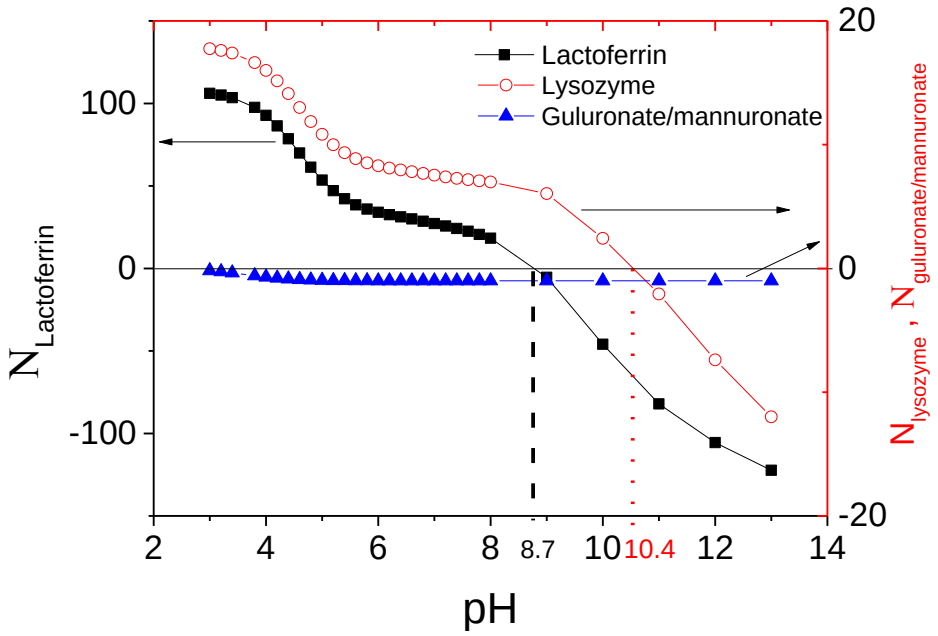

Figure 5-4. Number of charges (N) of lactoferrin, lysozyme, and guluronate or mannuronate as a function of pH.

The dashed lines indicate the predicted pI of the proteins (black line – lactoferrin, red line – lysozyme). The arrows direct to the Y-axis scale.

The number of charges per molecule of lysozyme and lactoferrin as a function of pH are plotted in Figure 5-4. Lactoferrin is more highly positively charged than lysozyme at the pH values of the microgel preparation (+7 and +2 net charge at pH 8 and 10 for lysozyme and +28 and +12 at pH 6 and 8 for lactoferrin). The higher positive net charge of lactoferrin is due to the larger number of basic residues in the lactoferrin vs lysozyme, i.e., 102 vs 18 residues, respectively, see Table 5.2. Based on the calculation, the predicted pI values for lysozyme and lactoferrin were at pH 10.4 and 8.7, respectively, which were close to the reported pI of pH 11 (lysozyme) and 8.5 (lactoferrin). This calculation gives us a good prediction of the number of charges at certain pH which later will be used to calculate the mole charge ratio between alginate and the proteins.

To further understand the differences between surface adsorption of lysozyme and lactoferrin, we estimated the mole charge ratio between the alginate and the proteins. The net charge of the monomer sugar unit of alginate

is around -1 throughout the pH > pK_a (~3.6) which could be extracted from Figure 5-4. With [alginate] and [protein] fixed at 1 wt.% and 0.1 wt.%, respectively, in a 100 g suspension of microgels, and from the known M_w of guluronic/mannuronic unit (194.14 g.mole^{-1}) and the protein, the mole charges of the proteins and sugar units of the alginate can be calculated via Eq.5-2, where N equals the number of charges of the corresponding compounds.

$$Mole\ charge = N\ x\ \frac{g\ of\ alginate\ or\ proteins\ or\ dyes}{M_w\ of\ alginate\ monomer\ or\ proteins\ or\ dye} \qquad \textbf{5-2}$$

The mole charge ratios between alginate and proteins are obtained by simply dividing the mole charge of alginate to the proteins.

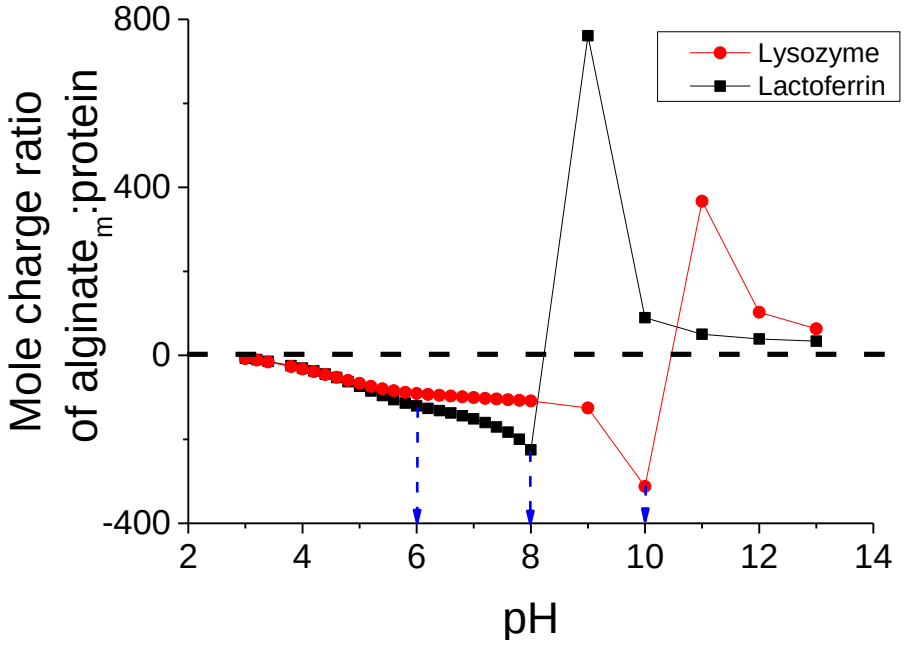

Figure 5-5. Plot of mole charge ratio of the alginate monomers (alginate$_m$) to lactoferrin and lysozyme as a function of pH at 1 wt.% alginate and 0.1 wt.% proteins.

The dashed blue lines indicate the pH levels used in the study (pH 6 and 8 for lactoferrin; pH 8 and 10 for lysozyme). The dashed black line indicates the mole charge ratio at 0.

The calculated mole charge ratio of alginate:protein is plotted against pH (Figure 5-5). Only mole charge ratios < 0 are really relevant, when the COO^- of guluronate or mannuronate units are negative and the proteins are positively charged, i.e., there are potential attractive electrostatic interactions between the

protein and the polysaccharide in this pH range. The sudden switch from negative to positive values occurs around the pI of the protein. Above this pH value both the protein and polysaccharide are negative and so the ratio becomes positive. Thereafter the ratio decreases again (though is still positive) as the charge on the alginate becomes fixed (approximately 2 pH units above the pK_a of the guluronate/mannuronate) but the charge on the proteins gradually becomes more negative until this in turn saturates as all the negatively charged amino acid chains become fully charged. However, across the full pH range, it is seen that there is far more charge on the alginate than on the protein. In particular at the pH values studied (pH 6 and 8 for lactoferrin; pH 8 and 10 for lysozyme), the calculated mole charge ratios of alginate:lactoferrin are -120 and -225 and for alginate:lysozyme -108 and -312, respectively. Thus, there is a clear excess of alginate negative charge that could potentially bind all the protein +ve sites, but this would be expected to have very little effect on the net charge of the alginate, i.e., have very little effect on the Ca^{2+}-induced gelation of the alginate, even ignoring the fact that not all the protein +ve sites would be available for binding, due to steric hindrance. Similarly, this calculation cannot discern whether or not one protein has a preferential binding compared to the other. There are many other factors, such as surface charge distribution or patches, which may affect the adsorption of the proteins to the alginate, which will be further explored below.

The positively charged lysine and arginine in lactoferrin are highly exposed on the outside of the helix and in patches (Baker & Baker, 2005), as a consequence of their non-even distribution in the polypeptide chain - see Figure 5-6a. This uneven distribution of charged surface patches probably favours lactoferrin to complex electrostatically with the outside of the microgel particles (see Figure 5-6b). Even though the mole fraction of Na/Na+Ca in lactoferrin containing microgels was also greater than 0.6, somehow adsorption on to the microgel surface was still exhibited by lactoferrin. Possibly this was due to a steric hindrance effect, the adsorbed lactoferrin layer forming a barrier preventing the ion exchange of Ca^{2+} with Na^{+}. In contrast, in lysozyme the positively charged amino acids at the surface are evenly distributed (see Figure 5-7), so there is not the same high density of positive charge favouring

association at the surface rather than encapsulation in the bulk of the microgel particles.

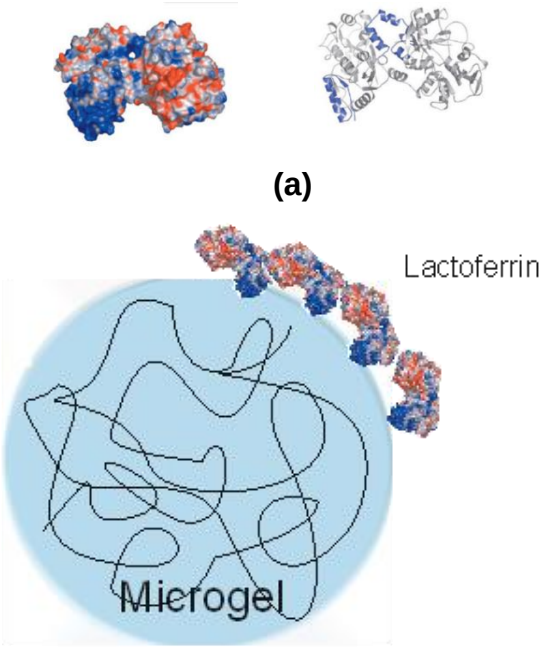

(a)

(b)

Figure 5-6. (a) Lactoferrin structure in 3D and ribbon diagram with the blue domain indicates the patches of positively charged amino acids mainly concentrated in N-terminus
(b) Schematic diagram of lactoferrin attachment to the surface of the microgel created a barrier for the lactoferrin to be incorporated inside the microgel due to unevenness distribution of charged surface patches.

(Figure after Baker & Baker, 2005)

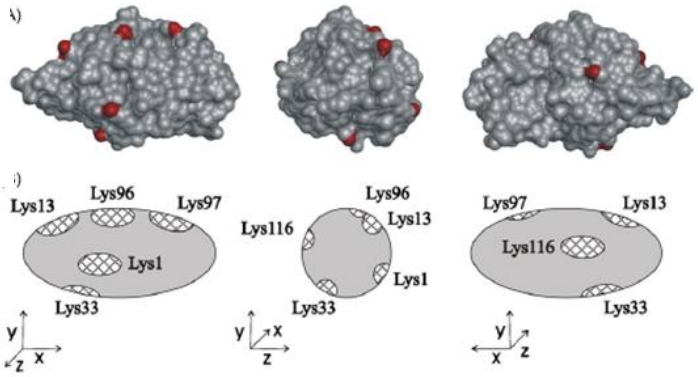

Figure 5-7. Schematic drawings of the location of lysine residues (N=6) on the lysozyme surfaces with three orientations in the x, y and z directions.

(Figure after Dismer & Hubbuch, 2007)

In summary, the larger size and more patchy distribution of positive charges on the lactoferrin may explain its greater apparent tendency to adsorb to the surface of the Ca-alginate microgel particles.

5.2.3 Calculation of mass ratio of lactoferrin covering the surface of a single particle of calcium alginate

The above considerations strongly point to lactoferrin adsorbing to the surface of the microgel particles and therefore it is worth calculating the minimum concentration of globular protein that would be needed to coat a single microgel particle with a certain size assuming no incorporation inside them occurs. This can be done from simple geometry assuming both the microgel particles and the protein molecules are hard spheres of known size. The assumption of sphericity is probably reasonable for lactoferrin (Nevinskii, Soboleva, Tuzikov, Buneva, & Nevinsky, 2009). According to Chen et al., 2014, lactoferrin has an inner diameter of 7-8 nm and outer diameter at 10-12 nm. The particle size distributions measured here for lactoferrin itself at pH 6 and 8 indicate a very slight shift to lower particle sizes as the pH decreased from 8 to 6, see Figure 5-8. The peaks in the distributions are 10 ± 2 nm, which is in a close agreement with the mentioned literature values, indicating no significant change in the state of aggregation of lactoferrin in this pH range.

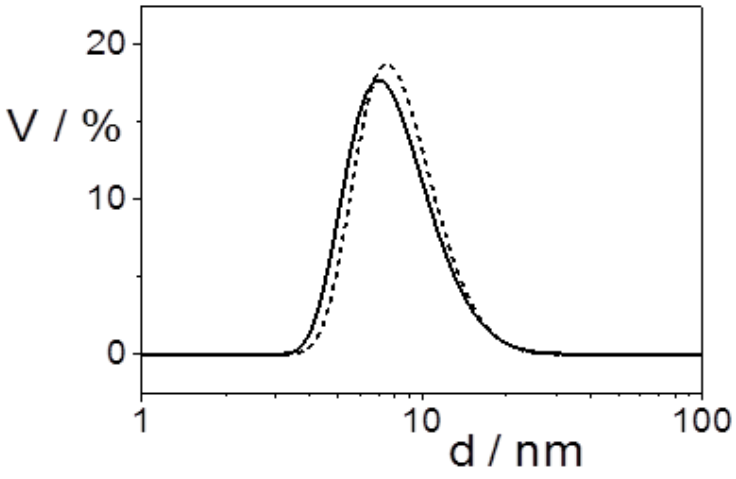

Figure 5-8 Particle size distribution of lactoferrin at concentration of 0.32 wt.% in bicarbonate buffer at pH 6 (solid line) and 8 (dashed line)

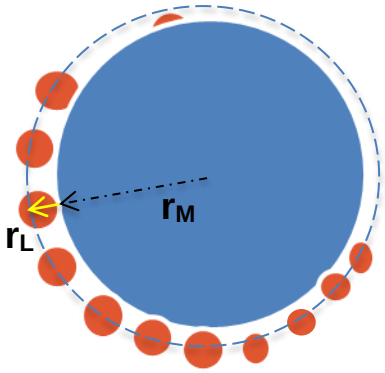

Figure 5-9. A schematic figure to illustrate the calculation of lactoferrin surface coverage

Assuming the radius of the microgel particles (r_M) varied from 50 nm to 250 nm and the radius of lactoferrin (r_L) at ~5 nm, the surface area of the microgel particle (A_m) and the cross section of the lactoferrin particles (A_L) can be calculated using the Eq.5-3 and Eq.5-4, respectively.

$$A_m = 4\pi(r_m + r_L)^2 \quad \textbf{5-3}$$

$$A_L = \pi {r_L}^2 \quad \textbf{5-4}$$

The number of lactoferrin particles (n) cover the surface area of a single microgel particle can be calculated via Eq.5-5.

$$n = \frac{A_m}{\pi r_L^2} \quad \textbf{5-5}$$

The conversion from the calculated n above to mass of lactoferrin (m) can be achieved via Eq.5-6, where N_A = Avogadro constant (6.022 x 10^{23} mol^{-1}), and M_w = molecular weight of lactoferrin.

$$m = \frac{n}{N} \text{ x } M_w \quad \textbf{5-6}$$

For the microgel particles, the volume (V) at varied radius (r_M) can be calculated via the following Eq.5-7.

$$V = \frac{4}{3}\,\pi\, r_M^3 \qquad \textbf{5-7}$$

The microgel volume (V) can be converted to mass using Eq.5-8, assuming a starting alginate concentration (C) of 1 wt.% and that all this alginate is converted into microgel particles with density (ρ) of ~1 g.cm^{-3}.

$$M = V\,x\,\rho\,x\,C \qquad \textbf{5-8}$$

Thus, the mass ratio between lactoferrin (m) and Ca-alginate microgel particles (M) is given by Eq.5-9

$$\frac{m}{M} = \frac{n\ x\ M_w}{N_A\ V\ \rho\ C} \qquad \textbf{5-9}$$

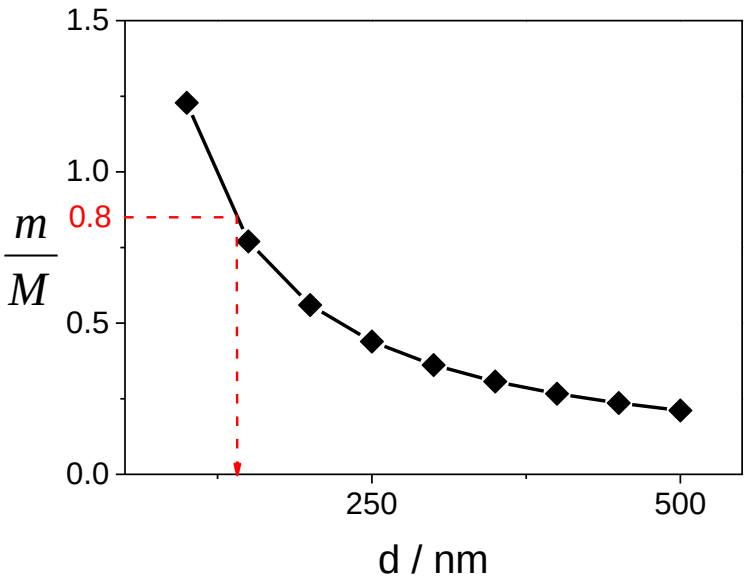

Figure 5-10. Theoretical mass ratio of lactoferrin to alginate (m/M) required to cover 10% of the surface of Ca-alginate microgel particles at different diameters (d).

Realistically, not all the surface can be completely covered by lactoferrin molecules, if it is assumed to be a hard sphere because there will always be gaps between the lactoferrin particles. Therefore, an additional assumption that has to be made is the maximum packing fraction of lactoferrin spheres on the surface of the microgel particles. This is again unknown, but as a first

assumption this was taken to be just 10% of the surface area of the gel particles, taking into account the fact that a complete charge reversal was not observed. shows the mass ratio of lactoferrin to calcium alginate particle ($\frac{m}{M}$) calculated using the equations above, plotted against the diameter of microgel particle (*d*) from 100 to 500 nm, assuming only 10% of the surface to be covered.

The trend in clearly illustrates that much higher ($\frac{m}{M}$) and therefore higher concentrations of lactoferrin than alginate would actually be required to limit the particle size below 100 nm, even if only 10% coverage was necessary to achieve stabilization. It is interesting that at the maximum concentration of lactoferrin used (0.8 wt.%, i.e., $\frac{m}{M}$ = 0.8) for 10% surface coverage corresponds to a microgel particle size of ca.150 nm, which, considering the simplicity of the model, is not so very far from the minimum of ca. 100 nm observed experimentally (see). These calculations also explain why the lactoferrin could only bring the ζ-potential a few mV more positive and not reverse the charge on the particle completely.

5.2.4 Encapsulation of water soluble dyes erioglaucine and methylene blue

There are some disagreements with the reported pK_a values of methylene blue from the literature findings, i.e., pK_a values varied widely from 0.4, 3.8, 4.4, 4.8, and 9.9 (Flury, Markus; Wai, 2003; Kallel et al., 2016; Sagara, Iizuka, & Niki, 1992; Sterner et al., 2016). Whilst, the pK_a values of erioglaucine (ER) were mostly reported as the pK_a values of Brilliant Blue which had similar chemical structure, i.e., 5.8 and 6.6 (Flury,& Wai, 2003; Germán-Heins & Flury, 2000; Ketelsen & Meyer-Windel, 1999). With such uncertainty, therefore the net charge of methylene blue and erioglaucine are calculated based on the pK_a values of the ionisable species in their chemical structures (Figure 5-11). Methylene Blue (MB) is a cationic dye with two dimethylamine groups and a phenothiazine with pK_a values of 10.73 and 2.52, respectively (Lide, 2010; Pobudkowska et al., 2016). Erioglaucine (ER) is a predominantly anionic dye with 3 (-ve) benzene sulfonate groups with pK_a of 0.7 (Gehring et al., 2014) and

2 (+ve) charges of ethylaniline groups with pK_a of 5.12 (Lide, 2010). The net charges of both dyes are plotted as a function of pH (Figure 5-12). At the pH used in subsequent encapsulation of these dyes, i.e., 6.8 ± 0.2, the net charges of ER were -3 and +1 for MB.

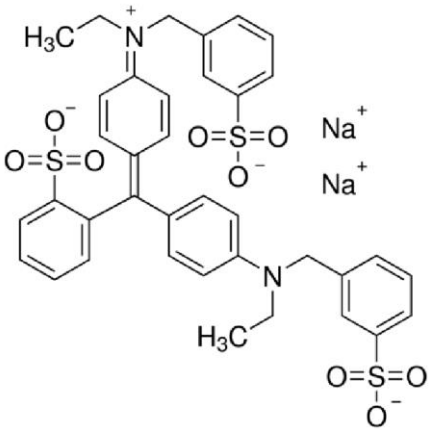

Erioglaucine disodium salt

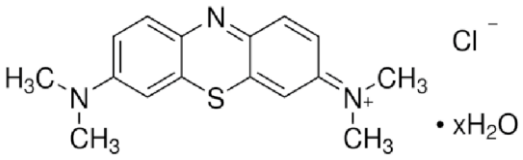

Methylene Blue

Figure 5-11. Chemical structures of water soluble dyes of erioglaucine and methylene blue

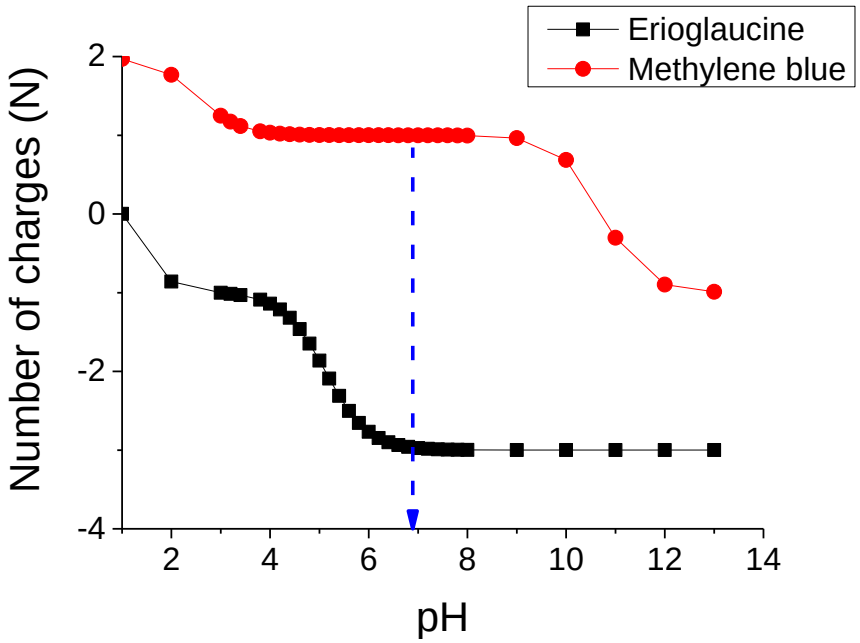

Figure 5-12. Total charges of erioglaucine and methylene blue as a function of pH. The dashed lines represent the elected pH in this study, i.e., 6.8 (blue).

5.2.4.1 The size of microgel particles containing dyes

Attempts to measure the particle sizes of the microgels containing dyes using the light scattering and confocal microscopy methods are fraught with many difficulties. In light scattering, obtaining the microgel particle size distribution was unsuccessful due to the ER absorption band at 630 nm interfering with the red light source of the He/Ne laser beam which excites at the same wavelength (632.8 nm). Moreover, the difference of the refractive indices between these microgel particles and the dispersed media of water was not large enough to obtain accurate measurements. Confocal measurements were employed to possibly locate the dyes and provide a rough estimate of the microgel particle size, but unfortunately ER and MB did not exhibit any fluorescence properties. There are some MB derivatives that are structurally modified as N-hydroxysuccimide-esters and maleimide derivatives to label amino groups (ATTO Gmbh, 2013), but these were not applicable to this polysaccharide-based microgel system.

Although size measurement here was difficult, we can assume their sizes based on previous findings. Previously, the particle mean diameter of alginate 1 wt.% and 10 mM Ca^{2+} could be as low as 100 nm (see Chapter 3), while the 2 wt.% alginate and 20 mM Ca^{2+} gave particles ≥ 3 μm (see Chapter 4). ImageJ analysis of micrographs of ER-containing microgels (Figure 5-13) confirmed similar results. The highest frequency of the particle size was in the size class < 0.4 um (average ~0.35 ± 0.03 um) for the microgels made with 1 %wt. alginate and 10 mM Ca^{2+}, while for microgels produced with 2 wt.% alginate and 20 mM Ca^{2+}, the highest frequency of particle size fell into the range between 1 - 2 μm with an average of 1.6 ± 0.28 μm. Hereafter, microgels made from 1 wt.% alginate + 10 mM Ca^{2+} and 2 wt.% alginate + 20 mM Ca^{2+} are labelled as Ca-ALG+dye (S) and Ca-ALG+dye (L), respectively, in which S and L stand for small and large with the encapsulated dyes of ER and MB.

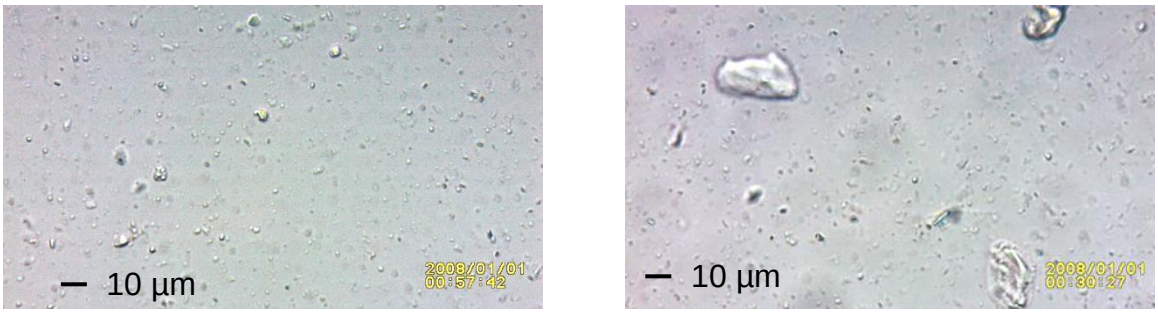

(a) (b)

Figure 5-13. Micrographs of erioglaucine encapsulated in Ca-alginate microgels produced via the jet homogenizer prepared from (a) 2 wt.% alginate+10ppm dye and 10 mM Ca^{2+} and (b) with 1 wt.% alginate+10 ppm dye and 20 mM Ca^{2+}, using 20x magnification lens.

5.2.4.2 Comparison of encapsulation of erioglaucine and methylene blue

The ER and MB were separated from the aqueous phase via magnetic field as for the water-insoluble encapsulation (see method in Chapter 2.2.2.5). The dye concentrations were determined from the absorbance values at 630 nm and 665 nm for λ_{max} of ER and MB, respectively, measured via UV-spectrophotometry. Figure 5-14 compares the concentration of dyes inside the microgels vs. outside the microgels in the aqueous phase, after particle formation. The expected concentration of the dye inside the microgel and outside (aqueous phase) upon mixing the alginate with Ca^{2+} in the jet homogenizer using D 80:20 block is 8 ppm. The ER concentrations in Ca+ALG+ER (S) were not significantly different, i.e., 8.1 ± 0.6 ppm inside vs. 8.6 ± 0.3 ppm outside, as might be expected. However, in Ca-ALG+ER (L), significantly lower [ER] was found in the microgels versus in the aqueous phase, i.e., 6.8 ± 0.7 ppm inside vs. 8.2 ± 0.6 ppm outside, with $p < 0.05$. These results suggested that larger particle sizes in Ca-ALG+ER (L) provided less specific surface area for the dye to be adsorbed on or into the microgel, thus less ER was retained in the microgel and more ER remained in aqueous phase.

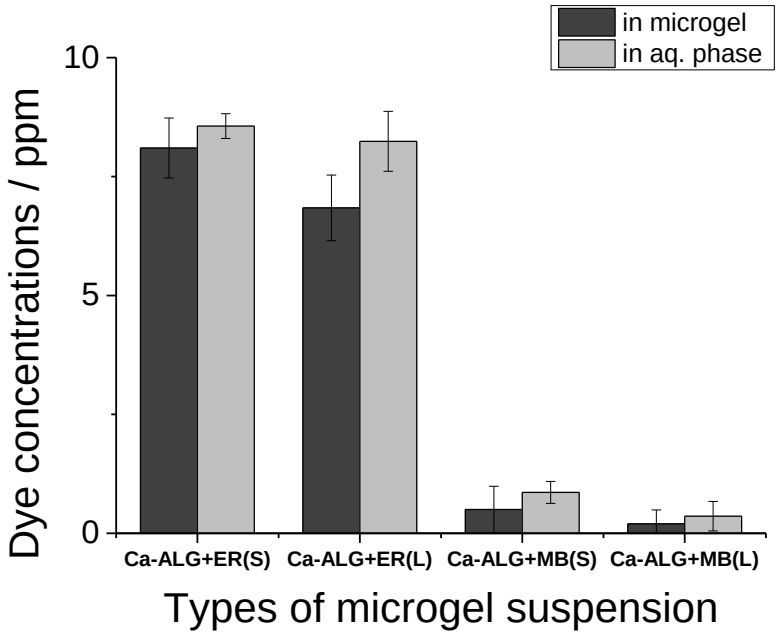

Figure 5-14. Concentrations of erioglaucine (ER) and methylene Blue (MB) in the microgel vs. in the aqueous phase

As a cationic dye, MB is expected to be adsorbed better to the anionic alginate, however Figure 5-14 shows the MB concentrations are low for both inside and outside (in aqueous phase) of Ca-ALG+MB(S) and (L) microgels, i.e., < 0.5 ppm, respectively. Such marginal MB concentration inside the microgels indicates inefficiency of the MB entrapment in the microgel. The ζ-potential values of the corresponding particles, shown in Table 5.3 also reveal no significant differences between Ca-ALG Blank(S) and Ca-ALG+MB(S), i.e., -54.5 vs. -56.6 mV, which indicate a minimal MB adsorption on the surface of the microgel particles. As a comparison, the ζ-potential of Ca-ALG+ER(S) was more negative in magnitude as compared to Ca+ALG Blank(S), i.e., -64.4 ± 10.8 vs. - 54.5 ± 3.6 mV, respectively, which signified ER adsorption onto the microgel surface. The MB concentrations in Ca-ALG+MB(S) and (L) outside (in aqueous phase) are also low, i.e., < 1 ppm for both, which is possibly attributed to the complex formation from cationic MB with the anionic alginate or MB dimerization that leads to precipitation during the microgel formation. The details about this precipitation formation will be discussed in section 5.2.4.3.

Table 5.3. Zeta potentials of the microgel particles with and without the water soluble dyes encapsulated

Type of microgels	ζ-potentials (mV)
Ca-ALG-Blank (S)	-54.5 ± 3.6
Ca-ALG+ER (S)	-64.4 ± 10.8
Ca-ALG+MB (S)	-56.6 ± 4.2

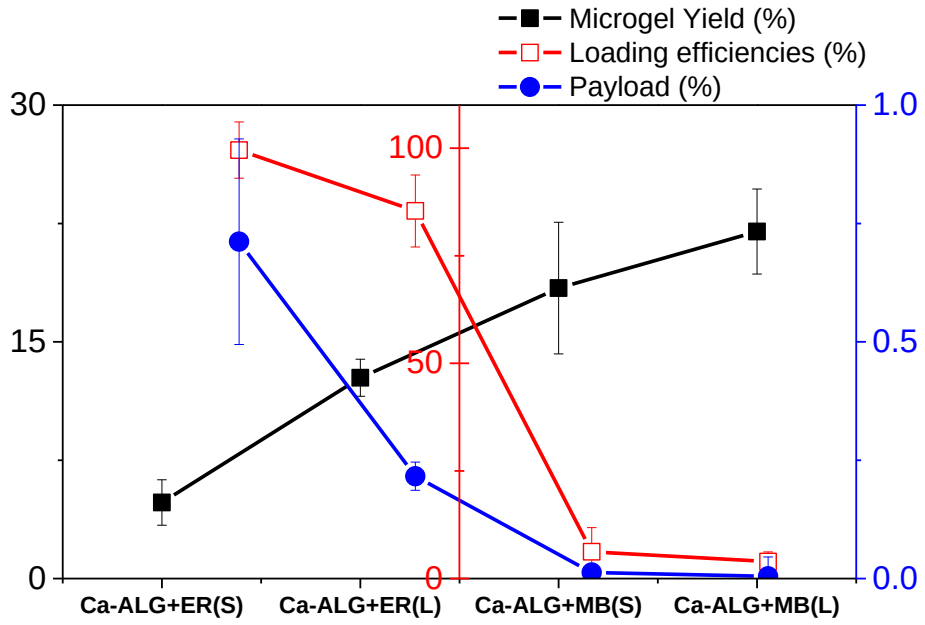

Figure 5-15. Microgel yield, loading efficiencies, and payloads of erioglaucine (ER) and methylene blue (MB) encapsulated in the ca-alginate microgels

The microgel yield, loading efficiencies, and payload were measured and calculated based on the equations outlined in previous chapter (Chapter. 4, Eq. 4-5, 4-6, 4-7). As depicted from the , the microgel yields of Ca+ALG+ER (S) and (L), i.e., 4.8 ± 1.4 % and 12.7 ± 1.2 %, were much lower than Ca+ALG+MB (S) and (L), 18.4 ± 6.2 % and 22 ± 3.9 %. Higher microgel yield in larger microgels of Ca+ALG+ER (L) and Ca+ALG+MB (L) were due to higher [alginate] as the starting material.

With the known initial dye concentration placed in the jet homogenizer (8 ppm expected concentration in microgel particles), the calculated loading efficiencies were 99.5 ± 6.5 % and 85.4 ± 8.3 %, and the payloads were 0.71 ± 0.22 % and 0.22 ± 0.03 %, in Ca-ALG+ER (S) and (L), respectively. Significantly higher loading efficiencies and payloads were obtained with Ca-ALG+ER (S) compared to Ca-ALG+ER (L) ($p < 0.05$) i.e., the smaller particles retained more of the dyes during the encapsulation. The loading efficiencies and payloads of ER in the microgels were quite high, especially when compared against water insoluble encapsulated microgels (in Chapter 4, section 4.2.8 and 4.2.9), which was up to 50 % more than with the water insoluble compounds. Owing to its high water solubility (i.e., 200 $mg.ml^{-1}$ as reported by Jank et al.,1998), ER is miscible in alginate solution, thus it is easily entrapped during Ca^{2+} bridging formation. Despite high water solubility of MB (i.e., 35 $mg.ml^{-1}$, as reported by Chen et al., 2008), the loading efficiencies (< 6 %) and payloads (± 0.01 %) were low in Ca-ALG+MB (S) and (L) possibly due to MB precipitation and low initial dye concentration.

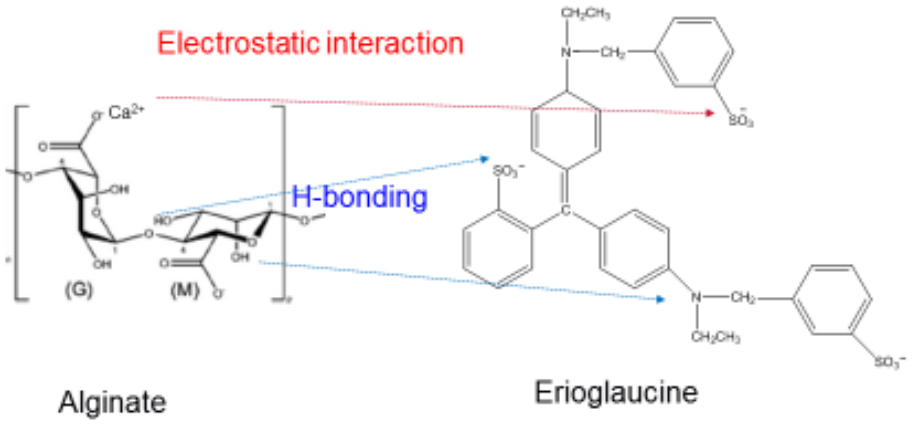

Figure 5-16. Possible interactions of Erioglaucine with alginate

It is seen that despite ER being an anionic dye, high loading efficiencies and payloads can be achieved, probably via binding with alginate and Ca^{2+}. At pH 6.8, the amine groups from the ethylaniline in ER have almost zero charge (+0.04), thus the net charge of ER (-3) was dominated mainly by the negatively charged sulfonate groups. illustrates some possible routes for the sorption of the ER to the microgel surface which could be promoted through ionic

crosslinking with Ca^{2+} and H-bonding at the sites where N and O atoms are located in ER (Liu et al., 2008).

Figure 5-17 shows the percentage release of these water soluble dyes encapsulated microgels during the dye extraction using Millipore water. Within 30 minutes, the ER was completely released up to 100 ± 4 % and 85 ± 5 % for Ca+ALG+ER (S) and (L), respectively. There was no further additional release of ER after 24 h and 48 h, indicated that within 30 minutes almost a complete release was achieved from the microgel particles. Although ER had high loading efficiencies and payloads, it was released rapidly on placing the particles in water, thus certainly due to the porous structure of the microgels.

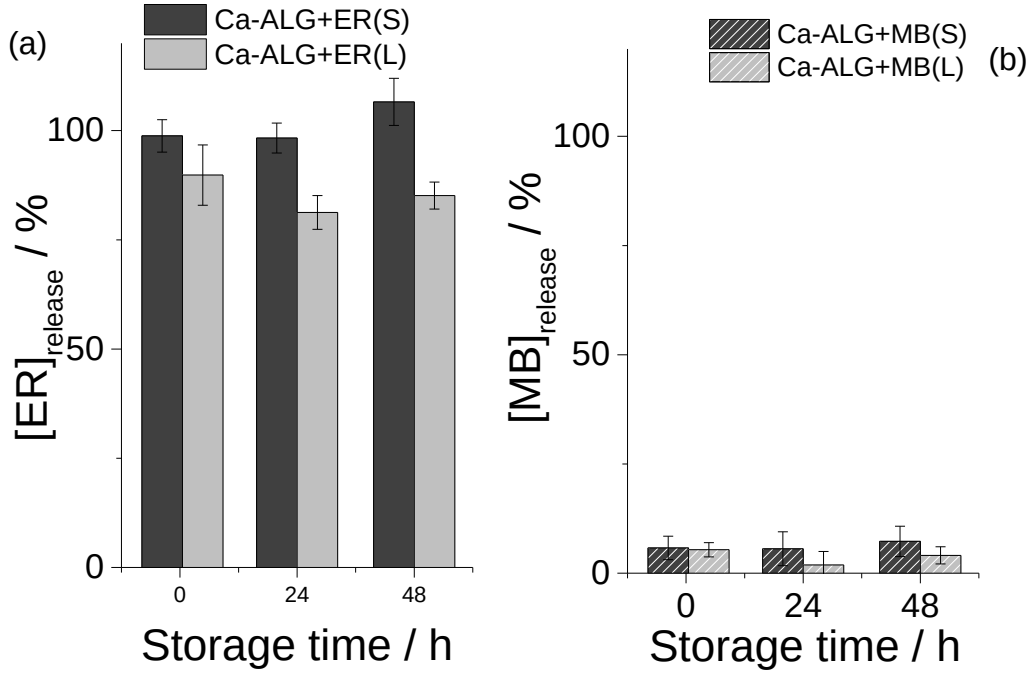

Figure 5-17. Percentage release of Erioglaucine/ER (a) and Methylene Blue/MB (b) from the Ca-alginate microgel particles prepared from 1 wt.% alginate and 10 mM Ca^{2+} for (S) and 2 wt.% alginate and 20 mM Ca^{2+} for (L) as a function of time during dye extraction

In MB containing microgels, low amounts of MB were released during the extraction in water over 30 minutes, i.e., < 5 %, which was possibly attributed to the precipitation formed during the microgel preparation. Tu et al. (2005) encapsulated MB in alginate microparticles (sizes 0.1–0.4 mm) made with 5 wt.% alginate and 1 M Ca^{2+} via a spray-coagulation method. They

observed a fast release of MB in simulated GI fluid. Within 5 minutes, 100 % release of MB was achieved in simulated GI fluid as compared to only 30 % of water insoluble 4-phenylazoanililine (PAA). However, the presence of salt and low pH in the simulated GI fluid would be expected to enhance dissolution.

5.2.4.3 Precipitation during Ca-ALG+MB production

Precipitation was visually detected during MB incorporation into the microgels. This precipitate could also be responsible for the large variability in the measurements, as indicated by large error bars in Ca+ALG+MB (S) and (L) (Figure 5-14 and Figure 5-17). The formation of the precipitate was postulated as due to the positive charge of the dimethylamine groups in MB side chains were instantly cross-linking with the COO^- groups in alginate chain. This strong electrostatic attraction between the two groups may lead to competition with Ca^{2+} for cross-linking with the alginate.

To confirm a strong interaction between MB and alginate, we therefore determined the mole charge ratios between these two compounds. At the pH used, i.e., 6.8 ± 0.2, each monomer of alginate would have a charge of -1, whilst the total charge of MB should be +1 at that pH (Figure 5-12). The [alginate] and [MB] used were 1 wt.% and 10 ppm, respectively, with M_w of 194.14 g.mole^{-1} for guluronic/mannuronic acid and 319.85 g.mole^{-1} for MB. From Eq. 5-2, the mole charges ratio between alginate and MB was 1648:1. Such a high ratio indicates that the MB would be unlikely to significantly interfere with gelation of the alginate via Ca^{2+}. (For completeness, the mole charge ratio between alginate and 10 mM Ca^{2+} is only 1.3:1). Therefore, one would expect MB to be encapsulated within the nascent microgel particles, but somehow it competes with Ca^{2+} cross-linking and it results in its precipitation.

According to Lipatova, Makarova, & Mezina (2016), the non-covalent complex formation of MB with alginate can be initiated as low as 1.15 x 10^{-5} M of [MB] and is stable in the pH range between 5.5 to 9. In the current study, 10 ppm of MB equals 3.12 x 10^{-5} M which is above the concentration limit for this complex formation and the pH is at 6.8 which is within the pH range mentioned above. They also discovered that a complete dye binding was achieved at 2:1 mole ratio of alginate to MB, which fitted into the concept of ‘neighbour

exclusion' binding, where 1 dye molecule binds with two base pairs. In our system, the mole ratio between alginate:MB was at 2.1:1 (based on 150 kDa molar mass of alginate) for 1 wt.% alginate or double this for 2 wt.% alginate. Considering the above, mixing of MB into the alginate phase before placing in the jet homogenizer is a mistake since it would serve as a precursor step of complex formation between MB and alginate. With hindsight therefore, the method of addition of any cationic species should be changed to avoid mixing them with the anionic polymer prior to particle formation.

Homem-De-Mello et al. (2007) have also shown MB is prone to form a dimer, either in "sandwich" or "head to tail" geometry (Figure 5-18), with higher dimer to monomer ratio as the dye concentration is increased from 10 to 60 μM in aqueous solution (Florence & Naorem, 2014). The [MB] used in our study was 10 ppm (~31 μM) which is therefore within the concentration range of this dimerization. The dimerization equilibrium is illustrated in Figure 5-19 with dimerization constant (K_D) of 2.38 x 10^3 at 30^{o}C in water. Florence and Naorem (2014) found K_D to be higher in water compared to in mixed organic solvents of lower dielectric constant. For example K_D = 1.1 x 10^3 in ethylene glycol. The normally high dielectric constant of water resulted in a decrease of intermolecular repulsion between the same charged species of the MB (Yazdani et al., 2012). The high K_D of MB in water might give rise to MB dimers prior to mixing into alginate in our system, leading to aggregate formation. Such precipitation would not have been observable due to the intense blue colour of the solutions. Lipatova et al. (2016) also discovered that there was a hypochromic shift of MB λ_{max} as it changed from monomeric to dimeric and aggregated form of MB-alginate, i.e., λ_{max} was shifted from 664 (monomeric) to 612 nm (dimer form) and 565 nm (ionic complex of MB and alginate). This blue shift was possibly responsible for lower [MB] measured at λ used in this study, i.e., 665 nm, which could affect the apparent microgel yields, loading efficiencies, and payloads of Ca+ALG+MB (S) and (L).

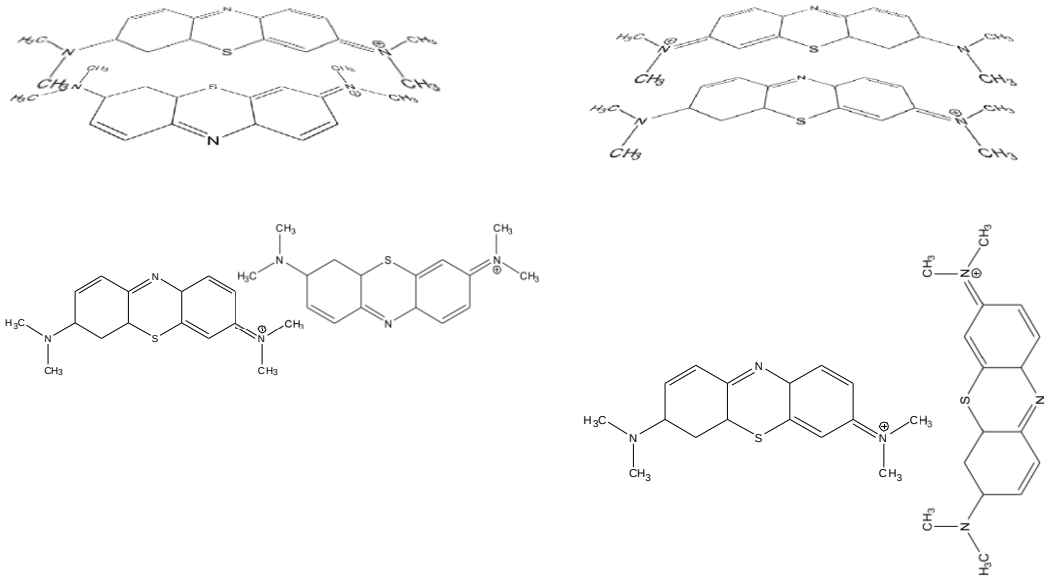

Figure 5-18. Four possible resonances of MB dimers, with a, b, ('sandwich') and c, d ('head to tail').

(Figure from Homem-De-Mello et al., 2007)

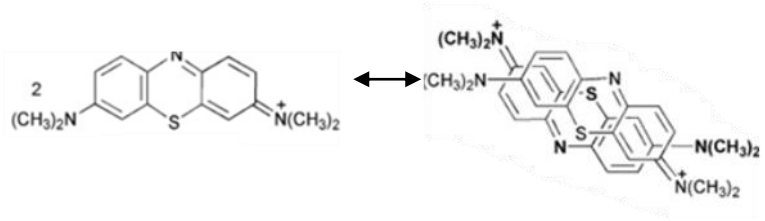

Figure 5-19. Dimerization equilibrium of $2MB_{monomer} \leftrightarrow MB_{dimer}$

(Figure from Yazdani et al., 2012)

5.3 Conclusions

Some control over the microgel particle size and ζ-potential can be exerted during microgel particle formation by including the oppositely charged globular protein of lactoferrin, but not lysozyme. Many factors possibly contributed to unsuccessful lysozyme adsorption onto the microgel particle surface, such as strong complex formation between lysozyme and alginate and Ca^{2+}, high Na^{+} content of the buffer, the relative small protein molecular size and evenness of positive surface charge. In contrast, there was good evidence for lactoferrin adsorption, probably due to its larger size and concentration of the positive charge into patches on the surface of the globular protein structure.

These effects with proteins seem to apply to some extent with water soluble dyes. Whilst one might expect a positively charged dye (MB) to be more easily trapped in the negatively charged microgel particles as they are formed, in fact a negatively charged dye (ER) seemed to be more easily encapsulated. This was probably because the negatively charged dyes might be more readily cross-linked into the microgel network via Ca^{2+} and/or H-bonding. The positively charged dyes can electrostatically complex with alginate too strongly and this inhibits their incorporation into microgel particles. The particle size of the microgel also plays a key role in entrapping higher [ER] inside the microgel owing to the greater surface area of smaller-sized particles. ER encapsulated microgels displayed a high loading efficiency and payload, but the ER was also released rapidly due to high porosity of the microgels formed.

In summary, a deep understanding of the molecular interactions between microgel components and the size, net charge and surface charge distribution of the materials being encapsulated is needed to allow successful encapsulation of water soluble compounds via the Leeds Jet Homogenizer method.

Chapter 6 Conclusions and Future Works

This chapter summarises the main findings described in previous chapters. All the experiments in this study have been performed to gain a better understanding of (1) some factors or parameters that govern microgel particle formation (2) the rheological properties of the microgel suspensions (3) the microgel particle yield, payload, and loading efficiency from the encapsulation (4) factors that affect the entrapment of water-soluble and water-insoluble compounds.

6.1 Factors that govern the microgel particle formation

Microgel particles formed via this method are tuneable in size with the following considerations:

a. The Leeds Jet Homogenizer (LJH) was capable of producing the microgel particles via flash precipitation method in conditions of highly turbulent mixing flow (Re > 10^4), high shear rate (10^6 s^{-1}), and high fluid velocity (nearly 100 $m.s^{-1}$). This method can be applied to form microgel particles from alginate or any Ca^{2+} sensitive biopolymers (such as κ-carrageenan and low methoxy pectin).
b. The Damkohler number (Da) plays a key role in determining the particle size. Thus, increasing the concentration of alginate and reducing the fluid velocity have generated larger particles because it increases the D_a.
c. Ca-alginate prepared from alginate high viscosity (HV) exhibited a larger particle size compared to low viscosity (LV) due to a longer chain of guluronate units (G) rather than any specific effect of the viscosity.
d. Increasing Ca^{2+} concentration from 2 mM to 10 mM mixed with 1 wt.% alginate does not have an impact on the particle sizes.
e. The microgel swelling and de-swelling phenomenon is certainly affected by the pH, where smaller particle sizes form at lower pH, except for tiliroside-containing microgels due to the presence of aggregates at low pH.

f. The particle size of the entrapped water-insoluble compounds also conformed to the final microgel particle sizes, i.e., the smaller the crystals, the smaller the final size of the microgel particles.

6.2 Rheological properties of Ca-alginate microgel suspensions

Some rheological properties that can be extracted from the findings are:

a. The estimated intrinsic viscosity ($[\eta]$) and M_w of the elected alginate low viscosity (LV) were 13.2 g.ml^{-1} and 168 kDa, respectively.
b. The apparent viscosity (η) of the microgel suspension was shear thinning up to $\gamma < 1$ s^{-1}, and then it reached a plateau η of Newtonian-like viscosity at $\gamma > 1$ s^{-1} at $\varphi \leq 0.044$, which followed the viscosity behaviour of the aqueous phase at low φ.
c. At higher φ ($\varphi \geq 0.065$), the microgel concentrate behaved more solid-like due to tighter packing of the microgel particles.

6.3 Microgel particle yield, payload, loading efficiencies from encapsulation.

The microgel particles were separated either via centrifugation or addition of magnetic nanoparticles (MNPs) to quantify the yield, payload, and loading efficiencies. The key drawbacks from the encapsulation study are the following:

a. Microgel particle yields prepared from 1 wt.% alginate and 10 mM were less than 5 % which was low. Nevertheless, it can be improved by introducing some nucleation agents, such as the water-insoluble compounds. The addition of water-insoluble crystals boosted the yield up to 10 % to 30 %.
b. The payloads of the water-insoluble compounds in the microgel particles were low (< 1.2 %) because their initial concentrations used were only 0.5 mM for polyphenols and 18.5 mM for β-carotene. However, despite the low payloads, the loading efficiencies were high, i.e., between 21 % to 58 %.

c. The payload and loading efficiencies of microgel particles containing water-soluble dyes were high but the dyes were released rapidly due to high porosity of the microgel particles.

6.4 Factors that affect the entrapment of encapsulated compounds onto or into the Ca-alginate microgel particles

Not all cationic compounds are expected to be entrapped onto or into the Ca-alginate microgel particles. For example, no adsorptions or entrapments were exerted by the cationic lysozyme and MB in the microgel particles because strong complexations between these compounds and the alginate were formed. Some factors that govern the encapsulation mechanism are postulated below:

a. The charge distribution on the surface of the encapsulated compounds whether they are in patches or not would determine their encapsulation fate. For example, the presence of patches on the surface charge of lactoferrin promoted the protein to be likely adsorbed on the surface of microgel.
b. The particle sizes of the encapsulated compounds also determine the locations or binding sites whether they are likely to be inside or outside of the microgel particles. The smaller size particles tended to be distributed internally while bigger particles are more likely to be at the surface of the microgel particles. The smaller particle size of the encapsulated compound also exhibited a greater payload.
c. The charge density of the encapsulated compounds also plays a part in determining their chances to be entrapped. The higher the charge density, the more binding sites were available to bind with the alginate, thus higher loading efficiencies were observed.

6.5 Future work

Possibilities for further exploration which may be beneficial to enhance the delivery system of Ca-alginate microgel particles and to maximize the potential capability of LJH for commercialization or scale-up purposes include:

- It is a challenge to control the release of water-soluble compounds encapsulated in highly porous microgels: thus some surface modification needs to be applied onto the microgel particles. Erioglaucine is easily trapped but also easily released, while lactoferrin has shown a capability to coat the surface of the microgel particles. It will be interesting to combine these two features as a model system to further enhance the delivery system of high water solubility compounds.
- The highest throughput of microfluidic device as developed by the Weitz group can produce 5.2 kg of microgel suspension per day with flow rate of 215 $ml.h^{-1}$ (Romanowsky et al., 2012). The throughput of the jet homogenizer can be much higher because the flow rate is about 15 $ml.s^{-1}$ or 55.5 $l.h^{-1}$, thus its potential for a scale up in production in a continuous system can be further exploited. Future work could involve a mathematical modelling by taking into account many factors such as the polymer concentration, pressure, Da, and fluid velocity. Although aggregation can be an issue in scaling up as pointed out by Gavi, Marchisio, & Barresi (2007) and Marchisio, Rivautella, & Barresi (2006), but perhaps an extra step of sonication after the particle formation can be implemented.
- Producing the microgel via the LJH is considered as a sustainable processing because of the low-energy consumption required for the operation. If recycling processes are included in the system, they can add an extra value to fulfil the sustainability criteria. The excess of Ca^{2+} or free alginate perhaps can be recycled back to generate more microgel particles. Although it may seem complicated, further work is needed to acquire information, such as the remaining concentrations of G and Ca^{2+} in the excess solution.
- Despite the advancement of nano- or microgel developments, there is also a progressive concern of nanotoxicity. Martirosyan & Schneider (2014) have highlighted some of the hazards or risks associated with the nanotechnology-derived foods, which can be a long-term pursuit for future research.

REFERENCES

Acosta, E. (2009). Bioavailability of nanoparticles in nutrient and nutraceutical delivery. *Current Opinion in Colloid & Interface Science*, *14*(1), 3–15.

Agulhon, P., Robitzer, M., & David, L. (2012). Structural Regime Identification in Ionotropic Alginate Gels: Influence of the Cation Nature and Alginate Structure. *Biomacromolecules*, *13*(1), 215–220.

Akkineni, A.R., Ahlfeld, T., Funk, A., Waske, A., & Lode, A. (2016). Highly Concentrated Alginate-Gellan Gum Composites for 3D Plotting of Complex Tissue. *Polymers*, *8*(5), 1–16.

Amara, C. Ben, Eghbal, N., Oulahal, N., Degraeve, P., & Gharsallaoui, A. (2016). Properties of lysozyme/sodium alginate complexes for the development of antimicrobial films. *Food Research International*, *89*, 272–280.

Amici, E., Tetradis-Meris, G., Pulido de Torres, C., & Jousse, F. (2008). Alginate gelation in microfluidic channels. *Food Hydrocolloids*, *22*(1), 97–104.

Anal, A.K., Bhopatkar, D., Tokura, S., Tamura, H., & Stevens, W.F. (2003). Chitosan-alginate multilayer beads for gastric passage and controlled intestinal release of protein. *Drug Development and Industrial Pharmacy*, *29*(6), 713–24.

Anal, A.K., & Singh, H. (2007). Recent advances in microencapsulation of probiotics for industrial applications and targeted delivery. *Trends in Food Science & Technology*, *18*(5), 240–251.

Astete, C.E., Sabliov, C.M., Watanabe, F., & Alexandru, B. (2009). Ca^{2+} Cross-linked alginic acid nanoparticles for solubilization of lipophilic natural colorants. *Journal of Agricultural and Food Chemistry*, *57*(16), 7505–7512.

ATTO Gmbh. (2013). Fluorescent Labels and Dyes. *Fluorescent Labels and Dyes: Catalogue*, *49*(0), 1–45.

Augst, A.D., Kong, H.J., & Mooney, D.J. (2006). Alginate hydrogels as biomaterials. *Macromolecular Bioscience*, *6*(8), 623–33.

Baker, E.N., & Baker, H.M. (2005). Molecular structure, binding properties and dynamics of lactoferrin. *Cellular and Molecular Life Sciences*, *62*(22), 2531–2539.

Barakat, M.F., El-Salamawy, K., El-Banna, M., Abdel-Hamid, M., & Abdel-Rehim Taha, A. (2001). Radiation effects on some dyes in non-aqueous solvents and in some polymeric films. *Radiation Physics and Chemistry*, *61*(2), 129–136.

Behbahani, E.S., Ghaedi, M., Abbaspour, M., & Rostamizadeh, K. (2017). Optimization and characterization of ultrasound assisted preparation of curcumin-loaded solid lipid nanoparticles: Application of central composite design, thermal analysis and X-ray diffraction techniques. *Ultrasonics Sonochemistry*, *38*, 271–280.

Ben, Y., Robb, I., Tonmukayakul, P., & Wang, Q. (2011). Microgels for Oil Delivery. In A. Fernandez-Nieves, H.M. Wyss, J. Mattsson, & D.A. Weitz (Eds.), *Microgel suspensions: fundamentals and applications* (pp. 407–422). Weinheim, Germany.

Bengoechea, C., Peinado, I., & McClements, D. J. (2011). Formation of protein nanoparticles by controlled heat treatment of lactoferrin: Factors affecting particle characteristics. *Food Hydrocolloids*, *25*(5), 1354–1360.

Bentley, P. J. (2013). *Preparation of Alginate Microparticles and Explanation of their Novel Functionality*. University of Leeds, Leeds, UK.

Berg, J. (2010). *An Introduction to Interfaces and Colloids: The Bridge to Nanoscience*. Singapore: World Scientific Publishing Co. Pte. Ltd.

Bokkhim, H., Bansal, N., Grøndahl, L., & Bhandari, B. (2016). Characterization of alginate–lactoferrin beads prepared by extrusion gelation method. *Food Hydrocolloids*, 53, 270-276.

Bokkhim, H., Bansal, N., Grøndahl, L., & Bhandari, B. (2015). Interactions between different forms of bovine lactoferrin and sodium alginate affect the properties of their mixtures. *Food Hydrocolloids*, *48*, 38–46.

Bordenave, N., Hamaker, B.R., & Ferruzzi, M.G. (2014). Nature and consequences of non-covalent interactions between flavonoids and macronutrients in foods. *Food and Function*, *5*, 18–34.

Braccini, I., & Pérez, S. (2001). Molecular basis of Ca^{2+}-induced gelation in

alginates and pectins: the egg-box model revisited. *Biomacromolecules*, *2*(4), 1089–96.

Braun, D.B. ., & Rosen, M.R. (2000). *Rheology Modifiers Handbook - Practical Use and Application*. William Andrew Publishing, Norwich, NY, USA.

Brun-Graeppi, A.K.A.S., Richard, C., Bessodes, M., Scherman, D., & Merten, O.-W. (2011). Cell microcarriers and microcapsules of stimuli-responsive polymers. *Journal of Controlled Release*, *149*(3), 209–24.

Burey, P., Bhandari, B.R., Howes, T., & Gidley, M.J. (2008). Hydrocolloid Gel Particles : Formation , Characterization , and Application. *Critical Reviews in Food Science and Nutrition*, *48*(5), 361–377.

Burgaud, I., Dickinson, E., & Nelson, P.V. (1990). An improved high-pressure homogenizer for making fine emulsions on a small scale. *International Journal of Food Science and Technology*, *25*, 39–46.

Bysell, H., & Malmsten, M. (2006). Visualizing the interaction between poly-L-lysine and poly(acrylic acid) microgels using microscopy techniques: Effect of electrostatics and peptide size. *Langmuir*, *22*(12), 5476–5484.

Caballero, F., Foradada, M., Miñarro, M., Pérez-Lozano, P., García-Montoya, E., Ticó, J.R., & Suñé-Negre, J.M. (2014). Characterization of alginate beads loaded with ibuprofen lysine salt and optimization of the preparation method. *International Journal of Pharmaceutics*, *460*(1-2), 181–8.

Cao-Hoang, L., Fougère, R., & Waché, Y. (2011). Increase in stability and change in supramolecular structure of β-carotene through encapsulation into polylactic acid nanoparticles. *Food Chemistry*, *124*(1), 42–49.

Carneiro-Da-Cunha, M.G., Cerqueira, M. A., Souza, B.W.S., Teixeira, J.A., & Vicente, A.A. (2011). Influence of concentration, ionic strength and pH on zeta potential and mean hydrodynamic diameter of edible polysaccharide solutions envisaged for multinanolayered films production. *Carbohydrate Polymers*, *85*(3), 522–528.

Casanova, H., & Higuita, L.P. (2011). Synthesis of calcium carbonate nanoparticles by reactive precipitation using a high pressure jet homogenizer. *Chemical Engineering Journal*, *175*, 569–578.

Cassin, G., Appelqvist, I., Normand, V., & Norton, I.T. (2000). Stress-induced compaction of concentrated dispersions of gel particles. *Colloid and*

Polymer Science, *278*(8), 777–782.

Cavalieri, F., Micheli, L., Zhou, M., Tortora, M., Palleschi, G., & Ashokkumar, M. (2013). Electrochemical investigation of the interaction between lysozyme-shelled microbubbles and vitamin C. *Analytical and Bioanalytical Chemistry*, *405*(16), 5531–5538.

Cegnar, M., & Ker, J. (2010). Self-assembled Polyelectrolyte Nanocomplexes of Alginate , Chitosan and Ovalbumin. *Acta Chim. Slov.*, *57*, 431–441.

Chandrasekar, V., Coupland, J.N., & Anantheswaran, R.C. (2017). Characterization of nisin containing chitosan-alginate microparticles. *Food Hydrocolloids*, *69*, 301–307.

Chen, J.P., & Lin, Y.S. (2007). Decolorization of azo dye by immobilized Pseudomonas luteola entrapped in alginate-silicate sol-gel beads. *Process Biochemistry*, *42*(6), 934–942.

Chen, L., Bai, G., Yang, R., Zang, J., Zhou, T., & Zhao, G. (2014). Encapsulation of β-carotene within ferritin nanocages greatly increases its water-solubility and thermal stability. *Food Chemistry*, *149*, 307–12.

Chen, L., Remondetto, G., Rouabhia, M., & Subirade, M. (2008). Kinetics of the breakdown of cross-linked soy protein films for drug delivery. *Biomaterials*, *29*(27), 3750–3756.

Ching, S.H., Bansal, N., & Bhandari, B. (2016). Rheology of emulsion-filled alginate microgel suspensions. *Food Res*, *80*, 50–60.

Clementi, F., Mancini, M., & Moresi, M. (1998). Rheology of alginate from Azotobacter vinelandii in aqueous dispersions. *Journal of Food Engineering*, *36*(1), 51–62.

Coronel-Aguilera, C.P., & San Martín-González, M.F. (2015). Encapsulation of spray dried β-carotene emulsion by fluidized bed coating technology. *LWT - Food Science and Technology*, *62*(1), 187–193.

Damodaran, S. (1996). Amino acids, peptides, and proteins. In O. R. Fennema (Ed.), *Food Chemistry* (3rd ed., p. 328). New York: Marcel Dekker, Inc.

Das, R.K., Kasoju, N., & Bora, U. (2010). Encapsulation of curcumin in alginate-chitosan-pluronic composite nanoparticles for delivery to cancer cells. *Nanomedicine : Nanotechnology, Biology, and Medicine*, *6*(1), 153–60.

Davies, J.L. (1963). The fading effect in methylene blue staining of wool fiber sections. *Textile Research Journal*, *33*, 400–402.

Davis, S. (2005). Electron Microscopy. In T. Cosgrove (Ed.), *Colloid Science: Principle, Methods, and applications* (pp. 265–282). Oxford, UK: Blackwell Publishing.

de Folter, J.W.J., & van Ruijven, Marjolein W.M.; and Velikov, K.P. (2012). Oil-in-water Pickering emulsions stabilized by colloidal particles from the water-insoluble protein zein. *Soft Matter*, *8*(25), 6807-15.

Del Rio, D., Rodriguez-Mateos, A., Spencer, J. P. E., Tognolini, M., Borges, G., & Crozier, A. (2013). Dietary (Poly)phenolics in Human Health: Structures, Bioavailability, and Evidence of Protective Effects Against Chronic Diseases. *Antioxidants & Redox Signaling*, *18*(14), 1818–92.

Destribats, M., Rouvet, M., Gehin-Delval, C., Schmitt, C., & Binks, B.P. (2014). Emulsions stabilised by whey protein microgel particles: towards food-grade Pickering emulsions. *Soft Matter*, *10*(36), 6941–54.

Dickinson, E. (2015). Microgels — an alternative colloidal ingredient for stabilization of food emulsions. *Trends in Food Science & Technology*, *43*(2), 178–188.

Dirksen, J.A., & Ring, T. A. (1991). Fundamentals of Crystallization: Kinetic Effects on Particle Size Distributions and Morphology. *Chem. Eng. Sci.*, *46*(10), 2389–2427.

Dismer, F., & Hubbuch, J. (2007). A novel approach to characterize the binding orientation of lysozyme on ion-exchange resins. *Journal of Chromatography A*, *1149*(2), 312–320.

Draget, K.I. (2009). *Handbook of Hydrocolloids*. (P. A. . Phillips, G.O. Williams, Ed.) *Handbook of Hydrocolloids* (2nd ed.). Woodhead Publishing.

Draget, K.I., Skja, G., & Smidsrød, O. (1997). Alginate based new materials. *International Journal of Biological Macromolecules*, *21*, 47–55.

Draget, K.I., Skjåk Bræk, G., & Smidsrød, O. (1994). Alginic acid gels: the effect of alginate chemical composition and molecular weight. *Carbohydrate Polymers*, *25*(1), 31–38.

Duman, O., Tunc, S., Polat, T.G., & Bozo, B.K. (2016). Synthesis of magnetic oxidized multiwalled carbon application in cationic Methylene Blue dye

adsorption. *Carbohydrate Polymers*, *147*, 79–88.

Eiselt, P., Yeh, J., Latvala, R.K., Shea, L. D., & Mooney, D.J. (2000). Porous carriers for biomedical applications based on alginate hydrogels. *Biomaterials*, *21*(19), 1921–7.

Ethève, J., & Déjardin, P. (2002). Adsorption kinetics of lysozyme on silica at pH 7.4: Correlation between streaming potential and adsorbed amount. *Langmuir*, *18*(5), 1777–1785.

Fang, Z. and Bhandari, B. (2010). Encapsulation of polyphenols - a review. *Trends in Food Science and Technology, 21*(10)*,* 510-523.

Fang, Y., Al-assaf, S., Phillips, G.O., Funami, T., Williams, P.A, Li, L., & Nishinari, K. (2007). Multiple Steps and Critical Behaviors of the Binding of Calcium to Alginate. *Journal of Physical Chemistry B*, *111*(10), 2456–2462.

Fernandez Farres, I., Douaire, M., & Norton, I.T. (2013). Rheology and tribological properties of Ca-alginate fluid gels produced by diffusion-controlled method. *Food Hydrocolloids*, *32*(1), 115–122.

Fernández Farrés, I., & Norton, I.T. (2014). Formation kinetics and rheology of alginate fluid gels produced by in-situ calcium release. *Food Hydrocolloids*, *40*, 76–84.

Florence, N., & Naorem, H. (2014). Dimerization of methylene blue in aqueous and mixed aqueous organic solvent: A spectroscopic study. *Journal of Molecular Liquids*, *198*, 255–258.

Flury, Markus; Wai, N.N. (2003). Dyes as tracers for vadose zone hydrology. *Reviews of Geophysics*, *41*(1), 1002.

Food Standards Agency. (2007). *FSA nutrient and food based guidelines for UK institutions 2007*. *FSA*. London: FSA.

Fu, S., Thacker, A., Sperger, D.M., Boni, R. L., Buckner, I.S., Velankar, S., Munsen, E., Block, L.H. (2011). Relevance of rheological properties of sodium alginate in solution to calcium alginate gel properties. *AAPS PharmSciTech*, *12*(2), 453–460.

Fuenzalida, J.P., Nareddy, P.K., Moreno-Villoslada, I., Moerschbacher, B.M., Swamy, M.J., Pan, S., Ostermeier, M., Goycoolea, F.M. (2016). On the role of alginate structure in complexing with lysozyme and application for enzyme delivery. *Food Hydrocolloids*, *53*, 239–248.

Galati, G., & O'Brien, P.J. (2004). Potential toxicity of flavonoids and other dietary phenolics: Significance for their chemopreventive and anticancer properties. *Free Radical Biology and Medicine*, *37*(3), 287–303.

Ganguly, S., & Chakraborty, S. (2009). Effective viscosity of nanoscale colloidal suspensions. *Journal of Applied Physics*, *106*(124309), 1–10.

Garcia-Alonsoa, J., Fakhrullin, R.F., & Paunov, V.N. (2010). Rapid and direct magnetization of GFP-reporter yeast for micro-screening systems. *Biosensors and Bioelectronics*, *25*(7), 1816–1819.

Gavi, E., Marchisio, D.L., & Barresi, A.A. (2007). CFD modelling and scale-up of Confined Impinging Jet Reactors. *Chemical Engineering Science*, *62*(8), 2228–2241.

Gehring, J., Schleheck, D., Luka, M., & Polarz, S. (2014). Aerosol-synthesis of mesoporous organosilica nanoparticles with highly reactive, superacidic surfaces comprising sulfonic acid entities. *Advanced Functional Materials*, *24*(8), 1140–1150.

George, M., & Abraham, T.E. (2006). Polyionic hydrocolloids for the intestinal delivery of protein drugs: alginate and chitosan-a review. *Journal of Controlled Release* , *114*(1), 1–14.

Germán-Heins, J., & Flury, M. (2000). Sorption of Brilliant Blue FCF in soils as affected by pH and ionic strength. *Geoderma*, *97*(1-2), 87–101.

Giménez-Bastida, J. A., Zielinski, H., Piskula, M., Zielinska, D., & Szawara-Nowak, D. (2016). Buckwheat bioactive compounds, their derived phenolic metabolites and their health benefits. *Molecular Nutrition & Food Research*, 1–10.

Gombotz, W. R., & Wee, S. F. (1998b). Protein release from alginate matrices. *Advanced Drug Delivery Review*, *31*, 267–285.

Goto, T., Teraminami, A., Lee, J.Y., Ohyama, K., Funakoshi, K., Kim, Y.I., Hirai, S., Uemura, T., Yu, R., Nobuyoki, T., Kawada, T. (2012). Tiliroside, a glycosidic flavonoid, ameliorates obesity-induced metabolic disorders via activation of adiponectin signaling followed by enhancement of fatty acid oxidation in liver and skeletal muscle in obese-diabetic mice. *Journal of Nutritional Biochemistry*, *23*(7), 768–776.

Goycoolea, F.M., Lollo, G., & Remun, C. (2009). Chitosan-Alginate Blended

Nanoparticles as Carriers for the Transmucosal Delivery of Macromolecules. *Biomacromolecules*, *10*(7), 1736–1743.

Grant, G.T., Morris, E.R, Reese, D.A., Smith, P.J.C., Thom, D. (1973). Biological interactions between polysaccharides and divalent cations: The egg-box model. *FEBS Letters*, *32*(1), 195–198.

Gul, K., Tak, A., Singh, A. K., Singh, P., Yousuf, B., & Wani, A.A. (2015). Chemistry, encapsulation, and health benefits of Beta-carotene - A review. *Cogent Food & Agriculture*, *1*(1), 1–12.

Han, J., Zhu, Z., Qian, H., Wohl, A.R., Beaman, C. J., Hoye, T.R., & Macosko, C.W. (2012). A Simple Confined Impingement Jets Mixer for Flash Nanoprecipitation. *Journal of Pharmaceutical Sciences*, *101*(10), 26–33.

Herrero-Martínez, J.M., Sanmartin, M., Rosés, M., Bosch, E., & Ràfols, C. (2005). Determination of dissociation constants of flavonoids by capillary electrophoresis. *Electrophoresis*, *26*(10), 1886–1895.

Homem-De-Mello, P., Mennucci, B., Tomasi, J., & Da Silva, A.B.F. (2007). Cationic dye dimers: A theoretical study. *Theoretical Chemistry Accounts*, *118*(2), 305–314.

Horiba Instrument Catalog. (2014). A Guidebook To Particle Size Analysis. *Horiba Instrument Catalog*, 1–32.

Hossain, M., Kabir, A., & Suresh Kumar, G. (2012). Binding of the phenothiazinium dye methylene blue with single stranded polyriboadenylic acid. *Dyes and Pigments*, *92*(3), 1376–1383.

Hughey, V.L., Johnson, E.A., & Wilger, P.A. (1989). Antibacterial activity of hen egg white lysozyme against *Listeria monocytogenes* Scott A in foods. *Appl Environ Microbiol*, *55*(3), 631–638.

Ianoş, R., Tăculescu, A., Păcurariu, C., & Lazău, I. (2012). Solution Combustion Synthesis and Characterization of Magnetite, Fe_3O_4 , Nanopowders. *Journal of the American Ceramic Society*, *95*(7), 2236–2240.

Jank, M., Koser, H., Lucking, F., Martienssen, M., & Wittchen, S. (1998). Decolorization and degradation of Erioglaucine (acid blue 9) dye in wastewater. *Environmental Technology*, *19*(7), 741–747.

Jannin, V., Chevrier, S.M. M., Dumont, C., Belotti, S., Chavant, Y., & Demarne,

F. (2015). Development of Self Emulsifying Lipid Formulations of BCS class II drugs with low to medium lipophilicity. *International Journal of Pharmaceutics*, *495*, 385–392.

Jha, M., Chakraborty, G., Bardhan, S., Debnath, B., & Saha, S.K. (2016). Unperturbed dimension, interaction parameters, zeta potential and rheology of sodium alginate in binary solvent mixtures. *Journal of Polymer Research*, *23*(162), 1–11.

Johnson, B.K., & Prud, R.K. (2003). Chemical Processing and Micromixing in Confined Impinging Jets. *AIChE Journal*, *49*(9), 2264-2282.

Joye, I.J., & McClements, D.J. (2014). Biopolymer-based nanoparticles and microparticles : Fabrication, characterization, and application. *Current Opinion in Colloid & Interface Science*, *19*(5), 417–427.

Kailasapathy, K. (2006). Survival of free and encapsulated probiotic bacteria and their effect on the sensory properties of yoghurt. *LWT - Food Science and Technology*, *39*(10), 1221–1227.

Kallel, F., Chaari, F., Bouaziz, F., Bettaieb, F., Ghorbel, R., & Ellouz, S. (2016). Sorption and desorption characteristics for the removal of a toxic dye , methylene blue from aqueous solution by a low cost agricultural by-product. *Journal of Molecular Liquids*, *219*, 279–288.

Kardos, N., Luche, J., Esigec, D.S., & Bourget, F.Le. (2001). Sonochemistry of carbohydrate compounds. *Carbohydrate Research*, *332*, 115–131.

Ketelsen, H., & Meyer-Windel, S. (1999). Adsorption of brilliant blue FCF by soils. *Geoderma*, *90*(1-2), 131–145.

Kreft, S., Knapp, M., & Kreft, I. (1999). Extraction of rutin from buckwheat (Fagopyrum esculentum moench) seeds and determination by capillary electrophoresis. *Journal of Agricultural and Food Chemistry*, *47*(11), 4649–4652.

Kuo, C.K., & Ma, P.X. (2001). Ionically crosslinked alginate hydrogels as scaffolds for tissue engineering: part 1. Structure, gelation rate and mechanical properties. *Biomaterials*, *22*(6), 511–21.

Lee, K.Y., & Mooney, D.J. (2012). Alginate: properties and biomedical applications. *Progress in Polymer Science*, *37*(1), 106–126.

León, R., Martín, M., Vigara, J., Vilchez, C., & Vega, J.M. (2003). Microalgae

mediated photoproduction of β-carotene in aqueous-organic two phase systems. *Biomolecular Engineering*, *20*(4-6), 177–182.

Lertsutthiwong, P., Noomun, K., Jongaroonngamsang, N., Rojsitthisak, P., & Nimmannit, U. (2008). Preparation of alginate nanocapsules containing turmeric oil. *Carbohydrate Polymers*, *74*(2), 209–214.

Lertsutthiwong, P., Rojsitthisak, P., & Nimmannit, U. (2009). Preparation of turmeric oil-loaded chitosan-alginate biopolymeric nanocapsules. *Materials Science & Engineering C*, *29*(3), 856–860.

Li, X., Xu, A., Xie, H., Yu, W., Xie, W., & Ma, X. (2010). Preparation of low molecular weight alginate by hydrogen peroxide depolymerization for tissue engineering. *Carbohydrate Polymers*, *79*(3), 660–664.

Li, Y., Hu, M., Du, Y., Xiao, H., & McClements, D.J. (2011). Control of lipase digestibility of emulsified lipids by encapsulation within calcium alginate beads. *Food Hydrocolloids*, *25*(1), 122–130.

Liburdi, K., Benucci, I., & Esti, M. (2014). Lysozyme in Wine: An Overview of Current and Future Applications. *Comprehensive Reviews in Food Science and Food Safety*, *13*(5), 1062–1073.

Lide, D.R. (2010). Dissociation Constants of Organic Acids and Bases in *CRC Handbook of Chemistry and Physics* (W.M. Haynes, Ed.), Boca Raton, Florida:Taylor and Francis.

Lipatova, I.M., Makarova, L.I., & Mezina, E.A. (2016). A spectrophotometric study of the complexation between methylene blue dye and sodium alginate. *Russian Journal of General Chemistry*, *86*(9), 2226–2231.

Liu, D., Guo, Y., Wang, Z., & Yuan, J. (2010). Exogenous lysozyme influences Clostridium perfringens colonization and intestinal barrier function in broiler chickens. *Avian Pathol*, *39*(1), 17–24.

Liu, H., You, L., Ye, X., Li, W., & Wu, Z. (2008). Adsorption kinetics of an organic dye by wet hybrid gel monoliths. *Journal of Sol-Gel Science and Technology*, *45*(3), 279–290.

Lonnerdal, B. and Iyer, S. (1995). Lactoferrin : Molecular structure and biological function. *Annu. Rev. Nutr.*, *15*, 93–110.

Luo, Z., Murray, B.S., Ross, A.L., Povey, M.J.W., Morgan, M.R.A., & Day, A.J. (2012). Effects of pH on the ability of flavonoids to act as Pickering

emulsion stabilizers. *Colloids and Surfaces B: Biointerfaces*, *92*, 84–90.

Luo, Z., Murray, B.S., Yusoff, A., Morgan, M.R.A, Povey, M.J.W., & Day, A.J. (2011). Particle-stabilizing effects of flavonoids at the oil-water interface. *Journal of Agricultural and Food Chemistry*, *59*(6), 2636–45.

Lyon, L.A., Hendrickson, G.A., Meng, Z., & Iyer, A.N.S. (2011). Exploiting the Optical Properties of Microgels as Microlenses and Photonic crystals in Sensing Applications. In A. Fernandez-Nieves, H. Wyss, J. Mattsson, & D.A. Weitz (Eds.), *Microgel suspensions: fundamentals and applications* (pp. 357–374). Wiley-VCH Verlag GmbH & Co., Weinheim, Germany.

Macedo, A.S., Quelhas, S., Silva, A.M., & Souto, E.B. (2014). Nanoemulsions for delivery of flavonoids: formulation and in vitro release of rutin as model drug. *Pharmaceutical Development and Technology*, *19*(6), 677–80.

Machado, A.H.E., Lundberg, D., Ribeiro, A.J., Veiga, F.J., Lindman, B., Miguel, M.G., & Olsson, U. (2012). Preparation of calcium alginate nanoparticles using water-in-oil (W/O) nanoemulsions. *Langmuir : The ACS Journal of Surfaces and Colloids*, *28*(9), 4131–41.

Mackie, W., Noy, R., & Sellen, D.B. (1980). Solution properties of sodium alginate. *Biopolymers*, *19*(10), 1839–1860.

Mahatnirunkul, T. (2013). *Preparation of Calcium Alginate Nanoparticles via a Jet Homogenizer*. University of Leeds, Leeds, UK.

Malsten, M. (2011). Microgels in Drug Delivery. In A. Fernandez-Nieves, H.M. Wyss, J. Mattsson, & D.A. Weitz (Eds.), *Microgel suspensions: fundamentals and applications* (pp. 375–405). Wiley-VCH Verlag GmbH & Co., Weinheim, Germany.

Malvern, I. (2011). *INFORM WHITE PAPER DYNAMIC LIGHT SCATTERING*.

Mancini, M., Moresi, M., & Sappino, F. (1996). Rheological behaviour of aqueous dispersions of algal sodium alginates. *Journal of Food Engineering*, *28*(3-4), 283–295.

Manwell, C. (1967). Molecular Palaeogenetics: Amino acid sequence homology in ribonuclease and lysozyme. *Comp. Biochem. Physiol.*, *23*, 383–406.

Marchisio, D., Rivautella, L., & Barresi, A.A. (2006). Design and Scale-Up of Chemical Reactors for Nanoparticle Precipitation. *AIChE*, *52*(5), 1877–1887.

Martirosyan, A., & Schneider, Y. (2014). Engineered Nanomaterials in Food : Implications for Food Safety and Consumer Health. *Int J of Env Res and Pub Health, 11*(6), 5720–5750.

Matsuda, H., Ninomiya, K., Shimoda, H., & Yoshikawa, M. (2002). Hepatoprotective principles from the flowers of Tilia argentea (linden): Structure requirements of tiliroside and mechanisms of action. *Bioorganic and Medicinal Chemistry*, *10*(3), 707–712.

Matsumiya, K., & Murray, B.S. (2016). Soybean protein isolate gel particles as foaming and emulsifying agents. *Food Hydrocolloids*, *60*, 206–215.

Mattea, F., Martín, Á., & Cocero, M.J. (2009). Carotenoid processing with supercritical fluids. *Journal of Food Engineering*, *93*(3), 255–265.

Matteucci, M.E., Hotze, M.A., Johnston, K.P., & Williams, R.O. (2006). Drug nanoparticles by antisolvent precipitation: Mixing energy versus surfactant stabilization. *Langmuir*, *22*(21), 8951–8959.

Mauludin, R., Müller, R.H., & Keck, C.M. (2009). Kinetic solubility and dissolution velocity of rutin nanocrystals. *European Journal of Pharmaceutical Sciences*, *36*(4-5), 502–510.

McCarthy, N.A., Kelly, A.L., O'Mahony, J.A., & Fenelon, M.A. (2014). Sensitivity of emulsions stabilised by bovine β-casein and lactoferrin to heat and $CaCl_2$. *Food Hydrocolloids*, *35*, 420–428.

McClements, D.J. (2012). Requirements for food ingredient and nutraceutical delivery systems. in *Encapsulation technologies and delivery systems for food ingredients and nutraceuticals* (D. J. McClements & N. Garti, Eds.). Woodhead Publishing, Oxford, UK.

McClements, D.J. (2015). *Nanoparticle- and Microparticle-Based Delivery Systems: Encapsulation, Protection, and Release of Active Compounds*. CRC Press, Taylor and Francis Group, Boca Raton, Florida.

McClements, D.J. (2017). Designing biopolymer microgels to encapsulate , protect and deliver bioactive components : Physicochemical aspects. *Advances in Colloid and Interface Science*, *240*, 31–59.

Meissner, P.E., Mandi, G., Coulibaly, B., Witte, S., Tapsoba, T., Mansmann, U., Rekngelshausen, J., Schiek, W., Jahn, A., Walter-Sack, I., Mikus, G., Burhenne, J., Riedel, K.D., Schirmer, R.H., Kouyate, B., Müller, O. (2006).

Methylene blue for malaria in Africa: results from a dose-finding study in combination with chloroquine. *Malaria Journal*, *5*, 84.

Menchicchi, B., Fuenzalida, J. P., Hensel, A., Swamy, M. J., David, L., Rochas, C., & Goycoolea, F.M. (2015). Biophysical Analysis of the Molecular Interactions between Polysaccharides and Mucin. *Biomacromolecules*, *16*(3), 924–935.

Misra, V., Misra, S. P., Dwivedi, M., & Gupta, S. C. (1994). The Loeffler's methylene blue stain: An inexpensive and rapid method for detection of Helicobacter pylori. *Journal of Gastroenterology and Hepatology*, *9*(5), 512–513.

Mohamadnia, Z., Zohuriaan-Mehr, K., Kabiri, K., Jamshidi, A., & Mobedi, H. (2007). Beads of Carrageenan-Alginate for Controlled Drug Delivery. *Journal of Bioactive and Compatible Polymers*, *22*(3), 342–356.

Morris, E.R. (1990). Shear-thinning of "random coil" polysaccharides: Characterisation by two parameters from a simple linear plot. *Carbohydrate Polymers*, *13*(1), 85–96.

Nakamura, M., Nishiyama, Y., Henmi, C., Iwanaga, S., Nakagawa, H., Yamaguchi, K., Akita, K., Mochizuki, S. Takiura, K. (2008). Ink Jet 3-D Digital Fabrication for Biological Tissue Manufacturing: Analysis of Alginate Microgel Beads Produced by Ink Jet Droplets for 3-D Tissue Fabrication. *Journal of Imaging Science and Technology*, *52*(6) 1-6.

Nevinskii, A.G., Soboleva, S.E., Tuzikov, F.V, Buneva, V.N., & Nevinsky, G.A. (2009). DNA, oligosaccharides, and mononucleotides stimulate oligomerization of human lactoferrin. *Journal of Molecular Recognition : JMR*, *22*(4), 330–42.

Nguyen, M.H., Yu, H., Kiew, T.Y., & Hadinoto, K. (2015). Cost-effective alternative to nano-encapsulation: Amorphous curcumin-chitosan nanoparticle complex exhibiting high payload and supersaturation generation. *European Journal of Pharmaceutics and Biopharmaceutics*, *96*, 1–10.

Ninomiya, K., Matsuda, H., Kubo, M., Morikawa, T., Nishida, N., & Yoshikawa, M. (2007). Potent anti-obese principle from Rosa canina: Structural requirements and mode of action of trans-tiliroside. *Bioorganic and*

Medicinal Chemistry Letters, *17*(11), 3059–3064.

Nobbmann, U., Connah, M., Fish, B., Varley, P., Gee, C., Mulot, S., Chen, J., Zhao, L., Lu, Y., Shen, F., Yi, J., Harding, S. E. (2007). Dynamic light scattering as a relative tool for assessing the molecular integrity and stability of monoclonal antibodies. *Biotechnology & Genetic Engineering Reviews*, *24*, 117–28.

Noel, J., Prokop, A., & Tanner, R.D. (2002). Foam fractionation of a dilute solution of bovine lactoferrin. *Applied Biochemistry and Biotechnology*, *98*, 395–402.

Nordgård, C.T. & Draget, K.I. (2011). Oligosaccharides as modulators of rheology in complex mucous systems. *Biomacromolecules*, *12*(8), 3084–3090.

Norton, I.T., Jarvis, D.A., & Foster, T.J. (1999). A molecular model for the formation and properties of fluid gels. *Int J Biol Macromol*, *26*(4), 255–261.

Okada, S., Tanaka, K., Sato, T., Ueno, H., Saito, S., Sato, K., Yamamoto, S., Kakizoe, T. (2002). Dose-response Trial of Lactoferrin in Patients with Chronic Hepatitis C, *Jpn. J. Cancer Res., 93*(September), 1063–1069.

Onishi, H., Koyama, K., Sakata, O., & Machida, Y. (2010). Preparation of chitosan / alginate / calcium complex microparticles loaded with lactoferrin and their efficacy on carrageenan-induced edema in rats. *Drug Development and Industrial Pharmacy, 36*(8), 879–884.

Ouwerx, C., Velings, N., Mestdagh, M., & Axelos, M.A. (1998). Physico-chemical properties and rheology of alginate gel beads formed with various divalent cations. *Polymer Gels and Networks, 6*(5), 393-408.

Padol, A.M., Draget, K.I., & Stokke, B.T. (2016). Effects of added oligoguluronate on mechanical properties of Ca - Alginate - oligoguluronate hydrogels depend on chain length of the alginate. *Carbohydrate Polymers*, *147*, 234–242.

Pamies, R., Schmidt, R. R., Martinez, M. del C. L., & Torre, J. G. de la. (2010). The influence of mono and divalent cations on dilute and non-dilute aqueous solutions of sodium alginates. *Carbohydrate Polymers*, *80*(1), 248–253.

Paques, J.P. (2015). Alginate nanospheres prepared by internal and external

gelation with nanoparticles. In L. M. Sagis (Ed.), *Microencapsulation and Microspheres for Food Applications* (pp. 39–55). Elsevier Inc.

Paques, J. P., Sagis, L. M. C., van Rijn, C. J. M., & van der Linden, E. (2014). Nanospheres of alginate prepared through w/o emulsification and internal gelation with nanoparticles of $CaCO_3$. *Food Hydrocolloids*, *40*, 182–188.

Paques, J.P., van der Linden, E., van Rijn, C.J.M., & Sagis, L.M.C. (2013). Alginate submicron beads prepared through w/o emulsification and gelation with $CaCl_2$ nanoparticles. *Food Hydrocolloids*, *31*(2), 428–434.

Paques, J.P., van der Linden, E., van Rijn, C.J.M., & Sagis, L.M.C. (2014). Preparation methods of alginate nanoparticles. *Advances in Colloid and Interface Science*, *209*, 163–71.

Paramera, E.I., Konteles, S.J., & Karathanos, V.T. (2011). Microencapsulation of curcumin in cells of Saccharomyces cerevisiae. *Food Chemistry*, *125*(3), 892–902.

Park, J.I., Tumarkin, E., & Kumacheva, E. (2010). Small, stable, and monodispersed bubbles encapsulated with biopolymers. *Macromolecular Rapid Communications*, *31*(2), 222–227.

Pashkovski, E. (2011). Applications of Biopolymer Microgels. In A. Fernandez-Nieves, H.M. Wyss, J. Mattsson, & D.A. Weitz (Eds.), *Microgel suspensions: fundamentals and applications* (pp. 423–450). Wiley-VCH Verlag GmbH & Co. Weinheim, Germany.

Pawar, S.N., & Edgar, K.J. (2012). Alginate derivatization: a review of chemistry, properties and applications. *Biomaterials*, *33*(11), 3279–305.

Peinado, I., Lesmes, U., Andrés, A., & McClements, D.J. (2010). Fabrication and morphological characterization of biopolymer particles formed by electrostatic complexation of heat treated lactoferrin and anionic polysaccharides. *Langmuir*, *26*(12), 9827–9834.

Pelton, R., & Hoare, T. (2011). Microgels and Their Synthesis: an Introduction. In. A. Fernandez-Nieves, H.M. Wyss, J. Mattsson, & D.A. Weitz (Eds.), *Microgel suspensions: fundamentals and applications* (pp. 3–25). Wiley-VCH Verlag GmbH & Co. Weinheim, Germany.

Perrin, D.D., and Dempsey, B. (1974). *Practical Limitations in the Use of Buffers*. London: Chapman and Hall.

Pobudkowska, A., Rafols, C., Subirats, X., Bosch, E., & Avdeef, A. (2016). Phenothiazines solution complexity - Determination of pKa and solubility-pH profiles exhibiting sub-micellar aggregation at 25 and 37ºC. *European Journal of Pharmaceutical Sciences*, *93*, 163–176.

Polowczyk, I., Bastrzyk, A., & Fiedot, M. (2016). Protein-mediated precipitation of calcium carbonate. *Materials*, *9*(11), 1–16.

Poncelet, D., Lencki, R., Beaulieu, C., Halle, J.P., Neufeid, R.J., & Fournier, A. (1992). Production of alginate beads by emulsification/internal gelation. I.Methodology. *Appl Microbiol Biotechnol*, *38*, 39–45.

Poon, W.C.K., Weeks, E.R., & Royall, C.P. (2012). On measuring colloidal volume fractions. *Soft Matter*, *8*(1), 21–30.

Prasad, S., Gupta, S.C., Tyagi, A.K., & Aggarwal, B.B. (2014). Curcumin, a component of golden spice: From bedside to bench and back. *Biotechnology Advances*, *32*(6), 1053–1064.

Proctor, V.A., Cunningham, F.E., & Fung, D.Y.C. (1988). The chemistry of lysozyme and its use as a food preservative and a pharmaceutical. *CRC Critical Reviews in Food Science and Nutrition*, *26*(4), 359–395.

Quong, D., Neufeld, R.J., Skjåk-Bræk, G., & Poncelet, D. (1998). External versus internal source of calcium during the gelation of alginate beads for DNA encapsulation. *Biotechnology and Bioengineering*, *57*(4), 438–446.

Ramnani, P., Chitarrari, R., Tuohy, K., Grant, J., Hotchkiss, S., Philp, K., Campbell, R., Gill, C., Rowland, I. (2012). In vitro fermentation and prebiotic potential of novel low molecular weight polysaccharides derived from agar and alginate seaweeds. *Anaerobe*, *18*(1), 1–6.

Rayner, M. (2015). Current status on novel ways for stabilizing food dispersions by oleosins , particles and microgels. *Current Opinion in Food Science*, *3*, 94–109.

Riaz, A., Shreedhar, B., Kamboj, M., & Natarajan, S. (2013). Methylene blue as an early diagnostic marker for oral precancer and cancer. *SpringerPlus*, *2*(1), 95.

Romanowsky, M.B., Abate, A.R., Rotem, A., Holtze, C., & Weitz, D.A. (2012). High throughput production of single core double emulsions in a parallelized microfluidic device. *Lab on Chip*, 802–807.

Rousseau, D. (2013). Current Opinion in Colloid & Interface Science Trends in structuring edible emulsions with Pickering fat crystals. *Current Opinion in Colloid & Interface Science*, *18*(4), 283–291.

Russ, N., Zielbauer, B.I., & Vilgis, T.A. (2014). Impact of sucrose and trehalose on different agarose-hydrocolloid systems. *Food Hydrocolloids*, *41*, 44–52.

Sagara, T., Iizuka, J., & Niki, K. (1992). Electroreflectance Study of the Redox Reaction of Methylene Blue Adsorbed on a Pyrolytic Graphite Electrode. *Langmuir*, *8*, 1018–1025.

Salvia-Trujillo, L., Qian, C., Martín-Belloso, O., & McClements, D.J. (2013). Influence of particle size on lipid digestion and β-carotene bioaccessibility in emulsions and nanoemulsions. *Food Chemistry*, *141*(2), 1475–1480.

Santos, A.C., Cunha, J., Veiga, F., Cordeiro-da-Silva, A., & Ribeiro, A.J. (2013). Ultrasonication of insulin-loaded microgel particles produced by internal gelation: impact on particle's size and insulin bioactivity. *Carbohydrate Polymers*, *98*(2), 1397–408.

Schmidt, S., Liu, T., Stephan, R., Phan, K., Martin, M., & Richtering, W. (2011). Influence of Microgel Architecture and Oil Polarity on Stabilization of Emulsions by Stimuli-Sensitive Core-Shell Poly (N-isopropylacrylamide-co-methacrylic acid) Microgels : Mickering versus Pickering Behavior ? *Langmuir*, *27*, 9801–9806.

Schmitt, C., Moitzi, C., Bovay, C., Rouvet, M., Bovetto, L., Donato, L., Leser, M.E., Schurtenberger, P., Stradner, A. (2010). Internal structure and colloidal behaviour of covalent whey protein microgels obtained by heat treatment. *Soft Matter*, *6*(19), 4876–4884.

Schmitt, V., & Ravaine, V. (2013). Surface compaction versus stretching in Pickering emulsions stabilised by microgels. *Current Opinion in Colloid & Interface Science*, *18*(6), 532–541.

Schneider, N., Becker, C.M., & Pischetsrieder, M. (2010). Analysis of lysozyme in cheese by immunocapture mass spectrometry. *Journal of Chromatography B: Analytical Technologies in the Biomedical and Life Sciences*, *878*(2), 201–206.

Seiffert, S. (2013). Small but Smart : Sensitive Microgel Capsules. *Angew. Chem. Int. Ed.*, *52*, 11462–11468.

Semenova, M., & Dickinson, E. (2010). *Biopolymers in Food Colloids: Thermodynamics and Molecular Interactions*. (G. Burlakova, E.; Zaikov, Eds.). Leiden, The Netherlands: Koninklijke Brill NV.

Sharma, R.A., Gescher, A.J., & Steward, W.P. (2005). Curcumin: The story so far. *European Journal of Cancer*, *41*(13), 1955–1968.

Shewan, H.M. ., & Stokes, J.R. (2012). Biopolymer microgel suspension rheology as a function of particle modulus and effective phase volume. In G.O. Williams, P.A. Phillips (Ed.), *Gums and Stabilisers for the Food Industry 16* (pp. 165–174). Cambridge, UK: Royal Society of Chemistry.

Shewan, H.M., & Stokes, J.R. (2015). Viscosity of soft spherical micro-hydrogel suspensions. *Journal of Colloid and Interface Science*, *442*, 75–81.

Shilpa, A., Agrawal, S.S., & Ray, A.R. (2003). Controlled Delivery of Drugs from Alginate Matrix. *Journal of Macromolecular Science, Part C: Polymer Reviews*, *43*(2), 187–221.

Soobrattee, M.A, Bahorun, T., & Aruoma, O.I. (2006). Chemopreventive actions of polyphenolic compounds in cancer. *BioFactors*, *27*(1-4), 19–35.

Souza, L. De, Madalena, D.A., Pinheiro, A.C., Teixeira, J.A., Vicente, A.A., & Ramos, Ó.L. (2017). Micro- and nano bio-based delivery systems for food applications : In vitro behavior. *Advances in Colloids and Interface Science*, *243*, 23–45.

Sterner, B., Harms, M., Wöll, S., Weigandt, M., Windbergs, M., & Lehr, C.M. (2016). The effect of polymer size and charge of molecules on permeation through synovial membrane and accumulation in hyaline articular cartilage. *European Journal of Pharmaceutics and Biopharmaceutics*, *101*, 126–136.

Stokke, B., Smidsroed, O., Zanetti, F., Strand, W., & Skjak-Braek, G. (1993). Distribution of uronate residues in alginate chains in relation to alginate gelling properties - 2: Enrichment of β-D-mannuronic acid and depletion of α-L-guluronic acid in sol fraction, *Carbohydrate Polymers*, *21*, 39-46.

Struder-Kypke, M. (2013). Confocal Laser Scanning Microscope Instructions Confocal Laser Scanning Microscope. University of Guelph, Canada, College of Biological Sciences.

Tang, W., Xu, H., Kopelman, R., & Philbert, M.A. (2004). Photodynamic characterization and in vitro application of methylene blue-containing

nanoparticle platforms. *Photochemistry and Photobiology*, *81*(2), 242–249.

Tokle, T., Lesmes, U., & McClements, D.J. (2010). Impact of electrostatic deposition of anionic polysaccharides on the stability of oil droplets coated by lactoferrin. *Journal of Agricultural and Food Chemistry*, *58*(17), 9825–9832.

Tønnesen, H.H. (2006). Solubility and stability of curcumin in solutions containing alginate and other viscosity modifying macromolecules: Studies of curcumin and curcuminoids. *Pharmazie*, *61*(8), 696–700.

Torres, O., Murray, B., & Sarkar, A. (2017). Design of novel emulsion microgel particles of tuneable size. *Food Hydrocolloids*, *71*, 47–59.

Tu, J., Bolla, S., Barr, J., Miedema, J., Li, X., & Jasti, B. (2005). Alginate microparticles prepared by spray-coagulation method: Preparation, drug loading and release characterization. *International Journal of Pharmaceutics*, *303*(1-2), 171–181.

van der Vaart, K., Rahmani, Y., Zargar, R., Hu, Z., Bonn, D., & Schall, P. (2013). Rheology of concentrated soft and hard-sphere suspensions. *Journal of Rheology*, *57*(4), 1195–1209.

Velings, N.M., & Mestdagh, M.M. (1995). Physico-chemical properties of alginate gel beads. *Polymer Gels and Networks*, *3*, 311-330.

Verras, A., & Ortiz de Montellano, P.R. (2006). Protein dynamics and imidazole binding in cytochrome P450 enzymes. *Biochemical Society Transactions*, *34*(Pt 6), 1170–2.

Wakabayashi, H., Yamauchi, K., & Takase, M. (2006). Lactoferrin research, technology and applications. *International Dairy Journal*, *16*(11), 1241–1251.

Wang, X., Sun, H., Xia, Y., Chen, C., Xu, H., Shan, H., & Lu, J.R. (2009). Lysozyme mediated calcium carbonate mineralization. *Journal of Colloid and Interface Science*, *332*(1), 96–103.

Wang, Z., Leung, M.H. M., Kee, T.W., & English, D.S. (2010). The role of charge in the surfactant-assisted stabilization of the natural product curcumin. *Langmuir*, *26*(8), 5520–5526.

Wells, L.A, & Sheardown, H. (2007). Extended release of high pI proteins from alginate microspheres via a novel encapsulation technique. *European*

Journal of Pharmaceutics and Biopharmaceutics, *65*(3), 329–35.

Won, K., Kim, S., Kim, K.J., Park, H.W., & Moon, S.J. (2005). Optimization of lipase entrapment in Ca-alginate gel beads. *Process Biochemistry*, *40*, 2149–2154.

Wu, L.Z., Sheng, Y.B., Xie, J. Bin, & Wang, W. (2008). Photoexcitation of tryptophan groups induced reduction of disulfide bonds in hen egg white lysozyme. *Journal of Molecular Structure*, *882*(1-3), 101–106.

Xia, Z., McClements, D.J., & Xiao, H. (2015). Influence of physical state of β-carotene (crystallized versus solubilized) on bioaccessibility. *Journal of Agricultural and Food Chemistry*, *63*(3), 990–997.

Yang, L., She, L., Zhou, J. G., Cao, Y., & Ma, X.M. (2006). Interaction of lysozyme during calcium carbonate precipitation at supramolecular level. *Inorganic Chemistry Communications*, *9*(2), 164–166.

Yazdani, O., Irandoust, M., Ghasemi, J.B., & Hooshmand, S. (2012). Thermodynamic study of the dimerization equilibrium of methylene blue, methylene green and thiazole orange at various surfactant concentrations and different ionic strengths and in mixed solvents by spectral titration and chemometric analysis. *Dyes and Pigments*, *92*(3), 1031–1041.

You, S.J., Udenigwe, C.C., Aluko, R.E., & Wu, J. (2010). Multifunctional peptides from egg white lysozyme. *Food Research International*, *43*(3), 848–855.

Zhang, T., Lv, C.Y., Chen, L.L., Bai, G., Zhao, G., & Xu, C. (2014). Encapsulation of anthocyanin molecules within a ferritin nanocage increases their stability and cell uptake efficiency. *Food Research International*, *62*, 183–192.

Zhang, Z.L., Zhou, M.L., Tang, Y., Li, F.L., Tang, Y.X., Shao, J.R., Xue, W.T., Wu, Y.M. (2012). Bioactive compounds in functional buckwheat food. *Food Research International*, *49*(1), 389–395.

Zhang, Z., Zhang, R., Chen, L., Tong, Q., & McClements, D. J. (2015). Designing hydrogel particles for controlled or targeted release of lipophilic bioactive agents in the gastrointestinal tract. *European Polymer Journal*, *72*, 698–716.

Zhang, Z., Zhang, R., & McClements, D. J. (2016). Encapsulation of beta-

carotene in alginate-based hydrogel beads: Impact on physicochemical stability and bioaccessibility. *Food Hydrocolloids*, *61*, 1–10.

Zhao, Y., Hu, F., Evans, J.J., & Harris, M.T. (2011). Study of sol-gel transition in calcium alginate system by population balance model. *Chemical Engineering Science*, *66*(5), 848–858.

Zheng, B., Zhang, Z., Chen, F., Luo, X., & McClements, D. J. (2017). Impact of delivery system type on curcumin stability: Comparison of curcumin degradation in aqueous solutions, emulsions, and hydrogel beads. *Food Hydrocolloids*, *71*, 187–197.